


MLF ANNUAL REPORT 2013

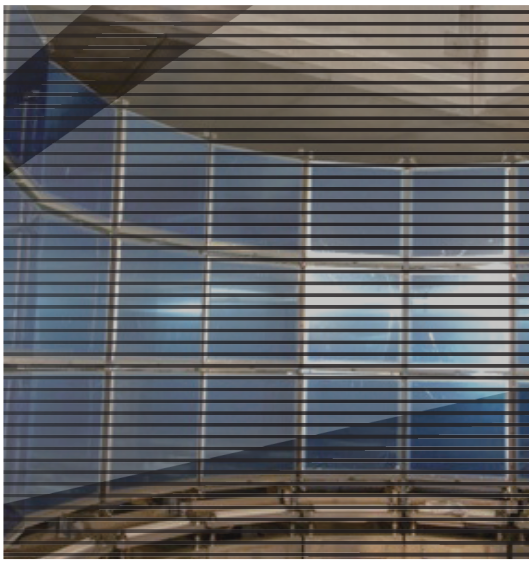
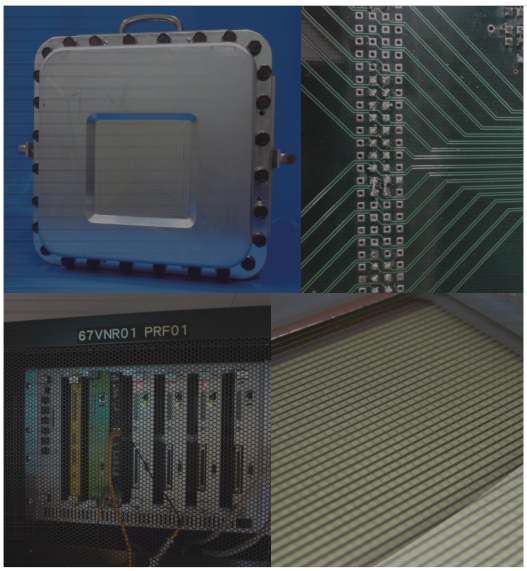



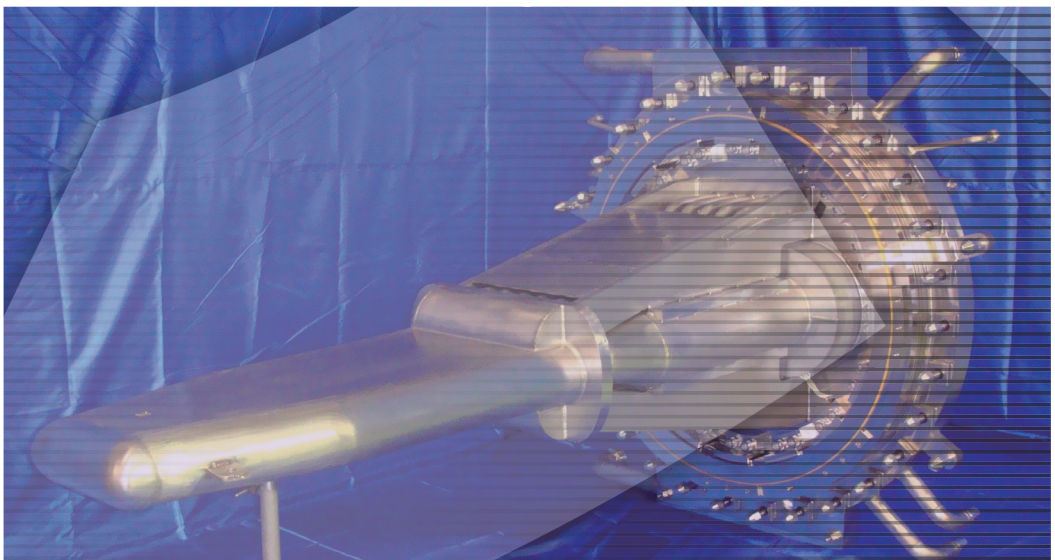

J-PARC/MLF

CROSS

J-PARC 14-03
KEK Progress Report 2014-4

J-PARC/MLF

Materials and Life Science Division
J-PARC Center
Tokai, Naka-gun, Ibaraki 319-1195, Japan
http://j-parc.jp/MatLife/en/index.html

J-PARC was jointly constructed and is now operated by the High Energy Accelerator Research Organization (KEK) and the Japan Atomic Energy Agency (JAEA).

CROSS

Comprehensive Research Organization for Science and Society
http://www.cross-tokai.jp/

Preface to the MLF Annual Report 2013

After the recovery from the disaster, which occurred in 2011, the facility had been operating quite steadily with a fairly high power at 200 kW and then 300 kW, starting from January 2012. However, an incident in the Hadron Facility, one of the three facilities in J-PARC, occurred at midnight on May 23, 2013. This incident forced the shutdown of the whole facility of J-PARC. J-PARC staffs made significant efforts and spent a long time to make assessment of the root cause of the incident, safety analysis, revision of the safety system/organization/manuals, safety drills, explanations to the local public and both the local and the central governments. Then finally we, MLF, were able to obtain an approval for resuming the operation of the facility in January 2014. The user program was seriously affected by the unexpected long shutdown, and more than half of the scheduled experiments for the 2013A term were canceled without any compensation. Here, I sincerely apologize to the MLF users for this incidence and hope to regain sustainable support and mutual reliance.

During the shutdown, we improved the target system and the helium bubbling system, by modifying a part of the mercury (Hg) cooling loop, and realized a full injection of helium bubbles into the Hg flaw. We found out that, during the operation in 2013, the vibration caused by the cavitation in the Hg-target on the proton bombardment had been drastically reduced, which may mitigate significantly the pitting damage on the target container.

When we called for proposals for 2013B in October 2013, we received a large number of applications. Although the operation time for the user program was very limited, we found a large over-subscription. We were impressed by the high expectations from our facility, and confirmed our responsibility to provide a stable operation to the users. Since then the number of applications is steadily increasing, accompanied by a steady increase of users. As of September 2014, the number of general proposals and that of unique users exceeded 750 and 1000 respectively. We are now preparing to ramp up the accelerator power to more than 500 kW in late November 2014. The MLF facility is now almost ready to become a world class user facility in the very near future.

Masatoshi Arai
Division Head of Materials and Life Science Division (MLF)

Three years have passed since CROSS-Tokai commenced operations in support of the user program on the Public Beamlines at the Materials and Life Science Experimental Facility of J-PARC (J-PARC MLF).

As required by the "*Promotion of Public Utilization of Specific Advanced Large-scale Research Facilities*" legislation, under which CROSS was appointed and operates, we are now fully engaged in facility promotion activities such as operating a fair and open proposal selection system for the MLF Public Beamlines, the provision of high-quality user support and the promotion of facility utilization by both academic and industrial researchers.

During 2013, CROSS-Tokai supported the user program on six fully-operational Public Beamlines: BL01 *4SEASONS*, BL02 *DNA*, BL11 *PLANET*, BL15 *TAIKAN*, BL17 *SHARAKU* and BL18 *SENJU*. In addition, construction work continued on the seventh Public Beamline, BL22 *RADEN*, which will be available to users in 2015. Unfortunately, user operations during the year were severely affected by the Hadron Facility incident and its aftereffects with beamtime being available during April-May 2013 and from mid-February to the end of March 2014 only.

A further important responsibility of CROSS-Tokai is the evaluation of Contract Beamlines at the MLF. During 2013, the Contract Beamline Evaluation Committee established by CROSS-Tokai during 2012, undertook and completed reviews of the operation and performance of the two Ibaraki Prefecture beamlines: BL03 *iBIX* and BL20 *iMATERIA*.

Special programs to promote facility utilization developed by CROSS-Tokai in 2012, continued to operate successfully during 2013 and a summary of these activities is presented in this Report. These include:

- **Trial Use** – a program that promotes the use of neutrons by first-time or novice users from both the industrial and academic sectors;
- **Elements Strategy Initiative** – an integrated strategic research program of the Japanese government that aims to promote the development of innovative materials and alternative technologies in the target areas of permanent magnets, catalysis and batteries, and electronic and structural materials; and,
- **Complementary Use** – a program designed to encourage and facilitate the complementary and collaborative use of pulsed neutrons (J-PARC MLF) and synchrotron radiation (SPring-8).

In the area of facility utilization promotion, we have in the last year joined with JASRI – our sister organization at SPring-8 – to develop a system of Complementary Use proposals. This system aims to encourage and facilitate complementary and collaborative use of multiple large-scale facilities – initially neutron and synchrotron radiation sources – in a single research project. We hope that, ultimately, the system will develop to a stage where users can make a single research proposal to multiple facilities.

I hope that this Annual Report will be a useful resource for anyone wishing to know more about the current status of the MLF, the recent scientific outcomes, the technical R&D projects that support the science program, and the operational details of our facility.

On behalf of the team at CROSS-Tokai, I extend a warm welcome to all researchers who wish to make use of the Public Beamlines at J-PARC MLF.

Hideaki Yokomizo
Director, CROSS-Tokai

---

* Research Center for Neutron Science and Technology, Comprehensive Research Organization for Science and Society
www.cross-tokai.jp

Contents

Neutron Science

Muon Science

Radiation Safety

What's new at the MLF in 2013?

MLF Operations in 2013

Organization Chart

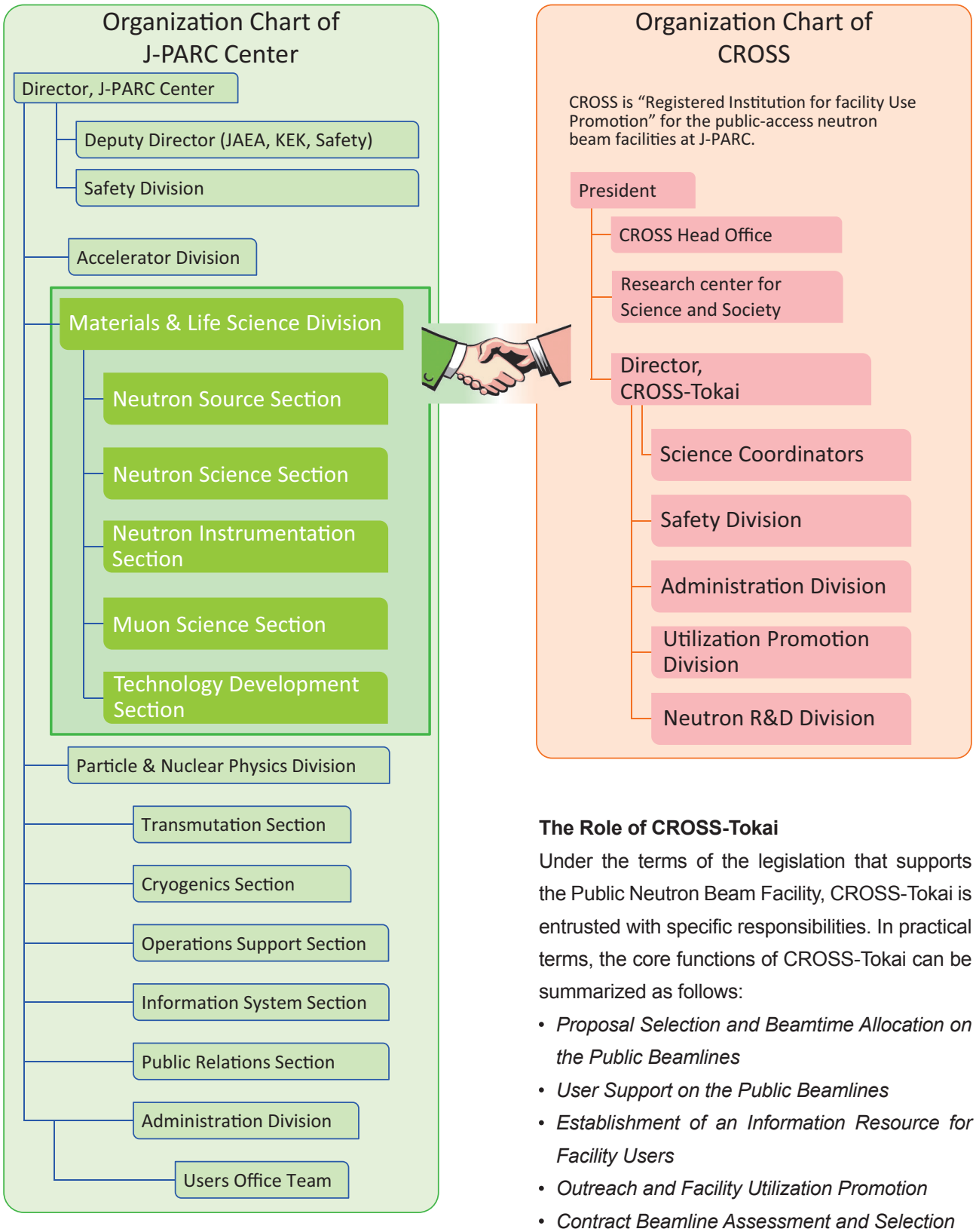

The Role of CROSS-Tokai

Under the terms of the legislation that supports the Public Neutron Beam Facility, CROSS-Tokai is entrusted with specific responsibilities. In practical terms, the core functions of CROSS-Tokai can be summarized as follows:

- *Proposal Selection and Beamtime Allocation on the Public Beamlines*
- *User Support on the Public Beamlines*
- *Establishment of an Information Resource for Facility Users*
- *Outreach and Facility Utilization Promotion*
- *Contract Beamline Assessment and Selection*

J-PARC MAP

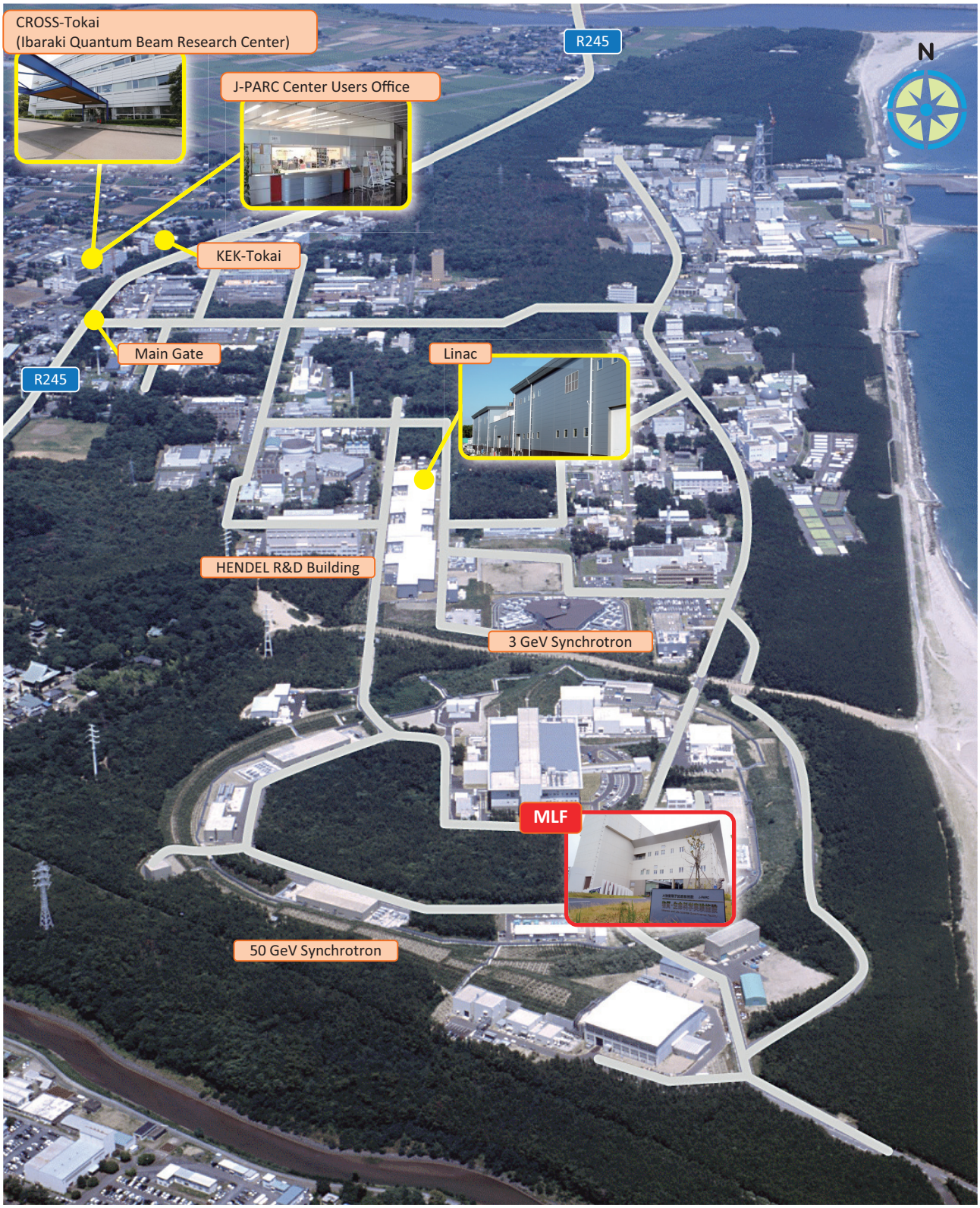
CROSS-Tokai
(Ibaraki Quantum Beam Research Center)
J-PARC Center Users Office
KEK-Tokai
Main Gate
R245
R245
N
Linac
HENDEL R&D Building
3 GeV Synchrotron
MLF
50 GeV Synchrotron

Muon and Neutron Instruments

Muon Source

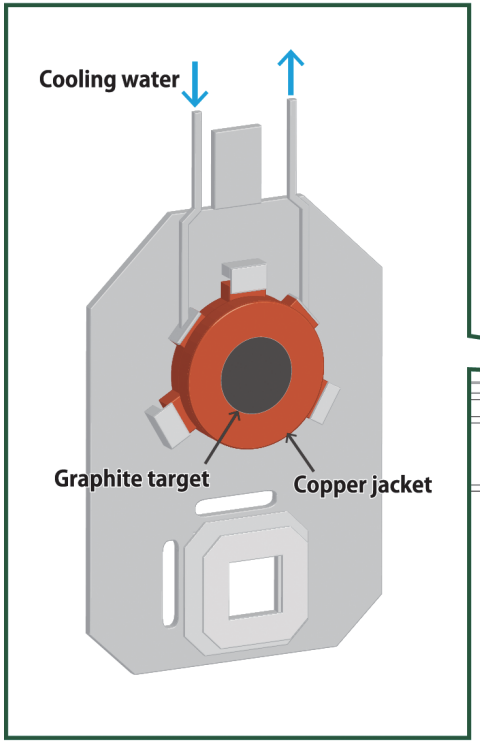

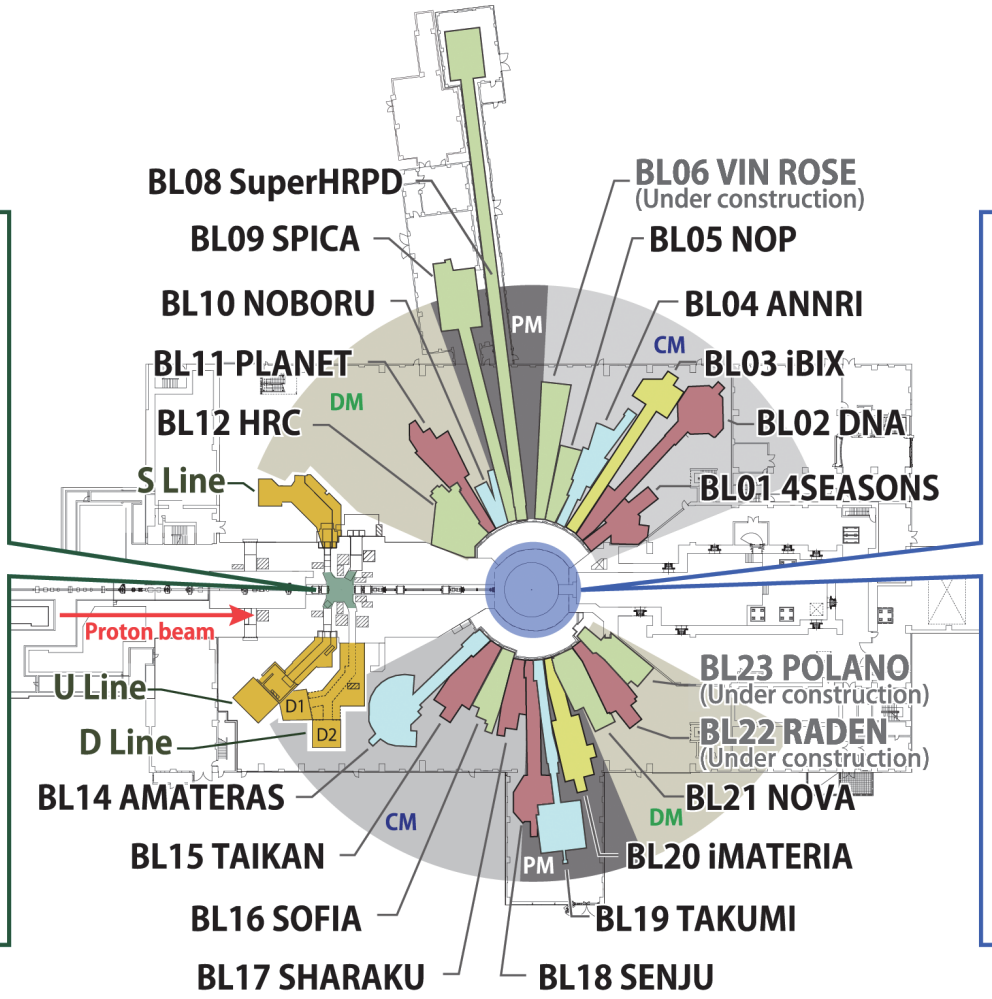

Neutron Source

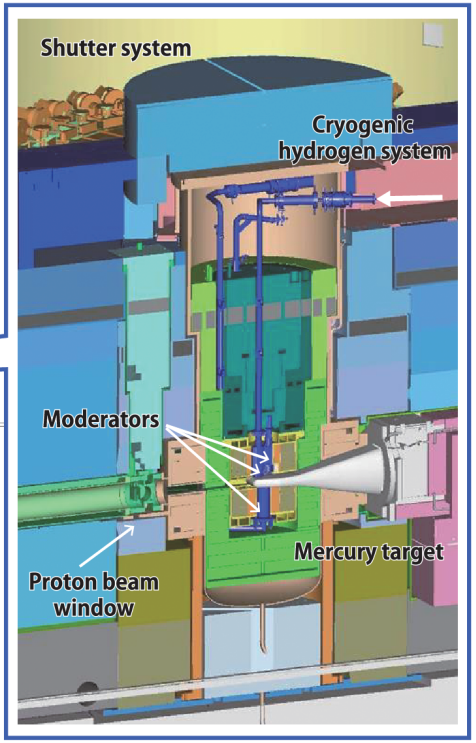

Muon Instruments

Neutron Instruments

JAEA

KEK

Public beam lines

Ibaraki Pref.

Type of moderators

CM Coupled moderator

DM Decoupled moderator

PM Poisoned moderator

Research and Development Highlights

Investigations of 3D Atomic Local Structures around Dopants by Neutron Atomic Resolution Holography

1. Introduction

The performance of most of functional materials can be controlled by doping; for instance, the electrical conductivity of silicon can be controlled by doping a very small amount of boron or phosphorus. Thus, understanding the distortions of local atomic structures around the dopants from the average structures is indispensable to clarify the mechanisms of functionability. Recently, pair distribution function (PDF) method, and X-ray absorption fine structure (XAFS) method are actively used for local structure investigations. However, these methods provide only information on the distance between atoms, and cannot observe 3D structures. Moreover, even for radiation X-rays, accurate observations of light elements, such as B, Li, H, in materials are difficult in spite of the importance of those elements.

The authors are developing the neutron atomic resolution holography (ARH) for investigations of local structures of light elements in materials. The ARH is the unique probe to observe 3D local atomic structures using interference between a wave, which is scattered by elements (object wave), and a wave, which is not scattered (reference wave) [1,2]. The detailed principles can be found in Ref.2. The advantages of ARH in comparison with other methods are as follows: (a) 3D atomic images can be visualized without models. (b) 3D local structures within ~20 Å around a dopant can be observed. (c) the center element can be selected. Photoelectron and fluorescent X-rays ARH have been already in practical use for materials science in Japan. However, light elements cannot be observed accurately by electrons or X-rays. To overcome this, Cser et al. proposed the neutron ARH in 2001 [3], and the first demonstration experiment was performed using a single crystal of $Al_4Ta_3O_{13}(OH)$ by Sur et al. in Chalk River Laboratory, Canada [4]. However, the neutron ARH is still in the demonstration stage. Thus, we aim at developing a neutron ARH for practical investigations in materials science.

2. Neutron ARH experiments

There are two types of neutron ARH experiments: normal method and inverse method [2]. The important difference is that the neutron intensity is measured for the normal method, while the intensity of prompt γ-ray is measured for inverse method. For experiments on BL10, the inverse method was used. The principle of the normal method can be found in Ref. 2 and 5, and is not explained here.

Figure 1 shows the principle of the inverse

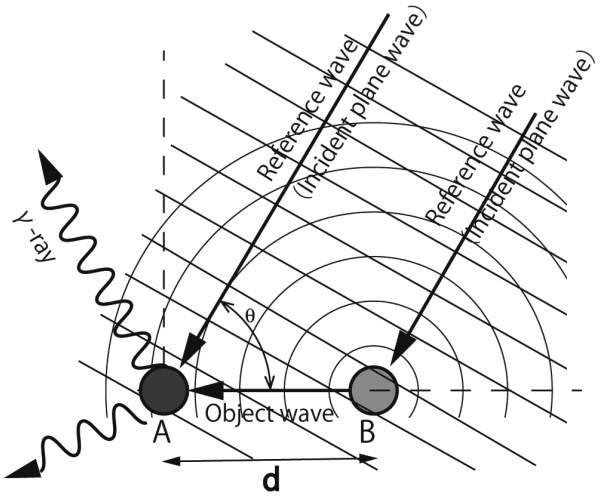

Figure 1. Principle of neutron ARH for the inverse method (from Ref.1).

method. The reference wave is the incident neutron beam as plane wave, and the object wave is spherical wave scattered by the element B. The interference between the reference and object wave generates standing wave in the sample; the intensity of the standing wave is dependent on the positional relation between elements A and B, and the direction of the incident beam. When element A has a large absorption cross-section, such as for B, γ-ray is generated isotropically by the absorption at element A. Since the intensity of the γ-ray is proportional to the amplitude of the standing wave at element A, the intensity map gives us information on interference, that is, a hologram. A hologram can be represented as follows:

$$I(\theta, \lambda) \cong 1 + 2Re\left(\frac{b}{2\pi d} e^{2\pi i d(\cos\theta - 1)/\lambda}\right) \quad (1)$$

where *b* is a scattering length of the nuclear, λ is wavelength of neutrons, *d* is the distance between elements A and B. Transformations from the holograms to atomic images can be found in Ref. 2.

We already performed the normal method neutron ARH experiments of a $PdH_{0.78}$ single crystal in JRR-3 of Japan Atomic Energy Agency, and succeeded in visualizing the atomic structure around a hydrogen [5]. However, the accuracy of the atomic image was not sufficient because of fake images (the so-called twin images). The main reason for the poor accuracy was that only the monochromatic beam with λ = 1.82 Å was used in the experiments; to avoid twin images, measurements using many wavelengths are effective. However, multi-wavelength experiments in reactor facilities require impracticably long measurement times. To overcome this, we are developing a novel technique, the pulsed neutron ARH by the inverse method. Since pulsed neutrons are white beams, a large number of holograms with different wavelengths can be obtained at once. Thus, we expect that pulsed neutron ARH can enhance drastically the accuracy of atomic images.

3. Results of Neutron ARH on BL10

In 2013, we performed the world's first pulsed neutron ARH experiments on BL10 at J-PARC by the inverse method, and obtained about 120 holograms with different wavelengths. The instrument consists of a γ-ray counter with Pb shield and a ϕ–ω goniometer. The intensity of the γ-ray was observed by the event recording method during continuous move of the goniometer. The sample was a single crystal of 1% Eu doped CaF_2, which is an important material for neutron scintillation counters under high temperature and humidity. Figure 2 shows typical holograms that have angular dependence on the intensity of the γ-ray from the sample. Since Eu has a large absorption cross section (4530 b at λ = 1.80 A), and those of Ca and F are relatively negligible, it means that the observed γ-ray was caused from the doped Eu; thus, the obtained holograms show the local structure around doped Eu.

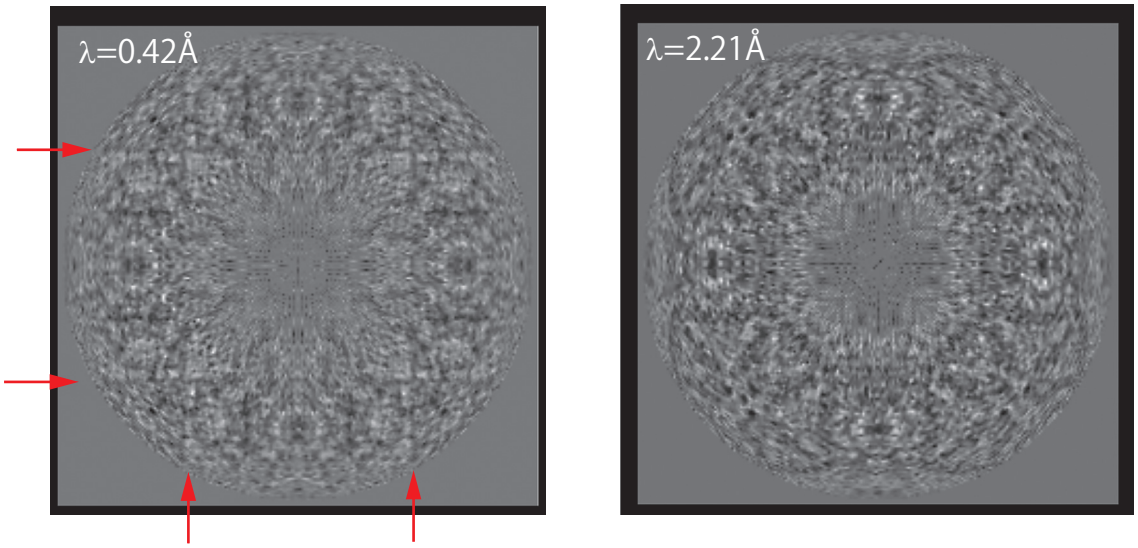

Figure 2. Obtained holograms on BL10 with wavelength of 0.42 Å and 2.21 Å. The red arrows show standing wave lines.

Some of the obtained holograms clearly show linear structures called standing wave lines (red arrows in Fig.2); the lines in Fig.2 indicate the direction of (001) axes around Eu. These standing wave lines definitely mean that we succeeded in observing the symmetry of the local structure around Eu in this sample. Though the analysis of 120 holograms is in progress, we confirmed that Eu occupies the Ca site as expected.

The results obtained from BL10 indicate that highly accurate local structure studies are possible by neutron ARH at J-PARC. Because of the importance of light atoms in functional materials, the neutron ARH will impact strongly the materials science. Since Japan is a leading country in this field, the neutron ARH experiments will be an important contribution of J-PARC to the world.

References

[1] K. Ohoyama, and K. Hayashi, Isotope News, 724, 14 (2014) in Japanese.

[2] K. Hayashi, N. Happo, S. Hosokawa, W. Hu, and T. Matsushita, J. Phys.: Condens. Matter, 24, 093201 (2012).

[3] L. Cser, G. Krexner, and Gy. Török, Europhys. Lett. 54, 747 (2001).

[4] B. Sur, R. B. Rogge, R. P. Hammond, V. N. P. Anghel, and J. Katsaras, Nature 414, 525 (2011).

[5] K. Hayashi, K. Ohoyama, S. Orimo, Y. Nakamori, H. Takahashi, and K. Shibata, Jpn. J. Appl. Phys. **47**, 2291 (2008).

K. Ohoyama[1,2], K. Hayashi[2], S. Hosokawa[3], N. Happo[4], M. Harada[5], and Y. Inamura[6]

[1]Advanced Institute for Materials Science, Tohoku Univ.; [2]Institute for Materials Research, Tohoku Univ.; [3]Dept. Phys., Kumamoto Univ.; [4]Hiroshima City Univ.; [5]Neutron Source Section, Materials and Life Science Division, J-PARC Center; [6]Neutron Science Section, Materials and Life Science Division, J-PARC Center

Magnetic Frustration in *5d* Iridium Spinel $CuIr_2S_4$ Investigated by Muon Spin Relaxation

1. Introduction

Lately, *5d* transition metal oxides are drawing considerable interest, as they might exhibit an unconventional ground state due to the strong spin-orbit (SO) coupling comparable with electron correlation. The strong SO coupling entangles the spin and orbital degrees of freedom, where the magnetic interaction of edge-shared $Ir^{4+}O_6$ octahedra is modeled by the quantum compass model [1]. The form of the exchange interaction depends on the spatial orientation of a given bond, leading to highly anisotropic (Ising type) interaction between the Ir ions.

In real materials, $CuIr_2S_4$ in its insulating phase would serve as an ideal stage of the quantum compass model, as it partly comprises an edge-shared $Ir^{4+}S_6$ network. We investigate the magnetic ground state of $(Cu_{1-x}Zn_x)Ir_2S_4$ using muon spin relaxation (μSR) [2]. The average charge state of $CuIr_2S_4$ yields $Ir^{+3.5}$ and exhibits a disproportionation to Ir^{3+} ($S = 0$) and Ir^{4+} ($J_{eff} = 1/2$) below the metal to insulator transition of $T_{M\text{-}I} \sim 230$ K [3]. The Zn^{2+} ions substituting Cu^{+} site introduces electrons onto the Ir site, partially lifting the frustration of the Ir^{4+} network by increasing the number of non-magnetic Ir^{3+} ions.

2. μSR measurement

We employed DΩ-1 spectrometer at D1 experimental area, MLF, J-PARC and M15 beamline at TRIUMF to measure zero-field / longitudinal-field (ZF/LF) μSR of $(Cu_{1-x}Zn_x)Ir_2S_4$. The zero-field time spectra are shown in Fig.1a. The development of the exponential component at low temperatures indicates that a glassy magnetism develops in $CuIr_2S_4$. The longitudinal response (Fig.1b), which could be described by the theoretical curves for static magnetism, confirms the glassy magnetism. The magnetic ground state changes when Zn ions are substituting Cu. Fig.1c and d indicate the zero-field muon spin relaxation for Zn substituted samples. With a very small doping of ~ 1%, the magnetic response

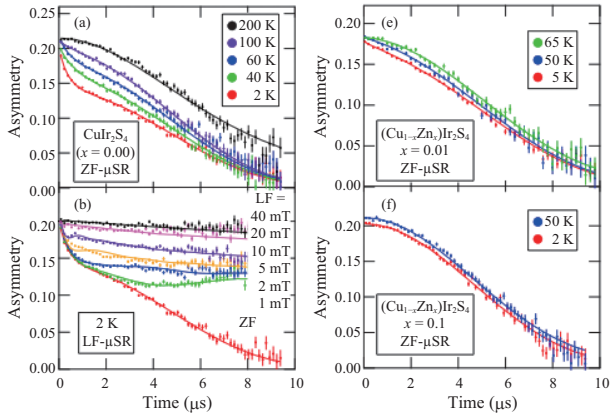

Figure 1. Muon spin relaxation spectra of $(Cu_{1-x}Zn_x)Ir_2S_4$. (a): in zero-field and (b) in magnetic field applied parallel to the muon spin direction (longitudinal fields). (c) and (d): Muon spin relaxation for doped samples.

is diminished and both the amplitude and the rate of the exponential relaxation are reduced.

3. Discussion and Conclusion

In Fig.2, the schematic arrangements of Ir^{3+} and Ir^{4+} of CuI_2S_4 are shown below the M-I transition. Although Ir^{3+} has neither spin nor orbital degrees of freedom, Ir^{4+} has them both alive: spin $S = 1/2$ and orbital $L = 1$. With the spin-orbit (SO) coupling within the single Ir^{4+} ions, $L + S = J_{eff} = 1/2$ spin becomes the good quantum number. The interaction between the neighboring Ir^{4+} ions becomes strongly anisotropic and orientational-dependent from the orbital part of $J_{eff} = 1/2$ spins. This situation is described by quantum compass model, in which many degrees of freedom are frustrated [1]. Together with M-I transition, $CuIr_2S_4$ exhibits a crystal structural change to octamer formation of Ir^{4+} network [3]. *With the SO interactions ignored*, this octamer formation lifts the geometrical frustration of $S = 1/2$ spins by tiling spin singlets consistently on the shortened Ir-Ir bonds [3]. This "octamer singlet" formation of $CuIr_2S_4$ results to a non-magnetic singlet state, which is disproved by our μSR measurement.

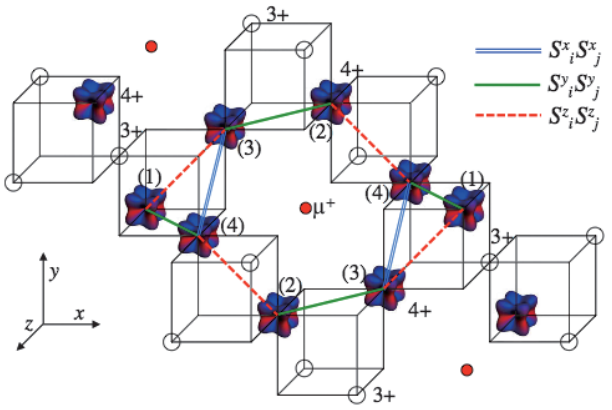

Figure 2. Quantum compass model on the Ir^{4+} octamer of $CuIr_2S_4$. J_{eff} = 1/2 spin which has an orbital component yields directional dependent interaction of Ising type.

The spin glass ground state observed in μSR measurement of $CuIr_2S_4$ suggests that some frustration is not perfectly lifted after the octamer formation. By substituting Ir^{4+} with non-magnetic Ir^{3+} as in $(Cu_{1-x}Zn_x)Ir_2S_4$, the ground state becomes non-magnetic, suggesting that the frustration is lifted by the non-magnetic doping. There has been no microscopic model for the cause of the left-over frustration, but the SO interaction of Ir ions should play an important role in the magnetism of $CuIr_2S_4$ spinels.

References

[1] G. Jackeli and G. Khaliullin, Phys. Rev. Lett. **102**, 017205 (2009).

[2] K. M. Kojima *et al.*, Phys. Rev. Lett. **112**, 087203, (2014).

[3] P. G. Radaeli *et al.*, Nature **416,** 155, (2002).

K. M. Kojima[1,2], R. Kadono[1,2], M. Miyazaki[1,2], M. Hiraishi[1,2], I. Yamauchi[1], A. Koda[1,2], Y. Tsuchiya[3], H. S. Suzuki[3], and H. Kitazawa[3]

[1]*Muon Science Section, Materials and Life Science Division, J-PARC center;* [2]*Insitute of Materials Structure Science, KEK;* [3]*Quantum Beam Unit, National Institute for Materials Science, (NIMS)*

SuperHRPD Finds Tiny Ru-O Bond Increments as Small as 0.0005 Å in Itinerant Ferromagnetic $SrRuO_3$

1. Introduction: *4d* & *5d* novel oxides

A strongly correlated electron system displays numerous physical phenomena, *i.e.* multiferroics, high T_c superconductor, quantum spin system and *etc*. with the coupling of lattice, spin, orbital and charge degree of freedom.

Among the current active research fields, the target of major efforts is the attempt to find novel magnetic phenomena in *4d* and *5d* oxides. In general, these *4d* and *5d* orbitals have more extended orbitals than the *3d* orbitals [1]. Then they have less Coulomb interaction *U* and exchange interaction *J*. Also, their large spin-orbit coupling is proportional to atomic number ~Z^4.

For the *5d* Ir oxides, Sr_2IrO_4 shows unexpected Mott insulator since large spin-orbit coupling opens band gap with total spin $J_{eff} = 1/2$ [2]. A_2IrO_3(A = Li, Na) have been described in the Kitaev-Heisenberg model [3]. Researchers are trying to find real Kitaev spin liquid system with strong spin-orbit coupling limit in the Kitaev-Heisenberg model. For *4d* Ru oxides, Ru t_{2g} orbital ordering reduces dimensionality from three dimensional networks to one dimensional Haldain chains effectively in $Tl_2Ru_2O_7$ [4]. Li_2RuO_3 is considered by spin liquid system induced by spin dimerization, which show the abrupt change of magnetic susceptibility and structure simultaneously [5]. These *4d* and *5d* novel magnetic materials stimulate the development of both theory and experiments.

2. $SrRuO_3$: *Invar* effect and Itinerant ferromagnetism

$A_{n+1}Ru_nO_{3n+1}$(A = Sr, Ca) is Ruddlesden-Popper series, which shows various physical phenomena with structural modification [2]. *i. e*. Sr_2RuO_4(n = 1) is rare example of triplet superconductor while Ca_2RuO_4 is Mott insulator. $SrRuO_3$(n = ∞) is ferromagnetic while $CaRuO_3$ is paramagnetic.

$SrRuO_3$ and $CaRuO_3$ are distorted ABO_3 perovskite with same *Pbnm* space group (SG 62, $a^-a^-c^+$) from Ideal cubic *Pm-3m* (SG 221, $a^0a^0a^0$). Glazer categorizes Glazer tilting system to describe distorted perovskite effectively by tilting rigid octahedron. Minus '–', plus '+', zero '0' represent out-of-phase tilting, in-phase tilting and no tilting of neighboring octahedrons respectively.

$SrRuO_3$ is a rare example of itinerant ferromagnetic among the *4d* oxides. Even though spatially extended *4d* orbitals, it has quite large magnetic moment ~1.4 μ_B/Ru and high ferromagnetic transition temperature T_c = 165 K. It also shows zero thermal expansion, the so called *Invar* effect, and the change of resistivity is below T_c. While bulk $CaRuO_3$ doesn't show any magnetic transition even though it is near the verge of ferromagnetic instability. Tensile stress can induce ferromagnetic state in $CaRuO_3$ film by lattice mismatch of the substrate [6]. The Goodenough-Kanamori-Anderson (GKA) rule with orbital configuration explained successively the 3d localized magnetism. But the GKA rule couldn't explain the itinerant ferromagnetism in $SrRuO_3$.

The physical properties of Ru ruthenates are very sensitive to tiny structural differences. Even though the crystal structure and ferromagnetic mechanism of $SrRuO_3$ are strongly correlated with each other, their detail relations are still unclear due to limitation of the diffractometer resolution. The SuperHRPD (BL08) beamline has been operating in MLF, J-PARC. At present, the highest resolution it approaches is $\Delta d/d = 0.035\%$.

Thus, to understand the *Invar* effect and the ferromagnetic properties of $SrRuO_3$ compared with paramagnetic $CaRuO_3$, we carried out Time-of-flight powder neutron diffraction with temperature scan from 10 K to 300 K at SuperHRPD in J-PARC [7]. We were able to measure the temperature dependence of the Ru-O bonds, which has not been detectable by the poor resolution diffractometer in previous studies.

RuO_6 octahedron has already been distorted on in-plane at room temperature. Ru-O bonds show

temperature dependence, which means that the octahedron is not rigid and deviates from the Glazer tilting assumption. In the *Pbnm* space group, lattice a is always smaller than lattice b under a rigid octahedron. We took into account the lattice constants with in-plane octahedron deformation that captures the anomaly of lattice inequality a > b. In addition, the octahedron becomes more symmetric at low temperature. This experimental result is quite different from LDA+U calculation which predicts that the Ru t_{2g} orbital ordering favors ferromagnetic ground states [8]. SuperHRPD detected tiny mean bond <Ru-O> increment of about 0.0005 Å below ferromagnetic transition. Ru magnetic moments and <Ru-O> bond increments follow mean field curve of magnetization altogether. Finally, we compared the <Ru-O> bonds and the Ru *4d*-O *2p* band width *W* obtained from empirical formula with paramagnetic $CaRuO_3$ and the reference of Colossal Magneto-Resistance (CMR) $La_{0.75}Ca_{0.25}MnO_3$ [9]. The <Ru-O> bond of paramagnetic $CaRuO_3$ follows usual thermal expansion while itinerant ferromagnetic $SrRuO_3$ shows increments of +0.0005 Å and CMR $La_{0.75}Ca_{0.25}MnO_3$ shows decrements of −0.005 Å below T_c. The structural variation of $SrRuO_3$ is one order smaller than CMR $La_{0.75}Ca_{0.25}MnO_3$. The bandwidth of $CaRuO_3$ keeps constant in the whole temperature range. But $SrRuO_3$ decreases its bandwidth while $La_{0.75}Ca_{0.25}MnO_3$ increases it. The increment <Ru-O> bonds and the localized bandwidth contribute to the Invar effect and possibly the ferromagnetism mechanism respectively in $SrRuO_3$. Most high resolution neutron diffractometers can find new relationships in strongly correlated electron systems, such as their structure and physical properties, which have not been accessible before due to the limitation of resolution.

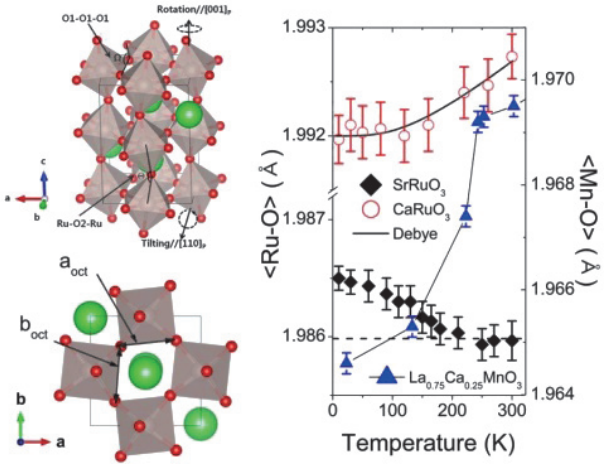

Figure 1. Glazer tilting description (*Pbnm*, $a^-a^-c^+$). Mean <Ru-O> and <Mn-O> bond of itinerant ferromagnetic $SrRuO_3$, paramagnetic $CaRuO_3$ and CMR $La_{0.75}Ca_{0.25}MnO_3$.

References

[1] Eva Pavarini *et al.*, Correlated Electrons: From Models to Materials Modeling and Simulation Vol. 2 Forschungszentrum Jülich (2012).

[2] B. J. Kim *et al.*, Phys. Rev. Lett. **101** (2008) 076402.

[3] Yogesh Singh *et al.*, Phys. Rev. Lett. **108**, 127203 (2012).

[4] Seongsu Lee *et al.*, Nat. Mater. **5** (2006) 471.

[5] G. Jackeli and D. I. Khomskii, Phys. Rev. Lett. **100** (2008) 147203.

[6] S. Tripathi. *et al.*, Sci. Rep. **4** (2014) 3877.

[7] Sanghyun Lee *et al.*, J. Phys.: Condens. Matter **25** (2013) 465601.

[8] H-T. Jeng *et al.*, Phys. Rev. Lett. **97** (2006) 067002.

[9] P. G. Radaelli *et al.*, Phys. Rev. B **56** (1997) 8265.

S. Lee[1,2], S. Torii[1,2], T. Kamiyama[1,2], and J.-G. Park[3]

[1]Neutron Science Section, Materials and Life Science Division, J-PARC center; [2]Insitute of Materials Structure Science, KEK; [3]Center for Correlated Electron Systems, Institute for Basic Science (IBS), Seoul 151,747, Korea

Visualization of Magnetic Field Distribution by Polarized Pulsed Neutron Imaging Inside the Power Magnetic Instruments

The loss reduction of power magnetic instruments such as motors and transformers is an urgent issue in preventing global warming because the loss produces heat increase. In order to reduce the loss, we have to design these equipment in suitable, however, we have little methods to inspect the design directly. In power magnetic instruments both the performances of magnetic materials and the magnetic field designs are important. The polarized pulsed neutron imaging developed in MLF [1] should be able to visualize both the distribution of the material magnetization and the magnetic field, so it is a promising method for magnetization analysis. An expected application is the motor analysis, by measurement of both the motor gap magnetic field and the motor core magnetization. The polarized pulsed neutron imaging in MLF is carried out at beam line BL10.

Among possible magnetic materials to be used for the motor core, amorphous films are expected to reduce the core loss significantly because of their small coercive forces. But they are also extremely sensitive to the stress produced in motor fabrication, which degrades their performance. The degradation could be reduced if the magnetic moments motion inside the motor core is visualized, so the observation through the core is important for the motor design.

Figures 1a) and 1b) show the magnetic moment distribution of the annealed amorphous foil of 25 μm in thickness measured by the polarized pulsed neutron imaging experiments. Because the sample was settled in a magnetic shield box, the results should reflect its residual magnetization state. Fig. 1a) shows the distribution of magnetization components along the horizontal direction (parallel to the X axis), where the red color means positive sign and the blue indicates negative one. Also, the corresponding magnetization vectors in the XY plane, which lies in the foil plane, are indicated by arrows. All the vectors are almost oriented in +Y direction (upward in this figure), but in the red area they incline to the left as they do to the right in the blue area. These areas can be recognized as “magnetic domains”, and their shape change by applying magnetic field is connected directly to the magnetization process. This is the first result showing that the magnetic domains of amorphous foil can be observed through the transmission technique.

The hysteresis loops of this sample, shown in Fig. 1c), suggest that the easy axis is oriented to the L direction, which is the same as Y direction. Therefore, our results showing that the averaged magnetization vector under zero magnetic field is directed to the Y direction, is consistent with the result of the hysteresis loops

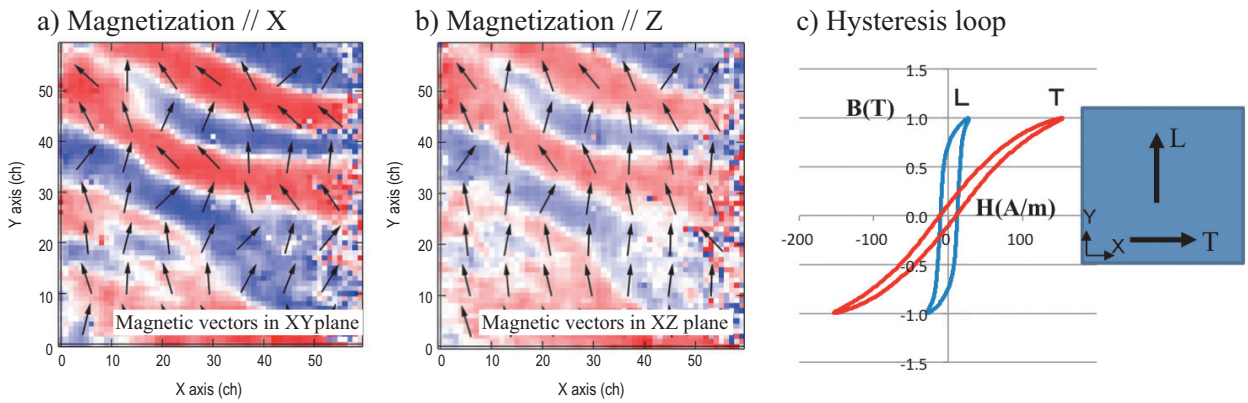

Figure 1. Magnetic domain observation by polarized pulsed neutron imaging.

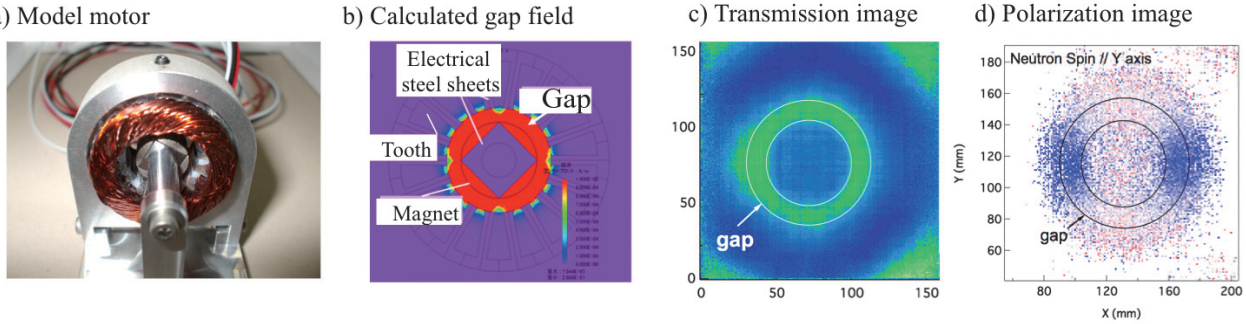

Figure 1. Motor observation by polarized pulsed neutron imaging.

On the other hand, Fig. 1b) shows the distribution of the magnetization component parallel to the beam propagation direction (Z axis), which is normal to the foil surface, and the arrows in this figure indicate magnetic vectors in the YZ plane. Similar magnetic domain structure as in Fig. 1a) was observed. This indicates the presence of perpendicular magnetization due to the perpendicular magnetic anisotropy. While this magnetization component is known as the reason for the degradation of magnetic performance, the presence of such a magnetic component inside the foil was confirmed experimentally for the first time.

Figure 2 shows the result of the motor gap observation. Fig. 2a) shows the model motor fabricated as frameless type so that the motor gap is open and observable by the eye. The stator and the rotor were held with an aluminum frame and an axe, so the holder caused neither neutron depolarization nor any distortion in the magnetic field distribution. On the rotor surface 4 crescent type magnets are stuck and the stator consists of 15 yoke teeth with coils wound by distributed type. Fig. 2b) shows the gap field in absolute value calculated without the coil current. At the center of the gap the maximum magnetic field intensity was 5 kOe. Figure 2c) shows the neutron transmission image of the motor sample. The opaque area at the center of this image corresponds to the rotor, and the surrounded ring-shaped bright area does the motor gap. The polarization image of the motor is shown in Fig. 2d). The neutron spin was along the Y axis. At both sides of the rotor, the neutron polarization kept its initial value, but it turned to zero in the other area. This result indicates that the neutron spin direction and the magnetic field direction were parallel to each other at both sides of the rotor that corresponds to the calculated field direction. Thus, we can analyze the direction of the magnetic field in the motor gap by means of the polarized neutron imaging technique.

From these results the polarized pulsed neutron imaging is found to be a powerful tool for magnetic analysis of the motor magnetization.

Reference

[1] T.Shinohara *et al.*, Nucl. Instrum. Meth., A **651**, 121 (2011).

T. Imagawa[1], T. Hirano[1], K. Souma[2], T. Shinohara[3], and H. Hayasida[4]
[1]Hitachi, Ltd.; [2]Hitachi Industrial Equipment Systems Co., Ltd.; [3]Neutron Science Section, Materials and Life Science Division, J-PARC Center; [4]Neutron R&D Division, CROSS-Tokai

Detection of High Elastic Strain in Fe_3Pt Using TAKUMI

1. Introduction

In most metals and alloys, the elastic limit obtained by experiments is less than 1%, although the first principle calculations suggest it may exceed 10%. It is well known that the movement or creation of dislocations prevent high elastic strain.

Exceptionally high elastic strain is known to appear in alloys with high elastic anisotropy (C_{44}/C'). For example, a large elastic strain of more than 1% was reported in Cu-Al-Ni and Ni-Mn-Ga shape memory alloys. Considering the high elastic strain in these alloys, we may expect that a very high elastic strain can be obtained when the elastic anisotropy becomes very large.

A representative alloy, in which we can expect very high elastic anisotropy, is a partly ordered Fe_3Pt with degree of order 0.75. This alloy exhibits second order like martensitic transformation from a cubic ($L1_2$-type) structure to a tetragonal ($L6_0$-type) structure near 90 K in the cooling process. The lattice parameters change continuously as shown in Fig. 1. Because of the softening in C' associated with the transformation, the anisotropy (C_{44}/C') is expected to become extremely high in the vicinity of the transformation temperature.

In the present study, we examined the elastic deformation of Fe_3Pt under the compressive stress applied in the [001] direction by using BL19 (TAKUMI) at J-PARC. We selected [001] as the compressive direction because the largest elastic strain is expected in this direction when softening in C' occurs.

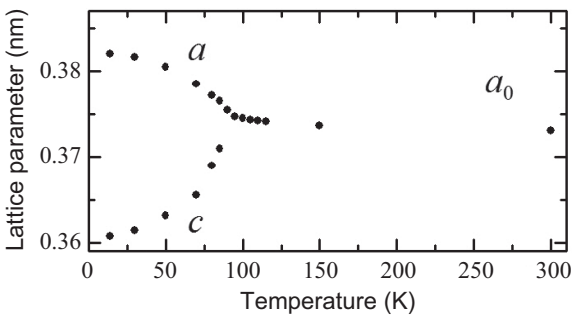

Figure 1. Temperature dependence of lattice parameters of Fe_3Pt [1].

2. Experiments

A single crystal of Fe_3Pt was grown by the floating zone method, and a specimen with dimensions of 9.8 mm × 2.6 mm × 2.5 mm was cut out. The specimen was heat-treated at 1373 K for 24 h and then at 923 K for 100 h to obtain the ordered $L1_2$-type structure with $S = 0.75$. The specimen of Fe_3Pt was compressed in the [001] direction at 93 K, which is slightly above the transformation temperature. The 002 reflection was detected by the + 90° detector, and 220 reflection was detected by the – 90° detector as schematically shown in Fig. 2.

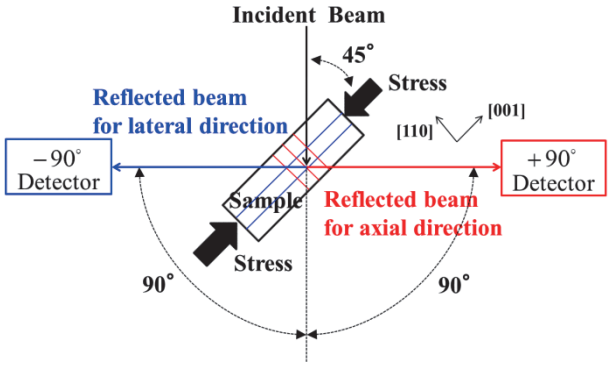

Figure 2. Experimental setup at BL19 TAKUMI [2].

3. Lattice Strain under stress

From the peak position of 002 and 220 reflections, we obtained the lattice parameters c and a under compressive stresses as shown in Fig. 3. We notice in Fig. 3 that c and a both change continuously and almost linearly. The change in c and a caused by the stress application exceeds the one produced by the temperature change from 90 K to 10 K.

Figure 4 shows the lattice strain (elastic strain) calculated by using the following equation:

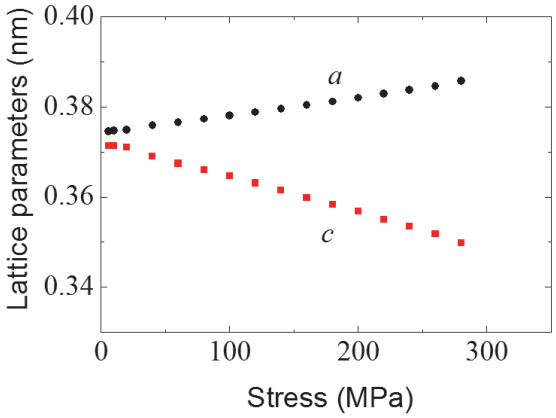

Figure 3. Stress dependence of lattice parameters at 93 K [2].

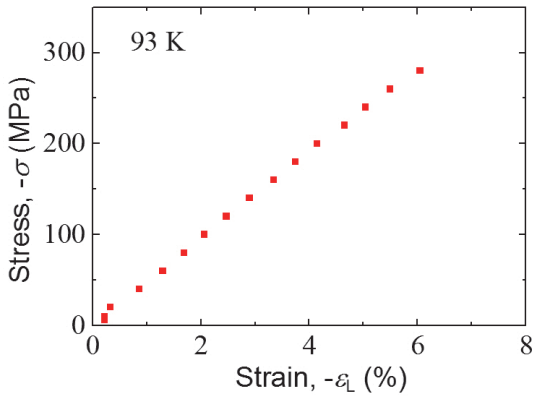

Figure 4. Stress dependence of lattice strain.

$$\varepsilon_L = \frac{c - c_0}{c_0} \times 100 \qquad (1)$$

It is clear that the lattice strain exceeds 6%. The strain agrees with that obtained by attaching a strain gage [3]. The Young's modulus obtained by the slope of Fig 4 is 4.7 GPa, being one order in magnitude smaller than that of conventional metals and alloys.

4. Summary

We confirmed by using TAKUMI that an Fe_3Pt with degree of order 0.75 exhibits a very large elastic strain of more than 6% when compressed in the [001] direction near 90 K.

References

[1] T. Fukuda, T. Sakamoto, T. Kakeshita, T. Takeuchi and K. Kishio, Mater. Trans. **45** (2004) 188.

[2] T. Yamaguchi, T. Fukuda, T. Kakeshita, S. Harjo and T. Nakamoto, Appl. Phys. Lett. **104** (2014) 231908.

[3] T. Fukuda and T. Kakeshita, Scripta Mater. **69** (2013) 89.

T. Fukuda[1], T. Yamaguchi[1], T. Kakeshita[1], S. Harjo[2], and T. Nakamoto[3]

[1]Department of Materials Science and Engineering, Graduate School of Engineering, Osaka University; [2]Neutron Science Section, Materials and Life Science Division, J-PARC center; [3]High Energy Accelerator Research Organization, KEK

Strengthening Mechanism of Advanced Steel with Deformation Induced Phase Transformation

1. Introduction

Transformation Induced Plasticity (TRIP) is one of important effects in the steel strengthening mechanism to improve strength and ductility, and to achieve an excellent high-speed deformation behavior. As shown in Figure 1, TRIP steels show high strength with relatively large elongation. Moreover, TRIP steels also show excellent shock absorption in case of collision, and therefore are applied in the body of cars.

The TRIP effect, as shown in Figure 2, occurs in steel containing a metastable phase (A phase), in which the A phase transforms into a different phase (M phase) during plastic deformation. Because the M phase steel is known to have high strength, the high strength of TRIP steels is predicted to be due to the transformation from the A to the M phases. However, there were almost no quantitative researches on this behavior to bring the TRIP effect, which showed the direct contribution of the M phase to the strength. We were challenged to understand this behavior using the neutron diffraction (ND), because this technique is the most appropriate tool to get microstructural information as bulk average. These kinds of studies have been conducted previously with un-satisfied results, because the separation of diffraction peaks of the matrix F and M phases could not be obtained due to the limited resolution of the instrument used [1].

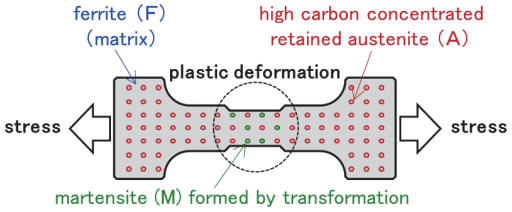

Figure 2. Illustration of TRIP effect.

2. Experiments

In situ neutron diffraction measurements during loading of a TRIP steel specimen with A phase volume fraction of about 11% was conducted at room temperature using TAKUMI which has the best resolution in $\Delta d/d$ of about 0.17% [2]. Thanks to the neutron flux and the flexible data acquisition/reduction, measurements during plastic deformation region (where TRIP effect occurred) were challenged to be conducted in a continuous manner. Conventionally the measurements within the plastic region have been conducted by holding strain or displacement, which might give low accuracy due to the occurrence of stress relaxation during the holding. The M phase amount might also change during the holding.

Figure 3 shows that the (211) diffraction peaks of the matrix and M phase at the plastic deformation region can be separated, because the stress relaxation was suppressed and therefore the accuracies of the peak positions were high.

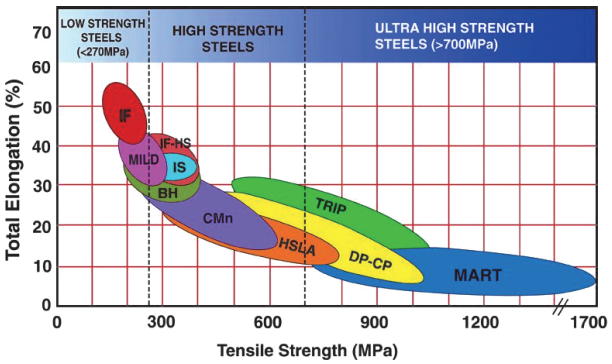

Figure 1. Strength and elongation properties of various steels.

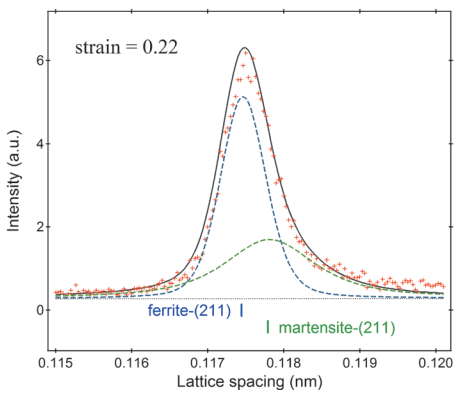

Figure 3. Diffraction pattern of (211) peaks at a plastic deformation.

3. Results and discussions

Peak positions of several (*hkl*) peaks of three phases were carefully determined by the peak separation procedure shown in Figure 3. Lattice strains during loading were then evaluated by comparing the peak positions obtained during loading to those obtained before deformation. It is clear from Figure 4 that, lattice strain sharing occurs among {*hkl*} family grains (intergranular strains) and also among constituent phases. The intergranular strains increase with increasing the applied strain. The average lattice strains of the A phase seem higher than the matrix, showing that the A phase (retained austenite with high carbon content) behaved as the harder phase compared to the matrix. The most interesting one is that the M phase lattice strains were possible to be estimated, and they show the largest values, proving that the M phase formed during transformation is the hardest phase.

It is necessary to confirm quantitatively the contribution of the M phase to the whole strength. The stress contribution from each phase can be estimated by multiplying the stress for each phase with each volume fraction for the same applied stress or strain condition. As shown in Figure 5, even though the stress contribution of the M phase is small at the early stage of the plastic region, it increases to become superior to that of the A phase at a large applied stress region due to the increase of the M phase volume fraction. When the balanced stresses were calculated from the stress contributions of the three phases using the mixture law, as it is clearly shown in Figure 5, the stress contribution of the M phase plays an important role in the whole strength.

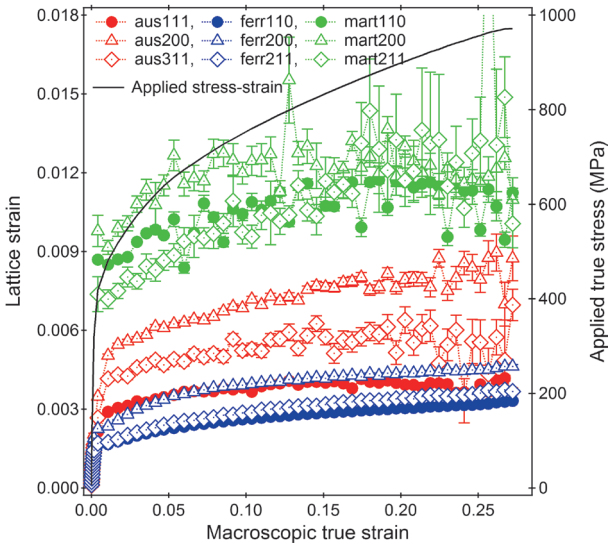

Figure 4. Lattice strains of typical {*hkl*} oriented grains as functions of applied strain [3].

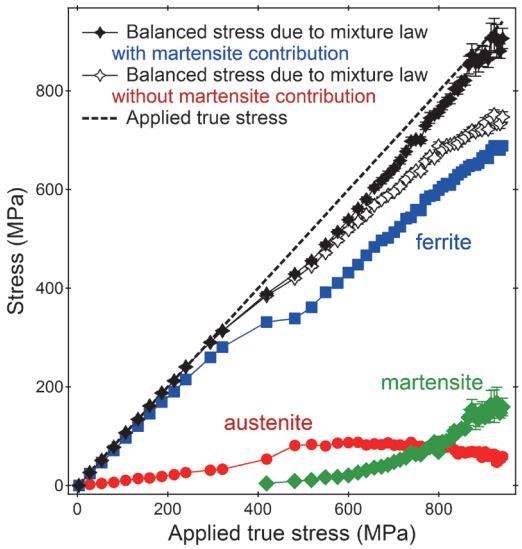

Figure 5. Stress contributions of the three phases in TRIP steel during deformation [3].

References

[1] O. Muransky, P. Sittner, J. Zrnik, E.C. Oliver, Acta mater. **56** (2008) 3367.

[2] S. Harjo, T. Ito, K. Aizawa, H. Arima, J. Abe, A. Moriai, T. Iwahashi, T. Kamiyama, Mater. Sci. Forum, **681** (2011) 443.

[3] S. Harjo, N. Tsuchida, W. Gong, J. Abe, K. Aizawa, Mater. Res. Soc. Symp. Proc. **1528** (2013).

S. Harjo[1], N. Tsuchida[2], W. Gong[1], J. Abe[1], and K. Aizawa[1]

[1]*Neutron Science Section, Materials and Life Science Division, J-PARC center;* [2]*Graduate School of Engineering, University of Hyogo*

Diffraction Study of High Neutron Absorbing Material $EuGa_4$ on SENJU

1. Introduction

Single crystal neutron diffraction provides fundamental but essential information about the structural and magnetic properties of materials. However, in neutron diffraction experiments it is problematic to use compounds containing rare earth elements like Sm, Eu, Gd, and Dy, because they are known as high neutron absorbers. Using a pulsed neutron, which includes a short wavelength, reduces the effect of neutron absorption by the sample, and allows efficient data collection. The time-of-flight neutron diffractometer SENJU at BL18 should become a powerful tool to study high neutron absorbing compounds.

$EuGa_4$ has a $BaAl_4$-type structure with I4/mmm symmetry and is considered a parent compound of the so-called 122 compounds that are rich in physical properties, including superconductivity and valence fluctuation. The bulk properties of $EuGa_4$ indicate an antiferromagnetic order at 16 K [1]. However, the magnetic structure of the compound is still unknown. The neutron diffraction experiment [2] was carried out to determine the effectiveness of SENJU in studying the high absorbing compounds and obtaining the structural information of an antiferromagnetic ordered $EuGa_4$.

2. Experiments and results

A single crystal $EuGa_4$ with size $5 \times 3 \times 1.5$ mm^3 was used for the experiment. Note that Eu in the present sample is not enriched by ^{153}Eu isotope but the natural one. The diffraction patterns were measured at 20.6 K (above T_N) and 4.2 K (below T_N). The wavelength range of an incident neutron was 0.4 Å ~ 4.4 Å at first-frame. Significant numbers of diffraction spots were clearly observed in spite of the high neutron absorption of Eu as shown in Figure 1. The obtained lattice parameters of $a = b = 4.376(2)$ Å and $c = 10.648(4)$ Å at 20.6 K agreed well with the values determined by X-ray diffraction. Diffraction intensities on $(h0l)^*$ reciprocal lattice plane at 20.6 K and 4.2 K were plotted in Figure 2. The magnetic reflections were clearly observed at the positions of $h + k + l \neq 2n$ at 4.2 K. The positions of these reflections indicated an antiferromagnetic ordered structure with propagation vector $\boldsymbol{q} = 0$.

3. Summary

Nuclear and magnetic reflections of $EuGa_4$ were successfully observed. Both crystal and magnetic structural information of Eu-based compound can be obtained on SENJU taking advantage of a wide wavelength range and large area detectors. Extensive studies on the magnetic properties of rare-earth based compounds, containing high neutron absorbing elements, will be conducted using the TOF neutron diffraction.

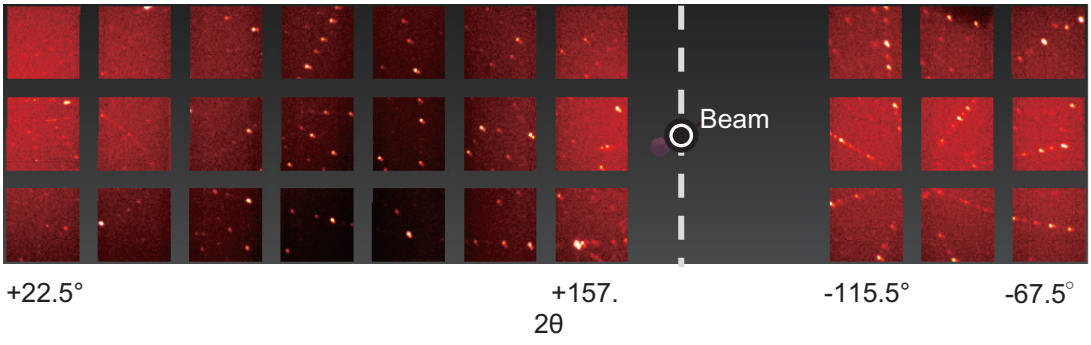

Figure 1. Neutron diffraction pattern of $EuGa_4$ on the detectors of SENJU at 20.6 K.

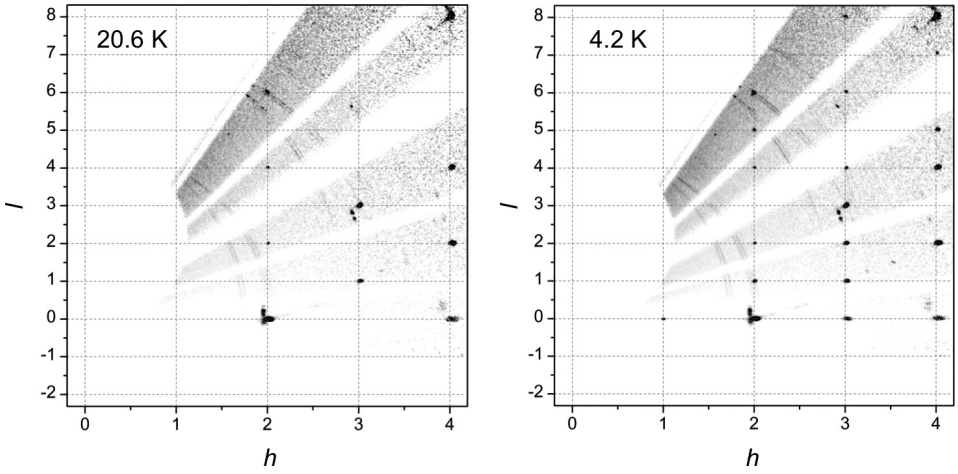

Figure 2. Neutron diffraction intensities on (*h*0*l*)* reciprocal lattice plane.

References

[1] A. Nakamura, Y. Hiranaka, M. Hedo, T. Nakama, Y. Miura, H. Tsutsumi, A. Mori, K. Ishida, K. Mitamura, Y. Hirose, K. Sugiyama, F. Honda, R. Settai, T. Takeuchi, M. Hagiwara, T. D. Matsuda, E. Yamamoto, Y. Haga, K. Matsubayashi, Y. Uwatoko, H. Harima and Y. Ōnuki: J. Phys. Soc. Jpn., **82** (2013) 104703.

[2] T. Kawasaki, K. Kaneko, N. Aso, A. Nakamura, M. Hedo, T. Nakama, Y. Ōnuki, T. Ohhara, R. Kiyanagi, K. Oikawa, I. Tamura, A. Nakao, K. Munakata, T. Hanashima: JPS Conf. Proc., **1** (2014) 014009.

T. Kawasaki[1], K. Kaneko[1,2], N. Aso[3], A. Nakamura[4], M. Hedo[3], T. Nakama[3], Y. Ōnuki[3], T. Ohhara[1], R. Kiyanagi[1], K. Oikawa[1], I. Tamura[1,5], A. Nakao[6], K. Munakata[6], and T. Hanashima[6]

[1]Neutron Science Section, Materials and Life Science Division, J-PARC Center; [2]Quantum Beam Science Center, JAEA; [3]Graduate School of Engineering and Science, University of the Ryukyus; [4]Faculty of Science, University of the Ryukyus; [5]Department of Research Reactor and Tandem Accelerator, JAEA; [6]Neutron R&D Division, CROSS-Tokai

Crystal Structures and Hydrogen Bonding in High-pressure and High-temperature Phases of $Ca(OD)_2$

1. Introduction

Calcium hydroxide (portlandite) belongs to brucite-type layered hydroxides with a CdI_2 structure, which has hydrogen bonds within the interlayer of MO_6 octahedral sheets. Pressure-induced changes in hydrogen bonding are important not only in materials science and crystallography, but also in geoscience, because these layered hydroxides are considered to be a model structure of hydrous minerals that transport water into the deep Earth.

Among the other isostructual hydroxides, portlandite has the largest Ca cation, which might cause unique pressure-induced phase transitions. Previous studies reported that portlandite undergoes a phase transition to a high-pressure (high-P) phase at 6–8 GPa and room temperature [1-3], and transforms into another high-pressure and high-temperature (high-PT) phase at $>$ 6 GPa, $>$ 200°C [4, 5]. The crystal structures of both phases have been determined by X-ray and/or neutron diffraction measurements [5, 6]. However, no *in-situ* neutron observation has been conducted previously under such high-PT conditions that the high-P and high-PT phases are stable. This is presumably due to technical difficulties of the high-P neutron diffraction and the characteristics of the sample; the single high-P phase can be obtained only under hydrostatic conditions above 10 GPa, still showing very weak signal. Furthermore, both high-P and high-PT phases are normally unquenchable at ambient condition.

In the present study, therefore, *in-situ* neutron diffraction measurements under high-P conditions were performed in order to clarify the unknown hydrogen positions in the various polymorphs. To overcome the previous difficulties described above, we used two different high-P apparatuses with recently developed techniques and improved accessible PT conditions [7].

2. Experimental

An initial sample of powder $Ca(OD)_2$ was synthesized from a mixture of CaO powder and excess D_2O in an autoclave at 220°C for 1 week. High-PT experiments were conducted using the multi-anvil apparatus with six independently acting 500t rams (6-axis press called “ATSUHIME”) at the new high-PT beamline “PLANET”. The neutron diffraction patterns were measured at 8.5 GPa under decreasing temperature from 400°C, 200°C, to room temperature. High-P experiments at room temperature were performed using a new anvil assembly [8], which was installed into a Paris-Edinburgh (P-E) press. The diffraction pattern of the high-P phase was obtained at 11 GPa. The lattice parameters and atomic positions were refined by Rietveld analytical method using GSAS software. The initial structure models were taken from previous studies [4-6].

Complementary data on the hydrogen bonds in $Ca(OD)_2$ were obtained via Raman spectroscopy in the region of the OH stretching vibration mode from separate experiments using a diamond anvil cell.

3. Results and discussion

Fig. 1 shows representative diffraction patterns of (a) the high-P phase measured at 11 GPa, room temperature using the P-E press, and (b) the high-PT phase measured at 8.5 GPa and 400°C using the 6-axis press. The refined crystal structures of both phases are shown in Fig. 2. The hydrogen positions for the high-P phase were first clarified. The hydrogen bonds in the high-P phase orientate randomly between the CaO polyhedral layers under high pressure. According to the obtained O(–D)...O distances and angles, the hydrogen bonds are bent and their strength is relatively weak, but slightly getting stronger with increasing pressure. The geometry of the hydrogen bond was quite consistent with the results from Raman spectroscopy. The structure of the high-PT phase was concordant with that observed previously in Ref. [5] for a recovered sample. Based on the obtained structures of the $Ca(OD)_2$ polymorphs, the phase transition mechanism involves the sliding

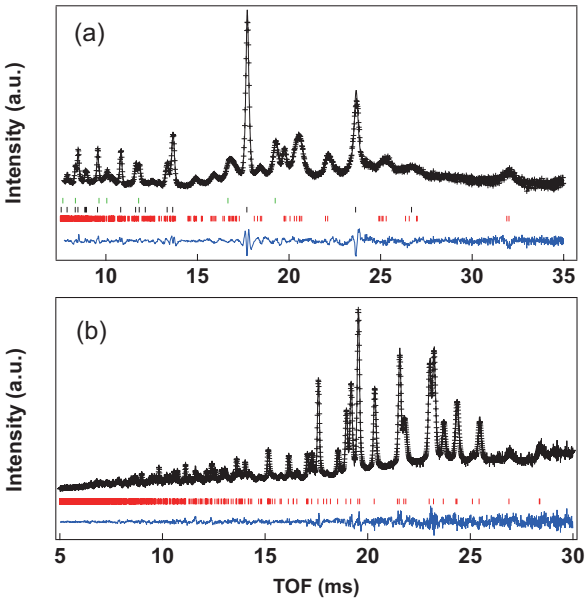

Figure 1. Neutron diffraction patterns of (a) high-P phase and (b) high-PT phase. "+" denotes the observed data points; the solid line denotes the calculated profile. Tick marks below the pattern show the positions of diffraction peaks calculated for (a) Ni (green), WC (black), and high-P phase (red), and (b) high-PT phase (red). The difference between the observed and the calculated profiles is shown by a blue line at the bottom of each plot.

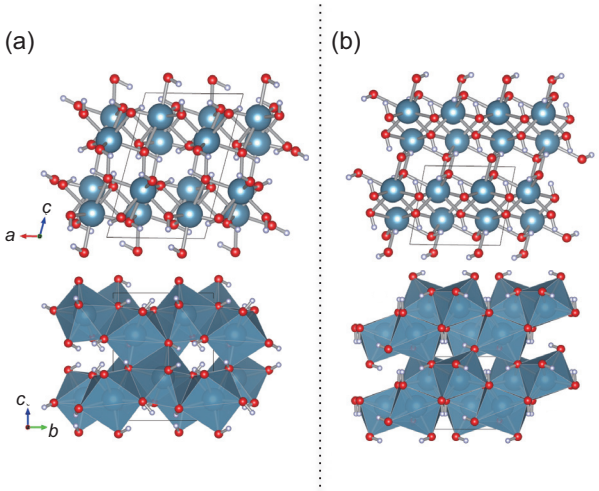

Figure 2. Crystal structures of $Ca(OD)_2$ (a) high-P phase and (b) high-PT phase. The biggest blue atom denotes Ca; the middle red atom oxygen, and the smallest white atom deuterium. For comparison, both structures are shown along corresponding directions (details in [6, 7]).

of the CaO polyhedral layers, position modulations of the Ca atoms, and recombination of the Ca–O bonds as shown in Fig. 2. The high-P phase seems metastable and transforms into the high-PT phase at high temperature with accompanying further structural relaxation and reorientation of the hydrogen bonds to form more stable hydrogen bonds.

References

[1] Ekbundit *et al.*, J. Solid State Chem., 126, 300–307 (1996).

[2] Catalli *et al.*, Geophys. Res. Lett., 35, L05312 (2008).

[3] Iizuka *et al.*, Phys. Chem. Minerals, 38, 777–785 (2011).

[4] Kunz *et al.*, High Press. Res., 14, 311–319 (1996).

[5] Leinenweber *et al.*, J. Solid State Chem., 132, 267–273 (1997).

[6] Iizuka *et al.*, American Mineralogist, 98, 1421–1428 (2013).

[7] Iizuka *et al.*, J. Solid State Chem., 218, 95–102 (2014).

[8] Iizuka *et al.*, High Press. Res., 32, 430–441 (2012).

R. Iizuka[1,2], K. Komatsu[3], H. Kagi[3], T. Nagai[4], A. Sano-Furukawa[5], T. Hattori[5], H. Gotou[6], and T. Yagi[3]

[1]Geodynamics Research Center, Ehime University; [2]Bayerisches Geoinstitut, Universität Bayreuth, Germany; [3]Geochemical Research Center, Graduate School of Science, The University of Tokyo; [4]Division of Earth and Planetary Sciences, Graduate School of Sciences, Hokkaido University; [5]Neutron Science Section, Materials and Life Science Division, J-PARC center; [6]Institute for Solid State Physics, The University of Tokyo

Neutron Crystal Structure Analysis of Human α-Thrombin-Inhibitor Complex using iBIX

1. Introduction

α-Thrombin is a serine protease which plays a central role in coagulation. It converts fibrinogen to fibrin monomer, which forms fibrin fiber to become a main component of the blood clot. Direct α-thrombin inhibitors (DTI) can be promising anticoagulant agents because they work only on α-thrombin, unlike warfarin or heparins, which affect the functions of many blot clot proteins. Bivalirudin is a DTI approved by FDA in US. It is a synthetic peptide whose amino acid sequence is dFPR-P-GGGG-D^{53}GDFEE-IPEEYL^{64}. It has two components connected with a poly glycine linker (GGGG). The N-terminal part, dFPRP, binds to and blocks the active site α-thrombin. Here, dF stands for D-phenylalanine. The C-terminal part following the linker is a part of hirudin, natural anticoagulant peptide from saliva of *Hirudo medicinalis,* the European medicinal leech. It binds to Exosite I of α-thrombin and blocks binding of fibrinogen molecules. For that reason, bivalirudin is a divalent anticoagulant, which has a small binding constant. Bivalirudin is hydrolyzed by α-thrombin to dFPR-COOH and NH_3-P-GGGG-D^{53}GDFEEIPEEYL^{64}. Since those two components have large binding constants for α-thrombin, the half-life of bivalirudin is around 25 minutes in patients. Figure 1 shows the 3D structure of α-thrombin-bivalirudin complex after the hydrolysis determined by X-ray crystallography. Under the crystallization condition, two products remain to bind to the α-thrombin molecule due to the high concentrations. From enzymatic viewpoint, the complex is regarded as an Enzyme-Product (EP) complex. I have tried to determine the protonation stats of the complex to understand the enzymatic mechanism of α-thrombin using neutron protein crystallography [1]. Since hydrolysis of serine protease involved migration of hydrogen atoms or hydrogen bond formations among protein, substrate and water molecules, neutron crystallography is an adequate tool to study the enzymatic reaction mechanism. The neutron crystallography of α-thrombin-bivaliudin complex is expected to provide information on the formation of the EP complex of serine proteases.

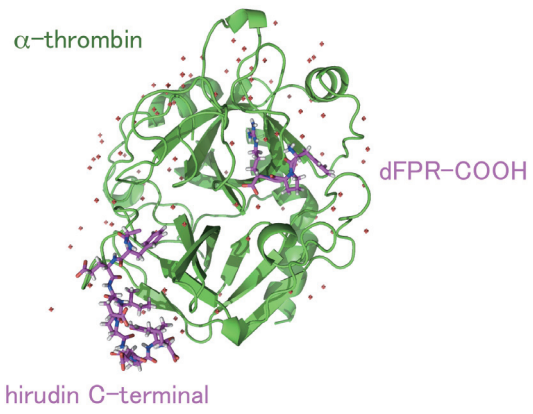

Figure 1. α-Thrombin-bivalirudin complex.

2. Diffraction experiment

The crystal of α-thrombin-bivalirudin was grown by a sitting drop vapor diffusion method with four-times macro-seeding procedures. The sample size was 3.5 mm^3. The crystal was soaked in an artificial mother liquor containing deuterium oxide to replace H atoms with D atoms in the crystal, which helps to reduce the background due to incoherent scattering of the H atoms. The sample was sealed in a quartz capillary with small amount of the soaking solution.

The sample was mounted on MLF BL03 iBIX. The beam power was 300 kW. The 25 Hz neutron pulse beam was irradiated for around 8 hours for each setting. The diffraction experiment was carried out at room temperature. To collect a data set enough for the structure analysis, diffraction patterns for 24 settings of crystal orientations were collected with 30 wavelength-shift fiber type scintillation counters developed for iBIX. The data reduction was carried out by using the program STARGazer v.1.0.0-rc3. The event data were transformed to the histogram data. Figure 2 shows a diffraction pattern detected by detector No. 10 ($2\theta = 51°$ at the detector

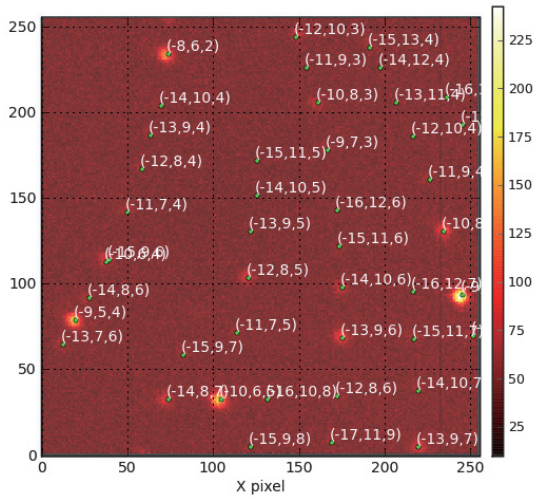

Figure 2. A TOF Laue pattern.

center). The diffraction spots were indexed and the intensities were integrated to obtain the hklFo data.

After the neutron diffraction experiment, X-ray diffraction experiments were carried out at Photon Factory AR-NW-12 (KEK) using the same crystalline sample.

3. Structure Refinement

The X-ray/neutron joint refinement was carried out using neutron and X-ray diffraction data sets, dealing with the program *PHENIX* suite version 1.8.3. Molecular modeling was done by the program *Coot* version 0.6. The crystallographic data, statistics for data collection and refinements extracted are shown in Table 1. The statistics indicates that quality of the neutron diffraction data obtained by iBIX is decent and the refinement was carried out successfully. The figure shows the 2mFo-DFc neutron scattering length density map and the OMIT map for deuterium atoms near the active site (drawn in cyan and magenta). Both maps show clear protonation of His57.

Table 1. Crystallgoraphic data.

	X-ray	Neutron
Space group, Z	*C*2, 4	
a, b, c / Å	71.04, 72.02, 72.36	
β / °	100.5	
Resolution / Å	36-1.6	20.4-2.0
R_{merge}	0.033	0.119
R_{work}	0.165	0.172
R_{free}	0.180	0.230

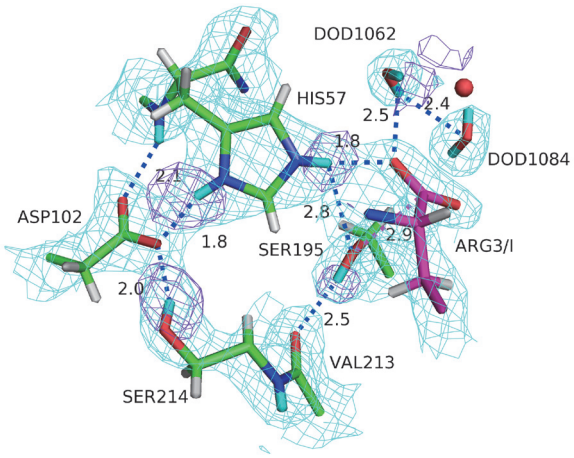

Figure 3. Neutron 2Fo-Fc and OMIT maps.

His57 forms a hydrogen bond to Arg3 of the product, not to Ser195. Hydroxyl group of Ser195 orients to Val213_O, although the length of O…D is little long at 2.5 Å. The freedom of the hydroxyl group might be a key to ease the dissociation of the product from α-thrombin to complete the hydrolysis reaction.

References

[1] T. Yamada *et al.*, Biochim. Biophys. Acta, **1834** (2013) 1532.

T. Yamada
Frontier Research Center for Applied Atomic Sciences, Ibaraki University

Neutron Diffraction Study for Reaction Mechanism of RNase A by using iBIX

1. Introduction

Bovine pancreatic ribonuclease A (RNase A) is a endoribonuclease that claves and hydrolyzes single-stranded RNA exclusively at pyrimidine nucleoside positions in two distinct steps. The mechanism of the cleavage reaction catalyzed by RNase A involves two key histidine residues, His12 and His119. It is important to know the protonation states of them in order to understand the hydrolysis mechanism of RNase A. Neutron protein crystallography is a powerful technique for problem solving. In previous reports, the protonation states of His12 and His119 for RNase A complexed with phosphate ion, uridine vanadate and phosphate free one have been investigated by neutron diffraction analysis [1-3].

In this study, neutron diffraction analysis of phosphate free RNase A has been carried out with high resolution and completeness data set collected by using iBIX in order to clarify the protonation states of two histidine residues in active site, and to elucidate the detailed mechanism of the cleavage reaction catalyzed by RNase A.

2. Neutron difftaction measurement

Neutron diffraction data set of bovine pancreatic RNase A were collected by IBARAKI biological crystal diffractometer iBIX in J-PARC [4,5]. The crystal of RNase A grew to 6.0 mm^3 (2.5 × 2.4 × 1 mm) in two weeks. The crystal was soaked in deuterated solution for 10 days to reduce the background scattering from H atoms, which have a large incoherent neutron scattering length.

The full data set for neutron structure analysis could be obtained in 7 days at 300 kW operation of accelerator power at J-PARC. The exposure time was 4 hour per setting. The total number of settings was 40. The crystal data and measurement conditions are shown in Table 1. One of the typical TOF diffraction patterns is shown in Fig. 1. The very sharp Bragg spots indicate that the quality of the crystal sample is sufficient to perform the neutron diffraction experiment.

Table 1. Crystal data and measurement conditions.

Temperature		(K)	293
Space group			$P2_1$
Unit-cell	*a*	(Å)	30.4
	b	(Å)	38.6
	c	(Å)	53.4
	β	(°)	105.8
Crystal size		(mm^3)	6.0
Accelerator power		(kW)	280
Range of wavelength		(Å)	1.6 ~ 4.6
Exposure time		(hours)	4.0
Total No. of settings			40
Total measurement time		(days)	7

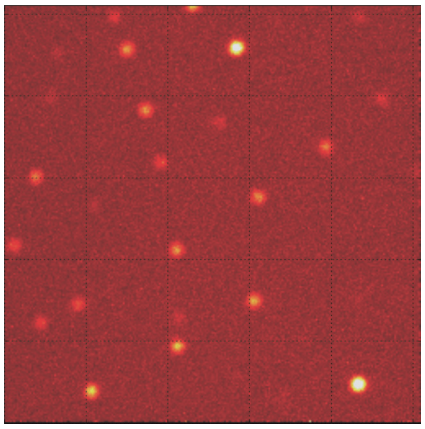

Figure 1. TOF diffraction pattern of RNase A obtained by using iBIX.

3. Structure analysis

The data reduction was carried out with the program STARGazer [4] developed for TOF diffraction data measured by iBIX. The data reduction was successfully completed and then the integrated intensities of the Bragg reflections could be obtained for the structure refinement. A total of 20,513 unique reflections were obtained with an overall R_{sym} of 13.5% from 67,740 observed reflections. The average of $I/\sigma(I)$ and redundancy were 8.1 and 3.3 respectively. The crystal data, measurement conditions, and the statistic of the data reduction and refinement are summarized in Table 2.

Table 2. The statistics of the data reduction and refinement.

No. of observed reflections		67,740
No. of unique reflections		20,513
Resolution	(Å)	1.4
Completeness	(%)	86.7
Average I/σ(I)		8.1
Redundancy		3.3
R_{sym}	(%)	13.5
R_{cryst}	(%)	19.4
R_{free}	(%)	22.0

The structure refinement was carried out using the program phenix.refine including PHENIX-1.8 [5]. The structure was determined by joint neutron and X-ray structure refinement. 10% of reflections, randomly selected, were assigned as a test set for cross validation. The final values of R_{cryst} and R_{free} were 19.5% and 22.0%, respectively, for completeness of 86.7% to a resolution of 1.4 Å.

The structure with high reliability and good data statistics could be obtained finally by comparing with the already-reported one [3].

2|Fo|-|Fc| neutron scattering length map around the active site including His 12 and His 119 is drawn in Fig. 2. We also calculated the |Fo|-|Fc| neutron scattering length density map after omitting $D^{\delta 1}$ and $D^{\varepsilon 2}$ of His12 and His119 in order to confirm their protonation states. These omit maps indicated that His12 is completely singly protonated and Hi119 is doubly protonated. Their protonation states are consistent with those in the first step of the putative mechanism of catalysis by RNase A. We could also observe a D atom of water molecule which is hydrogen bonded to $N^{\varepsilon 2}$ of His12.

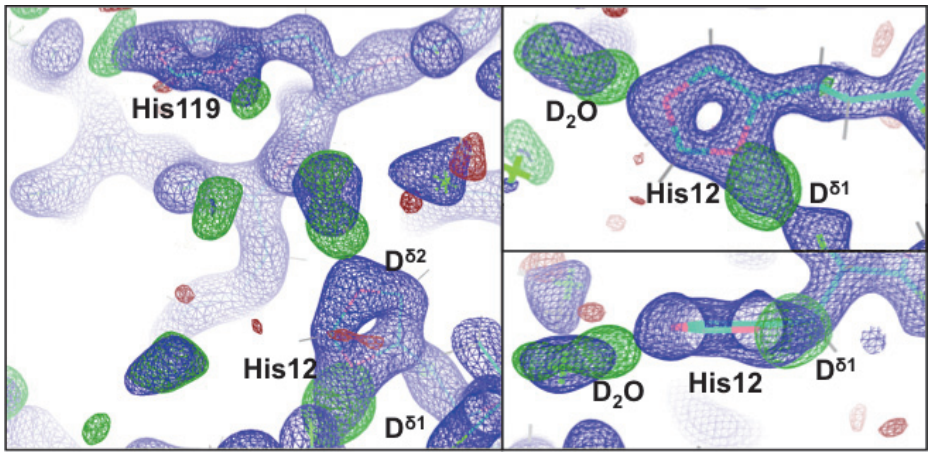

Figure 2. TOF diffraction pattern of RNase A obtained by using iBIX.

References

[1] A. Wlodawer *et al.*, Proc. Natl Acad. Sci. USA, **80** (1983) 3628–3631.

[2] A. Wlodawer, L. Sjölin, Biochemistry **22** (1983) 2720–2728.

[3] D. Yagi *et al.*, Acta Cryst. **D65** (2009) 892–899.

[4] I. Tanaka, K. Kusaka, T. Hosoya, N. Niimura, T. Ohhara, K. Kurihara, T. Yamada, Y. Ohnishi, K. Tomoyori and T. Yokoyama, Acta Cryst. D66 (2010) 1194–1197.

[5] K. Kusaka, T. Hosoya, T. Yamada, K. Tomoyori, T. Ohhara, M. Katagiri, K. Kurihara, I. Tanaka and N. Niimura, J. Synchrotron Rad. 20 (2013) 994–99.

[6] T. Ohhara *et al.*, NIMA **600** (2009) 195–197.

[7] P. Adams *et al.*, Acta Cryst. **D66** (2010) 213–221.

K. Kusaka[1], T. Yamada[1], K. Tomoyori[2], T. Hosoya[1], T. Ohhara[3], I. Tanaka[1], and N. Niimura[1]

[1]Frontier Research Center for Applied Atomic Sciences, Ibaraki University, Tokai; [2]Quantum Beam Science Center, JAEA; [3]Neutron Science Section, Materials and Life Science Division, J-PARC center

Local Structural Changes with Amorphization on Thermal Decomposition Reaction of $LiAl(ND_2)_4$

1. Introduction

Lithium aluminum amide $LiAl(NH_2)_4$ is of interest as a possible hydrogen storage material because the composite material consisting of $LiAl(NH_2)_4$ and LiH releases hydrogen gas by 6.1 mass% at temperatures below 400 K [1, 2]. A hydrogen desorption mechanism of the composite has been proposed, but it is still controversial because the decomposition mechanism of $LiAl(NH_2)_4$ is not well-understood. Our goal in the present report is to investigate the detailed structural properties before and after the decomposition of $LiAl(ND_2)_4$ using neutron total scattering and atomic pair distribution function (PDF) analysis.

2. Neutron Diffraction Measurements

The sample preparation of $LiAl(NH_2)_4$ is explained in a previous publication [3]. $LiAl(ND_2)_4$ was similarly prepared using LiD and ND_3 instead of LiH and NH_3, respectively. For the purpose of structural characterization of the decomposition products, $LiAl(ND_2)_4$ samples heat-treated at 433 K and 673 K were prepared using a heating rate of 5 K/min, which was then immediately cooled to room temperature under helium gas flow. $LiAl(ND_2)_4$ (60 mg) was examined before and after the decomposition for an exposure time of 11 h by ex situ neutron diffraction on the neutron total scattering spectrometer NOVA (BL21) connected to the 200 kW spallation neutron source at J-PARC.

3. Results and Discussion

Figure 1 shows the structure factor, *S(Q)*, of $LiAl(ND_2)_4$ (a) before and after heat treatment at (b) 433 K and (c) 673 K [4]. The data were obtained from the neutron scattering intensity, which was collected using the 45° detector bank of the NOVA spectrometer. During the heat treatment, the profile drastically changed from sharp diffraction peaks to broad diffuse scattering features, indicating the amorphization of the sample.

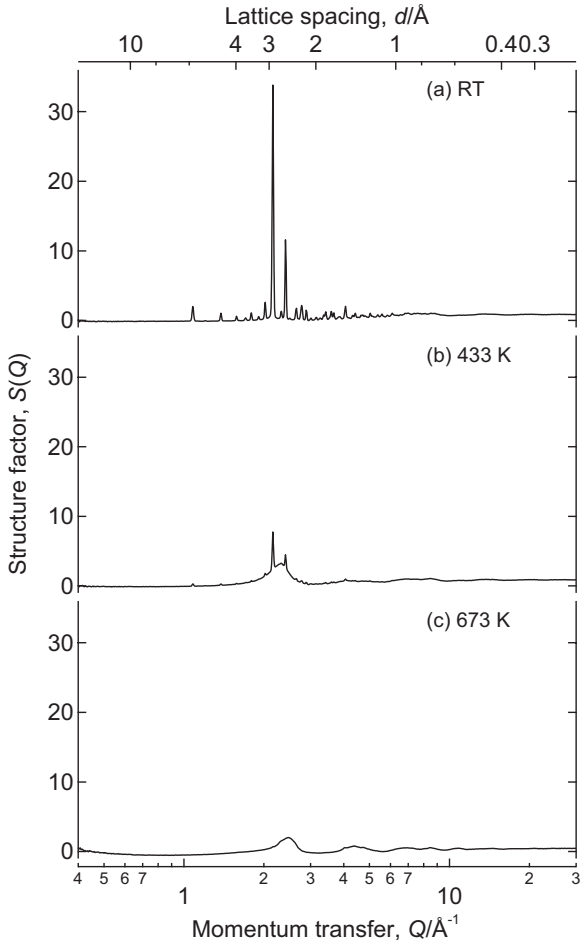

Figure 1. Structure factors, *S(Q)*, for the neutron scattering profiles of $LiAl(ND_2)_4$ (a) before and after heat treatment at (b) 433 K and (c) 673 K [4].

Figure 2 shows the atomic pair distribution function, *G(r)*, obtained by the Fourier transformation of *S(Q)* for $LiAl(ND_2)_4$ before and after the heat treatment [4]. We assumed that $LiAl(ND_2)_4$ decomposes to Li_3AlN_2 and AlN, shown as follows:

$$(1-x)\mathrm{LiAl(ND_2)_4} \rightarrow (1/3)x\mathrm{Li_3AlN_2} + (2/3)x\mathrm{AlN} + (8/3)x\mathrm{ND_3} \quad (1)$$

The PDF refinements of the *G(r)* profiles were performed in the region of $0.5 \leq r \leq 5.0$ Å, which includes more than 500 bonding pairs (383 $LiAl(ND_2)_4$, 113 Li_3AlN_2 and 64 AlN). Half and almost all of the

$LiAl(ND_2)_4$ decomposed at 433 K and 673 K, respectively. Therefore, we confirm that $LiAl(ND_2)_4$ decomposes to amorphous mixed phase including Li_3AlN_2 and AlN. This preliminary report on our local structural analysis, which includes the amorphization reaction, provides fundamental information not only for the decomposition process of $LiAl(NH_2)_4$ but also for the further study of possible hydrogen storage materials.

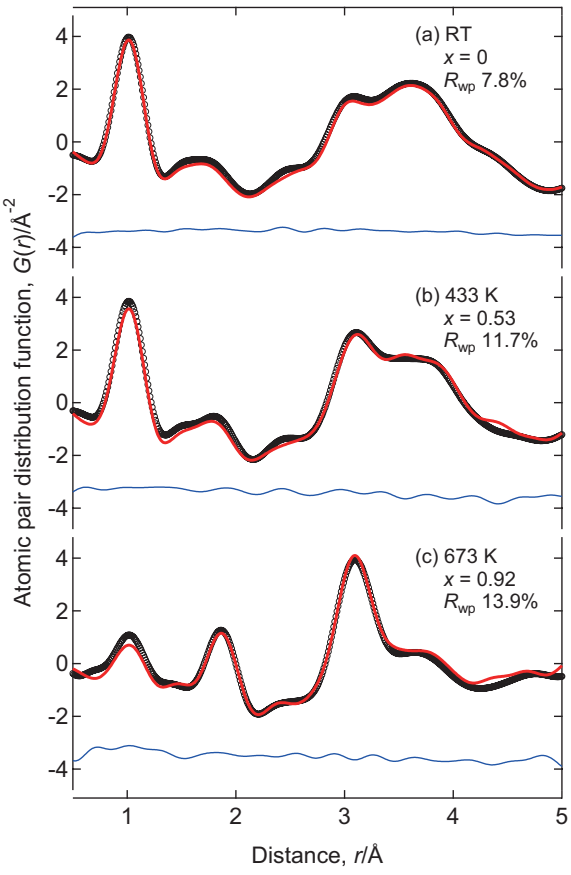

Figure 2. Atomic PDF, *G(r)*, for the neutron scattering profiles of $LiAl(ND_2)_4$ (a) before and after heat treatment at (b) 433 K and (c) 673 K [4]. PDF refinement results: observed (black circles), calculated (red line), and residual (blue line) scattering profiles. The reaction process, x in eq. (1), and statistical reliability factors, R_{wp}, obtained by PDF refinement of the G(r) profiles are shown.

4. Conclusions

We have attempted to elucidate the local structural changes that occur during the decomposition process that accompanies the amorphization of $LiAl(ND_2)_4$ using ex situ neutron total scattering measurements and PDF analysis. The structure factors of $LiAl(ND_2)_4$ before the decomposition were characterized by isolated $[ND_2]$ units. Atomic pair distribution functions after the heat treatment at 433 K and 673 K confirmed that $LiAl(ND_2)_4$ decomposed to amorphous mixed phases containing Li_3AlN_2 and AlN.

Acknowledgments

The authors would like to thank Mr. H. Oki and Mr. T. Iwase for their helpful assistance in the neutron scattering experiments. The work presented here is partially supported by the New Energy and Industrial Technology Development Organization (NEDO) under "Advanced Fundamental Research Project on Hydrogen Storage Materials'' and "Feasibility Study on Advanced Hydrogen Storage Materials for Automotive Applications (2012)", JSPS KAKENHI Grant Numbers 23686101, 24241034, and the Neutron Scattering Program Advisory Committee of IMSS, KEK (Proposal No. 2009S06).

References

[1] R. Janot, J.-B. Eymery and J.-M. Tarascon: J. Phys. Chem. C 111 (2007) 2335–2340.

[2] T. Ono, K. Shimoda, M. Tsubota, S. Kohara, T. Ichikawa, K. Kojima, M. Tansho, T. Shimizu and Y. Kojima: J. Phys. Chem. C 115 (2011) 10284–10291.

[3] T. Ono, K. Shimoda, M. Tsubota, S. Hino, K. Kojima, T. Ichikawa and Y. Kojima: J. Alloys Compd. 506 (2010) 297–301.

[4] K. Ikeda, T. Otomo, H. Ohshita, N. Kaneko, M. Tsubota, K. Suzuya, F. Fujisaki, T. Ono, T. Yamanaka, K. Shimoda, T. Ichikawa and Y. Kojima: Mater. Trans. 55 (2014) 1129–1133.

K. Ikeda[1,2], T. Otomo[1,2,3], H. Ohshita[1,2], N. Kaneko[1,2], M. Tsubota[2], K. Suzuya[1], F. Fujisaki[3], T. Ono[4], T. Yamanaka[4], K. Shimoda[5], T. Ichikawa[4,5], and Y. Kojima[4,5]

[1]Neutron Science Section, Materials and Life Science Division, J-PARC Center; [2]Institute of Materials Structure Science, KEK; [3]Department Materials Structure Science, The Graduate University for Advanced Studies; [4]Graduate School of Advanced Sciences of Matter, Hiroshima University, [5]Institute for Advanced Materials Research, Hiroshima University

Polymer Brush Layers at Water/Polymer Interfaces Formed by Segregation of Amphiphilic Block Copolymers

1. Introduction

A layer of polymer chains tethered by one end to a surface is called polymer brush and known to show various unique properties such as prevention of protein adsorption and anti-fouling activity. These polymer brushes have been usually fabricated by two methods: polymerization from the surface ("grafting-from" method) [1] and attaching polymer chain to the surface either chemically or physically ("grafting-to" method) [2, 3]. Herein we report a third method to fabricate hydrophilic brush layer utilizing spontaneous segregation of an amphiphilic block copolymer in a matrix of elastomer to water interface [4].

The surface segregation phenomena of copolymers with surface-active blocks should be useful for preparing such a brush layer spontaneously. Recently, we constructed such self-restoring segregation system using cross-linked poly(dimethyl siloxane) (PDMS) elastomer for matrix containing diblock copolymers of poly(ethylene glycol) (PEG) and PDMS, (PEG-PDMS), as amphiphilic copolymers. In this system, while the hydrophilic block with high surface energy avoids air surface it segregates to cover the interface between hydrophobic PDMS and water as schematically shown in Figure 1. This polymer brush hence realizes dynamic response to environmental changes, that is, the block copolymer chains still remaining in bulk are supplied to the damaged surface immediately if some of copolymers at the brush layer are removed due to physical damage like frictional ware and scratch.

In order to evaluate the density and length of the brush layers formed at D_2O/polymer interfaces, we performed neutron reflectivity measurements at SOFIA reflectometer in J-PARC/MLF [5, 6].

2. Results and discussion

Figure 2 shows neutron reflectivity curves at the D_2O/PDMS films containing 20 wt% of PEG-*b*-PDMS (M_n = 2100 – 1000) and at D_2O/neat PDMS. The reflectivity of neat PDMS shows only small fringes that correspond to the total thickness of the film on quartz substrate, whereas a fringe with a larger periodicity, Δq, appeared in the reflectivity of 20 wt% PEG-PDMS, which indicates the formation of relatively thin but well defined D_2O-swollen brush layer. To analyze the details of the interfacial structures, we computed the depth profiles of SLD using the multi-layer model. The scattering length density profiles obtained by fitting with box models are shown

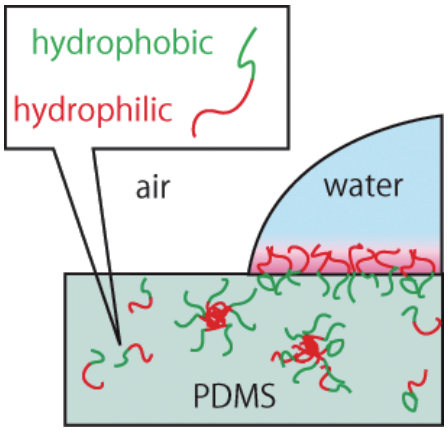

Figure 1. A schematic picture of the bulk and interfacial structures of PEG-PDMS in a mixture with PDMS in contact with air or water.

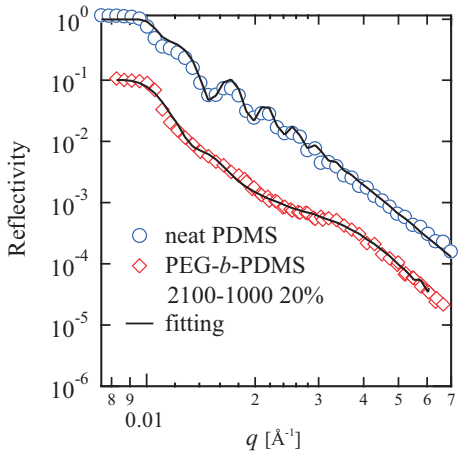

Figure 2. Neutron Reflectivities of sample films containing no copolymers (neat PDMS) and 20 wt% of PEG-*b*-PDMS (M_n = 2100 – 1000).

in Figure 3. The thickness of the brush layer R is evaluated to be about 15 nm, corresponding to 88% of the contour length of PEG block R_{max} (= 17 nm) with molecular weight of 2100. The brush density was calculated to be higher than 0.2 chains/nm^2 from the profile. Both the thickness and the grafting density indicate that a significantly dense brush layer is formed by the segregation of amphiphilic block copolymer, which is comparable to the polymer brush fabricated by the "grafting-from" method.

In order to explain why such a high-density and extremely stretched brush layer is formed by segregation process, we propose a model assuming that (i) energy gain due to the hydration of PEG block is the driving force for free energy change ΔF by segregation, (ii) stretching entropy loss of PEG chain competes with (i), and (iii) other effects such as surface energy gain and translational entropy loss by segregation of copolymers are ignorable. The most significant difference between the conventional brush and ours, created by segregation, is whether the grafting density σ is fixed or variable. If a conventional brush chain with fixed σ is placed in water, it will be swollen and stretched to be saturated at a certain volume fraction of water and the swelling stops because it gives only stretching entropic loss. On the other hand, our brush created by segregation of copolymer with variable σ stretches more in water and gets denser as far as possible with keeping the saturated volume fraction in order to maximize the free energy gain per unit area.

To verify this model, we have calculated ΔF by the formation of brush layer as a function of elongation R/R_{max} and σ. Figure 4 shows the calculated ΔF as a function of R/R_{max} and σ. This calculation semiquantitatively supports the idea that brushes with fixed σ reach only local stable point, whereas a brush created by segregation can be more stretched and denser to come to the global point. Our brush is more stretched and denser than the prediction of the model (R/R_{max} = 0.75 and σ = 0.019), and this is because enthalpy change is underestimated: PEG block gains energy not only by getting into favorable water but also by getting out from unfavorable PDMS via forming the brush layer.

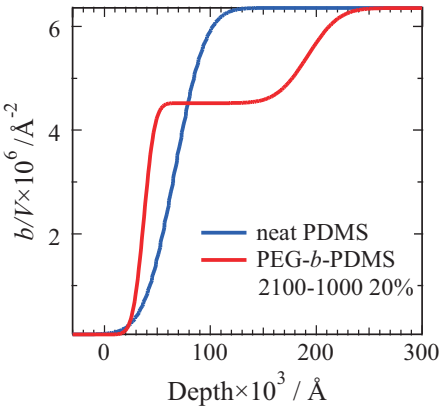

Figure 3. Scattering length density profiles at D_2O/sample interfaces obtained by fitting the reflectivity curves.

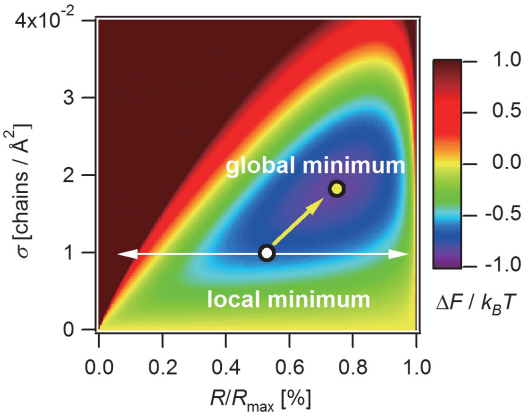

Figure 4. Calculated free energy change by hydration and stretching of PEG brush as a function of elongation R/R_{max} and grafting density σ.

References

[1] Y. Tsujii *et al.*, *Adv. Polym. Sci.* **197** (2006) 1.

[2] A. Halperin *et al.*, P. *Adv. Polym. Sci.* **100** (1992) 31.

[3] B. Zhao and W. Brittain, J. *Prog polym. Sci.* **25** (2000) 677.

[4] M. Inutsuka *et al.*, *ACS Macro Lett.* **2** (2013) 265.

[5] N. L. Yamada *et al.*, *Euro. Phys. J. Plus* **126** (2011) 108.

[6] K. Mitamura *et al.*, *Polymer J.* **45** (2013) 100.

M. Inutsuka[1], N. L. Yamada[2,3], K. Ito[1], and H. Yokoyama[1]

[1]*Graduate School of Frontier Sciences, the University of Tokyo;* [2]*Neutron Science Section, Materials and Life Science Division, J-PARC center;* [3]*Institute of Materials Structure Science, KEK*

Multistep Thickening of Nafion Thin Films in Water Studied by Optical and Neutron Reflectivity

1. Introduction

Known for its remarkable conductivity and durability, Nafion is widely used as a proton exchange film in polymer electrolyte fuel cells (PEFC). Those excellent electrochemical and mechanical properties of Nafion are associated with the characteristic network structure of the hydrated water phase. Extensive studies have revealed that the microstructure in the Nafion film depends on the swelling ratio. However, it appears to us that most studies conducted so far in this context are limited to bulk systems. Downsizing PEFC is one of the interesting developments in the near future. To accept such a challenge, all components in a PEFC including the polyelectrolyte film should therefore become smaller and/or thinner.

The physical properties of a polymer film are generally altered with decreasing thickness for films, especially when thinner than 100 nm. The effects of air and substrate interfaces on thin films are undoubtedly responsible for this thickness dependency. Works published in the current literature have shown that chain dynamics at the air and substrate interfaces should be enhanced and depressed in comparison with that in the internal region, respectively. This is because the ratio of interfacial area to the total volume of the film increases markedly with decreasing film thickness.

In this study, the thickness of thin Nafion films in water was characterized as a function of time by surface plasmon resonance (SPR) reflectivity in conjunction with neutron reflectivity (NR) measurements.

2. Results and Discussion [1]

Figure 1 shows the time dependence of the swelling ratio for Nafion films on silver and SiO_x substrates, respectively, after coming in contact with water. The swelling ratio here is defined as the value of the film thickness in water (h_w) divided by the thickness (h_0) in the dried state. Since the swelling ratio for the film became larger in water with increasing time, there is no doubt that water molecules were sorbed into the

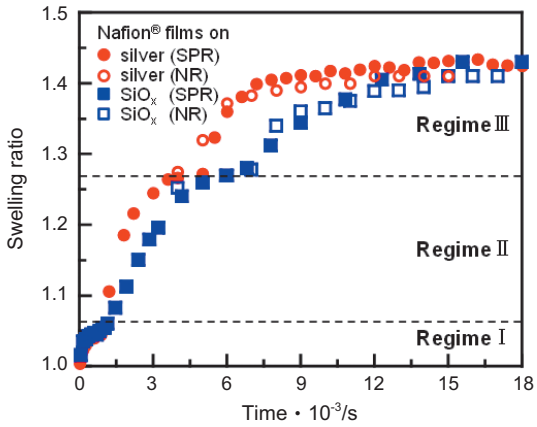

Figure 1. Time dependence of swelling ratio for Nafion films on silver (red) and SiO_x (blue) substrates with an h_0 of 47 nm and 49 nm, respectively, prior to coming in contact with water. The filled and open symbols are the data obtained SPR and neutron reflectivity measurements, respectively.

films. The thin Nafion films thickened in three steps named here regimes I, II and III. At first, the films asymptotically reached a swelling ratio of 1.05. Then, the films resumed thickening asymptotically up to 1.26. Finally, the swelling ratio reached 1.41. While the characteristic swelling ratio at the border between different regimes was neither dependent on the substrate species nor the film thickness, the swelling kinetics depended on the type of the substrate.

To examine the aggregation structure of our thin Nafion films near the substrate interface, NR measurements were conducted. In addition, NR analyses can verify our results obtained by SPR measurements. Figures 2(a) and (b) show the NR curves for Nafion films with an h_0 of 53 nm supported on silver and quartz substrates respectively in air and D_2O at various times. Here, D_2O was used instead of water. The solid lines denote the best-fit calculated reflectivity to the experimental ones based on the model (b/V) profiles normal to the interface shown in panels (c) and (d) of Figure 2, respectively. A model (b/V) profile with a moderately single hydrated interfacial layer was suitable to the Nafion film on the silver substrate. On the other hand, a model containing such

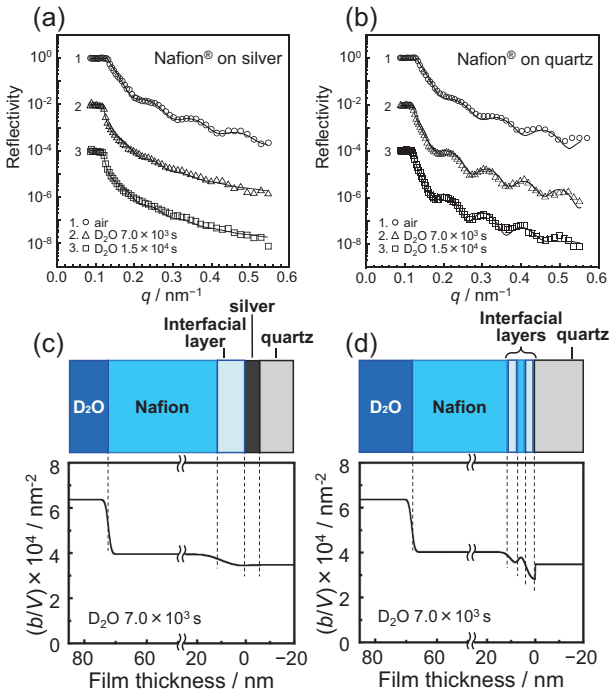

Figure 2. Neutron reflectivity curves for thin Nafion films with the original thickness (h_0) of 53 nm supported on (a) silver and (b) quartz substrates in air and D_2O. The curves are vertically offset for clarity. Experimental data sets are shown by symbols, and the best-fit curves calculated using the model (b/V) profiles shown in (c) and (d) are expressed by solid lines, respectively.

an interfacial layer structure with a total thickness of ca. 15 nm also gave a better fitting for the film on the quartz substrate. The (b/V) values of two layers in the interfacial region were lower than that in the internal region of Nafion. This indicates that H_2O was sorbed in the interfacial region before soaking it into D_2O. The swelling ratios evaluated from NR measurements are also plotted in Figure 2, and are consistent with the data from the SPR measurements.

It has been accepted that the swelling of bulk Nafion by water sorption is accompanied by a structural change [2, 3]. In short, the water first binds to sulfonic acid groups of the side chain portion of Nafion. When the water content in Nafion increases further, sphere-like ionic clusters are formed. The clusters finally connect to one another forming bridges. Interestingly, the swelling ratio for the structural transition, was coincident with the asymptotic swelling ratios in regimes I, II and III. Thus, the three-step sorption behavior shown in Figure 1 could be explained in terms of the structural evolution in the internal region of the film. Figure 3 shows a model for the swelling of a thin Nafion film. It is noteworthy that the hydrated layer is formed near the substrate.

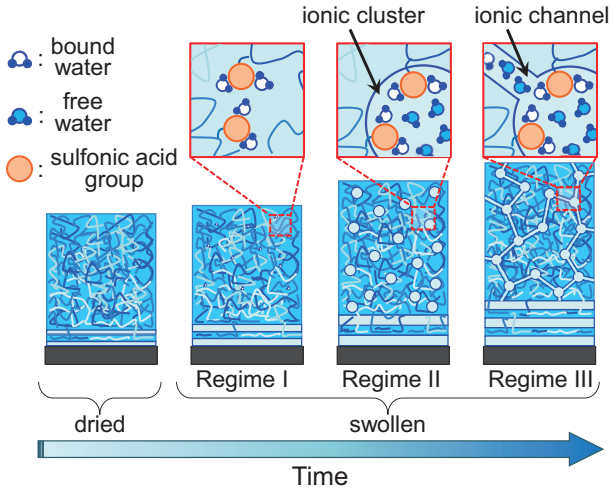

Figure 3. A schematic representation of the structural evolution in a thin Nafion film contacting water.

3. Conclusion

In conclusion, the water absorption kinetics and aggregation states in thin Nafion films were investigated by SPR and neutron reflectivity measurements. The water sorption behavior of thin Nafion films is divided into three regimes, which could be understood by using bulk system concepts, while its dynamics strongly depends on the substrate due to the interaction between the substrate and Nafion and/or the confinement effect.

References

[1] Y. Ogata, D. Kawaguchi, N. L. Yamada, K. Tanaka, *ACS Macro Lett.*, **36** (2013) 856.

[2] G. Gebel, J. Lambard, *Macromolecules* **30**, (1997) 7914.

[3] K. Schmidt-Rohr, Q. Chen, *Nat. Mater.* **7**, (2008) 75.

Y. Ogata[1], D. Kawaguchi[2], N. L. Yamada[3,4], and K. Tanaka[1,5]

[1]Department of Applied Chemistry and [2]Education Center for Global Leaders in Molecular Systems for Devices, Kyushu University; [3]Neutron Science Section, Materials and Life Science Division, J-PARC center; [4]Institute of Materials Structure Science, KEK; [5]International Institute for Carbon-neutral Energy Research (WPI-I2CNER), Kyushu University

Precise Evaluation of Angstrom-Ordered Mixed Interfaces in Solution Processed OLEDs: Influence on Carrier Transport Characteristics

Organic light-emitting devices (OLEDs) have distinguishing features like light weight, flexibility, high power efficiency, being surface light sources, etc. OLEDs have penetrated next-generation lighting, and the further growth of this market is anticipated [1]. Recently, a solution-process alternative to ordinary evaporation process has been rapidly developed to lower the cost. For now, the solution-processed OLEDs have inferior characteristics compared to the evaporation-processed OLEDs. The formation of clear organic/organic interfaces is important to improve the characteristics of the solution-processed OLEDs. However, it is not clear how the interface from solution process is formed. Therefore, we investigated the organic/organic interface from solution process.

We used neutron reflectometry (NR) to investigate the organic/organic interfaces. Layer structure along depth-direction can be obtained by analyzing the reflectivity curve using Parratt's formula [2]. Compared to other methods, such as secondary ion mass spectrometry, NR has the following advantages. NR is a non-destructive method, therefore there is no artifact created by destruction of the sample. Also, NR has intrinsic neutron wavelength-ordered resolution. The neutron wavelength used in experiment is angstrom-order, therefore depth-direction analysis with angstrom-ordered resolution is possible. X-ray reflectometry (XRR) also has these advantages. However, the investigation of the organic/organic interface by XRR is difficult, because the scattering length densities (SLDs) of organic layer for X-ray are close values among almost organic aromatic compounds. In contrast, the differences of the SLDs for NR can be enhanced by deuteration of material consisting of one layer (D/H contrast method).

We investigated the organic/organic interface of deuterated 4,4'-bis(*N*-carbazolyl) biphenyl (CBP) doped with *fac*-tris(2-phenylpyridyl) iridium(III) ($Ir(ppy)_3$) on hole transport polymer poly(9,9-dioctylfluorene-co-*N*-(4-butylphenyl)-diphenylamine) (TFB) [3]. TFB was spin-coated on the Si substrate and made insoluble by thermal annealing. CBP:$Ir(ppy)_3$ was spin-coated by using either of two solvents: 1,4-dioxane or cyclopentanone. Furthermore, the interface of deuterated CBP (CBP-d_{16}) doped with $Ir(ppy)_3$ on TFB was investigated to precisely evaluate the interface structure. The evaporated CBP-d_{16}:$Ir(ppy)_3$ on TFB was also evaluated. NR measurements were performed using the single frame mode of the BL16 SOFIA (SOFt Interface Analyzer) horizontal-type time-of-flight neutron reflectometer (2.0 Å $< \lambda <$ 8.8 Å) at J-PARC (Japan Proton Accelerator Research Complex)/MLF (Materials and Life Science Experimental Facility) [4]. Least squares analysis of the reflectivity profiles was performed using the Motofit reflectometry analysis program [5].

The reflectivity curves of TFB/CBP-d_{16}:$Ir(ppy)_3$ and the results of least-square fitting are shown in Fig. 1. Reflectivity curves were well fitted with two-organic layer models. The interface from the evaporation process was clear. The thicknesses and SLDs of TFB were the same as those of the TFB monolayer film. In the interfaces from solution process, the thicknesses and SLDs of TFB were increased from those of the TFB monolayer film. These show that CBP-d_{16} and $Ir(ppy)_3$ molecules mixed to swollen TFB layer. Similar results were obtained in TFB/CBP:$Ir(ppy)_3$ films. Cyclopentanone has stronger interaction with TFB than 1,4-dioxane. However, the swollen thicknesses were the same in both solvents. We assume that cross-linking points limited the increases of TFB thicknesses. The solvent difference affected the interfacial roughnesses. Cyclopentanone gave larger interfacial roughness than 1,4-dioxane. We assume that the interfacial roughness reflect the polymer end-chain. Swelling of polymer end-chain should not be limited by the cross-linking. The SLDs of CBP-d_{16}:$Ir(ppy)_3$ layers in TFB/ CBP-d_{16}:$Ir(ppy)_3$ were decreased by 3% from those of CBP-d_{16}:$Ir(ppy)_3$ monolayer films both in solvents. The CBP-d_{16} SLD value is almost twice

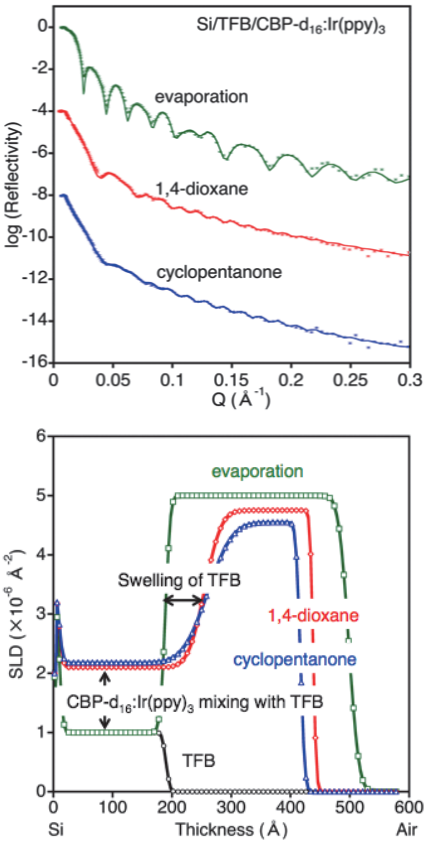

Figure 1. Reflectivity curves and SLD profiles. The reflectivity scale corresponds to the profile for Si/TFB/CBP-d_{16}:Ir(ppy)$_3$(evaporation). Other plots are offset for clarity.

the SLD of Ir(ppy)$_3$. This indicates that CBP-d_{16} is more mixed to swollen TFB layer than Ir(ppy)$_3$.

Hole only devices (HODs) were fabricated to investigate the effect of these interface structures on the characteristics of hole transport abilities. HODs with a structure of [ITO/PEDOT:PSS (40 nm)/TFB (20 nm)/CBP:12 wt% Ir(ppy)$_3$ (40 nm)/α-NPD (40 nm)/MoO_3 (5 nm)/Al (100 nm)] were fabricated, where the α-NPD, MoO_3, and Al layers were formed by evaporation. CBP:12 wt% Ir(ppy)$_3$ layers were evaporated or spin-coated by using either of 1,4-dioxane or cyclopentanone. The driving voltage of the evaporated device was lower than that of the spin-coated devices. Also, the driving voltage of the spin-coated device using 1,4-dioxane was lower than that of the spin-coated device using cyclopentanone. Fig. 2 shows the energy diagram of HOD with solution-processed CBP:12 wt% Ir(ppy)$_3$ layer. We assume that the causes for increase of the driving voltages are the decrease of the triphenyl amine density and hole trapping by HOMO level of Ir(ppy)$_3$ in mixed layer.

In conclusion, we investigated the TFB/CBP-d_{16}:Ir(ppy)$_3$ interfaces from solution processes by NR. We found swollen TFB layer and CBP-d_{16}:Ir(ppy)$_3$ mixing to swollen TFB layer. These interfacial mixings affected the device characteristics. The precise evaluation of the organic/organic interfaces and improvement of interfacial formation method are important to enhance the characteristics of solution-processed OLEDs.

We would like to thank the "Strategic Promotion of Innovative R&D Program" and the "Japan Regional Innovation Strategy Program by Excellence" of Japan Science and Technology Agency (JST) for their financial support. The NR experiment was approved by the Neutron Science Proposal Review Committee of J-PARC/MLF (Proposal No. 2012B0089) and supported by the Inter-University Research Program on Neutron Scattering of IMSS, KEK.

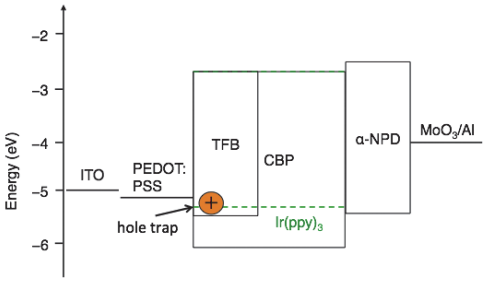

Figure 2. Energy diagram of solution processed HODs.

References

[1] H. Sasabe and J. Kido, *J. Mater. Chem. C.* **1**, 1699 (2013).

[2] R.-J. Roe, *Methods of X-ray and Neutron Scattering in Polymer Science*, Oxford University Press, New York, America, (2000).

[3] S. Ohisa *et al.*, *Adv. Mater. Interfaces*, in printing (DOI: 10.1002/admi.201400097).

[4] K. Mitamura *et al.*, *Polym. J.* **45**, 100 (2013).

[5] A. Nelson, *J. Phys.: Conf. Ser.* **251**, 012094 (2010).

S. Ohisa[1], G. Matsuba[1], N. L. Yamada[2,3], Y.-J. Pu[1], H. Sasabe[1], and J. Kido[1]

[1]*Graduate School of Science and Engineering, Yamagata University;* [2]*Neutron Science Section, Materials and Life Science Division, J-PARC center;* [3]*Institute of Materials Structure Science, KEK*

SANS and SAXS Studies on Aggregates Properties of a Novel Sugar-Type Surfactant in Aqueous Solution

1. Introduction

Recently, we successfully synthesized a novel sugar-type surfactant (C_{12}-*m*GEMA; GEMA is a glucosyloxyethyl methacrylate) with a dodecyl chain in a terminal group involving multi-sugar chains (*m*: the number of sugar) [1]. Figure 1 shows the chemical structure of C_{12}-*m*GEMA. By employing surface tension measurements, C_{12}-*m*GEMA was shown to exhibit a higher efficiency in lowering the surface tension of water. In addition, we found that C_{12}-*m*GEMA effectively acts as a stabilizer for synthesizing metal nanoparticles. However, no information was gathered on the aggregate structure formed by C_{12}-*m*GEMA in an aqueous solution. In this study, by using small-angle neutron scattering (SANS) and small-angle X-ray scattering (SAXS), we investigated the meso-scale aggregate behavior of the C_{12}-*m*GEMA in an aqueous solution depending on the number of sugar. The combined use of SANS and SAXS is one of the most effective techniques to quantitatively reveal aggregates of amphiphilic molecules in solutions.

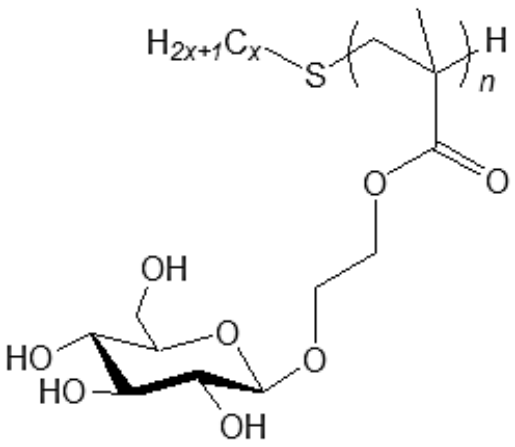

Figure 1. Chemical structure of amphiphilic multi-sugar type surfactant (C_{12}-*m*GEMA) with a hexadecyl chain in a terminal group and multi-sugar chains. GEMA is a glucosyloxyethyl methacrylate.

2. Experimental

C_{12}-*m*GEMA molecules with varying number of sugar from 3.0 to 7.1 were systematically synthesized according to a procedure described in the recent report [1]. After synthesis, we confirmed the chemical structure, including the number of sugar, by employing ^{1}H-NMR and elemental analysis. The C_{12}-*m*GEMA solutions were prepared by dissolving 25 mg/ml of C_{12}-*m*GEMA lyophilized powder in an aqueous solution. The pure D_2O (Cambridge Isotope Laboratories Inc., Andover, MA) was used for SANS measurements. SANS experiments were performed using the TAIKAN instrument installed on the BL15 beamline at the MLF, J-PARC (Tokai, Japan). The covered Q range was 0.015 – 3.0 Å^{-1} in one measurement, where Q is defined by $Q = 4\pi\sin(\theta/2)/\lambda$ (λ and θ represent the wavelength and the scattering angle, respectively). The exposure time for each sample was 3 hours. SAXS experiments were performed using the SAXS spectrometer installed on BL10C beamline at the Photon Factory, KEK (Tsukuba, Japan). The sample-to-detector distances were 1 m, and the X-ray wavelength was 1.488 Å. The covered Q-range was 0.01 – 0.3 Å^{-1}. The exposure times were 10 minutes. SANS and SAXS measurements were performed at an ambient temperature.

3. Result and Discussions

Figures 2(a) and 2(b) show SANS and SAXS profiles for C_{12}-*m*GEMA solutions depending on the number of sugar (*m*). SANS profiles were decreased drastically at around $Q = 0.05$ Å^{-1}. In contrast, SAXS profiles exhibited a bell-shaped peak profile in the Q-range of 0.15 Å^{-1} < Q < 0.3 Å^{-1}. The SAXS profiles consistently differed from the SANS results. In the case of SAXS for a micellar structure formed by amphiphilic molecules in water, the observed peak profile was attributed to greater difference in the scattering length density (so-called contrast) between hydrophilic and hydrophobic portions. On the

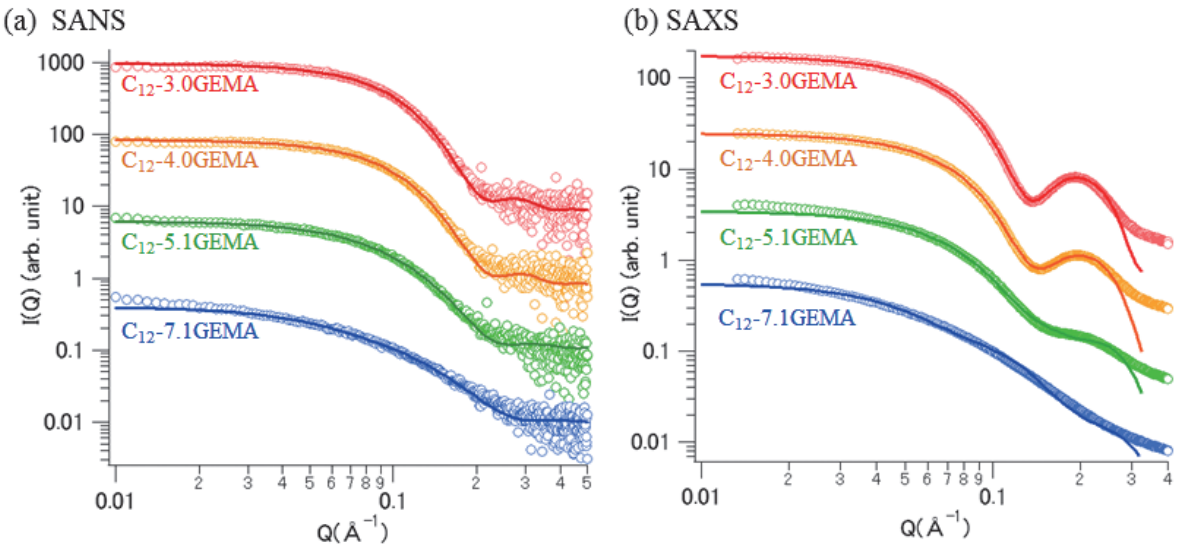

Figure 2. (a) SANS and (b) SAXS profiles for C_{12}-*m*GEMA in an aqueous solution with varying the number of sugar (*m*). Solid lines are the best fitted theoretical scattering curves. Each profile is vertically shifted to avoid overlapping.

other hand, in the case of SANS, when D_2O was used as a solvent, the contrast for the neutrons between the hydrophilic and the hydrophobic portions was lower than that between D_2O and amphiphilic molecules. Therefore, the peak profile was absent in the SANS profiles.

In Figure 2(a), in the *Q*-range of $Q > 0.1$ Å^{-1}, the SANS profile showed power law behavior $I(Q) \sim Q^{-a}$. The power law exponent (*a*) was decreased from 4.1 to 1.7 with increasing the number of sugar. In the SAXS profiles [shown in Figure 2(b)], the peak profile in the *Q*-range of 0.1 Å^{-1} < *Q* < 0.4 Å^{-1} gradually became broader.

To determine the structural parameters quantitatively, model-fitting analysis was performed on both the SANS and the SAXS profiles using a theoretical scattering function given by a product of the form factor *P*(*Q*) and the structure factor *S*(*Q*). We employed a core-shell prolate ellipsoid model for *P*(*Q*) and a hard sphere model given by the Percus-Yevick approximation [2]. All best-fit theoretical scattering curves are shown in Figures 2(a) and 2(b). The theoretical scattering curves appropriately agree with all experimental results. By increasing the number of sugar, the overall radius was slightly decreased from 1.9 to 1.4 nm, whereas the overall axis ratio was significantly increased from 1.6 to 4.2. The results suggest that the shape of micelles formed by C_{12}-*m*GEMA in an aqueous solution change from a spherical shape to an ellipsoid by increasing the number of sugar.

References

[1] Yoshimura *et al.*, in preparation
[2] J. Percus and G. J. Yevick, J. Phys. ReV. 110, 1 (1959).

K. Akutsu[1], H. Iwase[1], Y. Nakatani[2], and T. Yoshimura[2]
[1]Neutron R&D Division, CROSS-Tokai; [2]Research Group of Chemistry, Division of Natural Sciences, Nara Women's University

Neutron Brillouin Scattering of Hydrated β-Lactoglobulin

1. Introduction

The dynamics of biomolecules in water comprises not only micro- and millisecond-scale formational changes (e.g. domain motion of protein) but also pico- and femto-second-scale fluctuations. The former is directly related to the biological activity and/or function of protein (e.g. molecular recognition process), whereas the latter is concerned with the diffusive and vibrational motions of biomolecules and the surrounding water molecules. Hydration of biomolecules directly perturbs the latter dynamics to induce the former dynamics easily due to the conformational flexibilities of the biomolecules. Therefore, investigation of pico- and femto-second dynamics is highly needed for understanding a possible mechanism of the biological functions and the activities of biomolecules in water.

Many elastic and quasi-elastic neutron scattering measurements for hydrated proteins have revealed that the motions of hydrated proteins and hydration water change drastically with the hydration level and temperature [1, 2]. These dynamics are mainly reflected on the diffusive motion of protein atoms and hydration water molecules because of the energy resolution of micro-eV order. On the other hand, milli-eV dynamics corresponding to collective vibrational motion on the femto-second time scale is observed by inelastic X-ray scattering and neutron Brillouin scattering (NBS). There are few studies on the collective dynamics of hydrated proteins because of the difficulty of the measurements. Previously, we performed inelastic X-ray scattering of hydrated β-lactoglobulin at a few hydration levels [3]. The collective dynamics of hydrated proteins also changes depending on the hydration level. Orrechini et al. measured NBS of hydrated ribonuclease at room temperature [4] and revealed that the NBS spectra reflect the collective dynamics of hydration water of the protein.

In the present study, NBS of hydrated β-lactoglobline at 180 and 298 K was measured on the HRC spectrometer at BL12 of MLF to investigate whether or not the collective dynamics changes around the dynamic transition temperature (~ 220 K; the pico-second dynamics measurements revealed that the mean square displacement of some hydrated proteins increase remarkably at this temperature [5]).

2. Experimental

β-lactoglobline powder (SIGMA-ALDRICH) was used without further purification. The powder was dissolved in D_2O and lyophilized. The process was repeated three times to exchange labile hydrogens of the protein with deuterons. Then the dry protein powder was kept in a desiccator with saturated vapor of D_2O. The D_2O absorbed protein powder (with hydration level of 0.4) was sealed into a rectangle cell made of aluminum under helium atmosphere. The inner dimensions of the cell were 30 × 30 × 9.5 mm^3. Indium wire was used for sealing. The cell was stored in the vacuum chamber of the HRC spectrometer. A cryostat equipped in BL12 controlled the temperature of the sample.

Phonon excitations in the hydrated protein were measured at T = 300 K with E_i = 102 meV and ΔE = 2.0 meV. The data were accumulated typically for 2 days at each temperature.

3. Results

Figure 1 shows the scattering intensity of hydrated β-lactoglobline at 298 K. The spectrum showed shoulders due to symmetrical excitation peaks and a resolution-limited elastic peak. The excitation peaks were fitted with a damped harmonic oscillator scattering function convoluted with the resolution width multiplied by a temperature factor (Bose-Einstein factor). The peak positions $E_p(Q)$ were determined as a function of Q. The present analysis is identical to that for D_2O measured previously at BL12 [6].

In Fig. 2, the Q dependence of the $E_p(Q)$ values is shown at 180 and 298 K. At both temperatures, a dispersion relation is found. The slope indicates the velocity of the high-frequency sound.

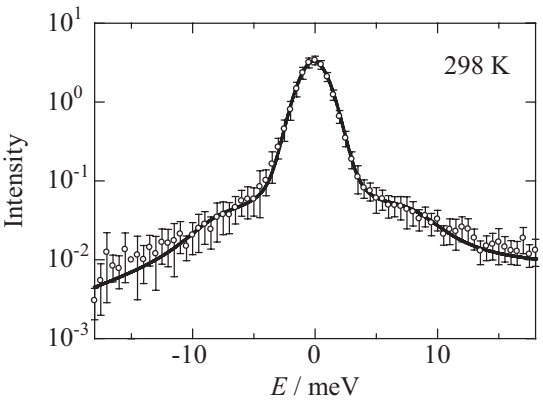

Figure 1. The NBS spectrum of hydrated β-lactoglobulin at a hydration level = 0.4 as a function of excitation energy E at Q = 5.0 nm^{-1} at 298 K. The solid line indicates the DHO fitting results.

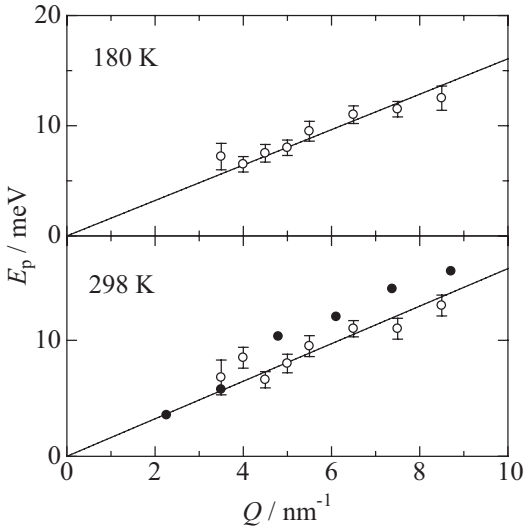

Figure 2. The dispersion relation between the inelastic excitation peak E_p(Q) and the momentum transfer Q for hydrated β-lactoglobulin at a hydration level = 0.4 at 180 K and 298 K. The open circles indicate the NBS results and the filled circles are the IXS ones [3]. The solid lines show the least-squares fits in the NBS results.

These values at 180 and 298 K are 2430 ± 80 and 2460 ± 110 ms^{-1}, respectively. The high-frequency sound velocity at 298 K is almost the same as that at 180 K within the experimental errors. That is, the dynamic transition at ~ 220 K is not very remarkable in femto-second collective dynamics of the hydrated protein. This is consistent with the results of the IXS measurement, where the high-frequency sound of hydrated lysozyme does not change drastically in the temperature range between 300 and 190 K [7].

The high-frequency sound velocity at 298 K in the present study is a little smaller than that obtained from the IXS experiments [3]. For neutron scattering, the contribution from deuterons is more dominant. The difference in the high-frequency sound velocity might be influenced by hydration of heavy water.

4. Future Plans

Femto-second dynamics observed with inelastic scattering is sensitive to atomic potentials which determine protein structure and interaction with hydration water. Molecular dynamics (MD) simulations of proteins require more realistic atomic potentials. The femto-second dynamics data can help to validate experimentally the atomic potentials using the MD simulations. Neutron scattering can provide information on the individual parts of proteins by using the H/D substitution technique. The dynamics of active sites of proteins is selectively obtained when partially deuterium labeled proteins are available. To connect function and activities of proteins with femto-second dynamics, investigation of different types of proteins is necessary.

References

[1] "Workshop on Hydration Processes in Biology: Theoretical and Experimental Approaches" (M.C. Bellissent-Funel, ed.), IOS Press, 1998.
[2] "Water: The Forgotten Biological Molecule" (D. Le Bihan, H. Fukuyama, eds.), Pan Stanford Publishing, 2011.
[3] K. Yoshida *et al.*, J. Chem. Phys. 133 (2010) 134501-1-7.
[4] A. Orecchini *et al.*, J. Am. Chem. Soc. 131 (2009) 4664–4669.
[5] W. Doster *et al.*, Nature 337 (1989) 754-756.
[6] S. Itoh *et al.*, J. Phys: Conference Series 502 (2014) 012043-1-5.
[7] Z. Wang *et al.*, J. Phys. Chem. B 117 (2013) 1186–1195.

K. Yoshida[1], T. Yamaguchi[1], D. Kawana[2], T. Yokoo[3,4], and S. Itoh[3,4]
[1]*Facluty of Science, Fukuoka University;* [2]*The Institute for Solid State Physics, The University of Tokyo;* [3]*Neutron Science Section, Materials and Life Science Division, J-PARC center;* [4]*Institute of Materials Structure Science, KEK*

Inelastic Neutron Scattering Study in Multiferroic Compound $NdFe_3(^{11}BO_3)_4$

1. Introduction

Symmetry breaking of time reversal and space inversion allows spontaneous order both in magnetism and dielectricity. The enhanced simultaneous order, multiferroics, has been extensively studied since the discovery of its experimental realization in the perovskite manganite $TbMnO_3$. The rare-earth iron borates $RFe_3(BO_3)_4$ (R = rare-earth metal) are a new family of multiferroic compounds. The crystal structure of $NdFe_3(BO_3)_4$ is shown in Fig. 1(a). Fe^{3+} ions carry $S = 5/2$ spins and Nd^{3+} ion carry $J = 9/2$ moments. FeO_6 octahedra form spiral chains with three-fold rotational symmetry along the crystallographic c-axis. Bulk property studies reported that an antiferromagnetic order of easy-plane type and spontaneous electric polarization simultaneously appeared at $T_N = 30$ K, and that the electric polarization was enhanced by applying magnetic field [1-3]. Neutron diffraction [4] revealed collinear magnetic order in the intermediate temperature range $T_N \geq T \geq T_{IC} = 13.5$ K in Fig. 1(b). Below T_{IC} incommensurate magnetic order appeared. In spite of accumulative studies on static properties, microscopic dynamics in wide energy wave number space has not been reported so far. In this report we study magnetic excitation by means of inelastic neutron scattering technique to identify the magnetic model in the multiferroic compound $NdFe_3(^{11}BO_3)_4$.

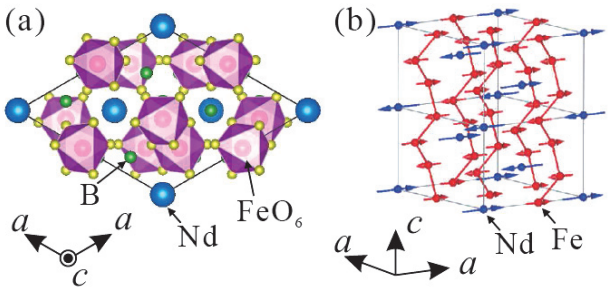

Figure 1. The crystal structure (a) and magnetic structure (b) of $NdFe_3(BO_3)_4$ (hexagonal, space-group $R32$).

2. Experimental Details

Single crystals of $NdFe_3(^{11}BO_3)_4$ were grown by a flux method. 22 pieces of single crystals were coaligned by using transmission X-ray Laue camera. The total mass of the crystals was 2.1 g. The inelastic neutron scattering experiment was performed at the High Resolution Chopper (HRC) spectrometer installed in MLF/J-PARC. The incident energy E_i was set to 11.46 meV. Soller collimator with a divergence angle of 1.5° was installed in front of the sample to eliminate the direct beam contamination, and a 200 Hz Fermi chopper, "S", was used to obtain high flux neutrons. The single crystals were mounted so that a^*c^* plane was horizontal. We set the sample temperature at 15 K in the commensurate ordered phase. The a^*-axis was initially parallel to the incident neutron beam and the crystals were rotated counterclockwise by 70 degrees with steps of 2 degrees.

3. Experimental results

We collected inelastic neutron spectrum, where well-defined excitations were observed. We extracted constant Q cuts from the data, fitted the data by Gaussian function, and plot the peak energies for each cut by filled circles as shown in Figs. 2(a) and (b). Here Q = (0, 0, –1.5) is the magnetic Bragg peak position. A dispersive excitation with band energy of 5.5 meV along the c^* direction was observed. An anisotropy gap with magnitude of about 0.5 meV was observed at Q = (0, 0, –1.5), which was consistent with a previous ESR study [5]. The excitation is ascribed to Fe^{3+} centered spin wave excitation which will be explained later. A flat excitation is observed at 1.3 meV. This mode is explained by the energy split of the Kramers doublet of the Nd^{3+} ion due to the exchange interaction with the Fe^{3+} ion. Anti-crossing is observed between the dispersive and non-dispersive modes, which means the existence of interaction between Fe^{3+} and Nd^{3+} ions. The magnetic excitations are more dispersive along the c^* direction in Fig. 2(a) than the a^* direction in Fig. 2(b), which

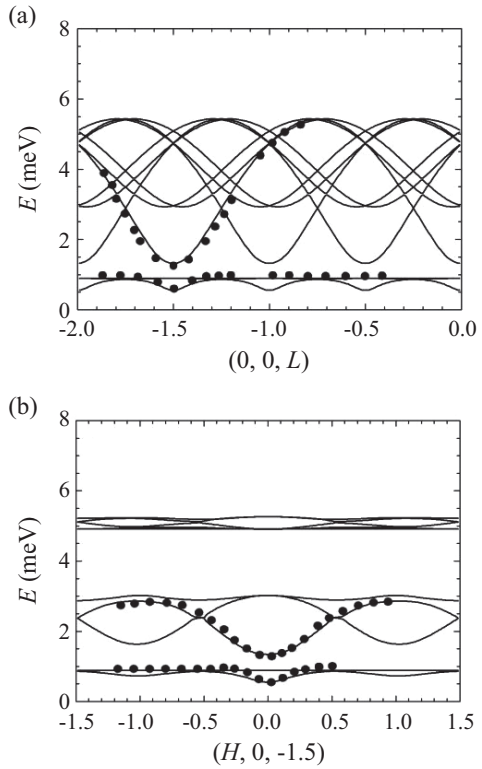

Figure 2. (a) Magnetic excitation along the c^*-direction. (b) Magnetic excitation along the a^*-direction.

means that the magnetic interaction along the *c* direction, i.e., the Fe^{3+} chain direction is dominant.

4. Analysis

In order to identify the magnetic model of $NdFe_3(^{11}BO_3)_4$, we performed spin wave calculation by using a Holstein-Primakoff transformation [6]. The minimal model of the Hamiltonian is as follows:

$$H = -\sum_{n.n} J_1 \mathbf{S}_i \cdot \mathbf{S}_j - \sum_{n.n.n} J_2 \mathbf{S}_i \cdot \mathbf{S}_j - \sum_{n.n} J_3 \mathbf{S}_i \cdot \mathbf{J}_k - \sum_i D_i \left(S_i^z\right)^2 - \sum_k h_{eff} J_k^z$$

The first term is the exchange interaction between Fe spins along the inchain direction and the second term is that along the interchain direction, which leads to the dispersion along the c^*- and a^*-directions, respectively. The third term is the interaction between Fe^{3+} and Nd^{3+} ions, which induces the anti-crossing of the spin wave of Fe^{3+} ions and the crystal field of Nd^{3+} ions. The forth term is the single ion anisotropy of Fe^{3+} ions. The last term is the energy split of Kramers doublet of Nd^{3+} ions due to the staggered field of Fe^{3+} ions.

Fit to the data is indicated by the solid curves in Figs. 2(a) and (b). The obtained parameters are J_1 = 0.48 meV, J_2 = 0.050 meV, J_3 = 0.027 meV, D = 0.005 meV, and h_{eff} = 0.135 meV. The reasonable fit to the data means that the dispersive excitation is dominantly explained by weakly coupled Fe^{3+} spin chains. The flat mode is dominated by the Zeeman split of the Kramers doublet of Nd^{3+} crystal field. Anti-crossing between Fe^{3+} spin wave and Nd^{3+} crystal field is ascribed to the interaction between Fe^{3+} and Nd^{3+} moments.

5. Conclusion

We measured the inelastic neutron spectrum in the multiferroic compound $NdFe_3(^{11}BO_3)_4$ by rotating the single crystals at the HRC spectrometer. The observed well-defined excitations were reasonably explained by spin-wave calculation based on our minimal magnetic model.

References

[1] N. Tristan, R. Klingeler, C. Hess, B. Büchner, E. Popova, I. A. Gudim, and L. N. Bezmaternykh, J. Magn. Magn. Mater. **316**, E621 (2007).

[2] A. M. Kadomtseva, Yu. F. Popov, G. P. Vorob'ev, A. P. Pyatakov, S. S. Krotov, K. I. Kamilov, V. Yu. Ivanov, A. A. Mukhin, A. K. Zvezdin, A. M. Kuz'menko, L. N. Bezmaternykh, I. A. Gudim, and V. L. Temerov, Low Temp. Phys. **36**, 511 (2010).

[3] A. K. Zvezdin, G. P. Vorob'ev, A. M. Kadomtseva, Yu. F. Popov, A. P. Pyatakov, L. N. Bezmaternykh A. V. Kuvardin, and E. A. Popova, JETP Lett. **83**, 11 (2006).

[4] P. Fischer, V. Pomjakushi, D. Sheptyakov, L. Keller M. Janoschek, B. Roessli, J. Schefer, G. Petrakovskii, L. Bezmaternikh, V. Temerov and D. Velikonov, J. Phys.:Condens. Matter **18**, 7975 (2006).

[5] A. M. Kuz'menko, A. A. Mukhin, V. Yu. Ivanov, A. M. Kadomtseva, and L. N. Bezaternykh, JETP Lett. **96**, 294 (2011).

[6] Albert W. Sáenz, Phys. Rev. **125**, 6 (1961).

S. Hayashida[1], M. Soda[1], K. Ohgushi[1], S. Itoh[2,3], T. Yokoo[2,3], and T. Masuda[1]

[1]*The Institute for Solid State Physics, The University of Tokyo;* [2]*Neutron Science Section, Materials and Life Science Division, J-PARC center;* [3]*Institute of Materials Structure Science, KEK*

Spin-Wave Dispersion in Nd-Fe-B Permanent Magnets Observed by Neutron Brillouin Scattering

1. Introduction

The permanent magnets with high coercivity have been under intensive study because of their application in high-power motors used in hybrid and electric vehicles. The Nd-Fe-B magnet is the most commonly used magnet with both high saturation magnetization and magneto-crystalline anisotropy. For understanding the coercivity mechanism, it is indispensable to know the intrinsic magnetic properties of magnetic materials.

Spin-wave dispersion in magnetic materials is very important as it provides a microscopic viewpoint for the phenomenological magnetic parameters. Along with the saturation magnetization, Curie temperature and magnetostatic energy, magnetocrystalline anisotropy (K1) and exchange stiffness constant (A) determine a wide range of magnetic properties in magnetic materials such as the domain-wall width, domain-wall energy, exchange length, hardness parameter, single-domain radius and anisotropy field.

Among the phenomenological magnetic parameters, the exchange stiffness constant is of particular importance in the magnetization reversal process as it measures the strength of the exchange interaction between the magnetic moments in a magnet. Thus, the exchange stiffness constant describes the non-uniform magnetization reversal process in a magnet.

2. Spin-wave dispersion measurement

However, measuring the exchange stiffness constant is rather difficult. The simplest determination of exchange stiffness constant from the Curie temperature has generally led to the lower bound for the exchange stiffness constant, because the molecular field theory omits the low-energy spin-wave excitations. Therefore, the exchange stiffness constant derived from the spin-wave stiffness constant either with spin-wave dispersion measurements is more realistic.

The best way to measure the exchange stiffness constant is derived from the spin-wave stiffness in the low-energy spin-wave dispersion, because the energy of the long-wavelength spin wave is associated with a gradual twist in the magnetization. Inelastic neutron scattering (INS) is the most direct method to determine the spin-wave dispersion, however, a large single-crystalline sample is needed for INS and the measurements for either polycrystalline or powder samples are difficult.

3. Neutron Brillouin scattering (NBS)

We propose the use of neutron Brillouin scattering (NBS) with sub-eV pulsed neutrons to determine the spin-wave dispersion in polycrystalline Nd-Fe-B magnets. NBS is an advantageous method for observing coherent excitations in non-single-crystalline materials. The dynamic structure factor for ferromagnetic spin-waves in polycrystalline samples was averaged and the scattering intensities were detected in the forward direction with a momentum transfer (Q) near 0, and were rapidly decreasing with an increasing Q. Neutrons with an incident energy (Ei) in the sub-eV region are necessary to measure meV-range low-energy excitations with high energy resolution. Furthermore, small scattering angles are required to detect the scattered neutrons. Recently, efforts in realizing the experimental conditions with the NBS method have been made with a high-resolution chopper spectrometer (HRC) installed at J-PARC/MLF [2, 3, 4].

4. NBS experiments at HRC in J-PARC/MLF

In the NBS function at HRC, a monochromatic incident neutron beam with energy Ei illuminated the sample and the energy transfer of the scattered neutrons was determined using the time-of-flight method. For the NBS measurements, scattered neutrons were collected with the two-dimensional bank of the PSD array at low scattering angles φ = 0.5 – 2.8°.

A polycrystalline Nd-Fe-B strip-cast sample was used for the NBS experiment. Natural boron was substituted for ^{11}B to reduce neutron absorption. The energy of the incident neutron beam was set at 257 meV with an energy bandwidth of 5.7 meV. NBS measurements were performed at sample temperatures of 300 K and 6 K.

5. Exchange stiffness constant determined by NBS

Figure 1 shows the spin-wave dispersion curve for an Nd-Fe-B magnet measured using NBS. We observed quadratic spin-wave dispersion, which is in good agreement with the previous inelastic neutron scattering results for a single crystal [5, 6].

The low-energy spin-wave dispersion in the limit of the small wave-vectors is described as $E(Q) = E_0 + Dsw\ Q^2$, where E_0 is the energy gap at $Q = 0$ and Dsw is the spin-wave stiffness constant. In NBS, Q values around 0 could not be accessed. Thus, $E_0 = 2.0$ meV was obtained from the bulk value of $K1 = 4.5$ MJ/m^3 [7]. The spin-wave stiffness constant D_{sw} was found by fitting the spin-wave dispersion. From the fitting we were able to determine $D_{sw} = 100.0 \pm 4.9$ meVÅ^2. From the spin-wave dispersion measurements we determined the exchange stiffness constant, A of 6.6 ± 0.3 pJ/m. This value is comparable to the reported values of 7.3 – 12.5 pJ/m [1] and the exchange stiffness constant measured by NBS was considered reliable, as NBS is a direct method in accessing the spin-wave properties of magnets.

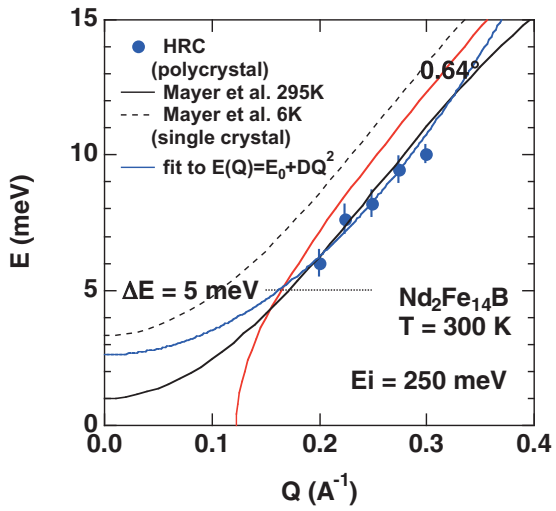

Figure 1. Spin-wave dispersion curves for the Nd-Fe-B magnet measured using NBS. The blue dot indicates the peak position observed using NBS. The blue line shows the fit of the experimental data to a quadratic equation. The red line shows the detection limit of the present NBS set up with the detector bank at 0.64°.

This work was supported in part by the Elements Strategy Initiative Center for Magnetic Materials (ESICMM) under the outsourcing project of MEXT. The sample fabrication was performed in part under the Magnetic Materials for High-Efficient Motors (MagHEM) project.

References

[1] H. Kronmüller and M. Fähnle, "Micromagnetism and the Microstructure of Ferromagnetic Solids", Cambridge University Press (2003).

[2] S. Itoh, T. Yokoo, S. Satoh, S. Yano, D. Kawana, J. Suzuki, and T. J. Sato, Nucl. Instr. Meth. Phys. Res. A 631, 90 (2011).

[3] S. Itoh, Y. Endoh, D. Kawana, Y. Kaneko, Y. Tokura, and M. Fujita, J. Phys. Soc. Jpn. **82**, 043001 (2013).

[4] S. Itoh, T. Yokoo, D. Kawana, and Y. Endoh, J. Phys. Soc. Jpn. **82**, SA034 (2013).

[5] H. M. Mayer, M. Steiner, N. Stüßer, H. Weinfurter, K. Kakurai, B. Dorner, P. A. Lindgård, K. N. Clausen, S. Hock, and W. Rodewalde, J. Magn. Magn. Mat. **97**, 210 (1991).

[6] H. M. Mayer, M. Steiner, N. Stüßer, H. Weinfurter, B. Dorner, P. A. Lindgård, K. N. Clausen, S. Hock, R. Verhoef, J. Magn. Magn. Mat. **104-107**, 1295 (1992).

[7] S. Hirosawa, Y. Matsuura, H. Yamamoto, S. Fujimura, M. Sagawa, and H. Yamauchi, J. Appl. Phys. **59**, 873 (1986).

[8] K. Ono, N. Inami, K. Saito, Y. Takeichi, M. Yano, T. Shoji, A. Manabe, A. Kato, Y. Kaneko, D. Kawana, T. Yokoo, and S. Itoh, J. Appl. Phys. **115**, 17A714 (2014).

K. Ono[1], N. Inami[1], K. Saito[1], Y. Takeichi[1], M. Yano[2], T. Shoji[2], A. Manabe[2], A. Kato[2], Y. Kaneko[3], D. Kawana[1], T. Yokoo[1,4], and S. Itoh[1,4]

[1]Institute of Materials Structure Science, KEK; [2]TOYOTA Motor Corporation; [3]Toyota Central R&D Labs. Inc.; [4]Neutron Science Section, Materials and Life Science Division, J-PARC center

Doping-Evolution of High-Energy Spin Excitation in the Electron-Doped $Pr_{1.4-x}La_{0.6}Ce_xCuO_4$

1. Introduction

In the research of high-transition-temperature superconductivity, the evolution of the spin excitation with doping is a fascinating and long-standing issue. It is well known that the conventional spin-wave excitation in Mott insulator La_2CuO_4 or $YBa_2Cu_3O_6$ turns into the hourglass shaped excitation by the hole-doping [1,2]. In the low-energy region, the spin excitation exhibits the incommensurate character with the propagation vector parallel to the CuO bonding direction in the superconducting (SC) phase, while the high-energy excitation remains spin-wave-like dispersion. Such a distinct doping-dependence of spin excitations separated by the energy is one of keys to understand the role of magnetism in the mechanism of superconductivity. In contrast to the progressive research in the hole-doped system, less is known about the entire spin excitation in the electron-doped cuprates. Fujita [3] and Wilson [4] separately observed the spin excitation up to ~ 200 meV in the SC sample and clarified a steeper excitation along the energy direction than in the undoped compound. This result suggests an increase in the zone boundary energy by the electron-doping, unlike the doping-independent high-energy dispersion in the hole-doped system. However, even in the parent compound, measurement of high-energy spin excitation up to the zone boundary is still missing. Thus, in order to confirm the electon-doping dependence of spin excitation and gain an insight into the electron-hole symmetry in the spin correlation, we performed pulsed neutron-scattering measurement on a series of $Pr_{1.4-x}La_{0.6}Ce_xCuO_4$ with different x.

2. Experimental details

High-energy inelastic neutron measurements were carried out on assembled single crystals of $x = 0$, 0.08 and 0.18 at the chopper spectrometer 4SEASONS (BL01). All samples used in this study are as-grown and non-superconducting crystal. To observe the spin excitations in wide energy and momentum spaces with the high efficiency, we applied a multi-E_i method, which was developed in J-PARC [5]. The samples were set so that the crystallographic c-axis was parallel to the incident neutron beam and cooled down to 6 K by a closed-cycle refrigerator.

3. Results and discussion

Fig. 1 shows the intensity contour map for the magnetic excitation after subtracting the non-magnetic background. Well-defined spin-wave excitation emerging from $h = 0.5$ was observed in the $x = 0$ sample. The zone boundary energy determined from the dispersion was ~ 320 meV. The intensity lying at ~ 100 meV in a wide momentum range corresponds to a crystal field excitation from Pr^{3+} ion. As seen in the figure, the high-energy excitation shows a drastic doping evolution, that is, the magnetic excitation gets steeper with increasing the Ce concentration. This trend can be clearly seen in the constant-energy spectrum sliced at 280 meV along h-direction through (0.5, 0.5) reciprocal position (Fig. 2). The magnetic intensity in $x = 0$ shows peaks at the $h = 0$ and ± 1, while the main peaks locate at $h = \pm 0.5$ in $x = 0.18$. This shift of the peak position from the zone-center to the zone-boundary is consistent with the elongation of the magnetic excitation toward the high-energy region. This trend is in stark contrast to a negligible doping dependence of high-energy spin excitation in the hole-doped LSCO. Thus, electron-hole asymmetry exists in the spin excitation against doping. We note that the elongation of magnetic excitation spectrum with electron-doping was observed by our recent resonant inelastic X-ray scattering measurement [6]. Such doping evolution would be difficult to understand within a simple model based on the localized spin picture, which takes only the nearest neighbor spin interaction into account. In the La_2CuO_4 [7], the existence of higher term exchange interaction is reported. More microscopic consideration is required to clarify the origin of anomalous doping evolution of spin excitation.

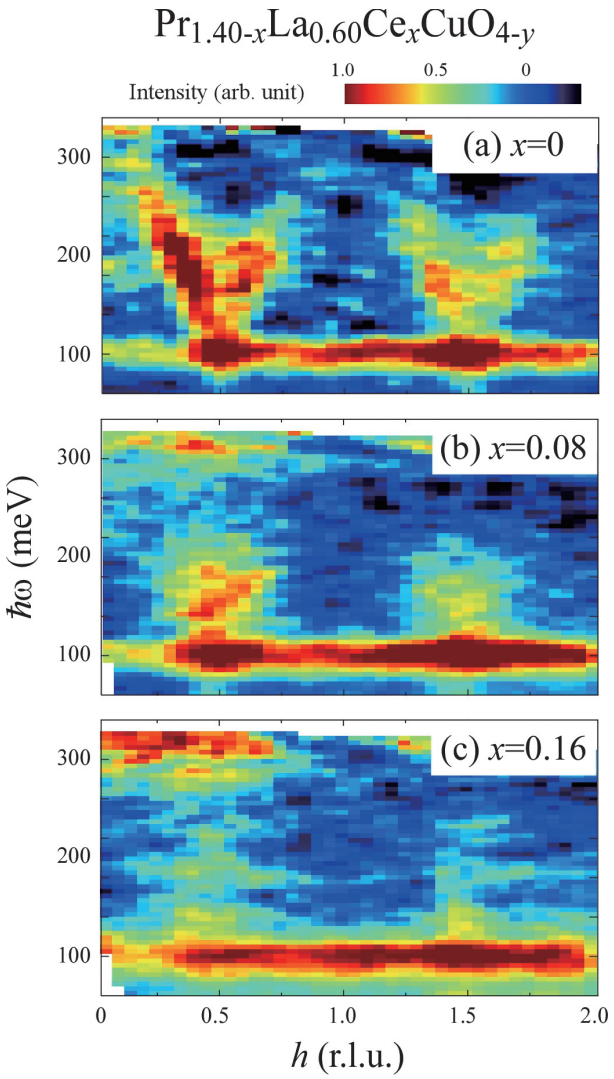

Figure 1. Spin excitation spectrum in the $Pr_{1.4-x}La_{0.6}Ce_xCuO_4$ with (a) $x = 0$, (b) 0.08 and (c) 0.18. To enhance the high energy excitation, the value of energy transfer was multiplied to the intensity after subtracting the background. The flat band around 100 meV is a crystal field excitation from Pr^{3+} ion.

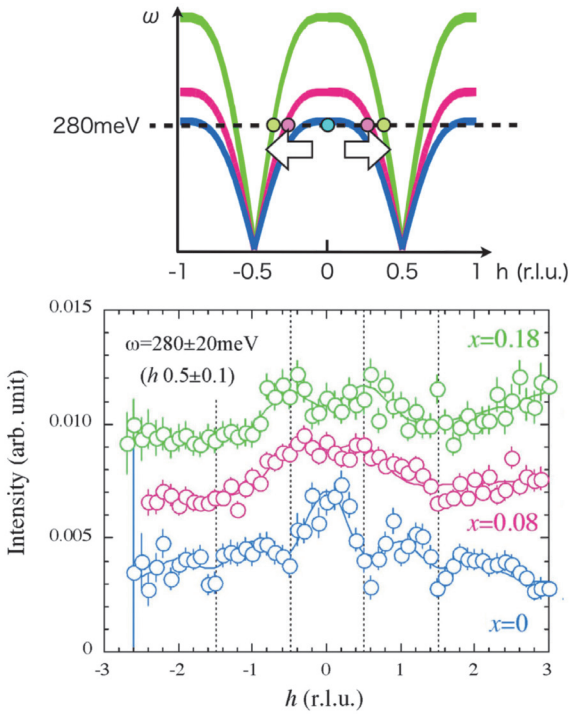

Figure 2. (Upper figure) Image of the doping evolution of spin excitation, which is suggested from the present neutron scattering experiment. (Lower figure) Constant energy spectrum in the $Pr_{1.4-x}La_{0.6}Ce_xCuO_4$ with x = 0 (blue), 0.08 (pink) and 0.18 (green) sliced at 280 meV.

4. Summary

We preformed neutron scattering measurement on the as-grown single crystal of $Pr_{1.4-x}La_{0.6}Ce_xCuO_4$ to evaluate the doping evolution of spin excitation in the electron-doped system. We found the elongation of spin excitation against doping, which is quite different from the negligible doping effect seen in the hole-doped system. Therefore, electron-hole asymmetry exists in the observed spin excitation against the doping.

References

[1] J. M. Tranquada *et al.*, Nature **375**, 531 (2004).
[2] S. M. Hayden *et al.*, Nature **375**, 534 (2004).
[3] M. Fujita *et al.*, J. Phys. Soc. Jpn., **75**, 093704 (2006).
[4] Stephen D. Wilson *et al.*, PRL **96**, 157001 (2006).
[5] M. Nakamura *et al.*, J. Phys. Soc. Jpn., **78**, 093002 (2009).
[6] K. Ishii *et al.*, Nature Comm. **5**, 3714 (2014).
[7] R. Coldea *et al.*, Phys. Rev. Lett. **86**, 5377 (2001).

M. Fujita[1], K. Ishii[2], K. Tsutsumi[3], K. Sato[3], and R. Kajimoto[4]

[1]Institute for Materials Research, Tohoku University; [2]Quntum Beam Science Center, Japan Atomic Energy Agency; [3]Department of Physics, Tohoku University; [4]Neutron Science Section, Materials and Life Science Division, J-PARC Center

Multiple-Probe Study of Highly Hydrogen Doped Fe-based superconductor $LaFeAsO_{1-x}H_x$

1. Introduction

The recent development of the hydrogenation technique in rare earth systems of Fe-based superconductors *RE*$FeAsO_{1-x}H_x$ (*RE*: rare earth) has succeeded in surpassing the limitation of the doping range available in fluorine doping [1]. In the case of $LaFeAsO_{1-x}H_x$, the existence of a secondary superconducting dome (SC2) around $0.2 \leq x \leq 0.4$ has been revealed [1]. Moreover, the maximum T_c of ~ 36 K in SC2 is higher than that of ~ 26 K in the first superconducting dome (SC1) around $0.05 \leq x \leq 0.2$, drawing broad attention regarding the difference in superconducting mechanism between SC1 and SC2. The relationship of SC2 with magnetism would be of particular interest in comparison to that of SC1. To investigate the origin of the two SC domes, we have performed a multiple probe study in the range $0.40 \leq x \leq 0.51$ using muon spin rotation/relaxation (μSR), powder neutron diffraction (ND), and X-ray diffraction (XRD) [2].

2. Multiple probe measurement

Figure 1 (a) shows zero field μSR time spectra for $x = 0.45$ measured using GPS spectrometer at PSI. Spectra above 80 K show slow relaxation, which is attributed to a paramagnetic state, while spectra below 80 K exhibit an oscillation with increased amplitude, indicating the development of the magnetically ordered phase. The temperature dependence of the magnetic volume fraction (MVF) was measured using DΩ1 spectrometer installed at the MUSE D1 area of MLF J-PARC. As hydrogen content x decreases, the onset of the magnetic transition temperature T_N and the MVF at the lowest temperature decreases [2]. Summation of MVF and superconducting volume fraction determined from susceptibility measurement is almost unity, indicating that magnetic and superconducting phases coexist and phase-separates in $0.4 \leq x \leq 0.45$, which is a marked contrast to the underdoped region.

To investigate the magnetic structure, neutron powder diffraction in x = 0.45 and $x = 0.51$ samples was performed in NOVA and S-HRPD in J-PARC MLF, respectively. Extra peaks indexed $(1/2, 1/2, n)_{T,M}$ ($n = 0, 1, 2$) were observed in the low-temperature where the subscripts T, M and N refer to the tetragonal cell, magnetic and nuclear peak, respectively (Figure 1(b)). The temperature dependence of the Bragg peak intensity and the corresponding muon magnetic signal intensity (MVF x precession frequency squared) is shown in Figure 1 (c). Intensities of magnetic peaks develop below T_N = 89(1) K, which is perfectly in line with the μSR result. Similar antiferromagnetic transition was also

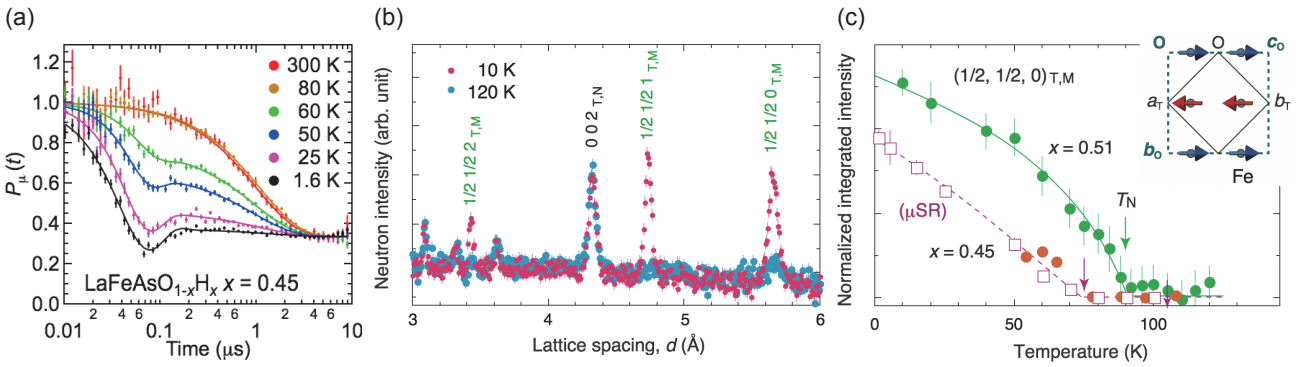

Figure 1. (a) μSR time spectra of $LaFeAsO_{1-x}H_x$ for $x = 0.45$. Spectra below 80 K exhibit fast relaxation with precession signal. (b) Neutron diffraction of x = 0.51 sample. At 10 K, there are additional Bragg peaks from magnetic order. (c) Temperature dependence of muon magnetic signal intensity (volume fraction x precession frequency squared) and neutron Bragg peak intensity.

observed below T_N = 76 K for x = 0.45. The magnetic structure is displayed in the inset of Figure 1 (c) and Figure 2. The spin arrangement is antiferromagnetic collinear structure, and the stacking of neighboring plane along the *c*-axis is ferromagnetic. The magnetic moment in x = 0.51 at 10 K is 1.21(1) μ_B, which is twice as large as that in x = 0 [3].

XRD of x = 0.51 performed at BL-8 in KEK-PF reveals that $(2, 2, 0)_T$ reflection exhibits peak splitting on cooling, whereas, that reflection of x = 0.45 exhibits simply slight broadening. In x = 0.51, (0, 0, L) reflection does not exhibit peak broadening, indicating the occurrence of the tetragonal to orthorhombic (T-O) structural transition. T-O transition temperature T_s ~ 95 K is determined from the temperature dependence of the lattice constant. Interestingly, c_T axis length shows an upturn below T_s. In x = 0.45, although an apparent T-O transition does not exist, the c_T axis anomaly appears below T_s' ~ 80 K as in the case of x = 0.51, which may be attributed to the insufficient coherence of the splitting of a_T and b_T in the low-temperature phase. The crystal structure below T_s in x = 0.51 is determined to be the orthorhombic *Aem*2 structure without inversion symmetry, which is different from *Cmme* structure with inversion symmetry of x = 0 [3,4]. In the *Cmme* structure, Fe atoms exhibit off-center deformation in the $FeAs_4$ tetrahedron, as shown in the inset of Figure 2.

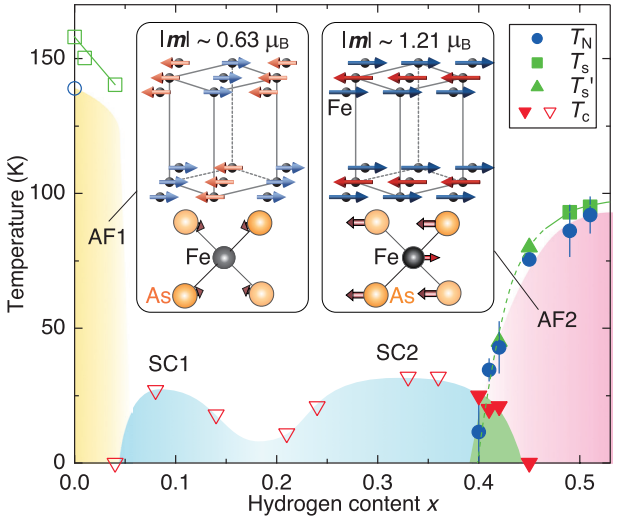

Figure 2. Crystal and magnetic phase diagram of $LaFeAsO_{1-x}H_x$. Filled blue circles, green squares, triangles indicate antiferromagnetic transition temperature (T_N) determined by μSR, structural transition temperature (T_s), and c_T-axis upturn temperature (T_s') determined by XRD, respectively. Insets show the magnetic structures of AF1 (left) and AF2 (right) determined by neutron diffraction, and the structures of $FeAs_4$ tetrahedron.

3. Phase Diagram and Discussion

The resultant temperature dependence of T_N (determined by μSR), T_s and c_T axis upturn temperature T_s' are summarized in Figure 2. The newly discovered antiferromagnetic phase (AF2) preceded by structural transition resembles the behavior of x = 0 phase (AF1). The two-dome SC phase diagram may be interpreted as the carrier doping starting from the left and right side of the parent compounds (x = 0 and x ~ 0.5), where the valley of T_c around x = 0.2 may be a crossover region or the over-doping from both sides of the phase diagram.

References

[1] S. Iimura *et al.*, Nat. Commun. 3 (2012) 943.

[2] M. Hiraishi *et al.*, Nat. Phys, **10**, 300 (2014).

[3] N. Qureshi *et al.*, Phys. Rev. B **82**, 184521 (2010).

[4] T. Nomura *et al.*, Supercond. Sci. Technol. **21**, 125028 (2008).

M. Hiraishi[1], S. Iimura[2], K. M. Kojima[1,3], J. Yamaura[4], H. Hiraka[1], K. Ikeda[1], P. Miao[1,3], Y. Ishikawa[1], S. Torii[1], M. Miyazaki[1,3], I. Yamauchi[1,3], A. Koda[1,3], K. Ishii[5], M. Yoshida[5,6], J. Mizuki[6], R. Kadono[1,3], R. Kumai[1,3], T. Kamiyama[1,3], T. Otomo[1,3], Y. Murakami[1,3], S. Matsuishi[4], and H. Hosono[2,4]

[1]Insitute of Materials Structure Science, KEK; [2]Materials and Structures Laboratory, Tokyo Institute of Technology; [3]Muon Science Section, Materials and Life Science Division, J-PARC center; [4]Materials Research Center for Element Strategy, Tokyo Institute of Technology; [5]SPring-8; [6]School of Science and Technology, Kwansei Gakuin University

Long Periodic Chiral Helimagnetic Ordering in $T_{1/3}MS_2$ (T = Transition Metal, M = Nb and Ta)

The concept of chirality, meaning left- or right-handedness, plays an essential role in symmetry properties of nature at all length scales, from elementary particles to cosmic science. In materials sciences, it is very important to understand the chirality in molecules, crystals and magnetic structures both from theoretical and experimental viewpoints. Recently, significant attention has been paid to the relationship between crystallographic chirality and that of magnetic structure, because the sense of a helical spin structure depends on the right- or left-handed chiral crystallographic structure that allows an asymmetric Dzyaloshinskii-Moriya (DM) interaction [1, 2]. Kishine *et al.* theoretically proposes that the chiral helimagnetic compounds can exhibit a new giant magnetoresistance effect due to the formation of a chiral magnetic soliton lattice [3, 4]. Under an applied field perpendicular to the helical axis in $Cr_{1/3}NbS_2$, the chiral magnetic soliton lattice was observed by means of Lorentz microscopy [5].

However, there have been few experimental results due to the difficulty in synthesizing suitable materials to realize such research. In chiral helimagnetic compounds, the pitch angle, mainly determined by the ratio of exchange interaction and DM interaction, is usually very small. As a result, the helimagnetic period can be hundreds of angstroms. Therefore, sometimes the Q resolution of thermal neutron diffraction experiments is not high enough to separate fundamental Bragg peaks and magnetic satellite peaks. As a consequence, some compounds with chiral helimagnetic ordering may be easily misinterpreted as having ferromagnetic ordering. In this sense, high Q resolution is the key to detect the long periodic helimagnetic satellite peaks.

$T_{1/3}MS_2$ (T = transition metal, M = Nb and Ta), intercalated system of 2H-MS_2, has a chiral crystal structure with a chiral space group $P6_322$. The chiral space group allows DM vector parallel to the crystallographic helical axis, and expects chiral helimagnetic ordering of the c-axis. Magnetization measurements show a variety of magnetic behaviors [6]; antiferromagnetism for $Fe_{1/3}NbS_2$, $Co_{1/3}NbS_2$, $Ni_{1/3}NbS_2$, $Co_{1/3}TaS_2$ and $Ni_{1/3}TaS_2$, and ferromagnetism for $Cr_{1/3}NbS_2$, $Mn_{1/3}NbS_2$, $Cr_{1/3}TaS_2$, $Mn_{1/3}TaS_2$ and $Fe_{1/3}TaS_2$.

In our single crystalline magnetization data, some of the above-mentioned ferromagnetic $T_{1/3}MS_2$ compounds show the magnetization-cusp, indicating the chiral helimagnetic ordering and formation of a chiral magnetic soliton lattice [7].

We performed super high resolution powder neutron diffraction experiments at BL08 (Super HRPD) in the Materials and Life Science Experimental Facility (MLF) of J-PARC. We obtained powder diffractograms of the ferromagnetic $T_{1/3}MS_2$. We succeeded in separating the nuclear and magnetic satellite peaks in $Cr_{1/3}NbS_2$ and $Cr_{1/3}TaS_2$. Figure 1 shows the data around the (0,0,4) and the (1,0,3) reflections. As indicated by the vertical arrows, the magnetic satellite peaks were observed at different d values from the nuclear peaks, and were indexed with the magnetic propagation vector $\boldsymbol{k}_{mag} = (0,0,\delta)$. The periods of the incommensurate magnetic ordering were determined to be 600 angstroms for $Cr_{1/3}NbS_2$ and 230 angstroms for $Cr_{1/3}TaS_2$. There was no peak splitting in $Mn_{1/3}NbS_2$ and $Fe_{1/3}TaS_2$. However, comparing the peak widths between paramagnetic and magnetic phase, we found apparent increase of the peak width in the magnetic phase of $Mn_{1/3}NbS_2$. If the increase is due to existence of magnetic satellite peaks, the period of the magnetic ordering can be over 2000 angstroms.

With determined magnetic propagation vectors, we performed magnetic structure analysis of the obtained diffraction data using Rietveld method. While $Fe_{1/3}TaS_2$ forms ferromagnetic structure along the c-axis, the magnetic structures of $Cr_{1/3}NbS_2$, $Cr_{1/3}TaS_2$ $Mn_{1/3}NbS_2$ are well interpreted by helimagnetic structure in the a-b plane with very long period, which is unique to chiral helimagnetic ordering.

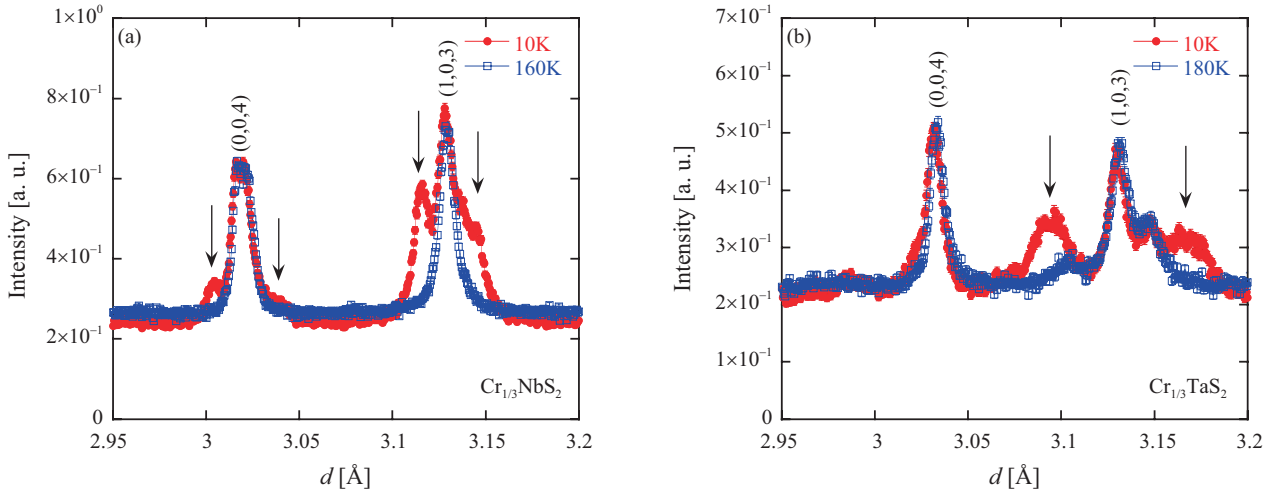

Figure 1. Powder diffraction profiles of the (0,0,4) and the (1,0,3) reflections in (a) $Cr_{1/3}NbS_2$ and (b) $Cr_{1/3}TaS_2$. The vertical arrows indicate magnetic satellite peaks.

References

[1] I. E. Dzyaloshinskii: J. Phys. Chem. Solids **4** (1958) 241.

[2] T. Moriya: Phys. Rev. **120** (1960) 91.

[3] J. Kishine, K. Inoue, and Y. Yoshida: Prog. Theor. Phys. Suppl. **159** (2005) 82.

[4] J. Kishine, I. Proskurin, and A. Ovchinnikov: Phys. Rev. Lett. **107** (2011) 017205.

[5] Y. Togawa, T. Koyama, K. Takayanagi, S. Mori, Y. Kousaka, J. Akimitsu, S. Nishihara, K. Inoue, A. Ovchinnikov, and J. Kishine: Phys. Rev. Lett. **108** (2012) 107202.

[6] S. S. P. Parkin and R. H. Friend, Phil. Mag. B **41** (1980) 65.

[7] Y. Kousaka, Y. Nakao, J. Kishine, M. Akita, K. Inoue, and J. Akimitsu, Nucl. Instr. Meth. Phys. Res. A **600** (2009) 250.

Y. Kousaka[1,2,3], T. Ogura[1], J. Akimitsu[1], K. Inoue[2,3], J. Zhang[4,5], P. Miao[4,6], S. Torii[4,7], and T. Kamiyama[4,6,7]

[1]Department of Physics and Mathematics, Aoyama-Gakuin University; [2]Graduate School of Science, Hiroshima University; [3]Center for Chiral Science, Hiroshima University; [4]Institute of Materials Structure Science, KEK; [5]IHEP, Chinese Academy of Science; [6]Graduate University for Advanced Studies (Sokendai); [7]Neutron Science Section, Materials and Life Science Division, J-PARC center

Detailed Study of the Phase Diagram of Fe-Based Superconductor $Ba(Fe_{1-x}Co_x)_2As_2$

1. Introduction

There are two different proposals concerning the superconducting mechanism of Fe-based systems. One of them considers the role of spin-fluctuation, because the superconductivity appears near the antiferromagnetic (AF) phase in the phase diagram (see Fig. 1 for $Ba(Fe_{1-x}Co_x)_2As_2$, for example). The other proposal considers the "orbital-fluctuation" defined by the electron occupancies between the 3dyz and 3dzx orbitals, because of the common existence of the tetragonal (Tet)-orthorhombic (Ort) structural transition found in various Fe-based systems at temperature T_S slightly higher than the AF transition temperature T_N (see Fig. 1) [1].

In addition to the above two temperatures, T_S and T_N, another temperature T^* ($= T_S + \eta$, the η value being not so clear but ~ 30 K at $x \sim 0.02$) has been added by observing the breakdown of the four-fold symmetry (C_4) of transport and other static quantities below T^* (the so-called "nematic state", $T_S < T < T^*$ [2, 3]), and extensive arguments have been made on its possible origin, because it is considered to be very informative to identify the superconducting mechanism, namely, to answer the question, "spins or orbitals?".

To study this issue in detail, we have carried out high-resolution neutron diffraction measurements, and based on the details, we show what induces the nematic state and approach the question about "spins or orbitals?".

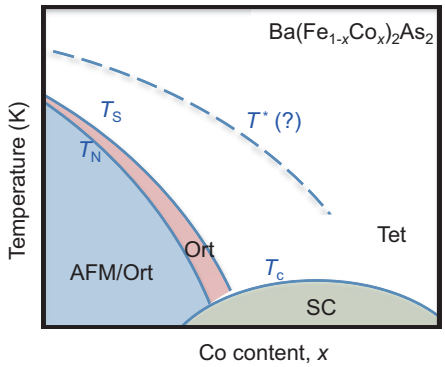

Figure 1. Phase diagram of $Ba(Fe_{1-x}Co_x)_2As_2$.

2. Experiments

We used BL-08 Super-HRPD of J-PARC. To avoid external stress from (1) surface effects, which may exist in finely pulverized samples, and from (2) effects of grease or other glues used to fix a single crystal sample to a holder, we used samples consisting of assemblies of mm-size crystallites of $Ba(Fe_{1-x}Co_x)_2As_2$. We also considered the effects of impurities doped to the system, and therefore used samples both with and without Co impurities.

3. Results and Discussion

Fig. 2 shows the example profiles taken for $BaFe_2As_2$. Their characteristics observed just below $T_S \sim 147.5$ K can be understood by considering the coexistence of two Ort phases with different magnitudes of the orthorhombicity: the broad center peak consists of two nearly Lorentzian-type ones with the smaller orthorhombicity than that of the outer two, as shown in the fitted curves. The widths of the $(h\ h\ l)_O$ Bragg reflections, the suffix o being the Ort notation, were found not to split even below T_S. In contrast, the $(400)_O$ / $(040)_O$ reflections, for example, exhibit significant T dependence in their width (FWHM) as shown in Figs. 3 and 4 even in the T region well above T_S.

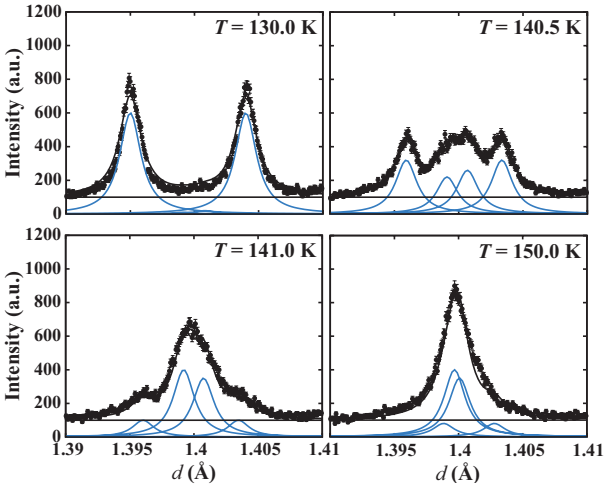

Figure 2. Example profiles obtained at $(400)_O$/$(040)_O$ Bragg reflections of $BaFe_2As_2$.

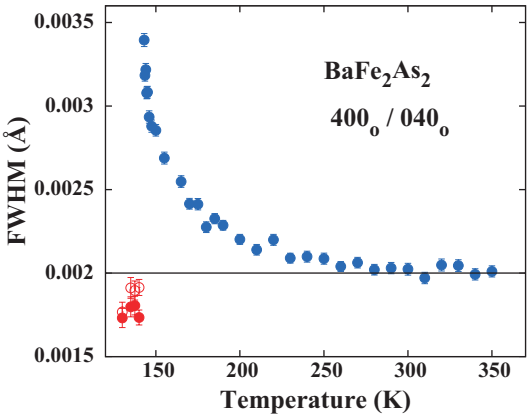

Figure 3. Width of the obtained $(400)_O/(040)_O$ raw reflection profiles against T.

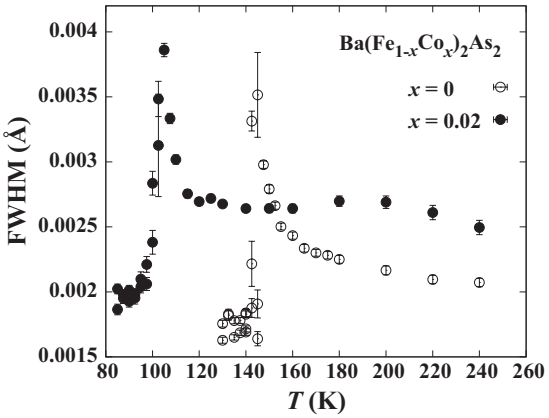

Figure 4. Temperature dependence of the width of the obtained $(400)_O/(040)_O$ of $x = 0$ and 0.02.

Since T dependence becomes visible with decreasing T, say, at ~270 K, the T dependent behavior of the width should begin at T higher than 270 K, because the value we observed includes the resolution broadening. This indicates that the broadening is surely due to the existence of the Ort distortion. One more thing we note here is that the FWHM exhibits no anomaly in the T dependence at around T^* ($> T_S$).

The question is why the broadening appears. If the Tet-Ort transition takes place homogeneously at T^*, we cannot expect the broadening on the Bragg reflection above T_S, because the dynamical fluctuation induces only the change of the Bragg intensity through the Debye-Waller factor. However, in the nematic phase, there is evidence that various static quantities exhibit the breakdown of the C_4 symmetry there. Moreover, the softening magnitude of the elastic constant C_{66} reaches its maximum at T_S [4], indicating that the almost second order transition takes place at T_S not T^*.

It is interesting to show in Fig. 4 the T dependence of the profile widths of $Ba(Fe_{1-x}Co_x)_2As_2$ with $x = 0$ and 0.02. We can see that the FWHM value increases with x in the high T-region. It is, we think, due to the finite size Ort domains pinned by lattice defects and Co impurities even at high T. It is consistent with the theoretical arguments proposed by Inoue *et al.* [5], which predicted the domain size of ~ 7 × 15 lattice spacing. The present picture is also consistent not only with the experimental report by Luo *et al.* [6] that no anomaly has been observed in the precise specific heat data at around T corresponding to T^*, but also with the fact that the largest softening of C_{66} is at $x = 0$, because as the volume fraction of the Ort domains increases with x, the softening magnitude at T_S decreases. As T approaches T_S, the Ort domains around the defects prevail and the FWHM's of the Bragg profiles increase as shown in Figs. 3 and 4. The imbalance of the Ort volumes with orthogonal a- and b-axes is an origin of the observed anisotropy of various static physical properties.

Finally, from the rather wide T region of the width change found in Figs. 3 and 4, we think that the orbital fluctuation would favor the origin of the nematic state, because the orbital-lattice coupling is larger than that of the spin-lattice one, implying that the former may be closely related to the origin of the superconductivity.

References

[1] H. Kontani and S. Onari, Phys. Rev. Lett. **104** (2010) 157001.

[2] J-H. Chu *et al.*, Science **329** (2012) 824.

[3] S. Kasahara *et al.*, Nature **486** (2012) 382.

[4] M. Yoshizawa *et al.*, J. Phys. Soc. Jpn. **81** (2012) 177001.

[5] Y. Inoue, Y. Yamakawa and H. Kontani, Phys. Rev. B **85** (2012) 224506-1.

[6] X. Luo *et al.*, arXiv:1407.6108 (2014).

K. Ikeuchi[1], M. Sato[1], S. Li[2,3], M. Toyoda[2,3], Y. Kobayashi[2,3], M. Itoh[2,3], P. Miao[4], S. Torii[4], Y. Ishikawa[4], and T. Kamiyama[4]

[1]Neutron R&D Division, CROSS-Tokai; [2]Neutron Science Section, Materials and Life Science Division, J-PARC center; [3]Insitute of Materials Structure Science, KEK; [4]Department of Physics, Nagoya University

Electrical Activity of Interstitial Hydrogen in $BaTiO_3$ Simulated with Positive Muons

1. Introduction

Multilayer ceramic capacitors (MLCCs) are fundamental components of electronic circuits and indispensable for state-of-the-art electronic devices, such as smartphones. Since the performance of MLCCs depends heavily on that of dielectric materials, the quality control of those is vitally important. As typical MLCCs involve nickel (easily oxidizable element) for internal electrodes, an annealing process to unify the dielectrics and internal electrodes is performed in a reducing atmosphere containing hydrogen. On the other hand, this process can cause insulation degradation of dielectric layers depending on the annealing conditions. Intensive studies are under way to identify the origin of the degradation.

In this work, we focused on the risk of unintentional incorporation of hydrogen into dielectric layers in the annealing process and studied its role in barium titanate ($BaTiO_3$), one of the most commonly used dielectrics in MLCCs. Similarly to other band insulators, the electronic properties of $BaTiO_3$ can change greatly upon the introduction of impurities. However, it is very difficult to detect spectroscopic signals from such trace amounts of hydrogen with conventional experimental techniques. To overcome this difficulty, we used positive muons instead of hydrogen.

2. Muonium as a pseudo-isotope of hydrogen

The positive muon is a lepton with a charge $+e$ and a rest mass of 105.7 MeV/c^2, which is about 1/9 of that of a proton. It is well established that a positive muon implanted in matter behaves as a light proton and creates a point defect analogous to an interstitial hydrogen impurity. A muon-electron bound state, called muonium, simulates the electronic state of interstitial hydrogen with high accuracy as shown in Fig. 1. Spectroscopic signals from muonium can be sensitively detected thanks to muon's radioactive decay. Therefore, with positive muons, one can imitate interstitial hydrogen impurities in $BaTiO_3$ in dilute limit and selectively probe their electrical activity.

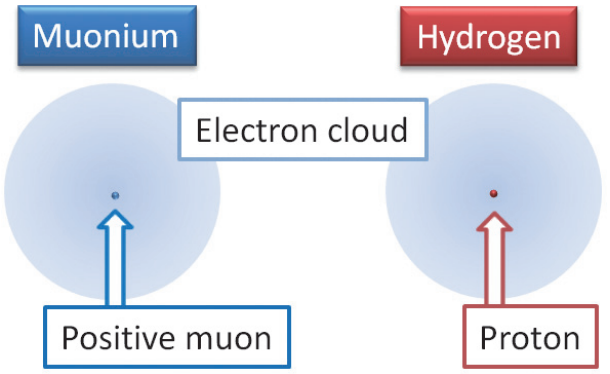

Figure 1. A schematic illustration of muonium and hydrogen in vacuum (1s state). The Bohr radius of muonium is identical to that of hydrogen except for a small correction (~ 0.5%) due to the difference of reduced mass.

3. Muon implantation experiments at the J-PARC muon facility

A positive muon beam was irradiated to a single crystalline sample of nominally undoped $BaTiO_3$ at the J-PARC muon facility and the local electronic structure around implanted muons was investigated by means of the muon spin rotation (μSR) technique. Details of the experiment were reported elsewhere [1].

Typical Fourier-transformed μSR spectra in a transverse field of 18.95 mT are shown in Fig. 2. A symmetric broad feature was found below about 80 K together with a bare muon (Mu^+) signal, assigned to paramagnetic muonium (Mu^0). A hyperfine coupling constant of Mu^0 was estimated to be ~ 1 MHz from the line width, which is about 10^{-3} that in vacuum (4463 MHz). This suggests that an electron cloud of Mu^0 spreads over several tens of unit cells in $BaTiO_3$ as shown in Fig. 3, and thus the electron binding energy is expected to be fairly small.

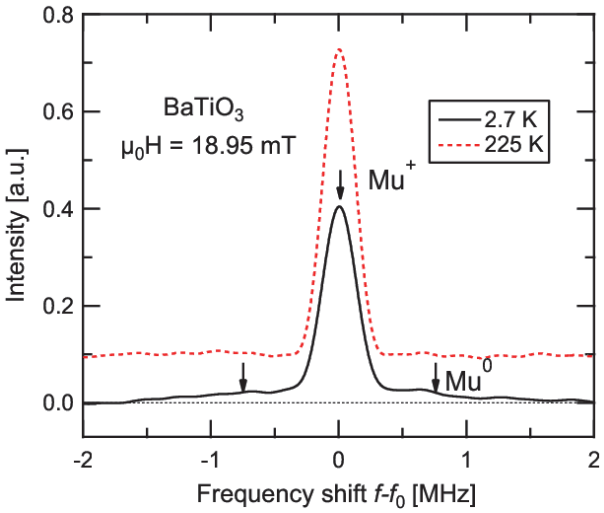

Figure 2. Fourier-transformed μSR spectra of $BaTiO_3$ in a transverse field of 18.95 mT at 2.7 K (solid curve) and 225 K (broken curve). f_0 = 2.569(1) MHz is a Larmor frequency of Mu^+.

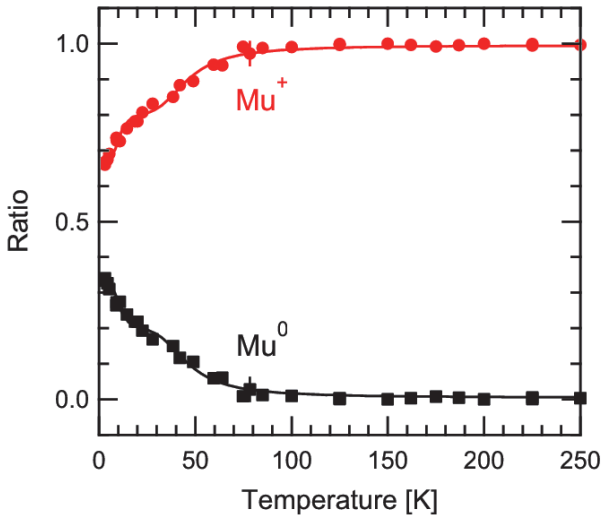

Figure 4. Ratios of muonium (Mu^0) and ionized muonium (Mu^+) signals as functions of temperature. Solid curves represent the best fits to an ionization model [3].

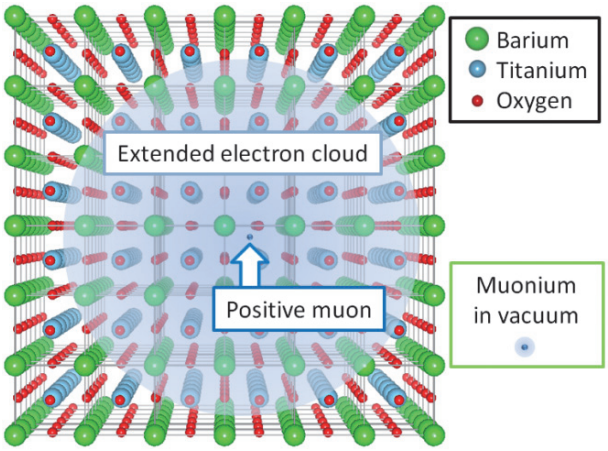

Figure 3. A schematic illustration of shallow muonium in $BaTiO_3$ and muonium in vacuum. The crystallographic illustration was produced by VESTA [2].

A Mu^0-to-Mu^+ conversion was observed with the rise of temperature as shown in Fig. 4, interpreted as an ionization process of Mu^0. The ionization energy was estimated to be ~ 10^{-2} eV based on an ionization model [3]. This is considerably smaller than the band gap of 3.2 eV and indicates that Mu^0 forms a shallow donor level just below the conduction band minimum. The electrons released from the shallow Mu^0 can move freely around the crystal and lead to electric conductivity, thus decreasing the insulating performance of $BaTiO_3$. Interstitial hydrogen impurities in $BaTiO_3$ also seem to form a shallow donor level in a similar way and cause insulation degradation at device operating temperatures.

The insights from this work can be applied to improve the performance of $BaTiO_3$-based MLCCs by reducing the risk of hydrogen incorporation in their fabrication processes.

References

[1] T. U. Ito, W. Higemoto, T. D. Matsuda, A. Koda, and K. Shimomura, Appl. Phys. Lett. **103**, 042905 (2013).

[2] K. Momma, and F. Izumi, J. Appl. Crystallogr. **44**, 1272–1276 (2011).

[3] S. F. J. Cox, J. L. Gavartin, J. S. Lord, S. P. Cottrell, J. M. Gil, H. V. Alberto, J. Piroto Duarte, R. C. Vilão, N. Ayres de Campos, D. J. Keeble, E. A. Davis, M. Charlton, and D. P. van der Werf, J. Phys.: Condens. Matter **18**, 1079–1119 (2006).

T. U. Ito[1,2], W. Higemoto[1,2], A. Koda[2,3], and K. Shimomura[2,3]

[1]Advanced Science Research Center, JAEA; [2]Muon Science Section, Materials and Life Science Division, J-PARC Center; [3]Institute of Materials Structure Science, KEK

Synthesis, Structure, and Conduction Mechanism of the Lithium Superionic Conductor $Li_{10+\delta}Ge_{1+\delta}P_{2-\delta}S_{12}$

1. Introduction

Among the various types of batteries currently under consideration for future applications, the all-solid-state configuration has become a promising candidate for high-energy and high-power-density batteries [1, 2]. In order to develop all solid-state batteries, the key issue is the lithium superionic conductors, which could be used for the solid electrolyte.

Recently, a superionic conductor, $Li_{10}GeP_2S_{12}$ (LGPS), has been found to have high lithium ionic conductivity of 10^{-2} S cm^{-1} at room temperature, which is similar to the conductivity value of the liquid electrolyte used for lithium ion batteries [2, 3]. Although materials offering extremely high lithium ionic conductivities have been developed, further studies clarifying the conduction mechanism and increasing the range of electrolyte materials are still necessary to allow the practical applications of these electrolytes. LGPS is known to have a three-dimensional framework structure composed of one-dimensional chains formed by $Ge(P)S_4$ tetrahedra and LiS_6 octahedra with edge sharing along the *c* direction of the tetragonal structure [3]. These one-dimensional chains are connected with each other through PS_4 octahedra by corner sharing.

Following the development of this LGPS-type parent structure with extremely high ionic conductivity, it was recognized that similar solid solution systems with different lithium contents might exhibit even higher levels of ionic conduction. In addition, cation and anion substitutions of the LGPS framework structure are also important means of achieving higher ionic conduction values. In the present study, a solid solution with an LGPS-type structure was produced based on a powder synthesis process that offers a practical means of fabricating solid electrolytes. The composition and ionic conductivity of this new solid solution system, $Li_{10+\delta}Ge_{1+\delta}P_{2-\delta}S_{12}$, were subsequently examined and the conduction mechanism within this material was studied using neutron diffraction analysis.

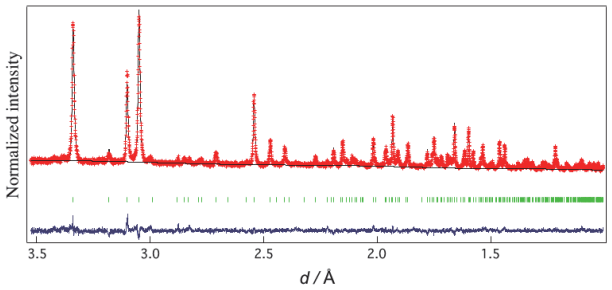

Figure 1. Neutron Rietveld refinement pattern for $Li_{10.35}Ge_{1.35}P_{1.65}S_{12}$ at 300 K. Red: observed intensities; black: calculated intensities; blue: difference plot. The green markers indicate the positions of the diffraction lines.

Neutron diffraction data were obtained using time-of-flight (TOF) diffractometers: SuperHRPD (BL08) [4] and iMATERIA (BL20) [5] at the Material and Life science Facility (MLF) of the Japan Proton Accelerator Research Complex (J-PARC). The diffraction data were collected for 12 h at several temperatures from 4.8 to 750 K. The structural parameters were refined using the Rietveld refinement programs Z-Rietveld [6]. During the neutron data analysis, the *d* region from 1.0 to 3.5 Å was used for the Rietveld analysis. The Z-MEM program was employed during calculations based on the maximum entropy method (MEM) [7]. Z-3D [8] was used to visualize the nuclear density map of the structure.

2. Results and discussion

The LGPS solid solutions fabricated were based on the Li_3PS_4 – Li_4GeS_4 pseudo-binary system, and compositions similar to the parent LGPS ($Li_{10}GeP_2S_{12}$) phase were synthesized according to the compositional formula $Li_{10+\delta}Ge_{1+\delta}P_{2-\delta}S_{12}$. Structural analysis was carried out based on a previously reported model incorporating three lithium sites (Li1 at 16*h*: *x*, *y*, *z*; Li2 at 4*d*: 1, 1/2, *z*, Li3 at 8*f*: *x*, *x*, 0), together with an Li4 site (Li4 at 4*c*: 0, 0, *z*) proposed as the result of molecular dynamics simulations [9]. Lithium ion distribution was visualized using the MEM analysis in conjunction with the neutron diffraction data obtained for $Li_{10.05}Ge_{1.05}P_{1.95}S_{12}$ ($\delta = 0.05$) at 100 and 750 K.

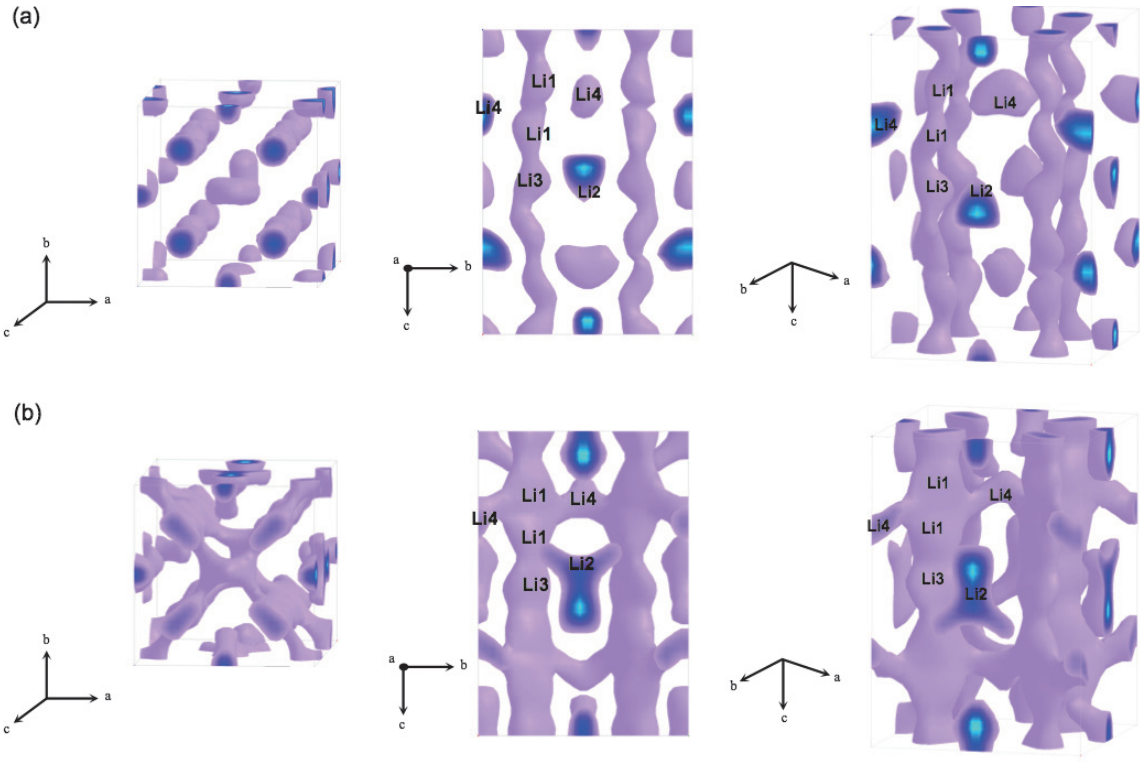

Figure 2. Atomic distributions in the $Li_{10.05}Ge_{1.05}P_{1.95}S_{12}$ ($\delta = 0.05$) unit cell at 100 K (a) and 750 K (b). The probability of an atom being present is indicated only for the negative scattering powers, which corresponds to the lithium ion distribution.

Figure 2 shows the atomic distribution in the unit cell, in which the probability of an atom being present is represented only for the negative scattering powers, which corresponds to the lithium ion distribution. At 100 K, the Li1, Li1, and Li3 sites are connected along the *c*-axis, while the other lithium sites (the Li2 and Li4 sites) are isolated from each other. The one-dimensional conduction pathway represents the primary means of lithium ion conduction at 100 K and this conduction pathway becomes more evident at 750 K. In addition, continuous lithium distribution between the Li1 and Li4 sites is now observed. These results demonstrate that the lithium conduction takes on a three-dimensional character, as opposed to the one-dimensional at higher temperatures. The LGPS structure is evidently well-suited to a three-dimensional conduction. Even though the one-dimensional conduction is dominant at lower temperatures, the pathway over the *ab* plane becomes evident at high temperatures.

References

[1] X. Xu *et al.*, *Chem. Mater.* **23** (2011) 3798.

[2] Y. Kato *et al.*, *Electrochemistry* **80** (2012) 749.

[3] N. Kamaya *et al.*, *Nat. Mater.* **10** (2011) 682.

[4] S. Torii *et al.*, *J. Phys. Soc. Jap.* **80** (2011) SB020.

[5] T. Ishigaki *et al.*, *Nucl. Inst. Meth. Phys. Res. A* **600** (2009) 189.

[6] R. Oishi *et al.*, *Nucl. Inst. Meth. Phys. Res. A* **600** (2009) 94.

[7] J. Zhang *et al.*, Z-MEM, Textbook of Z-Code Powder diffraction data analysis school, Tokyo, Japan, Mar 25-26, 2014.

[8] Y. Ishikawa *et al.*, Z-3D, Textbook of Z-Code Powder diffraction data analysis school, Tokyo, Japan, Mar 25-26, 2014.

[9] S. Adams *et al.*, *J. Mater. Chem.* **22** (2012) 7687.

O. Kwon[1], M. Hirayama[1], K. Suzuki[1], Y. Kato[2], T. Saito[2], M. Yonemura[3,4], T. Kamiyama[3,4], and R. Kanno[1]

[1]Department of Electronic Chemistry, Tokyo Institute of Technology; [2]Battery Research Division, Higashifuji Technical Center, Toyota Motor Corporation; [3]Neutron Science Section, Materials and Life Science Division, J-PARC center; [4]Insitute of Materials Structure Science, KEK

Development on Non-Destructive Elemental Analysis for Extraterrestrial Materials using a Muon Beam

1. Introduction

In 1971, Rosen [1] noted the great availability of muon beam analysis and proposed its application in the chemical analysis of tissues, as muon beam analysis would cause less damage to the host organism than neutron activation analyses. Muonic atom spectroscopy has been developed over the past four decades [2-4] as a non-destructive analytical method; however, for a real application, one had to wait for an intense muon source. The intense pulsed muon source, J-PARC MUSE (Japan Proton Accelerator Research Complex, MUon Science Establishment), was constructed and succeeded in providing a decay muon rate of 10^6 s^{-1} for a momentum of 60 MeV/c in November 2009, which is the most intense pulsed muon beam in the world [5, 6].

The stopping distances of both negative muons (~ tens of MeV/c) and muonic X-rays (more than several tens keV) are in the ranges of millimeters, which could potentially enable us to obtain the 3-D elemental map from the near surface to the interior of rocky samples by changing the momentum of the muon beam. Here, we report on the first trial of the depth profile analyses of a rock-sample simulant and carbonaceous meteorites [7]

2. Experiment 1 ~ depth profile analysis ~

At first, we tried the depth profile analysis of the four-layered sample that consists of SiO_2, C (graphite), BN (boron nitride) and SiO_2 using the D2 beam line at J-PARC MUSE, each with thickness of 1.5, 1.0, 1.3 and 1.5 mm. The negative muon beam was collimated to approximately 27 mm in diameter and focus on the 50 mm *75 mm *5.3 mm sample that was oriented at 45 degree to the beam. By changing the Muon's momentum from 37.5 MeV/c to 57.5 MeV/c, the generated high energy muonic X-rays were measured by two Ge detectors (one was planar type (LEPS) and the other was coaxial type (Loax)). Figure 1 shows the X-ray spectra obtained by LEPS. Our preliminary result successfully demonstrates that the muon beam analysis has a

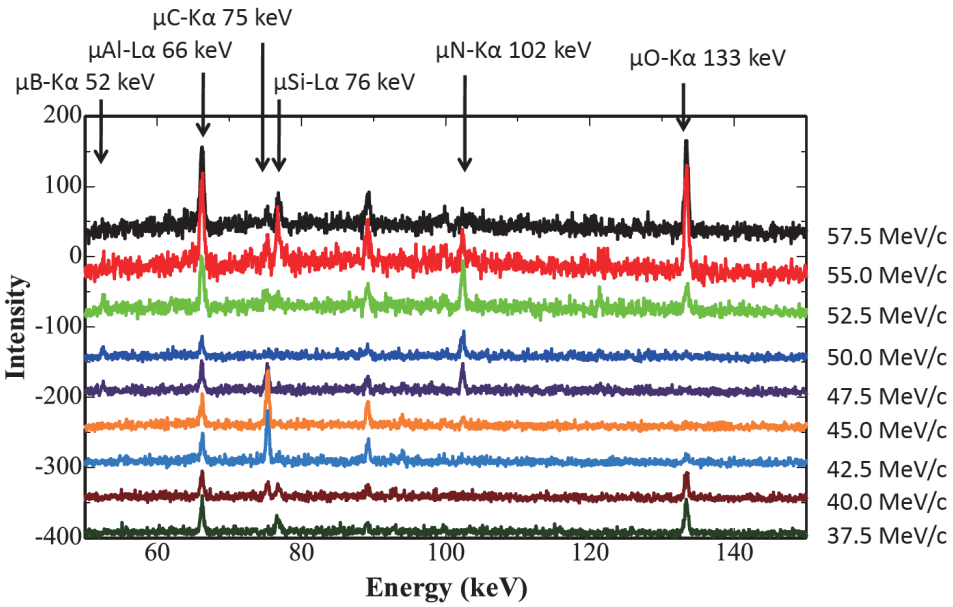

Figure 1. Muonic X-ray intensities are shown in arbitrary units with offset to compare the spectra obtained with different muon momenta (37.5-57.5 Mev/c).

potential to map non-destructively 3-D elemental distributions of light elements such as B, N, C, and O. The depth resolution is currently estimated to have a 10% uncertainty against the mean penetration depth of the muons.

3. Experiment 2 ~ elemental analysis of meteorite sample ~

Next, we carried out X-ray fluorescence spectroscopy for carbonaceous chondrites, Murchison and Allende. The negative muon beam, collimated to approximately 40 mm in diameter, irradiated to a ~ 5-mm-thick Murchison disk with the exposed surface area of ~ 50 mm × ~ 100 mm. Aluminium foil was used to hang the sample inside the chamber. The exposure time was approximately 13 hours, and the momentum of the incident muon beam was set at 16 MeV/c, corresponding to the penetration depth of ~ 70 μm. For Allende meteorite analysis, the muon beam was collimated to approximately 27 mm in diameter at the sample surface of 50 mm × 75 mm. The sample was also hung with less amounts of Al holder than for the Murchison meteorite to reduce the background signal of Al. The exposure time was approximately 10 hours, and the incident muon momentum was set at 34 MeV/c (with penetration depth of ~ 1 mm). As shown in Figure 2, significant counts of fluorescent X-rays of Mg, C, Si, Fe, Ca, and S from Murchison and those of Mg, Si, Fe, K, and Ca from Allende were detected. On the other hand, those of K from Murchison and C and S from Allende were not detected. This indicates that the detection limit of muonic fluorescent X-ray at the current analytical condition is about 1 weight percent in concentration. It should be noted that the signal of Al is background signal from a vacuum chamber and/or a sample holder.

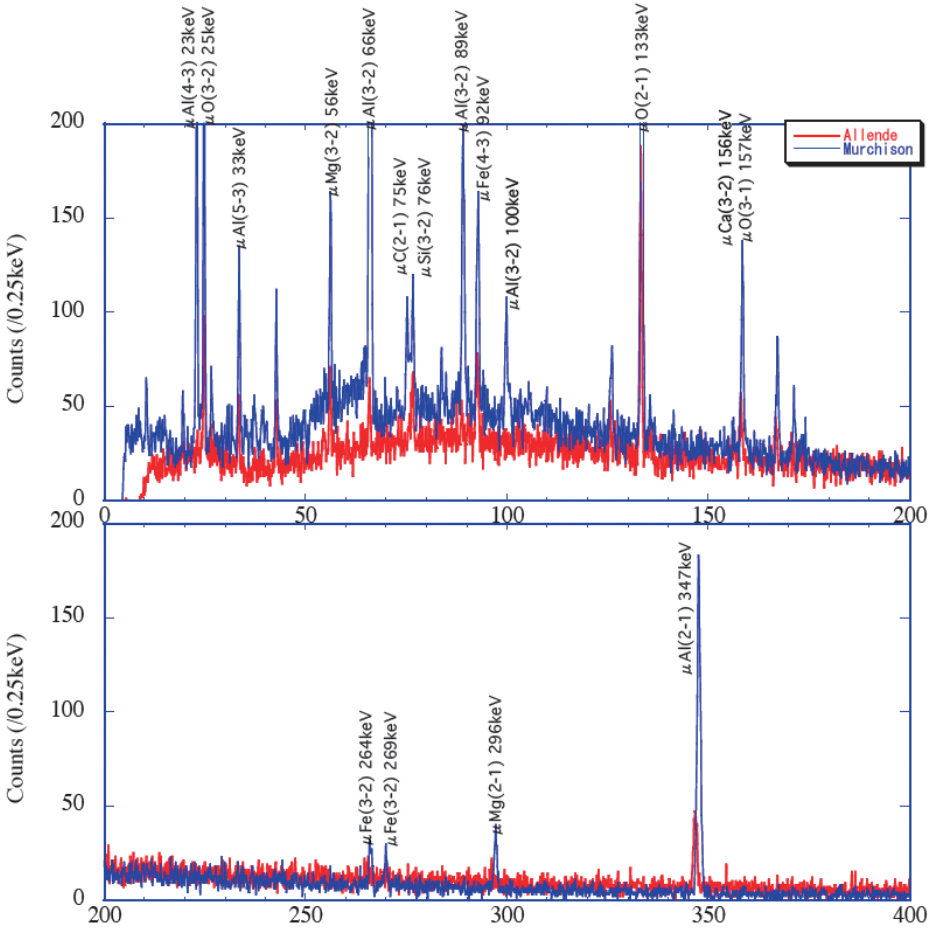

Figure 2. Muonic X-ray energy spectra from carbonaceous chondrites: Allende (red) and Murchison (blue) meteorites.

4. Experiment 3 ~ "see-through" analysis of Murchison in glass tube ~

Finally, we tried the measurement of Murchison meteorite sealed in a glass tube as a simulant of Hayabusa 2 samples collected from a C-type asteroid. Powdered Murchison meteorite weighing 610 mg was placed in a 50-mm-long SiO_2 glass tube, with inner and outer diameters of 4 and 6 mm, respectively. The muon beam collimated to approximately 25 mm in diameter, and the apparent cross section of the sample was 4 mm × 25 mm. After exposure to the muon beam with momentum of 37 MeV/c for approximately 24 hours, clear signals of Mg and marginally resolved signals of Fe were detected through the 1-mm thick glass wall (Fig. 3). Although O and Si are the major elements of rock samples, muonic X-rays of O and Si were emitted from the SiO_2 glass tube as well, which cannot be distinguished from the sample signals. Although further developments in analytical techniques are required, such as detector setting and collimation of the incident muon beam, our first attempt for the non-destructive elemental analysis of an extraterrestrial sample inside a glass tube succeeded with the detection of Mg and Fe.

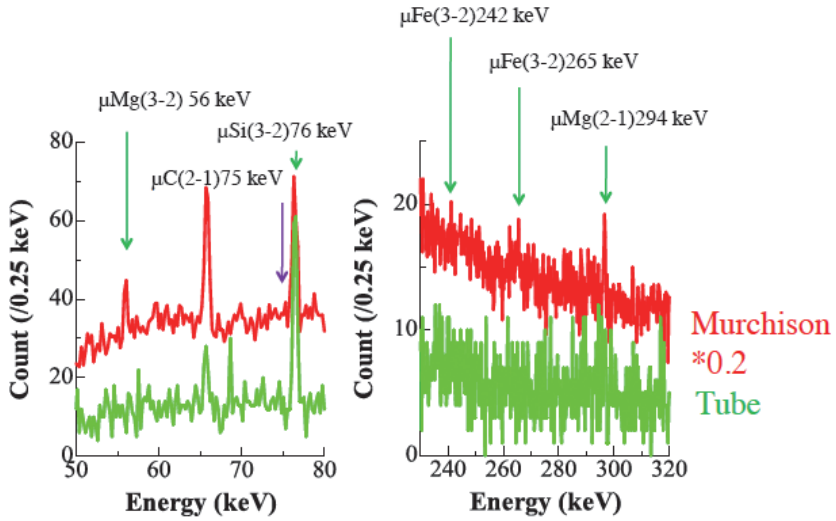

Figure 3. Muonic X-ray spectra from the powdered Murchison meteorite in a SiO_2 glass tube.

References

[1] L. Rosen, *Science* **173**, 490–497 (1971).

[2] H. Daniel, Nucl. Instrum. Methods Phys. Res., B **3,** 65–70 (1984).

[3] M. K. Kubo *et al*., J. Radioanal. Nucl. Chem. **278**, 777–781 (2008).

[4] K. Ninomiya *et al*., Bull. Chem. Soc. Jpn. **85**, 228–230 (2012).

[5] D. Cyranoski, Nature **456,** 426–427 (2008).

[6] Y. Miyake *et al*., Nucl. Instrum. Methods Phys. Res., A **600,** 22–24 (2009).

[7] K. Terada *et al*. Nature Scientific Reports **4,** 5072 (2014) DOI: 0.1038/srep050.

K. Terada[1], K. Ninomiya[1], T. Osawa[2], S. Tachibana[3], Y. Miyake[4,5], M. K. Kubo[6], N. Kawamura[4,5], W. Higemoto[7], A. Tsuchiyama[8], M. Ebihara[9], and M. Uesugi[10]

[1]Graduate School of Science, Osaka University; [2]Quantum Beam Science Center, JAEA; [3]Graduate School of Science, Hokkaido University; [4]Muon Science Section, Materials and Life Science Division, J-PARC Center; [5]Muon Science Laboratory, IMSS, High Energy Accelerator Research Organization; [6]Graduate School of Science, International Christian University; [7]Advanced Science Research Center, JAEA; [8]Graduate School of Science, Kyoto University; [9]Graduate School of Science and Engineering, Tokyo Metropolitan University; [10]JAXA Space Exploration Center, Japan Aerospace Exploration Agency

Superconducting Nanowire Neutron Detector

1. Introduction

Pulsed neutron sources such as J-PARC [1] have made an important impact in various branches of sciences and technologies, i.e., material analyses aiming at identifying the location of light atoms (hydrogen, carbon, and others) by means of neutron radiography. For example, one can observe the dynamics of carbons and water molecules in operating fuel cells and engines [2]. Spatial resolution remains on the level of several tens μm even in high-end neutron detectors [3].

We proposed a current-biased kinetic inductance detector (CB-KID) made of Nb nanowire. We intend to build a Nb CB-KIDs with the ^{10}B conversion layer [4]. We report the results of successful neutron detection using a CB-KID detector with the ^{10}B converter at J-PARC.

2. Current-biased kinetic inductance detector

The kinetic inductance L_k of a superconductor is expressed as $L_k = m_s l/n_s q_s^2 S$, where m_s is the mass of the Cooper pair, n_s is the density of the Cooper pairs, q_s is the electric charge for the Cooper pairs, l is the nanowire length in total, and S is the cross-section area. A Nb-based kinetic inductance detector is fed by the DC bias current I_b through a bias resistor. The voltage V across the detector is expressed by $V = I_b dL_k/dt + L_m dI_b/dt \simeq I_b dL_k/dt$, where the magnetic inductance L_m is supposed to be independent of time. This utilizes the method for sensing the dynamic nature of quasiparticle excitations and hence provides rapid response.

The nuclear reaction of ^{10}B with neutrons releases a huge amount of nuclear energy of 2.31 MeV or 2.79 MeV into restricted regime. In Fig. 1, we schematically show the method of how to identify the neutron arrival onto the detector. In the neutron reaction ^{10}B(n,^{4}He)^{7}Li, the two charged particles ^{4}He and ^{7}Li are simultaneously emitted in the opposite directions. Nuclear reaction energy would be used to break some Cooper pairs in the superconducting Nb nanowire and to cause a change in kinetic inductance in some portion of the nanowire.

A microwave kinetic inductance detector (MKID) has been remarkably successful because the frequency domain multiplexing can be achieved by a single stripline with many resonators [5]. It is also beneficial for MKIDs not to have DC bias current to reduce the Joule heating. However, the speed of the MKID system is not so fast, and remains on the order of μs. In the resonance circuit of the *LC* tank, there is a continuous energy exchange between the *L* component and the *C* component, which would prolong the overall response time of the detector while the quasiparticle dynamics itself is very fast, presumably on the order of ps. The Nb nanowire has been successfully used as a superconducting detector for various purposes.

Our CB-KID absolutely requires installing DC bias current leads, in which heat dissipation distributes

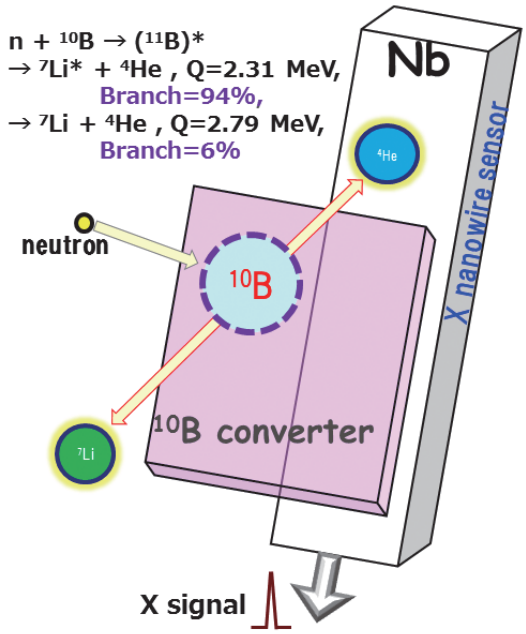

Figure 1. A Nb nanowire detector with the ^{10}B converter. A change in kinetic inductance is detected by readout circuits.

along the current leads. Usually, the multiplexing of the current bias leads to enhancement in Joule heating. We will explain how a series connection of CB-KIDs in the superconducting state works at 4 K. Even if we have many nanowires, we only need two lines which give the pathway for the incoming and outgoing currents between room temperature and 4 K. The request for exciting many CB-KIDs in view of wiring is not a heavy burden in terms of cryogenics design because there are only two leads.

3. Neutron irradiation to CB-KID

We carried out a neutron irradiation experiments to the Nb-based CB-KID with ^{10}B converter at the MLF (Materials and Life Science Experimental Facility), J-PARC. We used beam line NOBORU (BL10) [1]. The operating power of J-PARC was 300 kW, and this gave us 3×10^7 neutrons/s/pulse at BL10. The MLF pulse appears every 40 ms. We used a bismuth crystal filter of 50 mm thickness to reduce the burst gamma rays. As a result, the neutron intensity becomes 1.5×10^7 neutrons/s/pulse at the Nb-based CB-KID detector with ^{10}B converter.

The CB-KID consisting of superconducting Nb can be used as a neutron detector by overlaying a ^{10}B converter layer. The thickness of the Nb CB-KID is chosen as 40 nm and the line width is chosen as 1 μm on a single chip (22 mm × 22 mm silicon). At the center of the chip, the effective area (8 mm × 8 mm) is covered with a 200 nm thick ^{10}B converter layer, deposited by an electron beam evaporator under ultra-high-vacuum.

The Nb-based CB-KID detector was installed in a 4-K Gifford-McMahon (GM) refrigerator so as to cool the detector down to 4 K. We used a Nb wire of 1 μm width detector by feeding 100 μA as a bias current. In Fig. 2, we show that a signal from the CB-KID detector is of width on the order of ns. A signal was amplified by a differential low noise amplifier (NF SA-430F5, bandwidth 120 MHz), and was directly observed by a 2.5-GHz sampling digital oscilloscope.

We tried to observe the signal of the CB-KID when the neutron shutter of BL10 was closed. We were not able to observe any signal from the detector. On the other hand, a clear signal appeared, as shown in Fig. 2, when the neutron shutter was opened. This ensures that our CB-KID can detect neutron from the pulsed neutron source at J-PARC for the first time.

We succeeded in measuring the neutron flux from pulsed neutrons at BL10 of J-PARC as a function of time. As shown in Fig. 3, a histogram of averaged neutron in 0.1 ms mesh is in good agreement with that of the simulation. The vertical scale is divided by arrival time t to compensate a velocity-dependent cross section between neutron and ^{10}B. This is convincing evidence that our detector successfully detected pulsed neutrons from J-PARC.

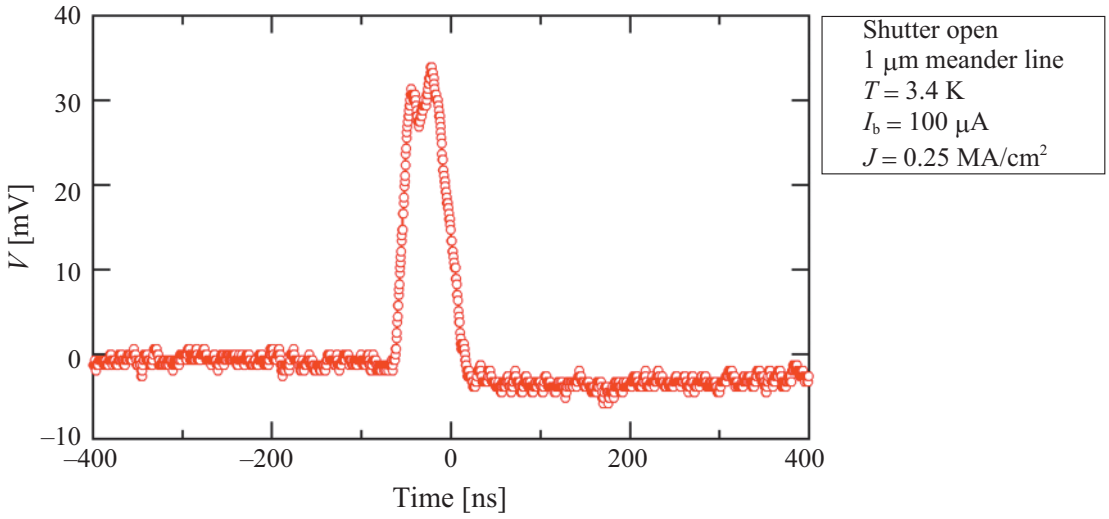

Figure 2. Signal from CB-KID when the shutter is opened. The temperature is 4.05 K, the bias current is 100 μA, and the Nb linewidth is 1 μm.

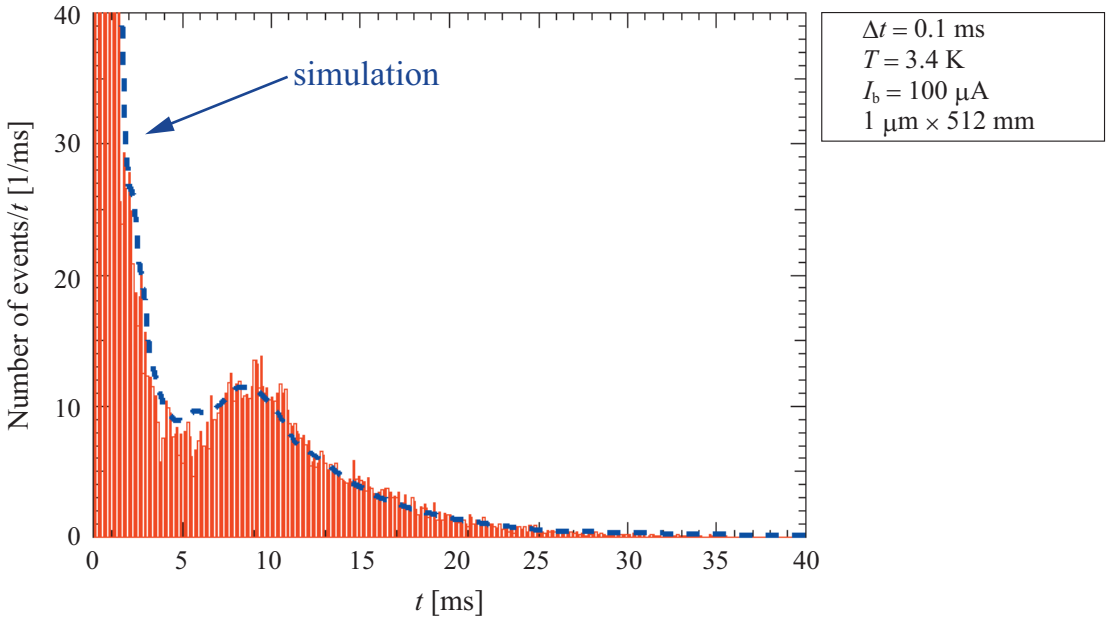

Figure 3. Averaged neutron flux as a function of time. The blue dash line shows the simulation result at BL10.

4. Conclusions

We demonstrated the sound operation of the novel CB-KID made of Nb nanowires operating at 4 K. The operating speed of CB-KID is much faster than an MKID [5]. The Nb-based CB-KID with ^{10}B conversion layer can work as a neutron detector.

The devices were fabricated in CRAVITY facilities at AIST. This work is partially supported by Grant-in-Aid for Scientific Research (S) (No. 23226019) and Grant-in-Aid for Young Scientists (B) (No. 26820130) from JSPS.

References

[1] F. Maekawa *et al.*, Nucl. Instrum. Meth. A, **620** (2010) 159.

[2] I. Manke *et al.*, Appl. Phys. Lett., **90** (2007) 184101.

[3] S. Tremsin *et al.*, Nucl. Instrum. Meth. A **652** (2011) 400.

[4] T. Ishida *et al.*, J Low Temp. Phys. **716** (2014) 216.

[5] J. Zmuidzinas, "Superconducting Microresonators: Physics and Applications", Annual Review of Condensed Matter Physics, Vol. **3:** 169-214, March 2012.

S. Miyajima[1,2], H. Shishido[1,2], Y. Narukami[1], N. Yoshioka[1], A. Fujimaki[3], M. Hidaka[4], K. Oikawa[5], M. Harada[5], T. Oku[5], M. Arai[5], and T. Ishida[1,2]

[1]Department of Physics and Electronics; [2]Insitute for Nanofabrication Research, Osaka Prefecture University; [3]Nagoya University; [4]Advanced Industrial Science and Technology; [5]Materials and Life Science Division, J-PARC Center

Neutron Source

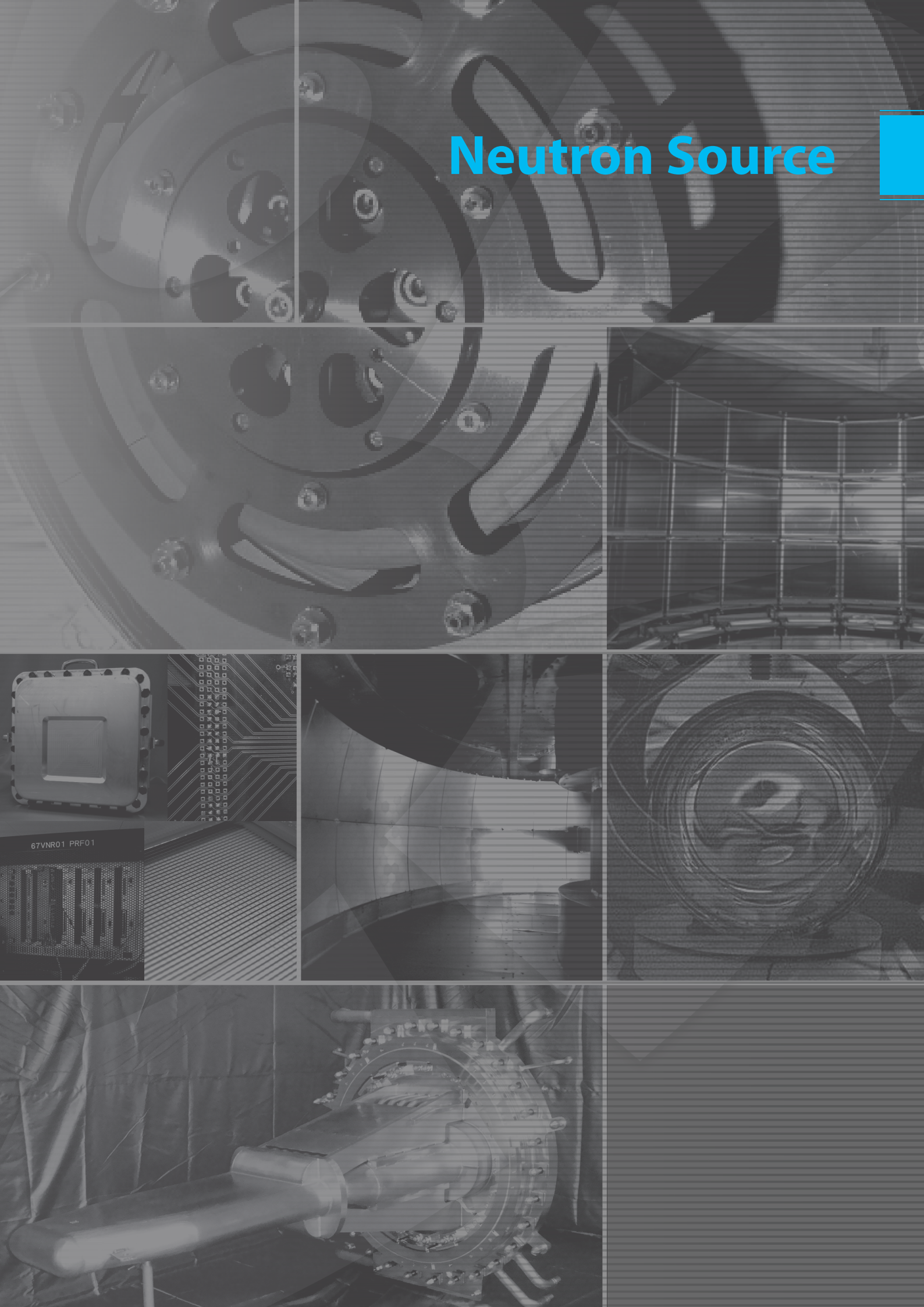

Progress of the Neutron Source Section

1. Mercury target system

In order to operate the pulsed spallation neutron source of J-PARC steadily under the rated proton beam of 1 MW, the most critical issue is to mitigate pressure waves generated in the mercury target by injecting intense proton beam, because it induces cavitation damage on the target vessel, which shortens its lifetime. To overcome this issue, we developed a technique to inject gas micro-bubbles into mercury. In 2012, for the first time in the world, we started supplying helium gas micro-bubbles in the running mercury circulation loop and confirmed that the vibration velocity on the target vessel initiated by the pressure waves was definitely decreased. However, the flow rate of helium gas did not reach the rated value because mercury was unexpectedly intruded from a vent line to a helium supply line through a surge tank.

Therefore, the most important task in 2013 was to recover the flow rate of gas-microbubbles in the mercury circulation system. During the maintenance period, we removed the mercury from the helium gas supply line by hands-on work and installed a gas-liquid separator as a counter measure. We also replaced the helium gas supply device with a new one with remote handling tools such as a master-slave manipulator and an in-cell crane.

As a result, the flow rate of gas micro-bubbles in the mercury was successfully increased from 2.5 l/min to 7.5 l/min suppressing the vibration velocity of the target vessel by 1/3 to 1/4.

2. 3 GeV proton beam transport facility

Flattening the proton beam profile is another effective technique to suppress the pressure wave generated in the mercury target, because the amount of cavitation damage is proportional to the 4^{th} power of the beam power. Since the current proton beam profile has a Gaussian distribution, we have installed two octupole magnets to suppress the beam profile upstream of the muon production target in the 3 GeV proton beam transport line. We investigated the performance of the ocutuplole magnets during the accelerator study period in February, 2014, and obtained a promising result, confirming that the peak of the proton beam profile has been reduced by about 40%.

At the end of the 3 GeV proton beam transport line, a proton beam window has been installed to create a boundary between the high vacuum environment in the transport line and the helium environment in the helium vessel, in which the target-moderator-reflector system is placed. During the maintenance period, the proton beam window was replaced for the first time. It was attached at the bottom of a 4-meter tall steel shielding plug and highly activated. It was lifted up into a big shielding cask with a remote handling gripper in it on the top of the neutron source station, and then moved to a storage area on the basement floor.

3. Cryogenic hydrogen circulation system

We replaced the accumulator of the cryogenic super-critical hydrogen circulation loop during the maintenance period. It has a bellows structure enclosing helium to make its volume variable up to 6.85 L so that it could control the pressure rise in the hydrogen loop induced by nuclear heating of 3.8 kW at the moderators when the 1-MW pulsed proton beam injects or stops.

The new accumulator has a diameter of 300 mm and unrestricted length of 85 mm, the same specifications as for the current accumulator. As the bellows consists of 5 blocks of welding bellows with 17 units in each of them, the plate thickness was increased from 0.4 mm to 0.8 mm in order to withstand a high pressure of 2.0 MPa. We inspected carefully the welding process and improved it through manufacturing a prototype of one block of welding bellows. Consequently, we successfully manufactured bellows that can expand and contract smoothly without hysteresis.

We also confirmed through actual operation with 300 kW proton beam that the pressure rise in the cryogenic super-critical hydrogen loop was mitigated at 20 kPa and it could reach 60 kPa for the 1 MW operation, which satisfied the design requirement.

4. Updates of the neutron shutter system

The neutron shutter system of J-PARC is driven by an electric servo motor. Since the operational beam power increased up to 200 kW in 2011, a failure indicating servo motor error occurred randomly several times. We found that it was caused by a single event effect at the semi-conductor part of the servo amplifier by neutrons produced at the target-moderator-reflector system. Therefore, all servo drives of the shutter system were replaced to the robust type, which does not include semi-conductors.

Further, in accordance of the construction of new instrument of imaging BL22, a shutter gate with three neutron extraction holes was newly manufactured and installed at the neutron source station.

5. Fabrication of spare components

In 2012, we started fabrication of a spare target vessel which has a double-wall structure with a narrow width of 2 mm at the beam window portion in view of extended lifetime of the target vessel. This design concept has been already adopted at the Spallation Neutron Source (SNS) of Oak Ridge National laboratory, showing that the pitting damage did not affect the outer wall, while the inner plate suffered damage in the form of penetration holes through the operating period of 2500 MWh (about half a year with 1 MW proton beam). In 2013, the spare target was completed and delivered to MLF. This type of target vessel would be in use from the latter half of 2014.

We have also started fabrication of a spare moderator (coupled moderator) and a reflector. It is estimated that manufacturing period will take three years. Calls for bids on the second decoupled and poisoned moderator will be started in 2014 and 2015, respectively. After all, the replacement of the moderator-reflector system is scheduled for 2019, which is based on the estimation that the lifetime of a moderator comes after a 6 MWy-irradiation.

H. Takada
Neutron Source Section, Materials and Life Science Division, J-PARC Center

Status of Proton Beam Commissioning of MLF

1. Beam commissioning

Due to the incident, which happened at the hadron hall of J-PARC, the user beam operation of MLF was canceled from the end of May to the end of July 2013. To avoid further incidents caused by the high power proton beam, we carefully reviewed our instruments and concluded that we can rely on them to prevent incidents. In the summer of 2013, a super conducting LINAC was installed to increase the beam energy from 181 MeV to 400 MeV. Due to the lower acceleration at the Rapid Cycling Synchrotron (RCS), which accelerates the proton beam to 3 GeV, the transverse emittance of the beam was increased at the exit of RCS. We assumed that the beam loss might increase along the beam transport line. The beam loss was, however, similar to the previous one. At the downstream near the muon production target, called M1, we observed a minor increase in the activation, mainly due to the radiation produced at the target.

Below we describe two subjects, which are topics of the beam commissioning: 1) The proton beam window was replaced; the window is a physical boundary between the high vacuum region at the accelerator and the helium area around the neutron target station. 2) To mitigate the damage at the mercury target vessel, octupole magnets were installed at the beam transport to reduce the peak current density at the target.

2. Replacement of proton beam window

In order to determine the lifetime of the proton beam window (PBW), made of aluminum alloy (Al5083), we watched the status of the PBW from the mercury target side. By placing a high zoom WEB camera and LED light, the surface of the PBW on the helium vessels side was clearly observed as shown in Fig. 1. At the center, a clear beam footprint was found. Some strange spots were found around the corner of the PBW. If those spots were caused by refraction or shadow, those spots could have been eliminated by changing the camera position. However, regardless of the camera position, spots were still found around the corner of the PBW, so we decided to replace the PBW in the summer of 2013.

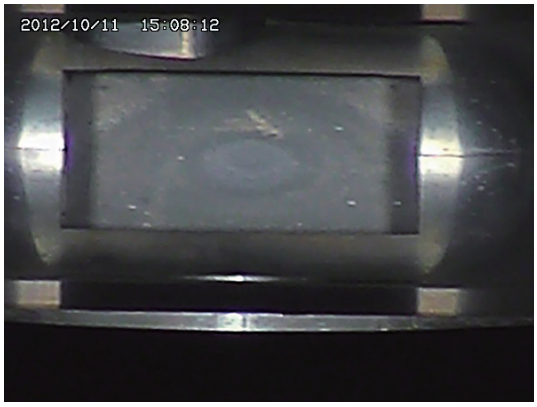

Figure 1. Surface of the 1st PBW observed by high zoom WEB camera in October 2012.

This was the first PBW replacement ever. Since the cooling water for the PBW had high activation, such as 5000 Bq/cc, the work had to be done carefully, especially when detaching the coupler for the water channel. To avoid contamination of radioactivity, a special house with local ventilation system was temporally built on the PBW. Since water could be evacuated completely and not a single drop of water remained in the channel, the decoupling work could be performed smoothly. Despite a few minor incidents during the replacement, such as breaking of a driven chain for the hatch in the cask, the replacement work was completed successfully. The seal performance of the new PBW was better than that of the first PBW.

The surface status of the first PBW after it was placed at the hot cell is shown in Fig. 2. Around the corner, we found many pitting holes. On the other hand, pitting holes could not be found at the center of the window. At the first mercury target vessel, the nickel mirror, which was placed for measurement of the vessel's vibration by the Laser Doppler Bibrometer, was completely corroded. The pitting

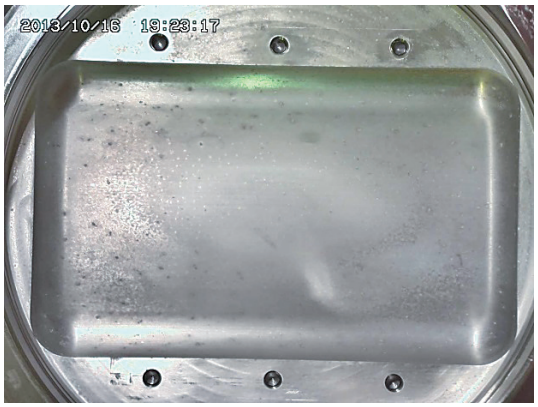

Figure 2. Surface of the 1st PBW at the helium vessel side observed at the hot cell.

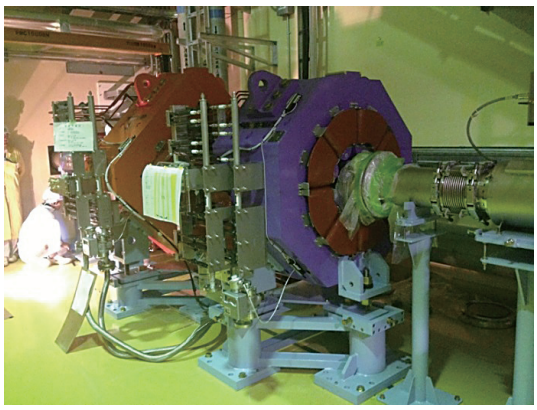

Figure 3. Octupole magnet installed at the beam transport.

holes were probably caused by reaction with the acid produced by the radiolysis of the impurity gas in the helium vessel. We concluded that the lifetime of the first PBW was determined by the corrosion due to acid in the helium vessel. To confirm the seal performance of the helium vessel, helium leak examination was performed and a small amount of leaking gas was detected. Due to radiation damage, the proton beam window has a life of about 3 years [1]. The examination of the surface status was important to estimate the lifetime. By observing the surface of the second PBW in the summer of 2014, we will determine its lifetime.

3. Installation of octupole magnet

In FY2012, octupole magnets were fabricated for beam flattering to decrease the peak current density at the mercury target. The installation of the octupole magnets began in September 2013 at the beam transport. For beam flattering in horizontal and vertical direction, two sets of octupole magnets are required. An octupole magnet for the horizontal direction was installed at the ceiling of tunnel M1 with open shielding, placed at about 5 m upstream of the muon production target. That was the first such trial after the facility was built. Due to the great earthquake, the gap of shielding at the ceiling was unusually narrow so that the moving of the shielding was difficult. For beam centering at the octupole magnet, two additional steering magnets were installed as well. For beam centering at the octupole, beam position monitors were installed at each octupole magnet. In the end of October 2013, the installation of the octupole magnets had finished, as shown in Fig. 3.

In February 2014, we performed beam tests with the octupole magnet. It was found that the beam shape complied with the design calculations. By excitation of the octupole magnet, the beam halo was converged at the target center. It was also found that the beam heat load in the vicinity of the target decreased.

To use safely the muon production target, which was a fixed target made of carbon graphite, until the summer of 2014, care of the beam treatment on the muon production target was required. To mitigate the damage at the muon target, the beam position was periodically shifted by creating a bump orbit. The octupole magnet cannot be utilized for the normal user beam operation with the bump orbit at the muon target because it makes current density peaks at the edge of the mercury target. After replacing the old one with a new rotating muon production target planned for September 2014, the octupole magnet can be utilized for user beam operations.

Reference

[1] S. Meigo *et al.*, Nucl. Matter 450 141-146 (2014).

S. Meigo[1], M. Ooi[1], A. Akutsu[1], T. Kawasahi[1], M. Nishikawa[1], K. Ikezaki[1], and H. Fujimori[2,3]

[1]Neutron Source Section, Materials and Life Science Division, J-PARC center; [2]Muon Science Section, Materials and Life Science Division, J-PARC center; [3]Institute of Materials Structure Science, KEK

Improvement of Pressure Wave Mitigation Function in Mercury Target System

1. Introduction

In order to mitigate pressure wave which causes pitting damage to the inner surface of the mercury vessel, micro bubbles of helium gas are injected into the mercury using the gas supply system installed on the target trolley. Helium gas used as the cover gas in the surge tank is compressed in the gas supply system and supplied to the bubbler in the target vessel. Helium gas accumulated on the upper surface of the mercury vessel flows into the surge tank through the vent line. When the operation of the gas supply system started in FY2012, we noticed that mercury unexpectedly intruded into the helium supply piping and the helium supply into the mercury circulation system was disturbed. The pressure difference in the vent line squirted mercury into the helium supply piping which was positioned at the opposite side of the vent line outlet at the top of the surge tank as shown in Fig. 1. In order to prevent the mercury intrusion into the helium gas piping, the valve on the vent line was closed, but the accumulated helium gas at the outlet of the mercury target clogged the main mercury pipe and the mercury flow rate decreased by 14%. Because the helium gas going back to the surge tank from the target vessel decreased, the helium gas supply to the bubbler also decreased, which led to the inadequate effect of the pressure wave mitigation.

In order to recover the pressure wave mitigation function in the mercury target system, the mercury in the helium gas piping was discharged by the hands-on work in the hot cell and a gas-liquid separator was installed by remote-handling.

Also, the pressure gauges in the mercury circulation system malfunctioned due to radiation damage and these pressure gauges were exchanged.

In this chapter we will show the details of these challenging maintenance works.

2. Discharge of mercury in Helium gas line and installation of gas-liquid separator in vent line

The discharge work of mercury in the helium gas line was performed with exchange work of the gas supply system to take away the mercury which blocked helium gas flow. Two methods for mercury discharge without the release of tritium in the helium gas line were applied. The first method involved a mercury collection pot with gas-liquid separate function set in the helium gas line and the mercury between the mercury target vessel and the gas supply system was discharged by pressurization (gas flow rate: ca. 10 m^3/h) from the mercury target vessel side. Mercury of ca. 150 cm^3 was collected. In the second method, a vacuum system as shown in Fig. 2 was prepared and a part of the helium gas line was cut paying the closest attention not to release mercury vapor ant tritium. The mercury was

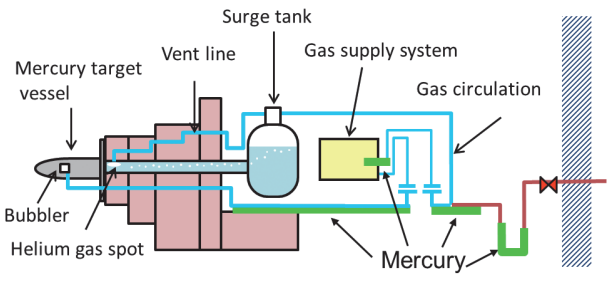

Figure 1. A schematic drawing of the mercury inflow in the helium gas line of the mercury target system.

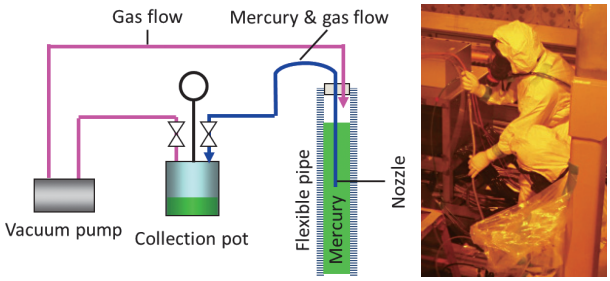

Figure 2. A schematic drawing of the vacuum system for the discharge of the mercury in the helium gas piping and photograph of the discharge work using the vacuum system in a hot cell.

sucked up from the end of the cut helium gas line. The vacuum system was a closed loop consisting of a nozzle, a collection pot with the gas-liquid separate function and a vacuum pump. It was possible to discharge about 1000 cm^3 of mercury, which matched projected amount.

Since there was a possibility that the mercury could come again into the gas supply system, a gas-liquid separator was installed in the vent line. The mercury collected by the gas-liquid separator is returned to the mercury circulation loop and the helium gas goes back to the surge tank. Thanks to the gas-liquid separator, the operation using the vent line is possible and the flow rate of helium gas for the bubble injection becomes 4 times higher than that before the maintenance.

The gas supply system was replaced, because mercury accumulation was confirmed in it. The new one has another gas-liquid separator to avoid mercury accumulation into the system due to the remaining mercury which could not be removed during the above-mentioned maintenance works.

These maintenance works were carried out in about three months and required about 250 man-days.

3. Exchange of pressure gauges

The radiation resistance of these pressure gauges was improved to prolong the lifetime by increasing the shielding performance of the shielding box including the pressure gauges. 7 pressure gauges in the mercury circulation system were exchanged by remote handling in about 2 weeks. In order to minimize the release of radioactive gas including tritium gas, the mercury circulation system was evacuated by the off gas process system to make the air flow from the atmosphere to inside the mercury circulation system. The pressure gage nozzles which were open to atmosphere were closed by rubber plugs when the pressure gauges were removed. It was confirmed that Osmium (Os^{185}) adhered to the wetted surface of the flange as shown in Fig. 3 and the maximum dose of the flange was 150 mSv/h.

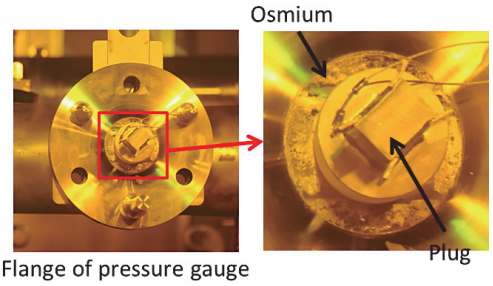

Figure 3. Photograph of the flange of the pressure gauge after removing the pressure gauge.

4. Effect of the recovery in the helium gas line

Time histories of the helium flow rate of the bubbling and the vibration velocity of the mercury vessel before and after the maintenance works are shown in Fig. 4. The helium flow rate was less than 0.1 m^3/h before the maintenance work, but it increased by 4 times after the maintenance work. Looking at Fig. 5, the vibration of the mercury target vessel could be reduced to about 1/3.

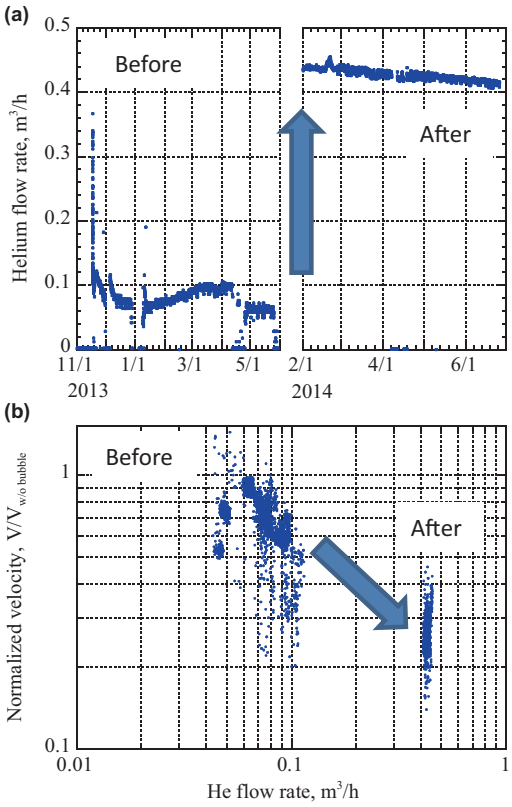

Figure 4. (a) Time history of the helium flow rate before and after maintenance. (b) Relationship between normalized vibration velocity and that without bubble and Helium flow rate.

T. Wakui, T. Naoe, H. Kogawa, K. Hanano, K. Haga, H. Kinoshita, K. Seki, T. Suzuki, and H. Ueno
Neutron Source Section, Materials and Life Science Division, J-PARC Centeri

Cryogenic Hydrogen System

1. Introduction

The J-PARC cryogenic hydrogen system provides cryogenic hydrogen at supercritical pressure of 1.5 MPa, with para-hydrogen concentration of more than 99% and temperature lower than 20 K, to three moderators generating high-performance cold pulsed neutron beams. This report describes the topics of the cryogenic hydrogen system in JFY2013.

2. Development of a partitionable accumulator with a high pressure tolerance and long cycles to failure

The temperature rise through each moderator caused by nuclear heating for a 1 MW proton beam operation is estimated to be 2.4 K at a circulation flow rate of 0.19 kg/s. We prepared a heater for thermal compensation and an accumulator with bellows structure to mitigate the pressure fluctuation caused by the proton beam on and off below the allowable pressure of 0.1 MPa.

A compact second accumulator is in use because a leakage through the welded bellows of the original accumulator was identified before the cool-down operation in February JFY2010 due to a lack of weld penetration between the large diameter bellows plates. However, the present accumulator has drawbacks, including a lower pressure tolerance (0.94 MPa) and large hysteresis during expansion and contraction, which can decrease the number of cycles to failure. After the summer of 2014, we plan to increase the proton beam power to reach our goal of 1 MW. We have developed a third accumulator with a higher pressure tolerance and long failure cycle to achieve the long-term stable operation of the 1-MW proton beam.

In JFY2012, we built a prototype welded bellows block, conducted a cycle test at a repetitive pressure variation of 2.0 MPa, and confirmed that its cycle to failure was 14,000 cycles, which is higher than the design value.

The third accumulator basically adopts the same structure and size as the second. The variable volume of the bellows required for the 1 MW proton beam operation is also estimated to be 2.0 L. The entire variable volume is determined to be more than 6 L. For the third accumulator design, the plate thickness of the welded bellows was increased from 0.4 mm to 0.8 mm to withstand a pressure of up to 2.0 MPa. Therefore, the effect of the spring constant on the pressure rise becomes larger.

The levelness accuracy was maintained within 1° throughout its manufacturing to avoid welding distortion and excessive contact between the guide ring and the guide pipe. We confirmed that the bellows can expand and contract smoothly without hysteresis, and the gradient agrees with a design spring constant of 76.1 N/mm, as shown in Fig.1.

Further, we adopt a new partitionable structure to replace the accumulator more easily and shorten the replacement process. In November of JFY2013, the third accumulator was installed into the hydrogen loop. The accumulator was replaced in less than 20 days by accessing it through the maintenance hatch. This process was shortened by half, compared with the replacement time (six weeks) required when the first accumulator had to be hoisted to the top flange of the cold box.

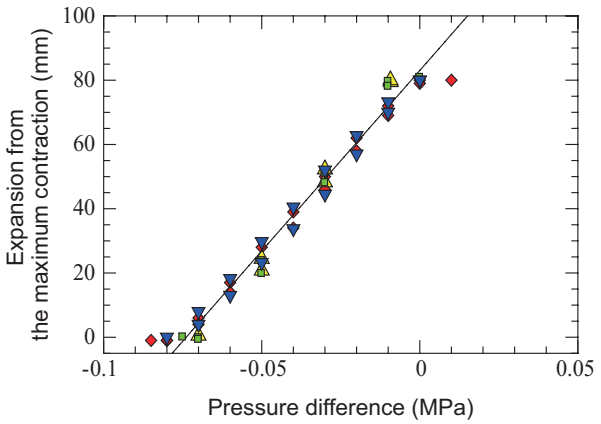

Figure 1. Displacement for the third accumulator.

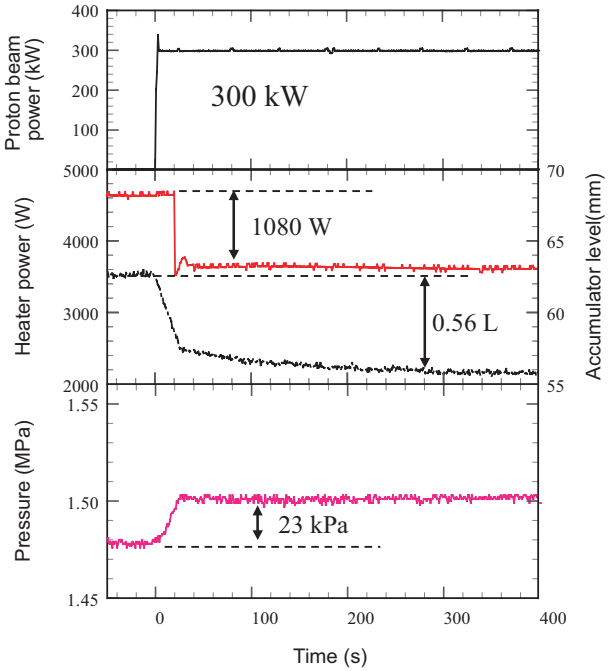

Figure 2. On-beam commissioning results.

The on-beam commissioning results for a 300 kW proton beam injection is shown in Fig.3. As soon as the proton beam is injected, the pressure rises and the accumulator contracts. After the feed-forward heater control is conducted, the pressure and temperature remain unchanged. We confirmed that the pressure rise is mitigated to 23 kPa

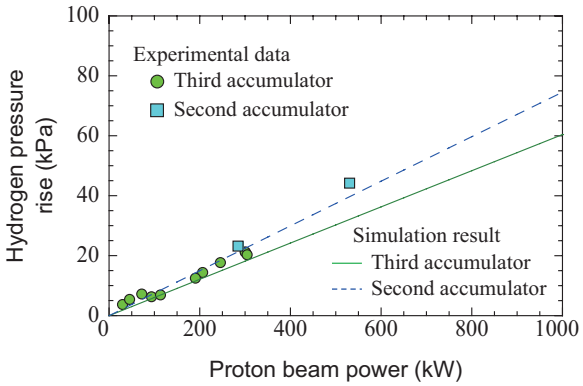

Figure 3. Effect of the proton beam power on the pressure rise.

by a bellows contraction of 0.56 L for 300 kW proton beam power.

The pressure rise increases in proportion to the proton beam power and agrees well with its predicted value. The analytical result indicates that the pressure rise would be 60 kPa for the 1 MW proton beam operation, which is 19% lower than that for the second accumulator. This is because the measured spring constant for the second accumulator becomes larger than the design value due to the large hysteresis. Thus, through the commissioning of the third accumulator, we confirmed that it satisfied the design requirements.

H. Tatsumoto, T. Aso, K. Ohtsu, Y. Kawakami, H. Muto, and S. Hasegawa
Neutron Source Section, Materials and Life Science Division, J-PARC Center

Modification of the MLF General Control System for Sustainable Long-Term Operation

1. Introduction

Fig. 1 represents the outline of the General Control System (GCS) in the MLF in 2013. It consists of several subsystems such as an integral control system for controlling muon and neutron targets, interlock system, servers, networks, and timing distribution system. In Fig. 1, the integral control and interlock system consists of personal computers (PC) and programmable logic controllers (PLC), such as general control panel (GCP), local control panels (LCP) and PPS management panel (PPS-MP), which are connected through networks for PLC links and metal cables. Their operations are executed by monitor and operation (MO) systems consisting of administrative control PCs (ACP), PPS operating PC, interlock monitoring PC (IM-PC), and so on. Although the GCS has worked stably since 2008, recently, the interlock and MO systems have been improved to ensure sustainable long- term operation and maintenance.

2. Interlock Systems

The interlock system has been modified to match the device upgrade of the target systems to ramp up the proton beam power and increase the user apparatuses year after year [1]. It consists of subsystems named MPS (Machine Protection System), TPS (Target Protection System) and PPS (Personnel Protection System). MPS's task is to protect an important machine from unusual beam irradiation. As shown in Fig. 1, after detecting the MPS signals from the LCPs, the MPS controller transmits an "Inhibit" signal to a central control room (CCR) of the J-PARC. Then the proton beam injection into the MLF is stopped by changing the distribution patterns of beam pulses by a scheduled timing system. If the beam pulse is detected during emission of the "Inhibit", the MPS signal for terminating the accelerator operation is transmitted to the CCR. The TPS is the interlock for preventing serious troubles with the mercury target. The TPS beam stop signal is transmitted to the CCR as "Target Status" through

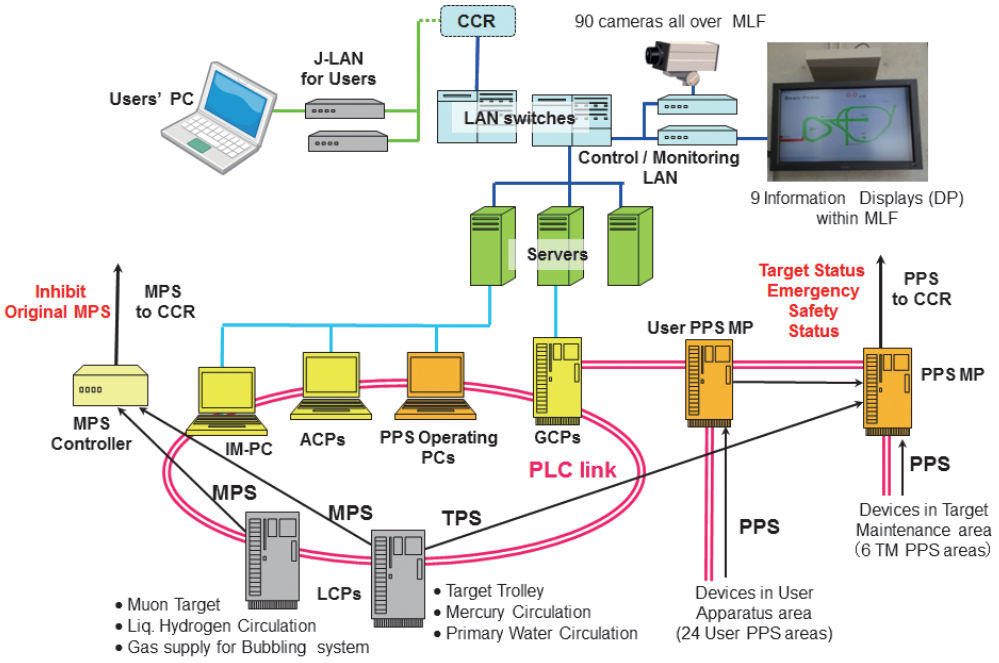

Figure 1. Outline of the MLF-GCS in 2013.

the PPS-MP. The 6 LCPs emit MPS signals through metal cables, with 3 of those LCPs also emitting TPS signals.

The PPS is the system that prevents exposure of the personnel to high radiation by controlling the entrance into high-radiation areas (PPS areas). The 6 PPS areas for target maintenance (TM) and 24 PPS areas for user apparatus are operated in the MLF. The PPS-MP transmits signals to the CCR to permit or prohibit beam injections, which are named “Target Status”, “Safety” for safe entrance into the PPS areas, “Emergency” for manual buttons in emergency, and “Status” for a key switch indicating beam permission. Since the beam stop procedure of the PPS requires high reliability, the ion-source is terminated in this procedure. The IM-PC collects and monitors detailed information about the 108 MPS, 10 TPS and PPS items through the PLC links in a lump.

3. Upgraded Full-scale MO Systems

Since 2012, we have been developing prototypes to upgrade the MO system both for the integral control system and PPS, based on EPICS, CSS and Postgre SQL as its framework, OPI, and server software [2]. After confirming that they work properly, as designed, in 2013 we built two full-scale upgraded MO systems. One is the MO system, which controls the devices for the target stations by using more than 130 operation screens and acquires operation data about 7000 items every second. The other is the system, which administers the PPS devices by using 6 screens and acquires data about 1400 items. They have been operated in parallel with the current systems during beam operation and maintenance for over half a year, and have been debugged, unlike the current ones, which are due to be replaced in 2014. The MO system for the PPS was already replaced completely by the upgraded one in the end of 2013.

References

[1] K. Sakai *et al.*, Progress in Nuclear Science and Technology **4** (2014) pp.264-267.

[2] K. Sakai *et al.*, MLF Annual Report 2012, pp.75-76 (2013).

K. Sakai, M. Ooi, and A. Watanabe

Neutron Source Section, Materials and Life Science Division, J-PARC Center

Scenes from the Neutron Target Station

Installation of octupole magnet from M1 tunnel.

Preparation of local room, called green house, with local ventilation system to prevent from contamination during replacement of the proton beam window.

Preparation for mercury discharge. Center person cut and welded helium gas pipe with mercury.

Installation of additional shielding wall to reduce external exposure of worker in a hot cell.

Hideki Ueno, Kohei Hanano and Takashi Wakui measuring amount of tritium in their expiration before and after mercury discharge work.

Hideki Ueno and Toru Suzuki exchanging pressure gauges by remote handling (manipulator and in-cell crane).

Neutron Science

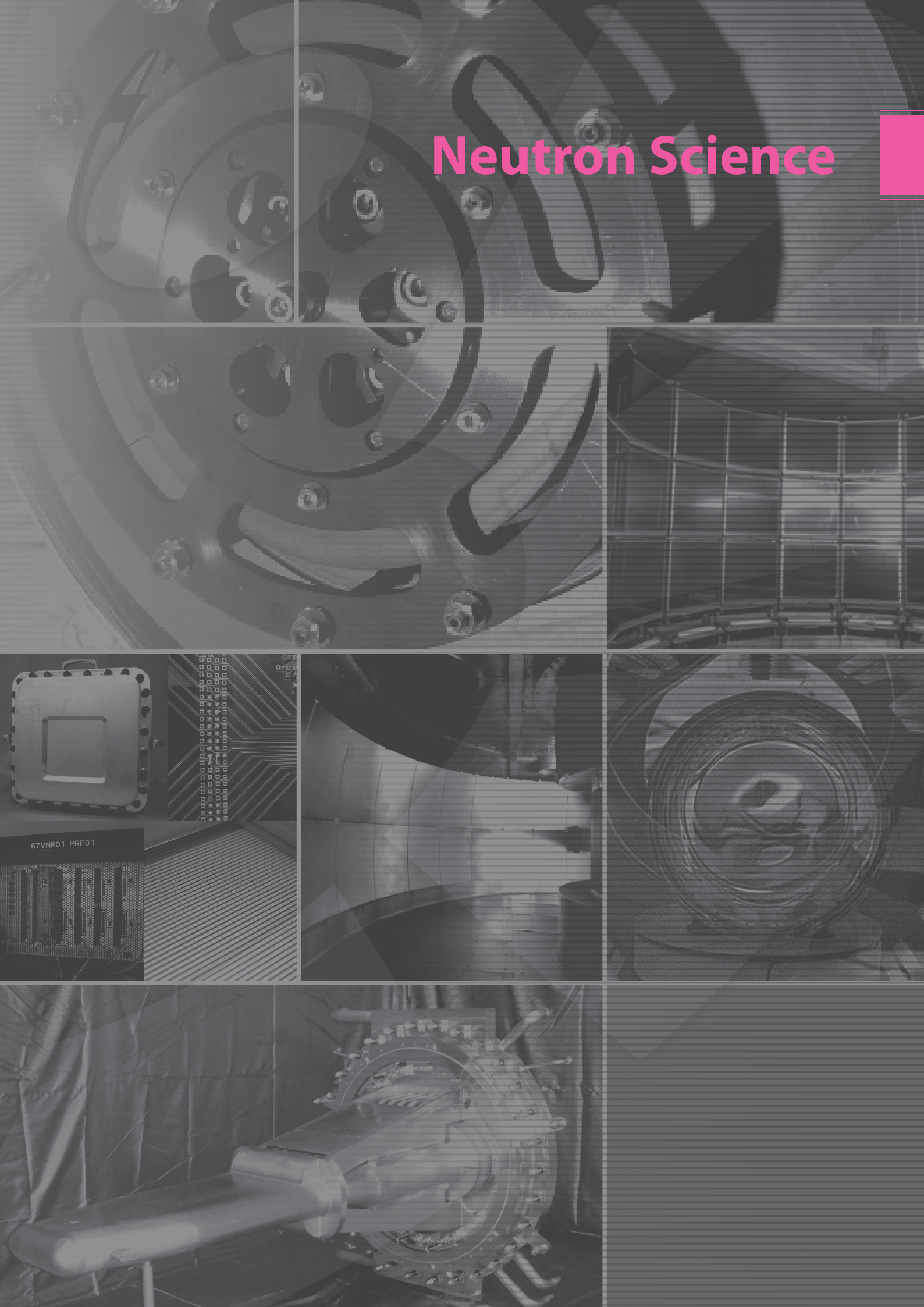

Neutron Science

1. User Program

In JFY 2013, the user program of neutron science has been carried out on 17 instruments (Fig. 1). The Special Environment Neutron Powder Diffractometer − SPICA was still in commissioning phase. After completion of the commissioning work in 2013A, BL11, the High Pressure Neutron Diffractometer – PLANET was introduced as a public beamline to be used in the user program from 2013B.

The user program of 2013A started on April 1, 2013 (Run#48) with 300 kW proton beam power. The Elements Strategic Initiative Program and the Complementary Use Program started in the same fiscal year. Unfortunately, the user program was interrupted during Run#49, on May 25, 2013, due to the radiological incident at the Hadron Experimental Facility. After the incident, all user programs, including the on-beam training of AONSA neutron school that was scheduled for the 18 - 19 of June, were cancelled without carrying over. The cancelled general proposals were recommended for re-submission in the next round. On February 17, 2014, more than eight months after the unexpected break, the user program resumed and was ended on April 6, 2014. Since the program operated for less than two months, only limited numbers of general proposals were accepted and conducted.

2. Instruments development and construction

In JFY 2013, the construction of three new instruments has progressed.

Kyoto University and KEK are installing the VIN ROSE at BL06, which consists of a neutron resonance spin echo (NRSE) instrument and a modulated intensity by zero effort (MIEZE) instrument. All supermirrors for neutron optical devices are deposited using the ion beam sputtering machine at KURRI (KUR-IBS). In JFY 2013, the guide mirrors and downstream concrete shielding were installed.

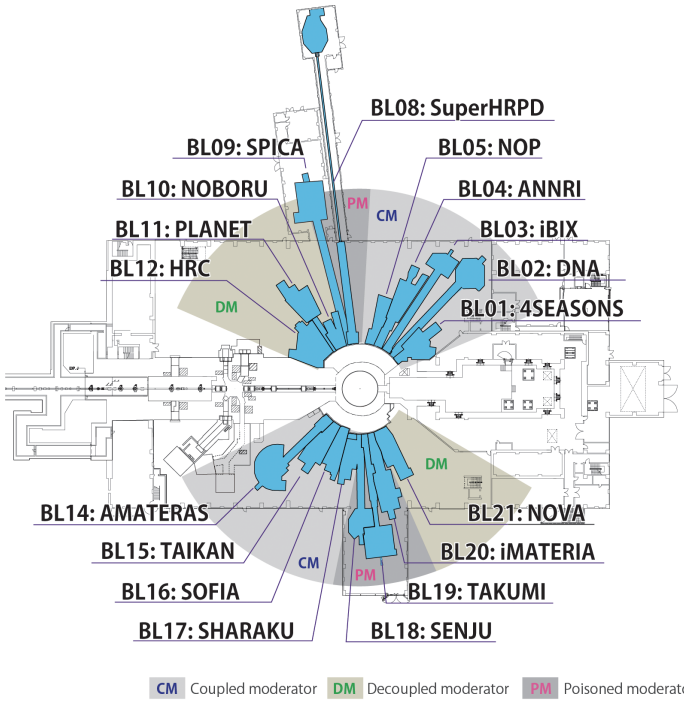

Figure 1. Layout of the neutron instruments at MLF as of JFY 2013. Three other instruments were under construction at BL06, 22 and 23.

At BL22, the construction work of the energy-resolved neutron imaging system, RADEN, continued. In JFY 2013 the shielding was completed. Optical devices, a rotary collimator, filters and slits were installed in the upstream position. Also, a standard shutter block of BL22 was replaced with one specifically designed for RADEN, with three different aperture openings.

The third one, the polarized neutron spectrometer POLANO is being constructed under the joint project between Tohoku University and KEK. The construction of the POLANO at BL23 started in FY2013, when the supplemental budgets were approved for both institutes. The basic design and construction of the shielding were completed, and supermirror guides and neutron choppers were manufactured.

Also, regular maintenance and upgrade works have been done for the existing instruments. For example, a beam-transport section of AMATERAS was upgraded. At TAKUMI, a cooling system for loading experiment was completed. A 6-8 type cell was introduced for the 6-axis multi-anvil press, ATSUHIME at PLANET, which can allow users to reach pressure of above 10 GPa. There are also other advancements in the beam lines, sample environments, development works on spin filters and detectors, etc., which can be seen in individual articles in this report.

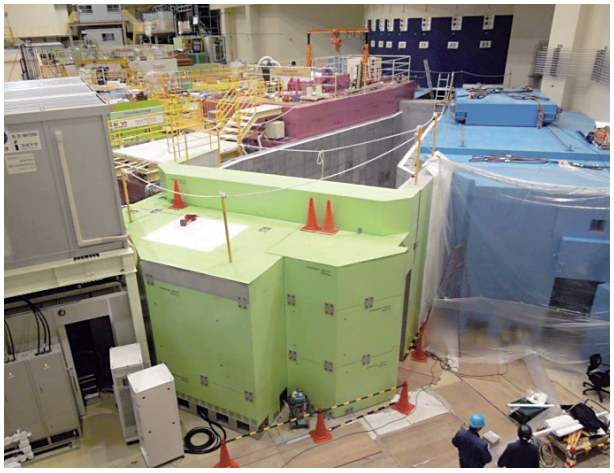

Figure 2. Construction site at BL22 and 23 (December 25, 2013). New instruments, RADEN and POLANO were under construction.

3. Safety

After the radiological incident at the Hadron Experimental Facility, the risk management system of J-PARC was fully reconstructed, introducing three response-stages to incidents, (1) Normal, (2) Alert and (3) Emergency. In MLF, whole manuals for operation and incident response were revised and several kinds of safety drills were carried out. In this report we will introduce in brief our responsibilities for the safety of the neutron-beam-line staff and the users.

a) Responsibility for the MLF operation and safety of the experimental halls

Almost all of the instrumental scientists in J-PARC and CROSS were qualified to join the Shift Leader team as a Sub Shift Leader, which is a newly introduced position assisting the Shift Leader, a person in charge of the MLF operation. When the Shift Leader suspects that an event happening at the moment jeopardizes safety, he/she declares “Alert Stage” to stop all operations of J-PARC and proceed with emergency calls to respond systematically to the suspected safety violation. The Sub Shift Leader also has the same responsibility along with the Shift Leader. After revising the memorandum on safety issues for the public-access neutron beam facilities at J-PARC between the registered institute CROSS and J-PARC, the staffs at CROSS also joined the safety line in J-PARC as Sub Shift Leaders of MLF. During the MLF operation period, the Shift Leader team maintains 24-hour watch by using protection systems and a camera monitoring system. The quick response to any troubles in the experimental halls will be improved by joining the teams of the beam line staff from J-PARC and CROSS.

b) Educating and qualifying staffs in all instrumental groups

The Manual for Neutron Instrument Leader has been re-issued. All Leaders trained the members of their instrumental group according to the manual for the Neutron Instrument Leader and an instrumental manual, which has been revised to comply with the revision of the upper safety regulations and the MLF operation manual. The Manager of Neutron Experiments (Dr. Aizawa) confirmed that the instrumental group members were well trained and the

Facility Manager (Dr. Arai, the MLF director) qualified them as the instrumental group staffs. For the BL's owned by Ibaraki Prefecture, Ibaraki Prefecture and J-PARC agreed on a notification process for the member list of the instrumental group with confirmation of the safety response.

4. Resultant outcomes

The research activities in neutron science at MLF resulted in more than one hundred papers. The number includes articles in influential journals such as Nature, Science.

We published a press release about the discovery of a new magnetic ordering phase in an iron-based superconductor $LaFeAs(O_{1-x}H_x)$ using multi-probe analysis. The new phase was found to be formed by fine changes in the structure for $x > 0.4$. This phase is adjacent to the second superconducting phase found previously in this material, but different from that in the host material ($x = 0$). Thus a new host material was found, and this is expected to be important for understanding the new mechanisms behind superconductivity.

Two staff members and one group of MLF received the 11th Japanese Society for Neutron Science (JSNS) awards. Dr. T. Shinohara (Fig. 3) was awarded the JSNS young researcher prize for his work on development of the magnetic field imaging using polarized pulsed neutrons. Dr. T. Kikuchi was honored with the JSNS young researcher prize for his work on the development of model-free analysis method on quasi-elastic neutron scattering and application to liquid water. Dr. K. Nakajima, Dr. S. Ohira-Kawamura, Dr. M. Nakamura, Dr. R. Kajimoto and Prof. M. Arai shared the JSNS technology prize for their work on the development of a chopper spectrometer with a pulse shaping chopper at a pulsed source. They received their award certificates at a ceremony at the 13th JSNS annual meeting held on December 12, 2013.

Figure 3. The President of the Japanese Neutron Science Society Prof. T. Kanaya gave Dr. T. Shinohara an award certificate for the JSNS young researcher prize.

K. Nakajima[1], Y. Kawakita[1], and S. Itoh[1,2]

[1]Neutron Science Section, Materials and Life Science Division, J-PARC Center; [2]Institute of Materials Structure Science, KEK

BL01: 4D-Space Access Neutron Spectrometer 4SEASONS

1. Introduction

4SEASONS is a thermal neutron Fermi-chopper spectrometer for inelastic scattering measurements in the energy range of 10^0–10^2 meV [1]. The instrument has been available to users since 2009, and became one of the public beamlines in 2011. Now it is stably operated by 6 instrumental scientists and 1 dedicated engineer. In fiscal year 2013, 15 general proposals, including 1 trial-use proposal and 1 urgent proposal, were approved, though only 8 of those could be conducted due to the unexpected shutdown associated with the Hadron incident in 2013A. 3 of the 15 general proposals were requested by international users. The major research subjects are magnetic excitations in strongly-correlated electron systems, such as superconductors and multiferroic materials, but the number of proposals to measure phonons in functional materials is gradually increasing.

Although the instrument operates successfully, it still leaves room for further upgrades, and a part of the designed specifications has not been achieved. Therefore, we continue to upgrade the instrument as well as the sample environment. Here we show examples of the major upgrades in fiscal year 2013.

2. Detectors

The vacuum scattering chamber of 4SEASONS is equipped with 11 detector banks. Each of the detector banks can hold 32 pieces of 2.5 m-long ^{3}He position sensitive detectors, and the whole detector banks can provide scattering angle in the range of −35.3° – +130.5° in the horizontal (Fig. 1). However, only 6 detector banks were fully occupied, resulting in the maximum scattering angle in the horizontal being only 54.5°. Increasing the number of detectors is one of the major issues necessary to achieve the designed specifications of the instrument, and especially important for studying phonons. Unfortunately, the recent shortage and resulting rising price of ^{3}He gas make it difficult to install a large number of detectors at once. Accordingly, we are trying to install a small number of detectors year by year. In fiscal year 2013, we added 29 detectors (Fig. 2), which increased the maximum scattering angle in the horizontal to 68.4° (Fig. 1). We will install more detectors in the next year to reach the maximum scattering angle > 80°.

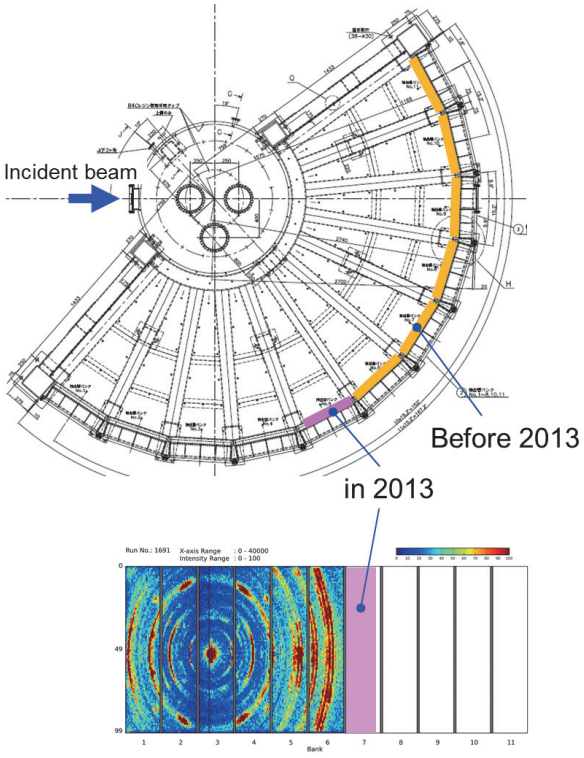

Figure 1. (Top) Drawing of the vacuum scattering chamber of 4SEASONS. The orange and pink marks show detectors which were already installed before fiscal year 2013, and installed in fiscal year 2013, respectively. (Bottom) Detector map of 4SEASONS showing Debye-Sheller rings from a powder sample. The pink region shows the region in which the detectors were installed in fiscal year 2013. There are no detectors installed in the white region.

3. Radial collimator

To minimize scattering from the sample environment, 4SEASONS utilizes the vacuum scattering chamber without any boundary between the sample

Figure 2. Installation of the detectors by the technical support staffs of MLF.

Figure 3. Radial collimator being installed on 4SEASONS by the technical support staffs.

space and the detectors. Nevertheless, the walls of the sample environment devices, e.g. cryostat and furnace, and the sample can inevitably produce scattering, which contaminates the inelastic scattering data. To minimize such unwanted scattering, we recently started to use a radial collimator (Fig. 3). This collimator, which was developed by the Technology Development Section of MLF, consists of 72 pieces of vertical blades surrounding the sample position, each of which is separated by 2.5°. It slowly oscillates to remove the inhomogeneity in the transmitted beam [2].

Although this brand-new device is still under test operation, it has already been utilized for several users' experiments. It proved to be effective in suppressing the background from the sample environment especially in phonon measurements. One of the biggest reasons is that acoustic phonons from the sample would often be overlapped by acoustic phonons from aluminum of the sample environment devices or a sample can because of the similarity in their lattice constants. On the other hand, a sample with a large dimension may not be suitable for the radial collimator, because of the low transmission of the collimator. Users who would like to use the radial collimator are advised to consult with the instrument group prior to their experiments.

References

[1] R. Kajimoto, M. Nakamura, Y. Inamura, F. Mizuno, K. Nakajima, S. Ohira-Kawamura, T. Yokoo, T. Nakatani, R. Maruyama, K. Soyama, K. Shibata, K. Suzuya, S. Sato, K. Aizawa, M. Arai, S. Wakimoto, M. Ishikado, S. Shamoto, M. Fujita, H. Hiraka, K. Ohoyama, K. Yamada, and C. H. Lee, J. Phys. Soc. Jpn. 80, SB025 (2011).

[2] M. Nakamura, Y. Kawakita, W. Kambara, K. Aoyama, R. Kajimoto, K. Nakajima, S. Ohira-Kawamura, K. Ikeuchi, T. Kikuchi, K. Iida, K. Kamazawa, and M. Ishikado, submitted to JPS Conf. Proc.

R. Kajimoto[1], M. Nakamura[1], Y. Inamura[1], K. Kamazawa[2], K. Ikeuchi[2], K. Iida[2], and M. Ishikado[2]

[1]Neutron Science Section, Materials and Life Science Division, J-PARC Center; [2]Neutron R&D Division, CROSS-Tokai

BL02: TOF type Si Crystal Analyzer near Backscattering Spectrometer DNA - Specification and Commissioning Results -

1. Introduction

A time-of-flight (TOF) Si crystal analyzer near-backscattering spectrometer (n-BSS), called *DNA*, is the first indirect geometry instrument, which uses the coupled moderator in MLF as a pulsed neutron source and is equipped with a high-speed pulse shaping disc chopper, aiming for a high energy resolution with high intensity. It aims to explore, in the nanosecond timescale, the dynamic behaviors of atoms and spins in bio-molecules, soft-materials, and so on. The instrumental overview and the present specifications for DNA are shown in Table 1 and Figure 1.

Table 1. Instrumental specifications of DNA.

Items	Specification
Neutron source (NS)	Coupled Liquid H_2 Moderator
L_1 (source-sample)	42 [m]
L_2 (sample-analyzer)	~ 2.3 [m]
L_3 (analyzer-detector)	~ 2.0 [m]
Pulse sharpening chopper (PS-chopper)	
	Max speed: 300 Hz at ~ 7.5 m from NS
(Precent Max speed: 225 Hz by 4 slits on one disc)	
Crystal Analyzer	
Crystal and reflection index	Si(111)
	Si(311) in test
Bragg angle of analyzers	~ 87.5 [deg.]
Energy resolution	
	~2.4 [μeV]: Si(111) with 10 mm Slit @225 Hz
	~3.5 [μeV]: Si(111) with 30 mm Slit @225 Hz
	~14 [μeV]: Si(111) without PS-chopper
	~12 [μeV]: Si(311) with 10 mm Slit @225 Hz.
Momentum range	$0.07 < Q < 1.86$ [A^{-1}]: Si(111)
	$0.60 < Q < 3.80$ [A^{-1}]: Si(311) in plan
Scan energy range:	
Si(111)	$-40 < E/\mu eV < 100$: Single pulse scan around E_f
	$-500 < E/\mu eV < 1500$:
	without PS-chopper in second frame
Si(311)	$-150 < E/\mu eV < 300$: Single pulse scan around E_f

(the specifications by the end of March 2014)

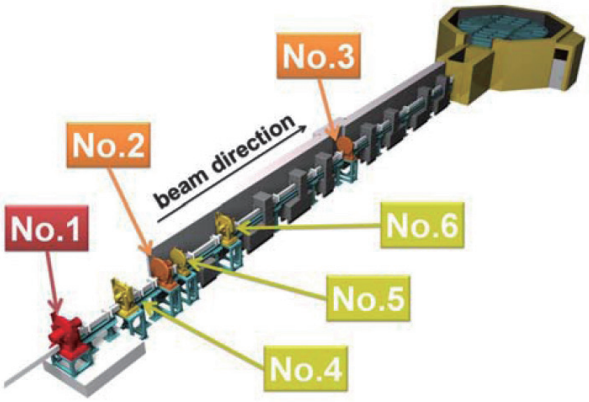

Figure 1. Overview of *DNA*. Each Number indicates a disc chopper installed on the beam line BL02.

2. Construction works in 2013

Almost all spectrometer components were installed before February 2012, with the exception of the No.1 high speed pulse shaping disc chopper. The No.1 chopper, which is designed as a counter-rotating double-disc chopper with maximum rotational frequency of 300 Hz, was set up with a double-disc during a short shut-down period in early April 2013 and commissioned at 225 Hz in end of April 2013.

To evaluate the incident neutron energy distribution at the sample position, and to measure the diffraction pattern from the powder sample, three diffraction-detector-units were installed in this period. The analyzer coverage was extended to a scattering-angle range from −18 degrees to +138 degrees in the horizontal plain by adding some crystal analyzer units, by the end of September 2013.

3. Beam Commissioning in 2013

The commissioning started from the beginning of February 2012. In this period, the pulse shaping high speed chopper could not be operated, then we operated the DNA spectrometer without the pulse sharpening chopper at energy resolution of ΔE ~ 14 μeV with wide energy transfer range: $-1000 < E / \mu eV < +1500$.

After installing the No.1 high speed chopper, the commissioning of high-resolution measurement was carried out by using single disc with slits of 10 mm and 30 mm widths at 225 Hz in the maximum rotational speed from the end of April 2013. At this point, the energy resolution of 2.4 μeV and 3.5 μeV with wide energy transfer range: $-40 < E / \mu eV < +100$ by one pulse scan, was achieved.

We realized an extremely low contribution of instrumental background S/N~ 10^5.

4. Implementation progress of the user program in 2013A and 2013B

The user program started from May 2012. The user program in 2013A, with 3 experiments, and in 2013B, with 3 experiments, was carried out and some of those experiments obtained new findings, which will be reported in near future.

Many experimental applications to the general user program from various scientific fields are expected in the future.

References

[1] N. Takahashi *et al.*, Journal of Physics and Chemistry of Solids 68, 2199-2203 (2007).

[2] N. Takahashi *et al.*, Journal of the Physical Society of Japan, 80, SB007 (2011).

K. Shibata[1], N. Takahashi[1], Y. Kawakita[1], K. Kamazawa[2], T. Yamada[2], M. Matuura[2], T. Tominaga[2], K. Nakajima[1], W. Kambara[1], M. Kobayashi[2], Y. Inamura[1], T. Nakatani[1], S. Kasai[2], K. Aizawa[1], and M. Arai[1]

[1]Neutron Science Section, Materials and Life Science Division, J-PARC Center; [2]Neutron R&D Division CROSS-Tokai

Current Status of IBARAKI Biological Crystal Diffractometer iBIX at BL03

1. Current Status

The IBARAKI biological crystal diffractometer, called iBIX, is a high performance time-of-flight neutron single crystal diffractometer designed to observe mainly the hydrogen, protonation and hydration structure of biological macro molecules and then to elucidate the basic mechanism of catalytic reaction and drug development based on the 3-dimensional molecular structure.

Starting from the end of 2008, iBIX with 14 detectors was made available for users' experiments supported by Ibaraki University [1]. In 2012, we completed the installation of 30 new detectors for the iBIX diffractometer (Fig. 1) [2]. The new iBIX is expected to become one of the world's best-performing neutron single crystal diffractometers for biological macro molecules. Since January 2013, the new iBIX has been available regularly to users' experiments for protein samples. The final specifications of the iBIX is shown in Table 1.

In FY2013, 3 organic compounds and 5 biological macromolecules were provided to the diffraction experiments by using iBIX. From these analyses, some scientifically interesting results could be obtained by using the characteristic of neutron structure analysis (eg. Observation of hydrated water related to catalytic reaction;possibility of new reaction mechanism).

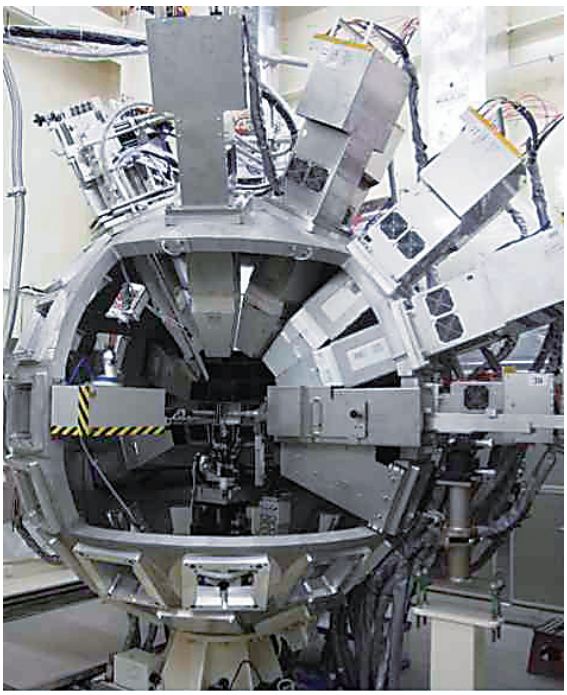

Figure 1. The iBIX Diffractometer.

Table 1. The final specifications of the iBIX.

Moderator	Coupled H_2 (para) 100 × 100 mm^2
Guide tube (m)	25
L1 (m)	40
L2 (m)	0.49
Max. unit cell length ($Å^3$)	~ 135^3
Measurement region in dspacing (Å)	$0.35 < d < 50$
Range of neutron wavelength (Å)	$0.5 < \lambda < 9.0$ or more
Neutron flux (neutrons/sec/cm^2)	7×10^7
Sample environment	Gas flow type cooling system, He: ~20 K, N_2: ~90 K
Detector	Two-dimensional, scintillator, wavelength shift fiber type
Size of sensitive area (mm^2)	133 × 133
Spatial resolution (mm)	Less than 1
Standard size of sample (mm^3)	1
Standard measurement time (days)	0.5 for Organic compounds 3 for Biological macromolecules

2. Development

In FY 2013, we prepared users manual and distribution package of the data reduction software "STARGazer" which will allow the iBIX users themselves to perform data reduction in their laboratory. At the same time, we held a software workshop for iBIX core users.

Some components of the data reduction software have been upgraded and newly developed in order to become a software system able to process data faster and in a more friendly way. For example, visualization components of peak search reflections were newly developed to check the peak search results. The component of data format conversion and statistics calculation was prepared to be applied for the structure analysis by users.

As of the hardware, we installed the new data acquisition system, which has faster data reading and writing function and larger storage than the previous one (Fig. 2). Also the pulse laser system was prepared as part of the utility equipment for sample environment and multi-purpose stage was developed to mount the utility equipment for sample environment with the sample (Fig. 2).

Figure 2. (a) New data acquisition system (b) multi purpose stage and (c) laser sysytem.

3. Feature prospects

In the future, the accelerator power of J-PARC will be improved at 1000 kW. The data reduction software should be upgraded continuously in order to become more user friendly and be available for samples with large unit cell and/or smaller volume for measurement of full data set. The wide pulse shape in TOF direction of coupled moderator and large unit cell of the samples cause overlap of the adjacent Bragg spots. Next year, we will start to develop the peak profile fitting method in order to improve the accuracy of the data reduction for the integrated intensities of Bragg reflections and to realize the method to de-convolute overlapping reflections.

As of the hardware, we should prepare the utility equipment for sample environment (e.g. heating and extension) and a fast and friendly measurement system before the accelerator power reaches 1 MW.

References

[1] I. Tanaka, K. Kusaka, T. Hosoya, N. Niimura, T. Ohhara, K. Kurihara, T. Yamada, Y. Ohnishi, K. Tomoyori and T. Yokoyama, Acta Cryst. **D66** (2010) 1194–1197.

[2] K. Kusaka, T. Hosoya, T. Yamada, K. Tomoyori, T. Ohhara, M. Katagiri, K. Kurihara, I. Tanaka and N. Niimura J. Synchrotron Rad. **20** (2013) 994–998.

K. Kusaka[1], T. Hosoya[1], T. Yamada[1], T. Ohhara[2], M.Katagiri[1], I. Tanaka[1], and N. Niimura[1]

[1]Frontier Research Center for Applied Atomic Sciences, Ibaraki University, Tokai; [2]Neutron Science Section, Materials and Life Science Division, J-PARC center

Study of the Energy Resolution of the Pulsed Neutron Beam Provided by ANNRI (BL04)

1. Introduction

The ANNRI (BL04) at J-PARC/MLF was constructed in order to measure the neutron capture cross-section as a function of the neutron energy in the thermal and epithermal neutron energy regions. The neutron energy resolution is important to ensure the quality of the cross-section data. The neutron energy is calculated by the time-of-flight (TOF) method. The TOF resolution is composed of the two factors: the time structure of the incident proton beam to the mercury target of the JSNS and the time uncertainty due to the neutron slowing-down process in the liquid hydrogen moderator. We studied the neutron energy resolution by simulation calculation, in which the above two factors were taken into account, and measurements of the time resolutions in the thermal and epithermal neutron energy regions.

2. Simulation

The simulation of the neutron slowing-down process was performed using the Monte-Carlo code PHITS [1]. The procedure is almost the same as explained in the reference [2]. At the JSNS, the incident proton beam is normally delivered in a double-bunch scheme and the time interval between the two bunches is 599 ns. Each bunch also has time width of 60 ns under the JSNS operation of 17.5 kW. We convoluted the time structure obtained by the simulation with the time structure originating from the proton beam and show the neutron pulse in Fig. 1. This Figure shows the relation between the time and energy at the moderator surface. In the case of the double-bunch mode, the pulse splits into two below about 10 eV. This is due to the double-bunch scheme and indicates that we need to treat this property carefully at analyzing experimental data obtained at ANNRI. Fig. 2 shows the time width in FWHM obtained by the data in Fig. 1. The time width is the same, below about 10 eV for both single- and double-bunch modes. The double-bunch mode approaches about 600 ns as the neutron energy increases. On the other hand, the single-bunch mode does about 60 ns. We calculated the energy resolution at the sample position (L = 21.5 m) on the basis of the time width in Fig. 2 and show it in Fig. 3. The energy resolution is almost equal or less than 1% below 100 eV. However, the energy resolution for the double-bunch mode deteriorates drastically as the neutron energy increases.

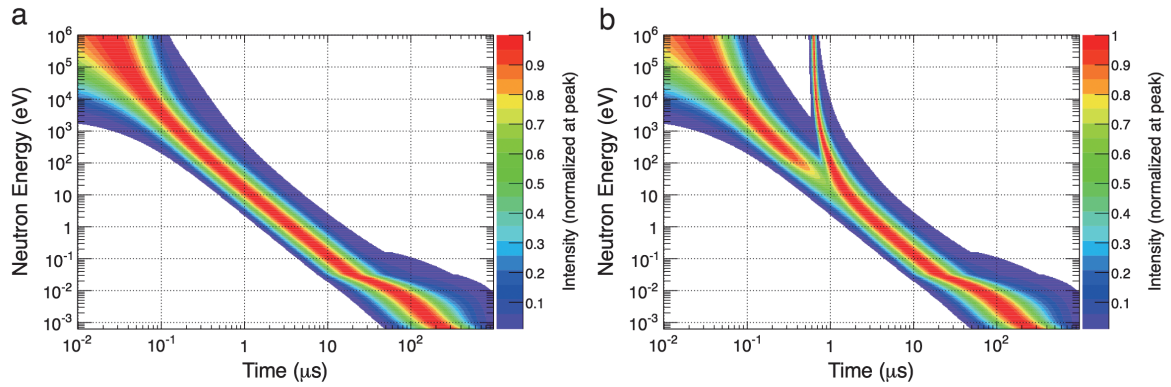

Figure 1. Two-dimensional plots of the time and energy of neutrons at the moderator surface. The time structure of the proton beam is taken into account. (a) and (b) are the results for the single- and double-bunch modes, respectively [3].

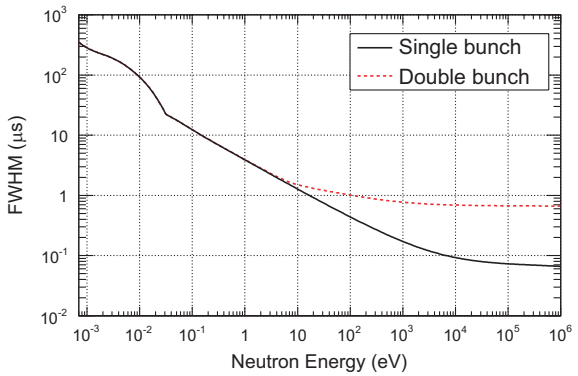

Figure 2. The FWHM values for the time structure by the simulation as a function of neutron energy. The solid and dashed lines represent the single- and double-bunch modes, respectively [3].

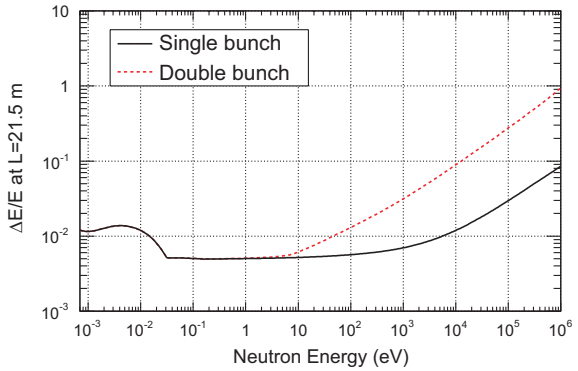

Figure 3. Neutron energy resolution at 21.5 m from the moderator based on the simulation. The solid and dashed lines represent the single- and double-bunch modes, respectively [3].

3. Measurements

We performed measurements of the time width of neutron pulses at the thermal and epithermal neutron energy regions using different methods.

In the thermal neutron energy region, we applied the diffraction method using a Mica sample. The sample was set at 28.5 m from the moderator in the beamline. Diffracted neutrons were detected by a He-3 neutron detector set at an angle of 162° with respect to the beamline downstream. Fig. 4 shows observed neutron pulses and comparison with the simulation calculation. The observed pulses consist of fast and slow components and these are perfectly reproduced by the simulation calculation. These two components can be represented by slowing-down and storage terms of the model function proposed by Ikeda and Carpenter [4]. We obtained pulse width in FWHM by fitting the pulses using the above model function.

In the epithermal neutron energy region, we applied resonances of the neutron capture reaction by Ta-181 at the single-bunch operation of the JSNS. A tantalum foil with a thickness of 0.1 or 0.01 mm was set at 29.54 m from the moderator in the beamline. Prompt gamma rays associated with the neutron capture reaction were detected by a plastic scintillation detector and the TOF data was recorded. Fig. 5 is the TOF spectrum obtained by the 0.1-mm thick sample. A lot of resonances were observed at the neutron energy indicated by the nuclear data library JENDL-3.3 [5]. We fitted 17 resonances by the function, which was obtained by the convolution of the intrinsic resonance shape expressed by the single-level Breit−Wigner, the neutron pulse expressed by the model function proposed by Ikeda and carpenter, the time structure of the proton beam, and the Doppler effect of Ta-181 nuclei. The widths of neutron pulses were obtained from the fit results.

4. Comparison of the simulation and measurements

Fig. 6 shows a comparison of the measurements and the simulation calculation. They are in agreement for the absolute value and trend depending on the neutron energy. This result means that the JSNS and ANNRI work properly. Furthermore, the simulation is reliable for deducing pulses in energy regions, which the measurements cannot access.

5. Conclusions and future prospects

The simulation and measurements of neutron pulses of the pulsed neutron beam at ANNRI were performed. They showed good agreement, which implies the reliability of the simulation calculation. The simulation revealed the energy resolution of ANNRI and the necessity for a special treatment for the neutron-capture cross-section data in the case of a double-bunch mode of the JSNS.

In this work, the neutron pulse was studied for the JSNS condition of 17.5 kW. The JSNS power is expected to become 1 MW in near future. The property of the neutron pulse may change by an increase of the JSNS power. Therefore, the pulse has to be checked by simulation and measurement on a continuing basis for precise analysis of the neutron capture cross-section data.

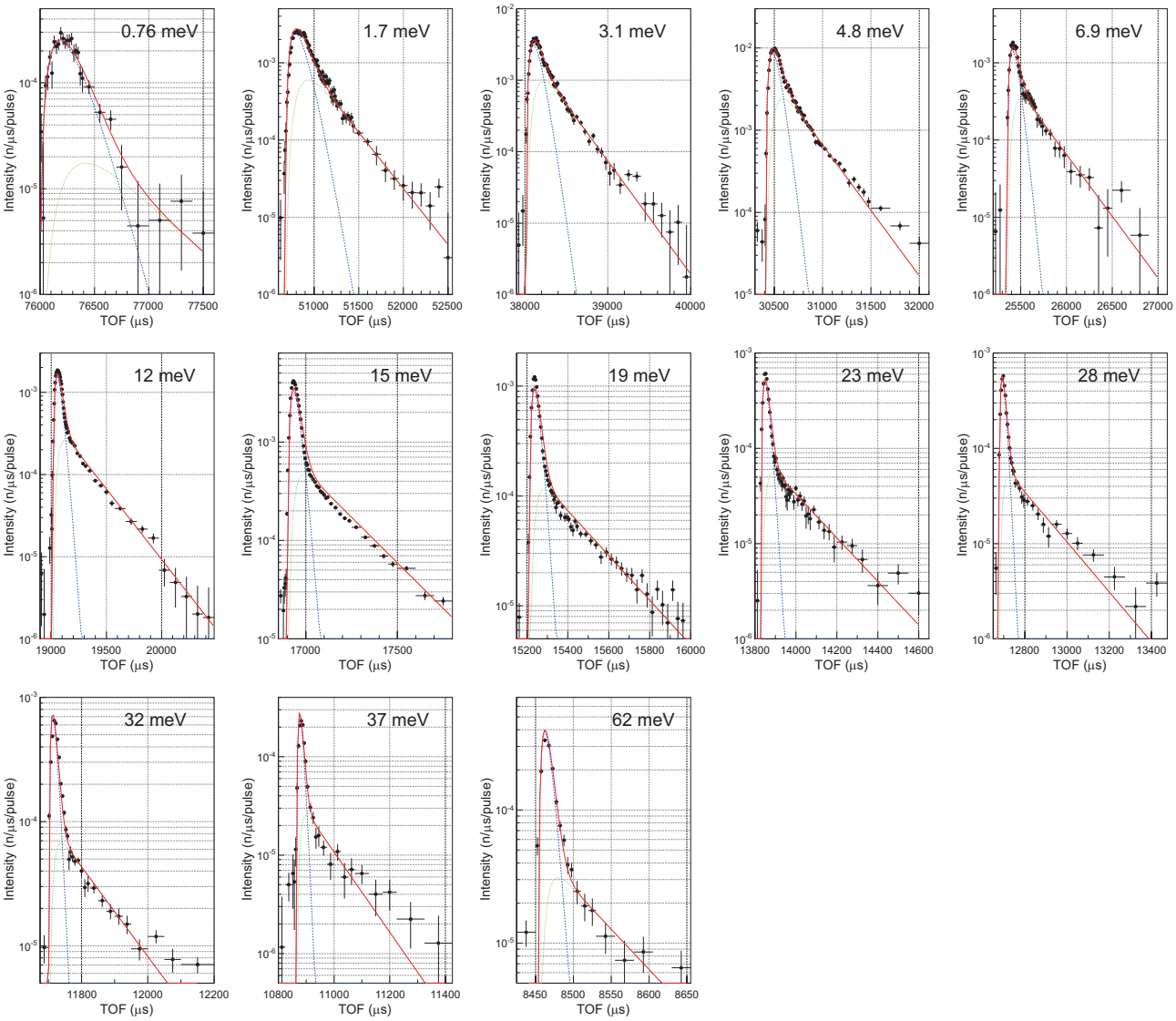

Figure 4. Comparison of measured diffractions (data points) with the time structures obtained by the simulation (solid lines). The value indicated in each figure corresponds to the neutron energy of the diffraction. The dashed and dotted lines are the slowing-down and storage terms in the model function proposed by Ikeda and Carpenter, respectively [3].

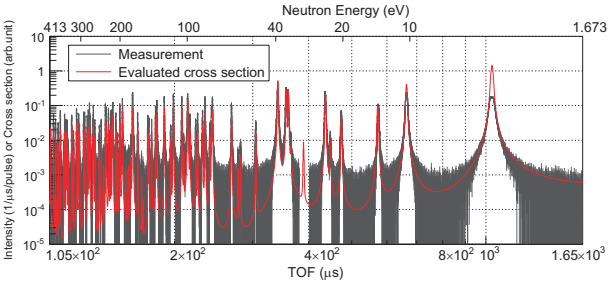

Figure 5. Measured TOF spectrum with the thick tantalum foil and the cross-section of the neutron capture reaction based on the nuclear data library JENDL-3.3 at a temperature of 300 K [3].

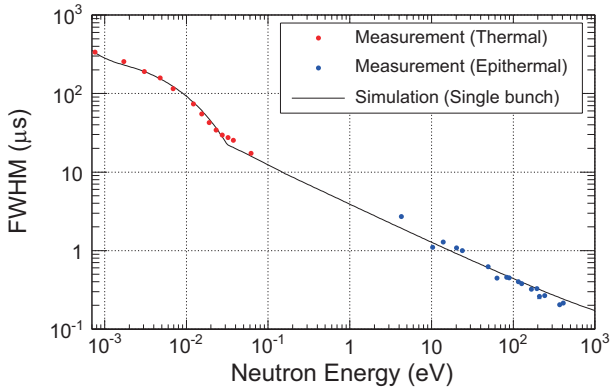

Figure 6. Comparison between the simulation and measurements of the FWHM values of the time structures of neutron pulses for single-bunch mode [3].

Acknowledgements

The present study is the result of “Study on nuclear data by using a high intensity pulsed neutron source for advanced nuclear system” entrusted to Hokkaido University by the Ministry of Education, Culture, Sports, Science, and Technology of Japan (MEXT). This work was supported by JSPS KAKENHI Grant no. 22226016.

References

[1] K. Niita *et al.*, PHITS: Particle and Heavy Ion Transport Code System, Version 2.23, JAEA-Data/Code 2010-022, 2010.

[2] K. Kino *et al.*, Nucl. Instrum. Methods Phys. Res. A626 (2011) 58.

[3] K. Kino *et al.*, Nucl. Instrum. Methods Phys. Res. A736 (2014) 66.

[4] S. Ikeda and J.M. Carpenter, Nucl. Instrum. Methods A239 (1985) 536.

[5] K. Shibata *et al.*, J. Nucl. Sci. Technol. 39 (2002) 112.

K. Kino[1], M. Furusaka[1], F. Hiraga[1], T. Kamiyama[1], and Y. Kiyanagi[2] on behalf of the ANNRI collaboration

[1]*Faculty of Engineering, Hokkaido University;* [2]*Graduate School of Engineering, Nagoya University*

Studies of Neutron Optics for Physics Researches

1. Introduction

At the NOP beamline (Neutron Optics and Physics) installed at the port BL05, the final preparation for neutron lifetime measurement, as well as some other researches and developments are continuing. The detailed analysis of commissioning data showed that certain challenges should be resolved. The time projection chamber (TPC) to detect neutron beta decay was upgraded to suppress background events and electric noises effectively. The UCN accelerator was improved to accept a wide range of neutron velocity. The simulation study for neutron scattering experiments to search middle-range force also progressed. Apparatus including gas target and scattering chamber was designed for the experiment at NOP.

2. Commissioning for neutron lifetime measurement

The recent values of neutron lifetime deviate far beyond the systematic errors claimed in the past and require further improvement to ensure consistency with the primordial Big Bang nucleosynthesis.

We are continuing the neutron lifetime measurement at the polarized beam branch of the NOP beamline installed at the port BL05 [1]. The system consists of a neutron chopper (SFC) and a gas chamber (TPC) for detecting the electrons from the neutron beta decays [2]. The TPC contains small amount of ^{3}He. The rate of the ^{3}He(n,p)^{3}H reaction is measured by counting the protons. The neutron lifetime is measured as the ratio of the electron events to the proton events. The detailed analysis of commissioning data told us some problems to be resolved. The TPC was upgraded to suppress background events and electric noises effectively.

We clearly observed neutron beta decay events and ^{3}He capture events in the commissioning data. Now we are checking the analysis procedure carefully.

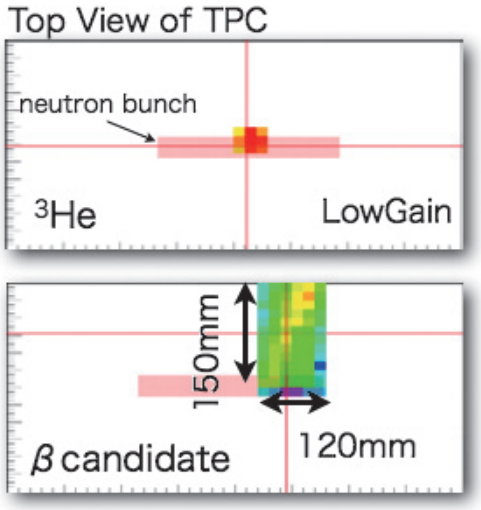

Figure 1. Typical event display for ^{3}He capture (top) and beta decay (bottom). They can be identified by deposit energy and track geometry.

3. UCN optics upgrade

Ultra Cold Neutrons (UCNs), which are neutrons with velocity of less than 7 m/s, are used mainly for particle physics. To get dense UCNs at the experimental position, the optical system “rebuncher” for neutron focusing was already demonstrated [3]. We improved the rebuncher to accept a wide range of neutron velocity so that the range of frequency of RF spin flipper for acceleration of UCNs was twice as large as previously demonstrated. The RF power was also increased for flipping efficiency. Now we are preparing the focusing experiment by using Doppler shifter on NOP [4]. We also develop a new type of neutron mirror for UCN guide tubes using deuterated diamond-like carbon film. A mirror with optical potential of 243 neV was fabricated successfully by the CVD method [5], which has an advantage to deposit inner surface. It is quite important to estimate the motions of UCNs to discuss the systematics in high precision experiments. We have also developed simulation tools based on GEANT4 to treat UCN’s motion [6].

4. Precision measurement of scattering from window material

A measurement of angular distribution of scattering cross section is planned for the search of unknown medium range interactions between neutrons and neutral atoms. We confirmed that the total cross section of silicon as a window material measured at NOP was in good agreement with the theoretical prediction. The simulation studies also advanced. The experimental apparatus, including gas target and scattering chamber, was designed based on the results of the simulations. Now we are preparing the experiment with full-setup at low divergence beam branch.

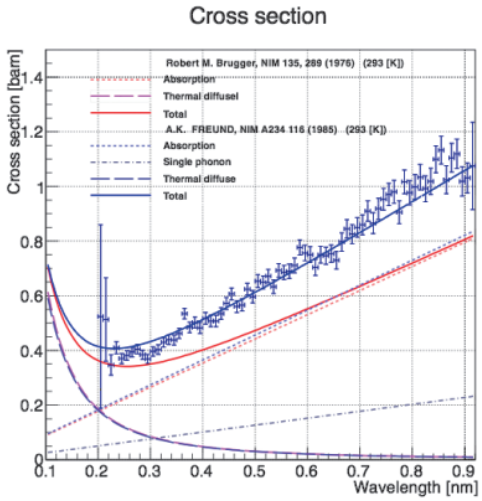

Figure 2. Measured total cross section by Silicon block as a function of the neutron wavelength. The blue solid line shows a theoretical line obtained by Freund et al.

References

[1] T. Ino *et al.*, J. Phys.: Conference Series **528** (2014) 012039.

[2] H. Otono, Dr. Sc. Dissertation (University of Tokyo, 2012).

[3] Y. Arimoto *et al.*, Phys. Rev. **A 86** (2012) 023843.

[4] K. Mishima *et al.*, J. Phys.: Conference Series **528** (2014) 012030.

[5] D. Sakurai *et al.*, J. Phys.: Conference Series **528** (2014) 012010.

[6] R. Katayama *et al.*, J. Phys.: Conference Series **528** (2014) 012031.

Y. Arimoto[1], T. Ino[2,3], S. Muto[3], K. Taketani[2,3], H. Oide[4], T. Yoshioka[5], H. Otono[5], T. Yamada[6], K. Mishima[6], S. Yamashita[6], H. Sumino[7], S. Imajo[8], Y. Iwashita[8], M. Yamada[9], Y. Seki[9], Y. Otake[9], Y. Yamagata[9], P. Geltenbort[10], K. Hirota[11], M. Kitaguchi[11], H. M. Shimizu[11], T. Shima[12], H. Funahashi13, K. Asahi[14], and Y. Kiyanagi[15]

[1]Accelerator Laboratory, KEK; [2]Neutron Science Section, Materials and Life Science Division, J-PARC center; [3]Institute of Materials Structure Science, KEK; [4]CERN; [5]Department of Physics, Kyushu University; [6]International Center for Elementary Particle Physics, University of Tokyo; [7]Department of Physics, University of Tokyo; [8]Institute for Chemical Research, Kyoto University; [9]RIKEN; [10]Institut Laue Langevin; [11]Department of Physics, Nagoya University; [12]Research Center for Nuclear Physics, Osaka University; [13]Institute for Liberal Arts and Science, Kyoto University; [14]Department of Physics, Tokyo Institute of Technology; [15]Faculty of Engineering, Hokkaido University

Advance Neutron Beam Line for VIllage of Neutron ResOnance Spin Echo Spectrometers (VIN ROSE) at BL06

Kyoto University and KEK are jointly installing two types of neutron spin echo (NSE) spectrometers at BL06, that is, a neutron resonance spin echo (NRSE) instrument and a modulated intensity by zero effort (MIEZE) instrument. The NSE technique is an essential spectroscopic method, which has achieved the highest neutron energy resolution at the present moment. NSE with a pulsed neutron source makes it possible to scan very efficiently wide spatiotemporal space. We named the beam line "VIN ROSE" (VIllage of Neutron ResOnance Spin Echo spectrometers), which will spawn a new field of spectroscopic methods [1].

In Figure 1, the schematic top view of BL06 beam line is shown. Both NRSE and MIEZE make use of neutron resonance spin flippers, which made it possible to design and install compact and multiple spectrometer machines in a narrow space. Another characteristic is the adoption of two curved guides rolling to create experimental space for two spectrometers and transport optimized neutron beams. By using the curved guide tubes, fast neutrons and gamma rays from the source are stopped by an iron beam dump at the upstream part of the instruments.

NRSE is suitable to study slow dynamics of soft condensed matter with high energy resolution, while MIEZE has a big advantage of flexible sample environments with potential to open new fields of study such as spin dynamics in strongly correlated systems. In Table 1, the planning instrumental specifications of VIN-ROSE are listed.

The neutron optical devices are key components of the spectrometers. Some of the devices, such as focusing mirror and related devices have been developed and improved step by step. All the supermirrors for these guides are deposited on silicon wafers with thickness of 3 mm by using the ion beam sputtering machine at Kyoto University (KUR-IBS) [1, 2]. The supermirrors are held precisely and covered by iron shields to reduce the dose level. The NRSE and MIEZE guides use $Q_c = 2.5$ and 3 supermirrors, respectively. Their high performance has been proven by neutron reflectivity measurements, etc.

In FY2013, the guide mirrors and the downstream concrete shielding were installed, and the instruments' commissioning has been started in FY2014. Figure 2 shows a picture of BL06 and the observed beam profiles with neutron imaging plate for the instruments.

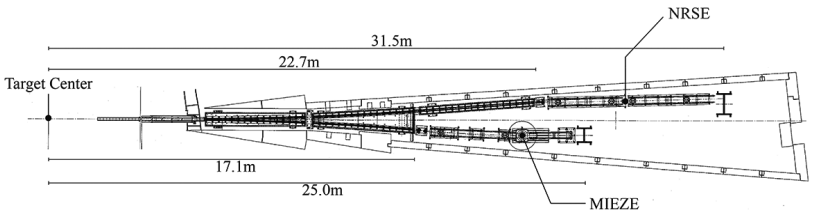

Figure 1. Schematic top view of MIEZE and NRSE beam line at BL06.

Table 1. Planning instrumental specifications of VIN-ROSE.

Spectrometer	Wavelength	Q range [Å^{-1}]	Fourier Time
MIEZE	$3 < \lambda < 13$ [Å]	$0.2 < Q < 3.5$	1 [ps] < t < 2 [ns]
NRSE	$5 < \lambda < 20$ [Å]	$0.02 < Q < 0.65$	0.1 [ns] < t < 0.1 [μs]

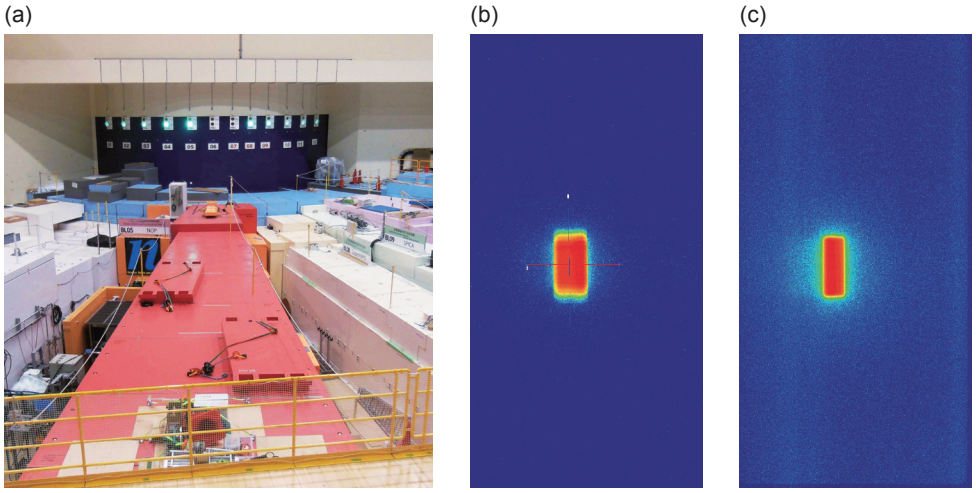

Figure 2. Picture of BL06 (a), observed neutron beam profiles for NRSE (b) and MIEZE (c), by neutron imaging plates, respectively.

References

[1] M. Hino, T. Oda, M. Kitaguch, N. L. Yamada, H. Sagehashi, Y. Kawabata, H. Seto, Physics Procedia 42 (2013) 136.

[2] M. Hino, H. Sunohara, Y. Yoshimura, R. Maruyama, S. Tasaki, H. Yoshino and Y. Kawabata., Nucl. Inst. Meth. A 529 (2004) 54.

H. Endo[1,2], M. Hino[3], T. Oda[3], N. L. Yamada[1,2], H. Seto[1,2], and Y. Kawabata[3]

[1]Neutron Science Section, Materials and Life Science Division, J-PARC Center; [2]Institute of Materials Structure Science, KEK; [3]Kyoto University Research Reactor Institute

Upgrade of SuperHRPD

1. Introduction

The super high resolution powder diffractometer SuperHRPD suffered damage by the Great East Japan Earthquake on the 11th of March 2011. The first stage of the restoration works had been carried out until March 2012. The beam time for the general user program started from April 2012 and all of the research proposals for fiscal year 2012 had been successfully conducted. The incident in the hadron facility happened at the beginning of FY 2013, which caused slight delay in the second stage of the restoration works that had been scheduled for the summer.

As part of the upgrade of the instrument, a new detector system of 8 mm diameter position sensitive detectors (PSDs) were installed at the backward detector bank and the number of detectors of the 90 degree bank was increased. The data acquisition system was completely changed to new computers and data storages.

2. Restoration works of the re-alignment of the guide tube and improvement of the beam line shielding

The earthquake caused optical deviation in the guide tube system. A complete restoration of the system was carried out during the beam shut down period in the summer of FY 2013. In this alignment work, the vacuum jacket of the guide tube and the guide tube support system were improved at the same time. The iron vacuum jackets of the curved guide section in the upstream were replaced with aluminum jackets. The lower weight of these aluminum jackets (Figure 1) simplified the support system. At the straight guide section without vacuum jacket in the downstream, about 50 m of the guide tube support system was also changed to aluminum, which made it lighter.

The beam line shield of the straight guide section was completely redesigned to concrete containing boron (Figure 2). The former beam line shield had a small clearance of a few cm around the guide tube. Since the earthquake caused deviation of the optical axis, it was necessary to adjust not only the guide tube but also the beam line shield. The new design of the beam line shield has a ten-odd cm clearance around the guide tube, which does not require adjustment and a large move of the shield at the time of re-alignment of the guide tube.

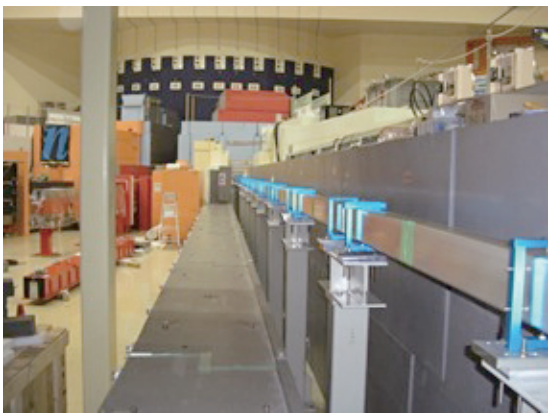

Figure 1. New aluminum vacuum jackets. One unit is about 2 m in length and a support pillar is installed in each unit.

Figure 2. New design of the beam line shield of the straight guide section. Concrete containing boron is used.

3. New detector system with 8 mm diameter position sensitive detector

Because of the insufficient initial budget and the delay of development in the high spatial-resolution

detector system, we initially installed 1/2 inch diameter position sensitive detectors (PSDs) that had been used at KENS facility of KEK. This imposed limit on the resolution compared with the designed one. Then we developed a new detector system based on 8 mm diameter PSDs and improved the resolution as shown below. The 16 PSDs with diameter of 8 mm were composed together into one unit and an amplifier circuit was connected to each PSD. In the new detector system, 8 amplifier circuits were built into one application specific integrated circuit (ASIC) chip and this made the circuit more compact (Figure 3).

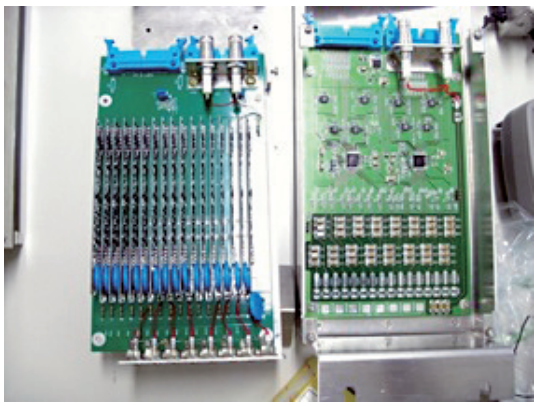

Figure 3. The conventional amplifier circuit (left) and the advanced one with an ASIC chip (right); the 16 amplifier circuits are accumulated in two ASIC chips.

The test measurement using the new detector system was performed in May 2013. In this measurement, four new detector units were arranged at the backward detector bank to cover the area of $2\theta = 157° \sim 172°$. A diamond powder sample enclosed in a sample holder of 6 mm in diameter was used. We were able to obtain a very sharp diffraction peak shown in Figure 4 with $\Delta d/d = 0.0637\%$. Since the resolution of the normal sample with the 1/2 inch PSDs system is about $\Delta d/d = 0.1\%$, it is evident that the improvement of the resolution has been achieved by the 8 mm PSDs system. All detectors of the backward bank of SuperHRPD were replaced with this new detector system during the beam shut down period in the summer of FY 2013.

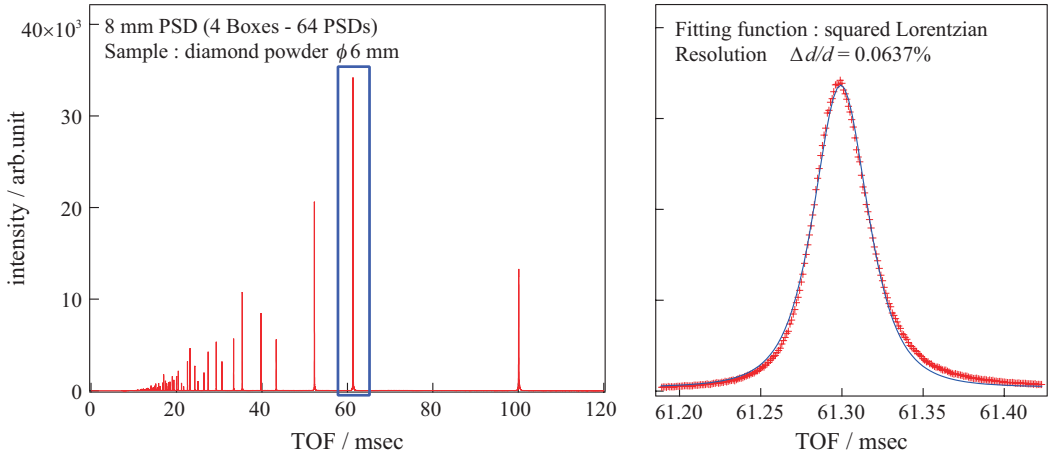

Figure 4. Neutron diffraction pattern of a diamond powder sample using the new detector system (left). The peak fitting result by squared Lorentzian function (right).

S. Torii[1,2], M. Yonemura[1,2], and T. Kamiyama[1,2]

[1]*Neutron Science Section, Materials and Life Science Division, J-PARC Center;* [2]*Institute of Materials Structure Science, KEK*

Development of an Advanced Special Neutron Powder Diffractometer under Extreme Environment for Materials

1. Introduction

The demands of batteries as energy storage have increased with the advancement of the technologies for compact and portable devices such as laptop computers and mobile phones. Additionally, hybrid vehicles (HV) and pure electronic vehicles (EV) using high performance batteries are designed to reduce the consumption of fossil fuels and contribute to the realization of a low carbon society. The lithium ion battery is a promising battery system candidate as energy storage for both small and large cells. However, the lithium ion battery is still under development to resolve the issues of cyclic life and high temperature use. Its capacity is also limited and needs to be improved.

The lithium ion battery works by lithium ion transfer between cathode and anode. The reactions of both electrodes are based on the de / intercalation of lithium ion from / into the materials of electrodes. When the lithium ions intercalate into material, the crystal structure changes. The information about the structural change of the electrode and the location of lithium ions in the crystal structure leads to improvements in the present lithium ion battery and the invention of an out-of-the-box battery.

In order to clarify at an atomic level the structures of cathode, anode and the interface between electrode and organic electrolyte, a new neutron powder diffractometer, SPICA, has been designed and constructed as one of the state-of-the-art measurement apparatuses. In comparison with X-ray, the neutron is well known to be a more powerful probe to get information about the location and movement of light elements such as hydrogen and lithium atoms. Therefore, the advantage of neutron diffraction will allow us to acquire more knowledge about the location and movement of lithium ions as well as the change of the atomic arrangement in the cathode, anode and electrolyte solution.

2. Present status

Several reference materials such as Si, CeO_2 and TiO_2 provided by the National Institute of Standards and Technology (NIST) were measured to confirm the reliability of the SPICA instrument. Figure 1 shows the typical diffraction data from the reference material, NIST TiO_2 powder, using all banks. All diffraction profiles indicated low background and good signal-to-noise ratio. A typical measurement time was 0.5 hr for 0.5 g of NIST Si powder at 25/3 Hz repetition.

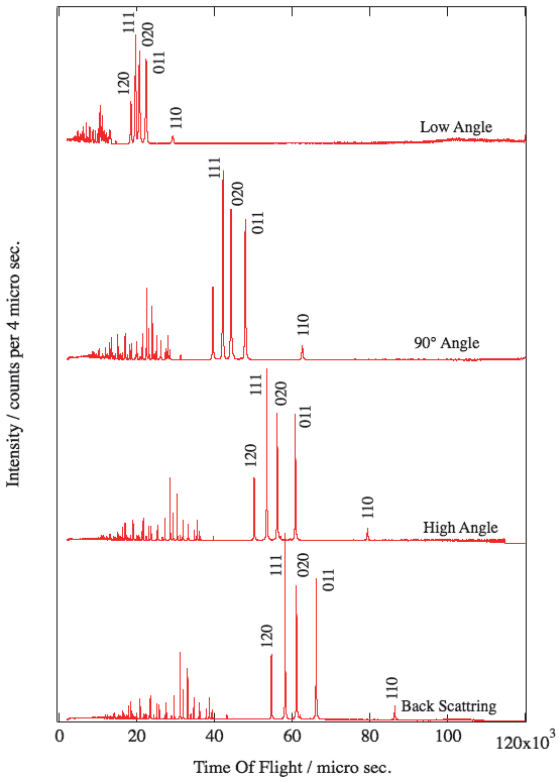

Figure 1. Diffraction profiles of the TiO_2 powder at low angle, 90° angle, high angle and back scattering banks.

Figure 2 shows the Rietveld refinement patterns of CeO_2 collected by back scattering and 90° banks. The observed intensities are consistent with those calculated from the structure model, which indicates the capability and reliability of the diffractometer. In

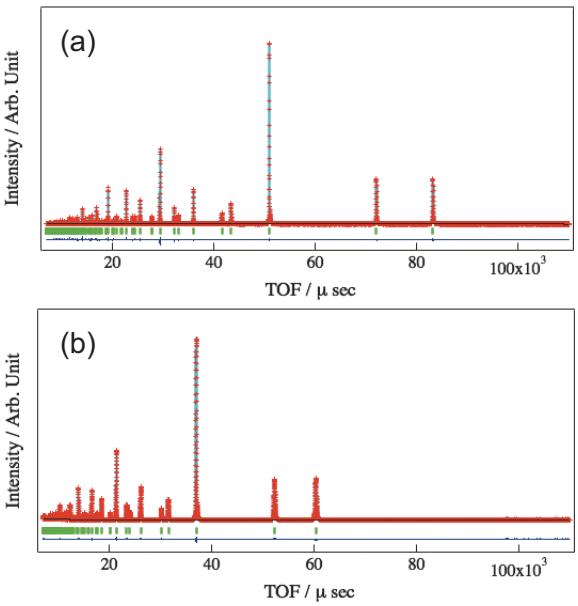

Figure 2. Rietveld refinement pattern of NIST CeO_2 on SPICA. Observed (red +), calculated (solid light blue line) and difference (dark blue line) data are plotted. (a) Back scattering banks and (b) 90° banks (air scattering chambers).

addition, SPICA gives expectation of structure refinement by in situ measurement. Figure 3 shows a typical example of *in situ* measurement for a commercialized Li-ion battery (LIB). The high capacity cell with nominal capacity 3000 mAh was charged and discharged between 4.25 and 2.5 V at currents of 0.1 A in constant current - constant voltage (CC-CV) charging and in constant current (CC) discharging. In situ neutron diffraction data were collected under cycle rates of 1/30 C in discharging and charging processes. The structural change of the material, which is dependent on the lithium content, is clearly observed. The lattice parameters for the anode and cathode materials as a function of the lithium content were extracted from

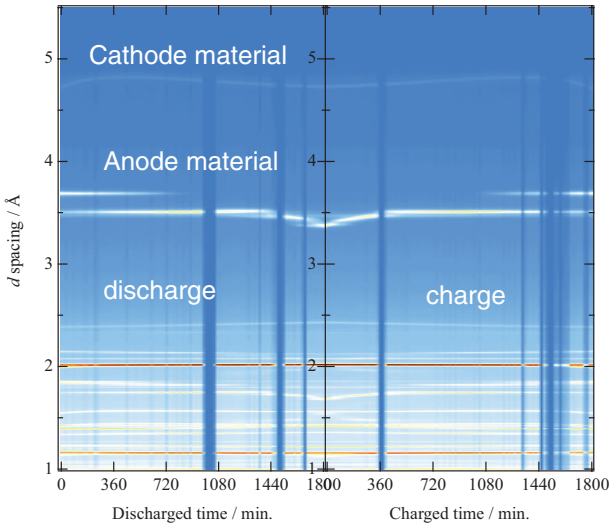

Figure 3. The changes of diffraction profiles in an 18650-type lithium battery as a function of discharge / charge time.

the diffraction pattern. The structure refinement is in progress. This promising result shows that SPICA has a high potential of structure refinement for in situ measurement.

The commissioning of the SPICA diffractometer is still continuing. Simultaneously, various kinds of test measurement using conventional samples have been carried out by the NEDO project members.

Acknowledgements

This work was supported by the Research and Development Initiative for Scientific Innovation of New Generation Batteries (RISING) project of the New Energy and Industrial Technology Development Organization (NEDO). The neutron scattering experiment was approved by the Neutron Scattering Program Advisory Committee of IMSS, KEK (Proposal No. 2009S10).

M. Yonemura[1,2], T. Fukunaga[3], K. Mori[3], T. Kamiyama[1,2], M. Nagao[2], Y. Ishikawa[2], S. Torii[1,2], Y. Onodera[3], R. Tomiyasu[2], H. Asano[2], T. Sakuma[4], T. Ishigaki[5], A. Hoshikawa[5], K. Aizawa[1], S. Harjo[1], K. Kino[6], R. Kanno[7], M. Hirayama[7], Y. Idemoto[8], N. Kitamura[8], H. Arai[9], and Y. Uchimoto[10]

[1]Neutron Science Section, Materials and Life Science Division, J-PARC center; [2]Institute of Materials Structure Science, KEK; [3]Research Reactor Institute, Kyoto Univ.; [4]Insitute of Appl. Beam Sci., Ibaraki Univ.; [5]FRC, Ibaraki Univ.; [6]Graduate School of Eng. Hokkaido Univ.; [7]Interdisciplinary Graduate School of Sci. and Eng. Tokyo Institute of Tech.; [8]Faculty of Sci. and Tech., Tokyo Univ. of Science; [9]RISING Project, Kyoto Univ.; [10]Graduate School of Human and Environmental Studies. Kyoto Univ.

BL10: NOBORU

In FY 2013, 9 general use proposals were carried out at NOBORU, but three of them have not been completed due to the Hadron incident on May 23. This year, we planned to study temporal changes in neutronic performance before and after the replacement of the Mercury target at the long-shutdown period, but unfortunately we failed to do it. During the shutdown period, we performed remodeling of the beam-line components.

A temporary light shutter, composed of 10 cm thick polyethylene and 2 cm thick ^{6}LiF tile, has been used in the experimental room of BL10 to prevent radioactivation of the imaging camera during data transportation time. The light shutter was installed at permanent position in the beam transport section of BL10 in November. It also works as a filter, which high-energy neutrons and γ-rays penetrate. A beam duct in the beam transport section, shown in the Fig.1, was also replaced by the new one at the same time. The new duct has a cross section of 112 mm^2 with a Gd_2O_3 painted scrapers opening of 100 mm^2. The old duct has a cross section of 100 mm^2, whose inner surface reflects cold neutrons significantly. These undesirable neutrons will be absorbed by the scrapers of the new duct.

Periodical measurement

To investigate neutronic performance as well as to keep JSNS in optimum operating condition in J-PARC, we periodically measured the neutron spectra at BL10 in the several conditions of instrumental devices, such as rotary collimator, B_4C slits, and so on. Figure 2 shows an example setting for the periodical measurement at BL10. Figure 3 shows the neutron spectra measured by the same settings in May, 2013 and in Feb., 2014. The proton beam power in each measurement was about 300 kW. The hole size of rotary collimator and adjacent aperture size of B_4C slit 1 were changed between (a) and (b), whereas the other settings were the same in each experiment. A little difference in the neutron intensity was observed after normalization. The energy-dependent attenuation ratio would be attributed to the increased air path of 1.1 m after the remodeling of the beam-line components.

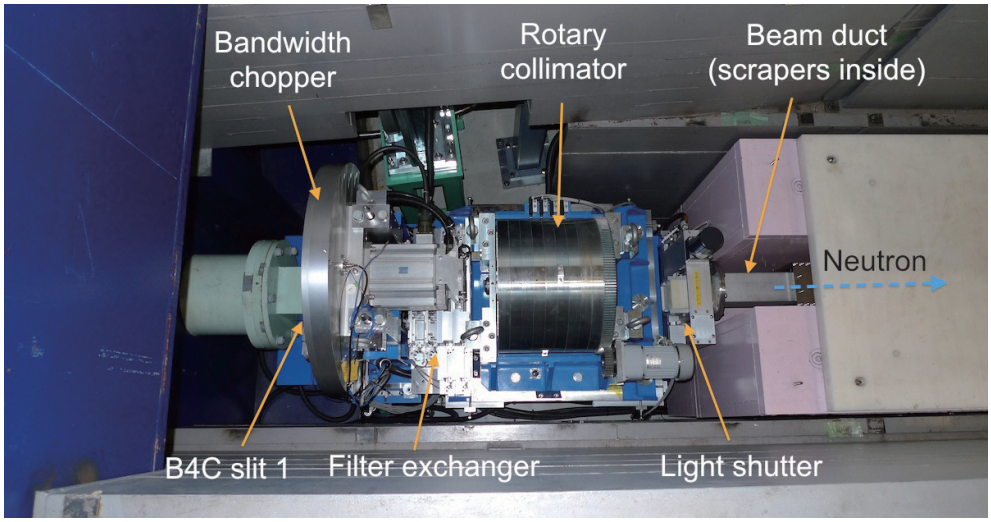

Figure 1. Picture of the beam line components of BL10 at around 8 m position.

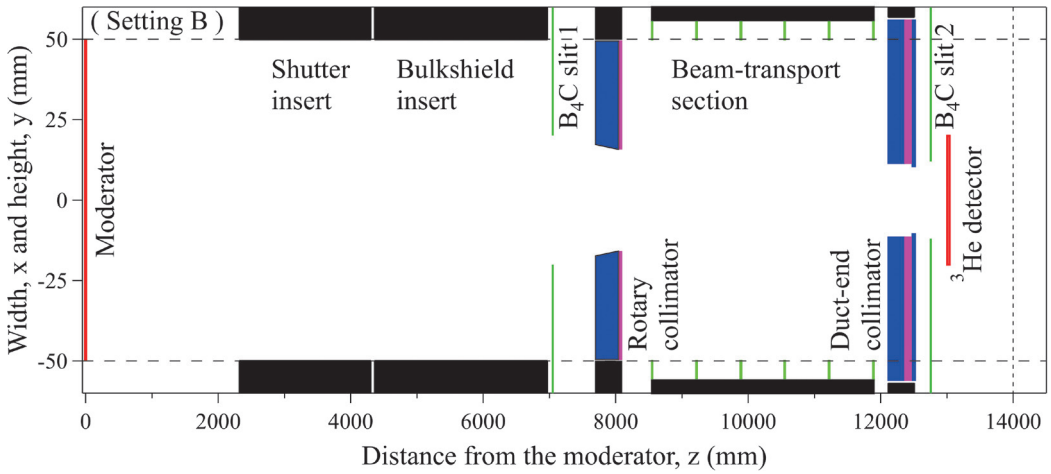

Figure 2. Beam-line components of BL10 and the collimation setting for the periodical measurement.

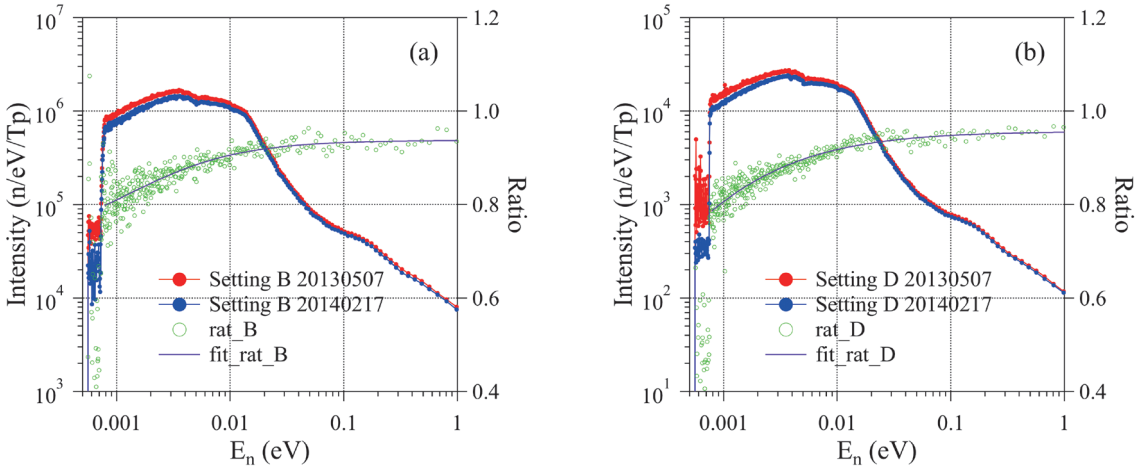

Figure 3. Measured neutron spectra in May, 2013 and Feb. 2014 in different collimation setting.

References

[1] M. Harada *et al.*, to be submitted to Proceedings of the J-PARC Symposium 2014.

K. Oikawa, and M. Harada
Neutron Science Section, Materials and Life Science Division, J-PARC center

BL11: High-Pressure Neutron Beamline PLANET Opened for General Users

1. Introduction

The PLANET is the beamline dedicated for high-pressure diffraction experiments. The construction of the beamline was completed in JFY 2012, and the beamline was opened to general users from JFY 2013. Here, we report on recent results and developments we are working on now.

The beamline has a high resolution and wide accessible *d*-range enough to conduct structure analysis of crystalline and liquid materials [1-2]. The severe incident and receiving collimators make it possible to obtain the signal only from the sample surrounded by many materials, such as a sample container, heater and pressure transmitting medium. Appreciating those benefits, many users from various science fields are now coming to use the PLANET (Fig. 1).

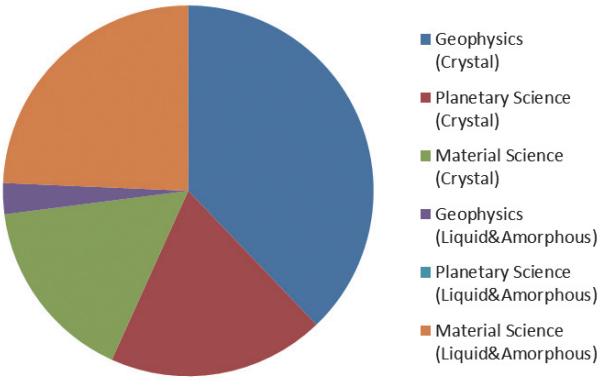

Figure 1. Statistics of the users from various science fields from 2013 to 2014.

2. Typical example

Structure analysis of crystalline materials

Figure 2 shows the temperature dependence of the neutron diffraction patterns of portlandite $Ca(OD)_2$ at 3 GPa. Thanks to the radial collimators, no contamination from a sample container and a heater was observed and all the peaks were assigned as portlandite. The quality is high enough to conduct Rietveld analysis. The detailed results from the structure analysis will be shown elsewhere.

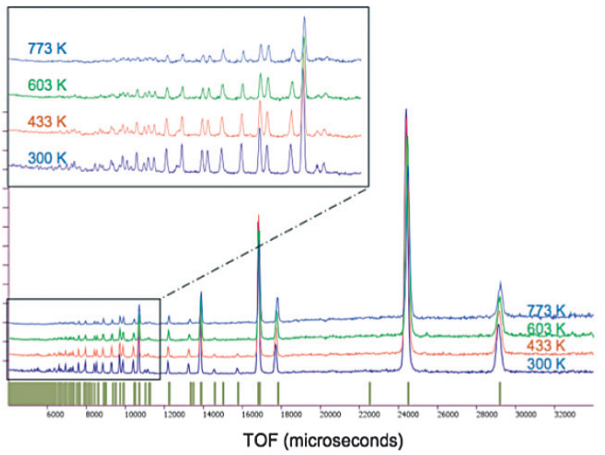

Figure 2. Temperature dependence of the diffraction pattern of $Ca(OD)_2$ at 3 GPa.

Structure analysis of amorphous materials

The PLANET offers the opportunity to investigate the structure of the amorphous and liquid materials under high pressure. To test the feasibility, we took the data for SiO_2 glass. First, we checked the consistency between our ambient data and the widely accepted one, and confirmed it. Figure 3 shows the structure factor at high pressures up to 10 GPa obtained after several corrections. The pressure dependence indicates marked changes in the intermediate range order, which is consistent with the previously reported high-pressure behavior. The details will be shown elsewhere.

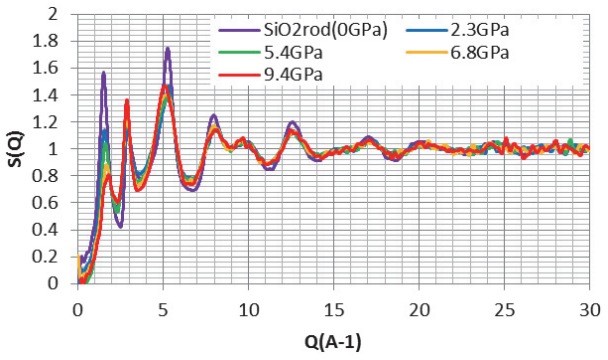

Figure 3. Pressure dependence of the structure factor S(Q) of the SiO_2 glass up to about 10 GPa.

3. Extension of the accessible *PT*-conditions using 6-8 type cell

The 6-6 type cell has been used successfully in the 6-axis multi-anvil press (ATSUHIME), but the available *PT* conditions were limited to below 10 GPa and 2000 K. To extend the accessible *PT* range, we applied a 6-8 type cell assembly to ATSUHIME. The cell consists of eight second-stage anvils, gaskets and a furnace assembly (Fig. 4). The cubes of a SiC sintered diamond with truncated edge length (TEL) of 5 mm were used as the second stage anvils, where the initial volume of the sample was 6 mm^3.

We tested the pressure generation using an internal pressure standard of NaCl, and confirmed the generation of 16 GPa at 1600 kN based on the equation of state of NaCl (Fig. 5). The heating test was also conducted at up to 1273 K at 1600 kN. During the heating to 1073 K, the pressure was decreased to 14 GPa due to the relaxation of the gasket materials. The 6-8 type cell allows us to investigate the structure of the material under the pressure of above 10 GPa. Figure 6 shows an example, the diffraction pattern of $CaSiO_3$ perovskite that is one of the major components of the Earth's lower mantle. This phase is stable only at pressures above 14 GPa and unquenchable to ambient condition, thus the

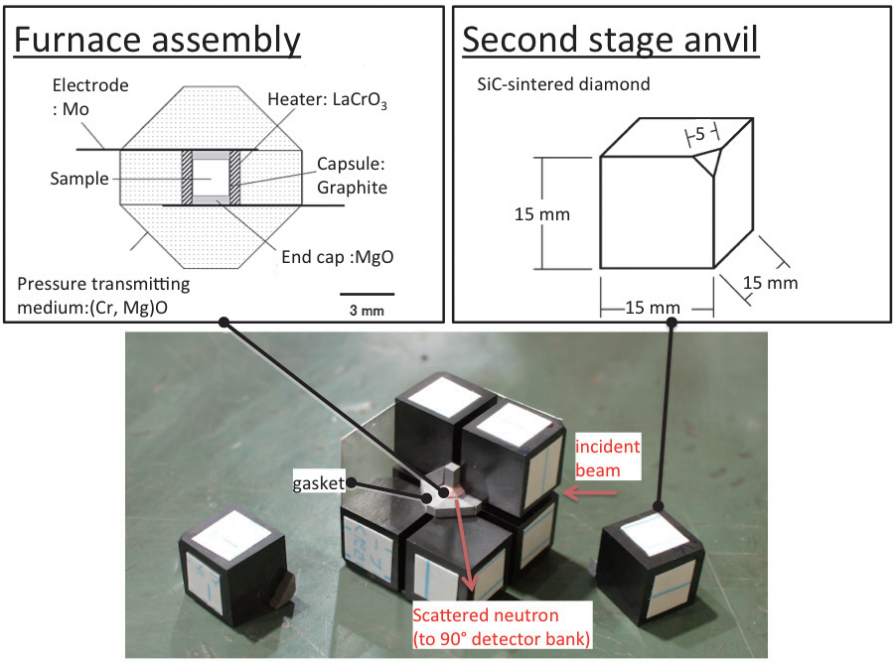

Figure 4. Photograph of a 6-8 type cell and schematic drawings of the furnace assembly and the second stage anvil.

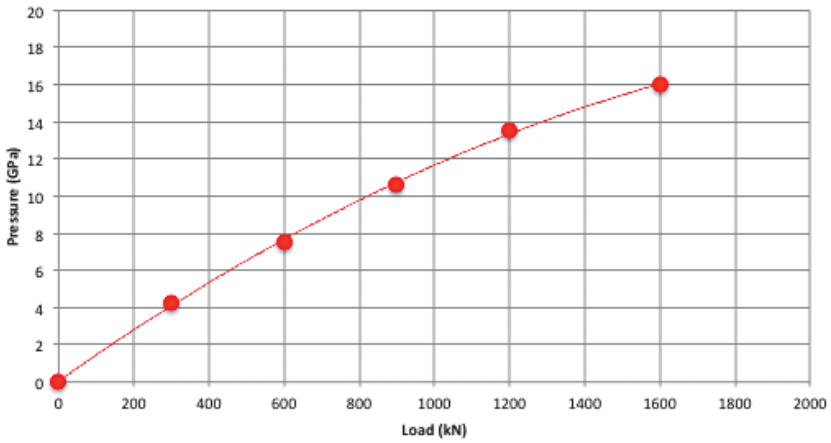

Figure 5. Pressure generation curve for a 6-8 cell with TEL of 5 mm. The horizontal axis is the load applied to the bottom ram.

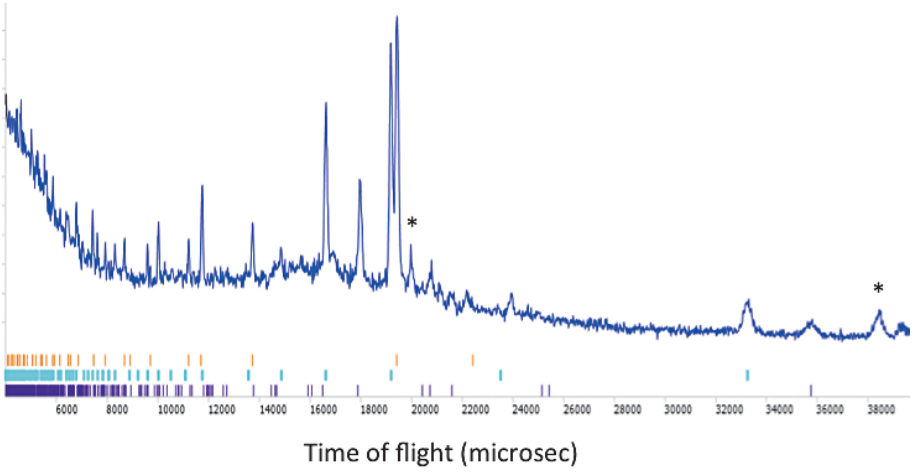

Figure 6. Diffraction pattern of $CaSiO_3$ perovskite obtained at 15.4 GPa with a 6-8 cell. The tick marks show the calculated peak positions for the cubic $CaSiO_3$ (cyan), MgO (orange) and $LaCrO_3$ (purple). The stars indicate the peaks that can be indexed with the orthorhombic cell.

in-situ experiment is necessary. Previous X-ray diffraction and theoretical studies showed that the unit cell is not cubic, but the detailed crystal structure is yet to be revealed. In this study, the calcium perovskite was successfully synthesized from the starting material of wollastonite under pressure by keeping it at 1373 K for 3 hours. The diffraction was taken at 15.4 GPa for 36 hours after the temperature decreased to room level. We found marked peaks, which had not been observed in the previous x-ray studies, thanks to the different scattering length of Ca, Si and O for neutrons. Those are indexed with an orthorhombic cell, and the detail refinement of the crystal structure is now in progress.

References

[1] H. Arima, T. Hattori, K. Komatsu, J. Ab, W. Utsumi, H. Kagi, A. Suzuki, K. Suzuya, T. Kamiyama, M. Arai, and T. Yagi, J. Phys. Conf. Ser., **215** (2004) 023025.

[2] T. Hattori, A. Sano-Furukawa, A. Yamada, H. Arima, W. Utsumi, H. Kagi, MLF Annual Report, (2012) 96–97

Acknowledgement

Authors thank to Dr. Nagai for kindly offering the data of portlandite.

T. Hattori[1,2], A. Sano-Furukawa[1,2], K. Funakoshi[3], J. Abe[3], and S. Machida[3]

[1]Neutron Science Section, Materials and Life Science Division, J-PARC Center; [2]Quantum Beam Science Center, JAEA; [3]Neutron R&D Division CROSS-Tokai

High Resolution Chopper Spectrometer at BL12

1. Introduction

The High Resolution Chopper Spectrometer (HRC) is being operated at BL12 to study dynamics in condensed matters with high resolutions using relatively high energy neutrons. A research project using the HRC is being conducted to observe wide range of correlated electron systems. We performed experiments concerning these subjects and introduced instrumental improvements.

2. Instrumentation

An experimental control environment was developed to combine the measurements of neutron counts with the control of devices such as choppers, temperature controllers, goniometers, vacuum system, and so on, as shown in Fig. 1 [1]. The HRC Control Platform was developed and installed on the computer named DAQ-OP (DAQ operator). The HRC Device Control Software controls the devices as well as the DAQ middleware (DAQ MW) via Control LAN through the Platform. The HRC Experiment Control Software executes a sequence composing begin/end of measurements and controls of devices. At present, almost all the devices on the HRC can be controlled through this platform and their operations connected with the data acquisition (begin/end of measurements). In order to optimize the computing environment, the composition of the computers was improved.

We also developed software to analyze single crystal sample data as well as powder sample data. The analyzed data can be transformed to the standard Mslice format for convenience of the users. The process for alignment of the sample crystal became very easy. The excitation spectra in the three-dimensional system on the four-dimensional energy-momentum space can be also measured by rotating the sample crystal axis, and visualized.

In order to cool down the sample stably, a GM-type refrigerator was installed. This refrigerator shows a good cooling performance by improving the

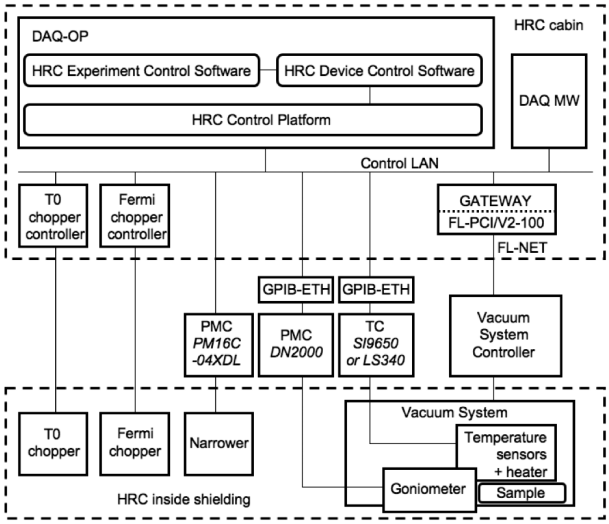

Figure 1. Experimental control environment on HRC. PMC, TC, GPIB-ETH represent a pulse motor controller, a temperature controller, a GPIB/Ethernet converter, respectively. The vacuum system is accessible through the Gateway server and the FL-net. The incident neutron beam is controlled by the Fermi chopper and the narrower, and the sample environment such as the temperature and the crystal angle is controlled. The operation status of the T0 chopper and the vacuum system is monitored.

radiation shielding, and we have confirmed that the lowest temperature available by using this refrigerator is 3 K. A cryomagnet to apply a magnetic field of up to 14 T to the sample was designed, manufactured and delivered. We started the commissioning at the Guide Hall of JRR-3M, and confirmed that it was successfully operated with the maximum magnetic field of 14 T.

During the partial mounting of the new PSDs, a vacuum leakage occurred in March 2014. To find the leakage point, all the thin Al windows were removed and replaced by thick plates, because of the safety regulations. The low angle detectors mounted outside the vacuum were removed. Fortunately, the leakage points were at the vacuum connections of PSDs, not at the Al windows. At present, although the high vacuum has been recovered, the low angle detectors mounted outside the vacuum are

still removed. However, the PSDs for the neutron Brillouin scattering (NBS) experiments are mounted in the vacuum and operational.

3. NBS Experiments

NBS is an advantageous method for observing coherent excitations in non single-crystal materials. Owing to the kinematic constraints of neutron spectroscopy, incident neutron energy in the sub-eV region with a high resolution is necessary, and the scattered neutrons need to be detected at very low scattering angles, for measuring scattering in the forward direction near (000). On the HRC, the background reduction at low angles down to 0.5° successfully showed that the NBS method was feasible. As we previously reported, spin waves in a polycrystalline ferromagnet $La_{0.8}Sr_{0.2}MnO_3$ (T_C = 316 K) observed on the HRC well agreed with the previous result from the single crystal sample, as shown in Fig. 2(a). This shows the feasibility of the NBS on the HRC.

The spin waves in a polycrystalline ferromagnet, $SrRuO_3$ (T_C ~ 160 K), were similarly measured. For this material, a large single crystal suitable for inelastic neutron scattering experiments has not yet been synthesized. As shown in Fig. 2 (a), the spin wave dispersion relation was well fitted to $E = E_0 + DQ^2$ with an apparent energy gap E_0. The possible reason for this characteristic feature is an induced spin anisotropy from a spin-orbit coupling acting on the Ru 4d orbital.

$Nd_2Fe_{14}B$ is a well-known strong permanent magnet, and all spins are aligned along the c*-axis at room temperature. In a previous inelastic neutron scattering experiment using a single crystal, a spin wave branch was detected only along the c*-axis around (002). We performed NBS experiments in a $Nd_2Fe_{14}{}^{11}B$ polycrystalline sample at room temperature. The observed peak positions were on the dispersion curve along the c*-axis reported in the previous experiment (Fig. 2(b)).

Phononic excitations in a liquid D_2O were measured at room temperature on the HRC. The excitation peaks showed broad energy spectra. The observed dispersion relation well agreed with that for the fast sound observed in the previous experiment at $Q \geq 0.35$ Å^{-1} using a steady state neutron source. The experiment on the HRC extended the data points to the lower Q (Fig. 2(c)).

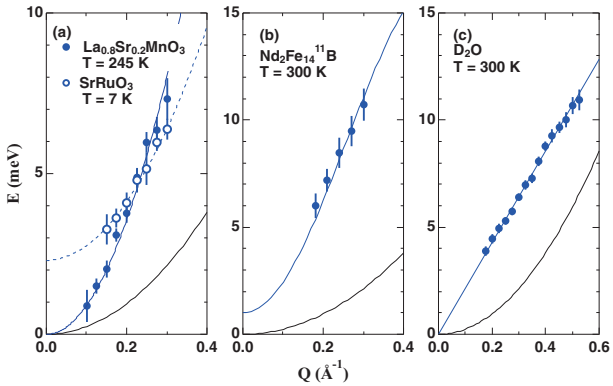

Figure 2. Dispersion relations obtained by the NBS experiments on the HRC: spin waves in $La_{0.8}Sr_{0.2}MnO_3$ and $SrRuO_3$ (a), spin waves in $Nd_2Fe_{14}{}^{11}B$ at 300 K (b), and phononic excitations in D_2O at 300 K (c). The blue solid lines are determined by previous experiments. The dashed line in (a) is a fitted curve to $E = E_0 + DQ^2$ with constants E_0 and D. The solid black lines are the upper boundary accessible by using conventional spectrometers with the lowest angle of 5°.

References

[1] S. Itoh, T. Yokoo, D. Kawana, H. Yoshizawa, T. Masuda, M. Soda, T. J. Sato, S. Satoh, M. Sakaguchi and S. Muto, J. Phys. Soc. Jpn. 82 SA033 (2013).

[2] S. Itoh, T. Yokoo, D. Kawana, Y. Kaneko, Y. Tokura, M. Fujita, K. Yoshida, K. Saito, N. Inami, Y. Takeichi, K. Ono, Y. Endoh, J. Phys.: Conf. Series 502 012043 (2014).

S. Itoh[1,2], T. Yokoo[1,2], T. Masuda[3], H. Yoshizawa[3], M. Soda[3], Y. Ikeda[3], S. Ibuka[2], T. Asami[3], R. Sugiura[3], D. Kawana[3], T. Shinozaki[3], and Y. Ihata[4]

[1]Neutron Science Section, Materials and Life Science Division, J-PARC center; [2]Institute of Materials Structure Science, KEK; [3]The Institute for Solid State Physics, The University of Tokyo; [4]Technology Development Section, Materials and Life Science Division, J-PARC Center

BL14 AMATERAS

1. Introduction

AMATERAS (Fig. 1) had five staff members after Dr. Chiba-Kamoshida joined as outsourcing staff in April 2013, which resulted in more substantial user support after eight months of the beam-off period of J-PARC. We made efforts to improve the instrumental activities, such as an upgrade of the beam-transport section and on-beam commissioning of several new devices as mentioned below. It should be also reported here that two works related to AMATERAS received awards from the Japanese Society for Neutron Science (JSNS), namely the development of a chopper spectrometer with a pulse-shaping chopper at a pulsed source by Dr. Nakajima et al. (Fig. 2) and the development of a model-free analysis method on quasi-elastic neutron scattering and its application to liquid water by Dr. Kikuchi [1].

Figure 1. Photo of AMATERAS (in September, 2013).

2. Instrumental activities

In JFY2013, the following instrumental activities were carried out: 1) commissioning of sample environment devices, 2) replacement of defective components and 3) upgrade of components. Also, regular maintenance of components and regular performance tests were carried out as routine works. 12 days of instrument-group-use beam-time were spent for on-beam parts of the above activities.

In the beginning of 2013A, an operation test of a BL-common 7 T cryomanget on AMATERAS was carried out (Fig. 3). Magnetic fields of up to 4 T were successfully achieved. Since we were concerned that the scattering chamber of AMATERAS, which is made of steel, might cause serious damage to the magnet due to magnetic force, we did not try to apply an even higher field. As we expected, huge background from the outer vacuum chamber, radiation shields and a support ring for the magnet was observed. Still we could observe a field dependence of magnetic excitations in a powder sample by subtracting background data obtained from an empty scan.

During the long shutdown period of MLF, the beam-transport section was upgraded (Fig. 4). The discrepancy between the intensity expected from

Figure 2. Photo of the award ceremony at the JSNS meeting.

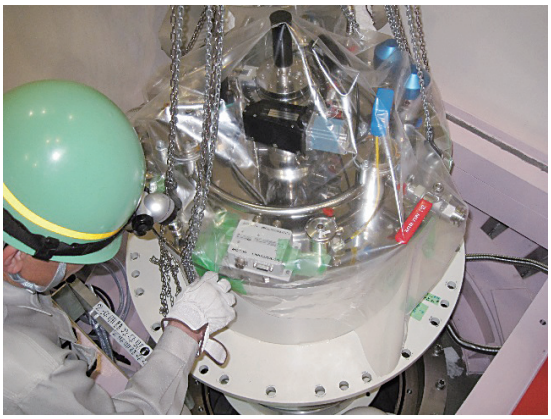

Figure 3. A BL-common 7 T cryomanget on AMATERAS.

Figure 4. Re-alignment of AMATERAS beam-transport.

simulation and that observed in real measurements was one of the serious problems of AMATERAS. Misalignment of guide tubes and performance of a part of mirrors had been suspected to be the source of this problem. Therefore, we replaced the mirrors (8.6 m in length) and re-aligned full-part of the beam-transport. The performance after this upgrade was checked in the 2013B period. The intensity became 1.2 times larger in a low-energy region (E_i < 5 meV) and nearly twice in a high-energy region (E_i > 80 meV) compared to the previous intensity. However it is still lower than the simulated intensity. We continue our investigation, including checking the validity of the simulation.

As with the other major instrumental activities, replacement of a defective detector tube, installing a Cd film attenuator, and background reduction study were done in JFY 2013.

3. User Program

There was a wide variety in the research fields of the proposals on AMATERAS. In the 2013A and 2013B periods, 14 general use proposals were accepted, and six proposals were listed on the reserved subjects. We also accepted two project use proposals, which are 'Study of structure and electronic properties of functional materials at BL14' (PI: T. Masuda) and 'Project research on structure and dynamics of protonic, superionic and amorphous functional materials using AMATERAS' (PI: Y. Inamura), and one element strategy use proposal, 'Neutron-scattering research on element-strategy project for electronic materials' (PI: Y. Murakami). Due to the incident at the Hadron Experimental Facility, five general use experiments were cancelled or interrupted. The beamtime for the project use and element strategy use experiments were also reduced.

Reference

[1] T. Kikuchi *et al.*, Phys. Rev. E 87, 062314 (2013).

K. Nakajima, S. Ohira-Kawamura, T. Kikuchi, and Y. Kawakita
Neutron Science Section, Materials and Life Science Division, J-PARC Center

Upgrading of TAIKAN and Needs of the Users

The small and wide angle neutron scattering instrument TAIKAN (BL15) has been developed and upgraded to analyze microstructures or hierarchical structures of substances in various scientific fields precisely and efficiently with a 1 MW spallation neutron source in J-PARC. In FY2013 these activities, user support, and research activities were done at TAIKAN by the staff shown in Fig. 1, as well as by other staff.

The detector system of TAIKAN is composed of 5 detector banks: the small-, middle-, high-, ultra-small-angle, and backward detector banks. On the small-angle detector bank in a vacuum scattering chamber, 128 ^{3}He PSD tubes were additionally installed. The numbers of ^{3}He PSD tubes then increased to 760, 304, 104, and 48 for the small-, middle-, high-angle, and backward detector banks, respectively. Figure 2 shows a photo of the small-angle detector bank after installing the ^{3}He PSD tubes.

The software for data analysis was newly developed by Y. Inamura and T. Ito, *et al*. in order to solve completely the problems with the reliability and efficiency of the previous software. Figure 3 shows one of the windows of the new software. The window shows a 3D image of the detector arrangement and scattering data of a standard sample, silver behenate.

Figure 1. Group photo of the staff in charge of TAIKAN.

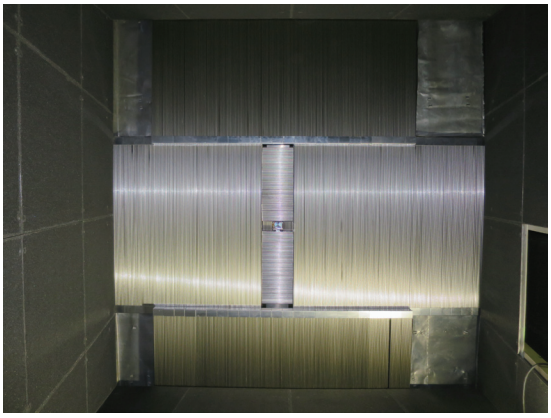

Figure 2. Photo of the small-angle detector bank.

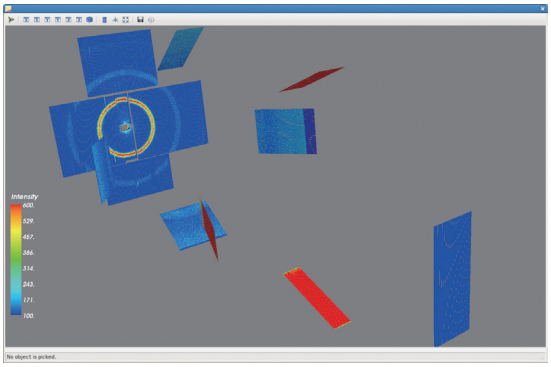

Figure 3. 3D image of the detector arrangement and scattering data drawn by the new software. The data shows the scattering from a standard sample, silver behenate.

A T0 chopper was installed just downstream of the first disk chopper in order to suppress the high-energy neutrons and γ-rays generated at the neutron source. The rotational frequency of the chopper is usually 25 Hz, but 50 Hz can also be chosen.

Figure 4 shows the statistics of the application for using TAIKAN in the period from 2011B to 2014A. In the scientific field of the application, “Soft matter, Chemistry” is the most numerous at 45%. There are other scientific fields with high percentages, which are “Electronic, Magnetic”, “Structural”, “Biology, Life”, “Environment, Energy”, and “Instrument”, where “Structural” denotes structural materials such

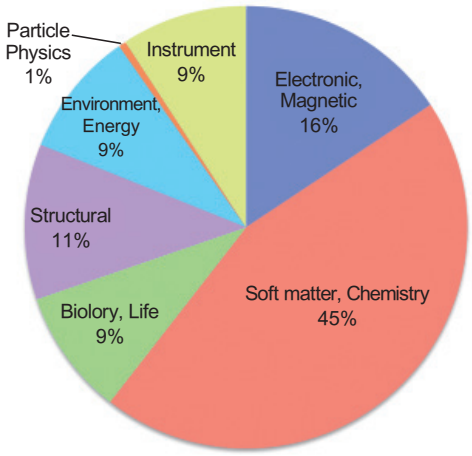

Figure 4. The scientific applications proposed to TAIKAN in the period from 2011B to 2014A.

as steels, “Environment, Energy” denotes battery and catalyst materials, and “Instrument” denotes the development and upgrading of TAIKAN. Most SANS users are international users in the scientific field of “Soft matter, Chemistry”. However, among the applicants of TAIKAN, the percentage of those involved in other scientific fields is also high. This seems to reflect applicants’ needs for precise and efficient analysis of microstructures or hierachical structures of substances with TAIKAN.

In order to respond to the needs of users in various scientific fields, an electromagnet and a tensile load cell were introduced.

Figure 5 shows a photo of a 0.2Tesla-electromagnet for the experiment of electronic and magnetic substances. In order to cool a sample, a 4K-cryostat can be installed between the coils of the electromagnet. A horizontal magnetic field can be applied to the sample either along the beam direction or perpendicular to it.

Figure 6 shows a photo of a tensile load cell for the experiment of soft matters. A sample can be set inside a gas chamber. The initial interval between two chucks is 10 to 15 mm. The stroke is less than 100 mm. The tensile force is 1 N to 1 kN. The head speed is 0.01 to 100 mm/min. The temperature of the sample can be controlled between RT and 300°C.

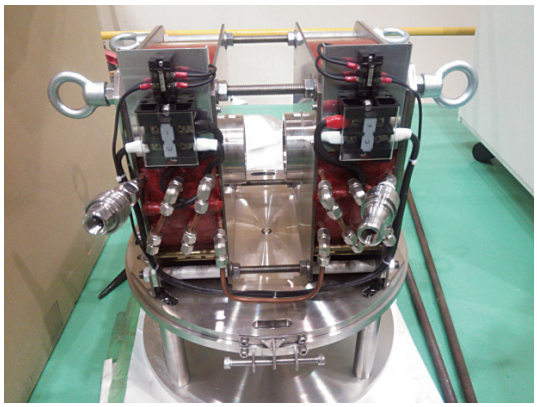

Figure 5. Photo of a 0.2Tesla-electromagnet.

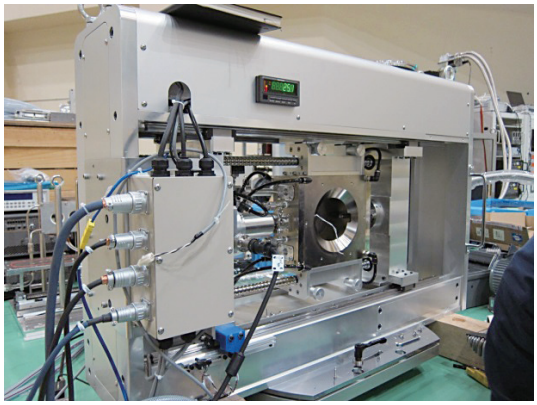

Figure 6. Photo of a tensile load cell.

J. Suzuki[1,2], S. Takata[1], K. Ohishi[2], H. Iwase[2], T. Tominaga[1,2], T. Morikawa[2], M. Sahara[2], T. Hosoya[1], Y. Inamura[1], T. Ito[2], T. Nakatani[1], T. Shinohara[1], T. Oku[1], K. Suzuya[1], K. Aizawa[1], M. Arai[1], T. Otomo[1,3], and M. Sugiyama[4]

[1]Neutron Science Section, Materials and Life Science Division, J-PARC Center; [2]Neutron R&D Division, CROSS-Tokai; [3]Institute of Materials Structure Science, KEK; [4]Research Reactor Institute, Kyoto University

Development of Sample Environments of SOFIA Reflectometer for Seconds-Order Time Slicing Measurement

Neutron reflectometry (NR) is very useful for investigations on structures of surfaces and buried interfaces composed of soft materials. A beam line (BL) 16 in J-PARC/MLF is dedicated for a horizontal type neutron reflectometer. At BL16, two downward neutron beams (2.22° and 5.71°) are transported from a coupled hydrogen moderator to irradiate free surface such as air-water interface. In order to realize a neutron reflectivity measurement with a high flux neutron beam at J-PARC/MLF as early as possible, we started to accept the neutron beam with "ARISA-II" reflectometer relocated from the KENS facility in 2008 [1]. However, the motion range of the slits, sample and detector stages were so short that only the 2.22° beam line at BL16 was used, because the components of ARISA were not designed for this beam line. This is a serious disadvantage in an air-liquid interface measurement to observe high-q region with a high incident angle.

To overcome this problem, ARISA-II was replaced with a brand-new reflectometer "SOFIA (SOFt-Interface Analyzer)" in 2011 through the collaboration between JST/ERATO and KEK [2, 3]. Figure 1 shows a schematic drawing of SOFIA in the experimental hutch. With the new slit, sample, and detector stages, we can accept the 5.71° beam line as well as the 2.22° beam line. This enables us to measure NR over wide scattering vector (q) region on free liquid surfaces. Also, the slit system can finely collimate to irradiate an area of 10 mm × 10 mm, a typical sample size for synchrotron light sources, with an angular resolution of 3%.

SOFIA reflectometer normally utilizes a white neutron beam with a wavelength band of 0.2 nm to 0.88 nm with repetition of 25 Hz produced by pulsed proton beam of J-PARC, in which the wavelength can be evaluated by a time-of-flight method using the relationship of a wavelength and mass of de Broglie wave:

$$\lambda = \frac{h}{mv},$$

where λ, h, m, and v are the wavelength, Planck's constrant, mass, and velocity, respectively. Using this method, we can scan a wide momentum transfer $q(= 4\pi\sin\theta/\lambda)$ at a time in a reflectivity profile, even with a fixed incident angle of neutron θ. This is the big advantage for time-slicing measurement because reflectivity profile with wide-q data can be acquired without any angle scan. For extending the q-region, SOFIA equips double frame mode in which the wavelength band of 0.2 nm to 1.76 nm is available by chopping every two neutron pulses. In order to take full advantage of wide wavelength band of SOFIA, we developed sample environments for time-slicing measurement: one is for solid-liquid contact measurement and the other one is for temperature-jump measurement.

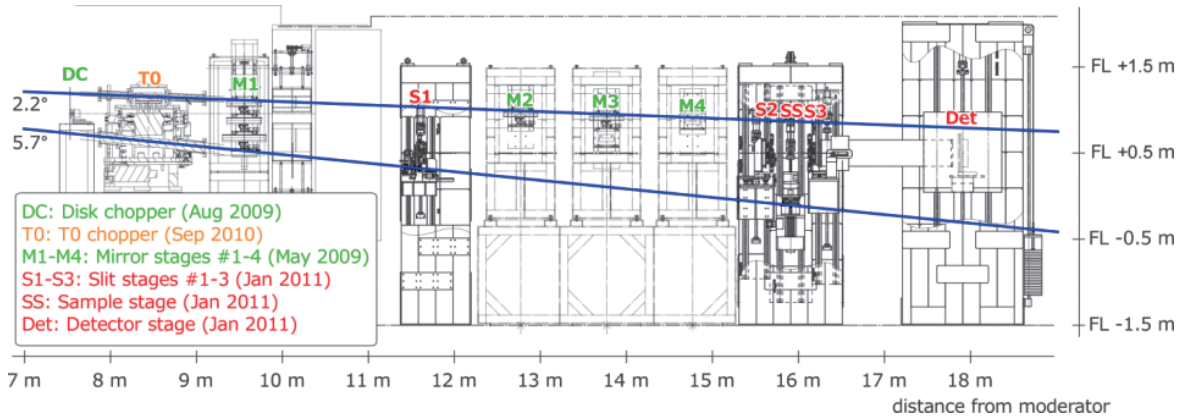

Figure 1. Side view of SOFIA reflectometer placed at BL16 in J-PARC/MLF.

Figure 2 shows a photograph of a sample cell for a solid-liquid contact measurement. A sample substrate with 3 inch in diameter is packed with a tub made of a borosilicate-glass. The tub has two apertures: one is to inject liquid and the other is for an air vent. The liquid sample in a container falls down by opening the electromagnetic valve, and then gets in contact with the sample substrate. To avoid evaporation of the liquid, the liquid container is connected with the air vent. This way, the liquid can be introduced remotely after sample position alignment.

Figure 3 shows a photograph of a sample cell for temperature-jump measurement. 100 W IR laser is introduced into an evacuable chamber through a rod and magnifying lenses to homogenize and magnify the laser, respectively. The size of the laser at the sample position is 2 inch in diameter, in which the sample is irradiated with the laser from the backside. The temperature of the sample is measured by a radiation thermometer, and the laser power is regulated by a PID controller. This way, the laser can be turned on remotely after sample position alignment.

First, we performed test workings with these sample cells and confirmed that both system can change the environments within 10 seconds. Next,

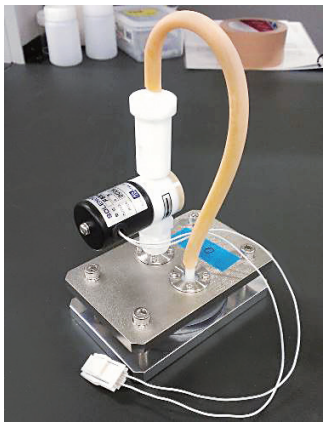

Figure 2. Photograph of a sample cell for a solid-liquid contact measurement.

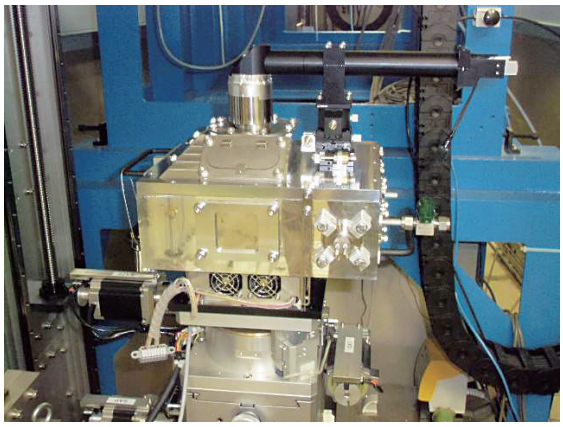

Figure 3. Photographs of a sample cell for a temperature-jump measurement.

we actually performed time-slicing measurements with phospholipid multi-layer on a Si substrate in contact with heavy water for a solid-liquid contact measurement, and with thin film of deuterated polystyrene on a Si substrate for a temperature-jump measurement. The test experiments were successfully done, and remarkably, the accumulation time of 20 seconds was enough in both cases [4].

In the future, the beam current of J-PARC will be upgraded to 1 MW, over 3 times higher than now. Moreover, we are planning to upgrade a detector that have high efficiency and count rate. These enable us to shorten the accumulation time by ten times, that is, second-order time slicing measurement will be available. Then, the sample environments developed in this study will play an essential role in achieving that.

References

[1] K. Mitamura *et al.*, J. Phys. Conf. Ser. **272** (2011) 012017.

[2] N. L. Yamada *et al.*, Euro. Phys. J. Plus **126** (2011) 108.

[3] K. Mitamura *et al.*, Polymer J. **45** (2013) 100.

[4] N. L. Yamada *et al.*, in preparation.

N. L. Yamada[1,2], K. Mitamura[3,4], N. Torikai[5], H. Sagehashi[2], S. Sato[2], H. Seto[1,2], T. Oda[6], M. Hino[6], M. Furusaka[7], and A. Takahara[3,4]

[1]Neutron Science Section, Materials and Life Science Division, J-PARC center; [2]Institute of Materials Structure Science, KEK; [3]JST, ERATO, Takahara Soft Interfaces Project; [4]Institute for Materials Chemistry and Engineering, Kyushu University; [5]Graduate School of Engineering, Mie University; [6]Research Reactor Institute, Kyoto University; [7]Department of Quantum Science and Engineering, Hokkaido University

BL17 Polarized Neutron Reflectometer, SHARAKU

1. Introduction

Neutron reflectometry is now widely recognized as an indispensable technique for development of nanotechnology and investigation in the field of surface and interface sciences. The polarized neutron reflectometer SHARAKU, named after the famous Japanese ukiyo-e printer, was installed at BL17 as the second reflectometer of the MLF.

SOPHIA, the first MLF reflectometer, constructed at BL16, can measure neutron reflectivity from the free surface and interface because BL16 is a beam line that delivers neutron beams downwards. On the other hand, BL17 is a normal horizontal beam line. Thus we designed SHARAKU as a polarized neutron reflectometer with vertical sample geometry.

The construction of SHARAKU was completed in the beginning of 2012, and then we started the commissioning and a small portion of the user program. Now SHARAKU is widely open to international users. However, we have been improving the reflectometer and making it user-friendly. In this article we report the progress achieved in this fiscal year.

2. Installation of a new vacuum chamber

We installed a new vacuum chamber in between a sample position and a detector bank. The chamber is composed of two cells along the beam line, and each cell has an elevator as shown in Fig. 1. An electromagnet to keep the neutron polarization is set on the elevator in the upstream cell, and a spin flipper and a spin analyzer are set on the elevator in the downstream cell. These elevators enable us to quickly and safely switch between the two setups for polarization and non-polarization analysis mode. We had to use a crane to mount and dismount the spin analyzer, and it took almost an hour without the elevators. But now the switching time is reduced to five minutes and all we have to do is to push a button on a touch panel of a controller. Figure 2 shows this new chamber.

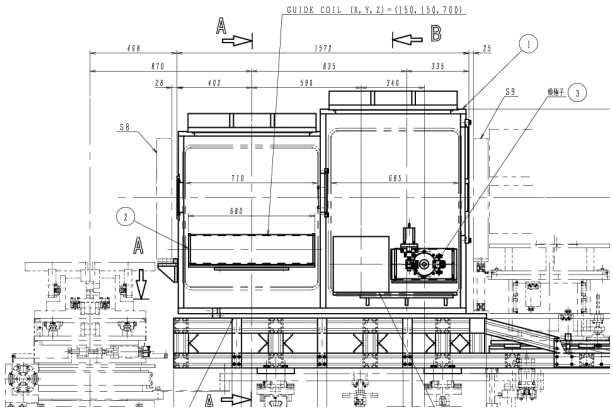

Figure 1. Cross sectional view of the newly installed vacuum chamber.

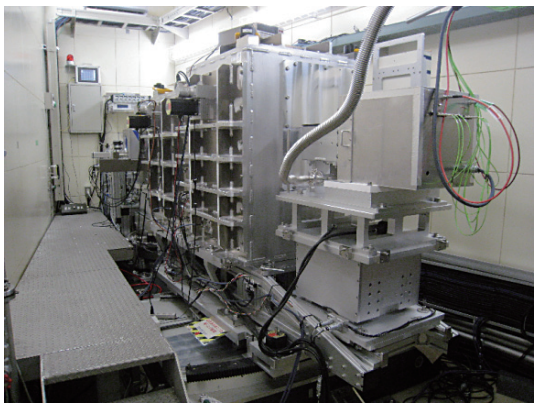

Figure 2. A picture of SHARAKU with the newly installed vacuum chamber and a multi-wire type position sensitive chamber (MWPC). This picture was taken at the detector side (downstream of the beam line).

3. Installation of a two-dimensional position sensitive detector

At the end of the 2013B term the main detector of BL17 was a ^{3}He tube without position sensitivity. We have prepared three types of two-dimensional (2D) position-sensitive detector (PSD) for a variety of advanced reflectometry applications, such as off-specular reflection, grazing incidence small-angle neutron scattering (GISANS), and grazing incidence diffraction (GID) measurements.

The first is a multi-wire type position-sensitive proportional chamber (MWPC). This detector has better spatial resolution than other detectors, high counting-rate, and high efficiency. The second is a 2D scintillation detector using a wavelength-shifting-fiber (WLSF) readout. The effective area is 256 mm $\times$ 256 mm with 4 mm $\times$ 4 mm spatial resolution. The last one is a scintillation detector based on a position-sensitive photomultiplier. The effective area is 100 mmϕ in diameter with 0.5 mm $\times$ 0.5 mm spatial resolution.

The performance of these detectors was evaluated using a DAQ system of BL17, and it was confirmed that all detectors performed satisfactorily as expected. Figure 3 displays a GUI panel for analysis of the 2D data obtained by the 2D-PSDs.

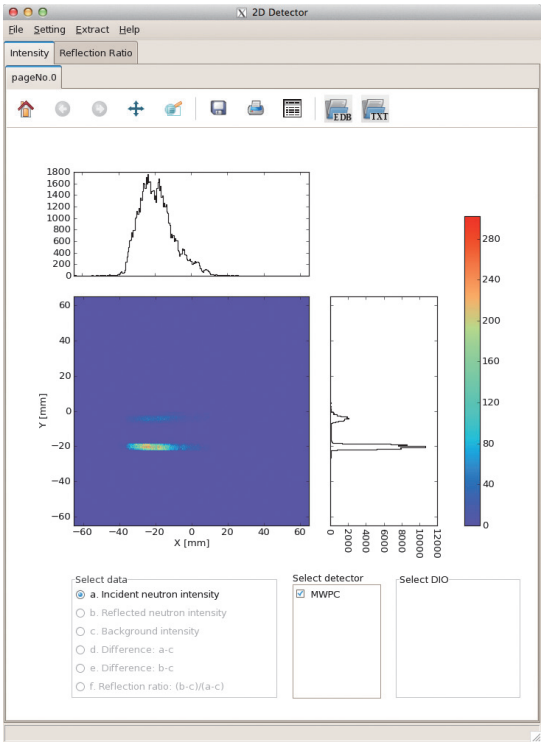

Figure 3. Two-dimensional intensity map of an incident and a reflected neutron beam and their profiles along two diagonal directions extracted from data taken by a multi-wire type position-sensitive chamber (MWPC).

References

[1] M. Takeda *et al.*, *Chinese J. Phys.* **50** (2012) 161.

[2] K. Toh, T. Nakamura, K. Sakasai, K. Soyama, and H. Yamagihshi, J. of Phys.; Conf. Ser. **528** (2014) 012405.

M. Takeda[1,2,3], D. Yamazaki[2], K. Soyama[2,3], K. Aizawa[2], M. Arai[2], Y. Inamura[2], T. Nakatani[2], S. Sakasai[2], K. Toh[2], H. Yamagishi[2], T. Nakamura[2], N. Miyata[4], M. Mizusawa[4], K. Akutsu[4], S. Kasai[4], and M. Katagiri[5]

[1]Quantum Beam Science Center, JAEA; [2]Materials and Life Science Division, J-PARC Center; [3]Department of Research Reactor and Tandem Accelerator, JAEA; [4]Neutron R&D Division, CROSS-Tokai; [5]Frontier Research Center for Applied Atomic Science, Ibaraki University

BL18: Current Status of SENJU

SENJU is a TOF single-crystal neutron diffractometer designed for precise crystal and magnetic structure analyses under multiple extreme environments such as low-temperature, high-pressure and high-magnetic field, and also designed for taking diffraction intensities of small single crystals with less than 1.0 mm^3 down to 0.1 mm^3 in volume.

In 2013, we added 6 area detectors, and determined the accurate and precise parameters for all area detectors by using basic diffraction method of a standard sample. In addition, we carried out diffraction measurements of Zr-based bulk metal glass to evaluate it as a material of piston-cylinder type high pressure cell.

1. Addition of 6 area-detectors

For a single crystal diffractometer, covering a large area around the sample position is very important to reduce the measurement time for one sample. After the launch of SENJU in March 2012, SENJU had been operated with 31 wavelength shift fiber (WLSF) type scintillation area detectors [1]. SENJU was originally designed to have 37 area detectors. In April 2013, we added 6 detectors as shown in Fig.1. Three of them were set on a back-scattering detector bank (S1: 2θ = 157.5 deg), and another three were on a low angle detector bank (S5: 2θ = 45.0 deg). Diffraction measurements of a ruby single crystal showed that the efficiency and uniformity of the new 6 detectors were similar to those of the original 31 detectors.

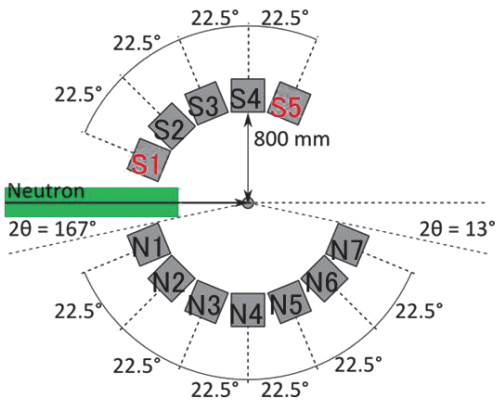

Figure 1. Arrangement of area detectors at SENJU (top view). 3 detectors were added to the S1 bank and other 3 to the S5 bank.

2. Determination of accurate and precise detector parameters

The instrumental parameters, including the positions of the detectors and the neutron flight path length, were determined in order to obtain accurate lattice parameters of the samples. Since the instrumental parameters correlate with each other, series of different measurements were needed to obtain the unique values for each parameter. As the first step of the procedure, a powder diffraction pattern of diamond was measured to determine the scattering angle of 90 deg utilizing the nature of the Debye-Sheller ring, which lines up vertically at 90 deg. On this measurement, we determined the actual 2θ angle of the 90-deg detector. Simultaneously, we determined the total neutron path length from the neutron source to the detector of the 90-deg bank ($L_1 + L_2$). As a next step, a Bragg reflection was repeatedly measured as the sample crystal was rotated in small steps. From this data, the equatorial plane parameters and the distance between the sample and the detectors L_2 were determined for the detectors settled at the horizontal plane. Consequently, the equipment parameters of the 90-deg detector were precisely determined without using any material constant. As a third step, many Bragg reflections from a standard sample were measured by the step scan of the crystal. This measurement gives a unique reciprocal lattice using the 90-deg detector. Then, the positions of the Bragg reflections of other detectors were adjusted so that the positional parameters of each detector were determined. As a result, the lattice parameters can be obtained with the accuracy of about 0.05% using the determined instrumental parameters.

3. Evaluation of bulk metal-glass as a material for high-pressure cell

For single crystal neutron diffraction measurements under high pressure, the piston-cylinder type sample cell has an ideal geometry because the apparatus has a wide opening accessible direction for incoming and scattered neutrons, if the cylinder material is transparent enough for neutrons. As a material for the new piston-cylinder cell, we have focused on the Zr-based bulk metallic glasses (Zr-BMGs), which have ideal properties as a cylinder material in terms of exceptional tensile strengths, plasticity, no sharp Bragg peaks and transparency for neutrons.

Neutron diffractions for a cast rod of Zr-BMG with a diameter of 12 mm and a length of 15 mm, which will be used as a cylinder material and the empty piston-cylinder made of CuBe alloy with outer/inner diameters of 8.8/2.5 mm as a reference were measured at SENJU. It was confirmed that the Zr-BMG is amorphous; no sharp Bragg peaks were found in the pattern (Fig.2 (a)), except a broad hallow ring. On the other hand, lots of peaks with a slight texture were observed for CuBe cylinder (Fig.2 (b)).

4. User program

Three general proposals were conducted in 2013A, and four general proposals in 2013B. In addition, four project uses were also carried out.

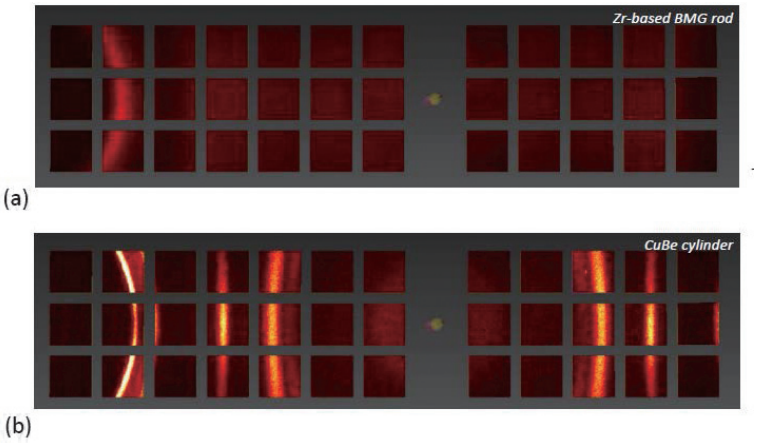

Figure 2. Comparison of neutron diffraction for (a) a rod of Zr-BMG and (b) an empty cell made of CuBe, measured at SENJU.

T. Ohhara[1], R. Kiyanagi[1], T. Kawasaki[1], K. Oikawa[1], I. Tamura[1,2], K. Kaneko[1,3], A. Nakao[4], T. Hanashima[4], K. Munakata[4], T. Moyoshi[4], T. Kuroda[4], Y. Kawamura[4], Y. Noda[1,5]

[1]Neutron Science Section, Materials and Life Science Division, J-PARC Center; [2]Department of Research Reactor and Tandem Accelerator, JAEA; [3]Quantum Beam Science Center, JAEA; [4]Neutron R&D Division, CROSS-Tokai; [5]HANARO, KAERI

Engineering Studies at BL19-TAKUMI

1. Introduction & present status

Regretfully, TAKUMI had to cancel many excellent proposals for the 2013A period due to the HADRON incident. The TAKUMI team is also thankful that the users resubmitted their proposals for the 2013B period. Many excellent experiments with various kinds of materials covering residual strain mappings and various kinds of in situ measurements while loading at room temperature, low and high temperatures, have been conducted.

TAKUMI operated approximately 75 days during 2013 FY and the beam time allocation according to experiment type is shown in Figure 2. The percentage of strain mapping is almost unchanged while the in situ studies increased compared to 2012 FY.

Figure 1. TAKUMI team performs alignments of the sample positions and theodolites routinely.

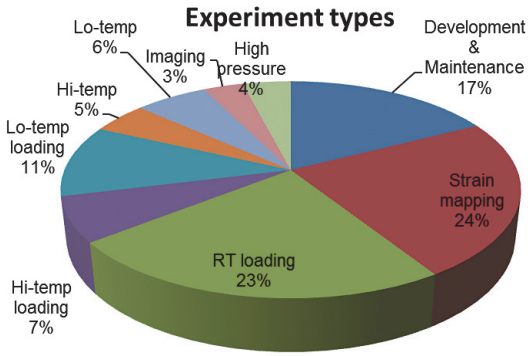

Figure 2. Beam time allocation by experiment type at TAKUMI during 2013 FY.

2. New sample environments

A new sample environmental device, the 100 K cooling system for loading experiments (Figure 3), has been commissioned and is ready to be used in the user program. The 100 K cooling system for loading experiments is a compact vacuum chamber equipped with loading specimen jigs; it can be mounted on the standard 50 kN loading machine of TAKUMI. The temperature of specimen jigs can be set in a range from 77 K to 473 K with an accuracy of about ± 1 K by controlling liquid nitrogen flow and heater power. The standard specimen shape is a dog bone type cylinder for tension and/or compression.

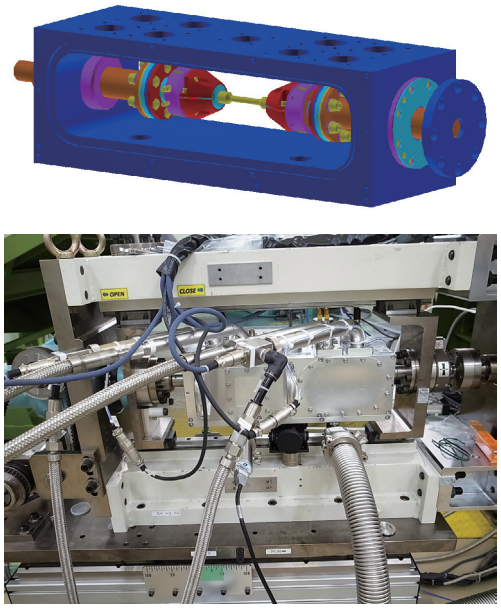

Figure 3. Illustration (up) and photo (bottom) of the 100 K cooling system for loading experiments.

3. Selected topics

There are many excellent results from experiments done during 2013 FY, and also excellent publications in 2013 FY. We regret that only three topics will be briefly introduced here, while the topics about the high elastic strain in Fe_3Pt [1] and the

strengthening mechanism of advanced steel (TRIP) [2] are introduced in different chapters of this report.

Internal strains in ITER CS conductor [3,4]

Measurements of internal strains in the superconducting constituent (Nb_3Sn phase in Nb_3Sn strand) in two cable-in-conduit conductors (CICC) for the International Thermonuclear Experimental Reactor were performed. From the internal strain measurements in a CICC for the central solenoidal magnets after the similar performance test, in the full-size shape as used in the performance test (3.6 m long) and in 100 mm long cut bars. Three main results were obtained. (1) The residual strain difference before and after the cutting to 100 mm long bar was about 0.1%, (2) a large relaxation on residual thermal strain was observed at the high field zone, and (3) the large relaxation on residual thermal strain at the high field zone was found mainly in a cross-sectional side where the Lorentz force coming in.

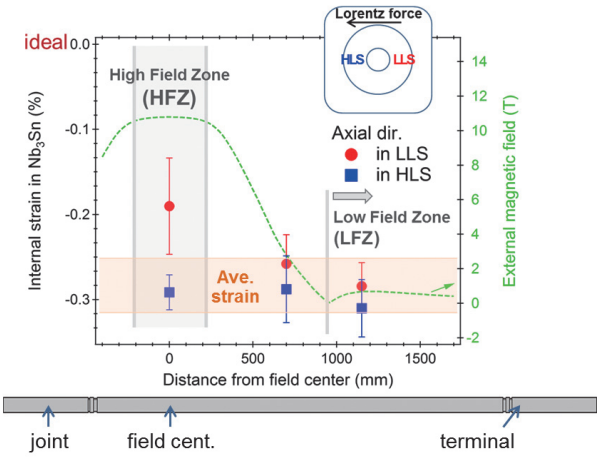

Figure 4. Internal strains of Nb_3Sn phase for the axial direction and the history of external field during the SULTAN test. The internal strain is shifted from the average strain to the tensile side (and peak broadening is also observed) at the LLS of the HFZ by the cyclic test.

Internal strains in rebar embedded in air-cured concrete [5]

In the modern society, architectural and civil engineering structures such as reinforced concrete buildings require high seismic performance to minimize the "megarisk" exposure to urban earthquake hazards. In the reinforced concrete structures, the bond resistance between rebar and concrete is an important parameter for determinig its performance and it has been typically evaluated by measuring the strain distribution along the embedded rebar. Here we present an in-situ strain and stress measurement for the rebar in the reinforced concrete using time-of-flight neutron diffraction as a novel alternative technique to the typical strain gauges. It was demonstrated in this study that the three-dimensional deformation behavior of the embedded rebar in normal-strength concrete, cured in air, can be accurately measured under pull-out loading using time-of-flight neutron diffraction.

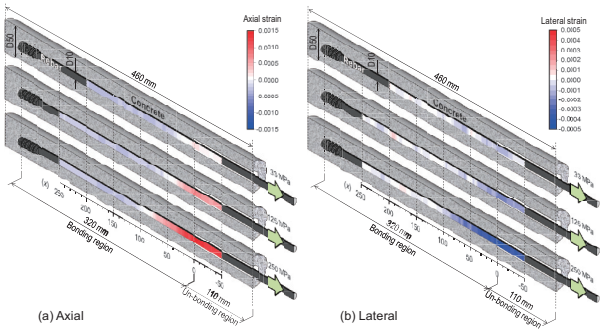

Figure 5. Internal strain distributions in rebar embedded in concrete measured at external stresses of 33 MPa, 125 MPa and 250 MPa. The absolute values of lattice strains in the axial direction and in the lateral direction, are linearly increased towards the end of the bonding region (x = 0). Portions where the changes in the lattice strain occur correspond to anchorage zones, and its lengths are increased with increasing the external stresses, followed by increases in the lattice strain at the bonding region.

Tensile behaviors of newly developed LPSO Mg-Zn-Y alloys [6]

The tensile behavior of single-phase 18R-Long period stacking ordered structure (LPSO) Mg-Zn-Y alloys and two-phase Mg-Zn-Y alloys which consist of Mg matrix and 18R-LPSO phase were studied by in-situ pulsed-neutron diffraction technique under tensile stress. Anisotropic behavior between the a-axis and c-axis in the 18R-LPSO structure was observed for the single-phase LPSO Mg-Zn-Y casted alloy from the elastic region under tensile stress. On the other hand, two-phase Mg-Zn-Y alloys with low 18R-LPSO phase concentration, which were produced by

extrusion, have isotropic behavior until the yield point under tensile stress, and the 18R-LPSO phase acts as a strengthening phase in the plastic region.

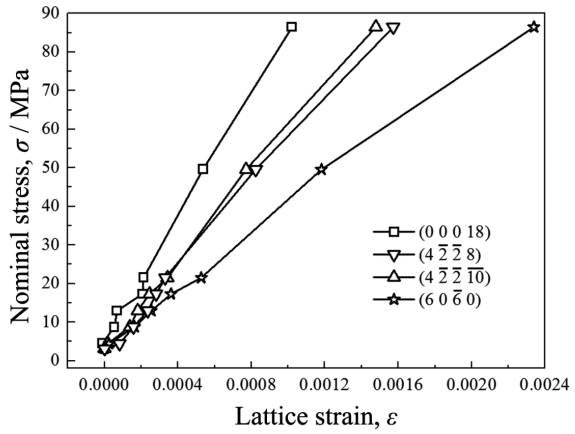

Figure 6. Tensile behavior of the as-cast $Mg_{85}Zn_6Y_9$ in the axial direction. Lattice strains for (60$\bar{6}$0) and (00018) planes indicate those being parallel to the a-axis and the c-axis, respectively, while lattice strains for (4$\bar{2}\bar{2}$8) and (4$\bar{2}\bar{2}\bar{10}$) indicate those being non-parallel to both the a-axis and the c-axis. The lattice strains seem to have nearly linear relation to the macroscopic stress until the specimen was broken.

References

[1] T. Yamaguchi, T. Fukuda, T. Kakeshita, S. Harjo and T. Nakamoto, Appl. Phys. Lett. **104** (2014) 231908.

[2] S. Harjo, N. Tsuchida, W. Gong, J. Abe, K. Aizawa, Mater. Res. Soc. Symp. Proc. **1528** (2013).

[3] T. Hemmi, S. Harjo, Y. Nunoya, H. Kajitani, N. Koizumi, K. Aizawa, S. Machiya and K. Osamura, Supercond. Sci. Technol., **26** (2013) 084002.

[4] S. Harjo, T. Hemmi, J. Abe, W. Gong, Y. Nunoya, K. Aizawa, T. Ito, N. Koizumi, S. Machiya, K. Osamura, Mater. Sci. Forum, **777** (2014) 84–91.

[5] H. Suzuki, K. Kusunoki, Y. Hatanaka, T. Mukai, A. Tasai, M. Kanematsu, K. Kabayama and S. Harjo, Meas. Sci. Technol., **25** (2014) 025602.

[6] K. Aizawa, W. Gong, S. Harjo, J. Abe, T. Iwahashi, T. Kamiyama, Mater. Trans., **54** (2013) 1083–1086.

S. Harjo, K. Aizawa, T. Kawasaki, W. Gong, and T. Iwahashi

Neutron Science Section, Materials and Life Science Division, J-PARC center

Current Status of the Versatile Neutron Diffractometer, iMATERIA

1. Introduction

Ibaraki prefecture, the local government in Japan in the area where the J-PARC sites are located, has decided to build a versatile neutron diffractometer (IBARAKI Materials Design Diffractometer, iMATERIA [1]) to promote industrial applications for the neutron beam in J-PARC. iMATERIA is planned to be a high throughput diffractometer so that materials engineers and scientists could use it like the chemical analytical instruments in their materials development process.

This diffractometer is designed to look at a decoupled-poisoned liquid hydrogen moderator (36 mm, off-centered) (BL20), and to have an incident flight path (L1) of 26.5 m with three wavelength selection disk-choppers and straight neutron guides with a total length of 14.0 m. The instrumental parameters are listed in Table 1. There are four detector banks, including a low angle and a small angle scattering detector bank. The angular coverage of each detector bank is also shown in Table 1. The rotation speeds for the disk-choppers are the same with a pulse repetition rate of "25 Hz" for the most applications (in normal mode). In this case, the diffractometer covers $0.18 < d\ (Å) < 2.5$ with $\Delta d/d = 0.16\%$ at the high resolution bank (BS bank) and covers $2.5 < d\ (Å) < 800$ at three detector banks of 90 degree, low angle and small angle while gradually changing resolution. When the speed for the wavelength selection disk-choppers is reduced to "12.5 Hz "(in wide-d mode), we can access a wider d-range, $0.18 < d\ (Å) < 5$ with $\Delta d/d = 0.16\%$, and $5 < d\ (Å) < 800$ while gradually changing resolution.

2. Current status

The three banks, high resolution bank (BS bank), special environment bank (90 degree bank) and low angle bank, are operational and the small angle bank is under commissioning. It takes about 10 minutes ("25 Hz" in normal mode) to obtain a 'Rietveld-quality' data in high resolution bank at "300 kW" beam power for about "1 g" of standard oxide samples.

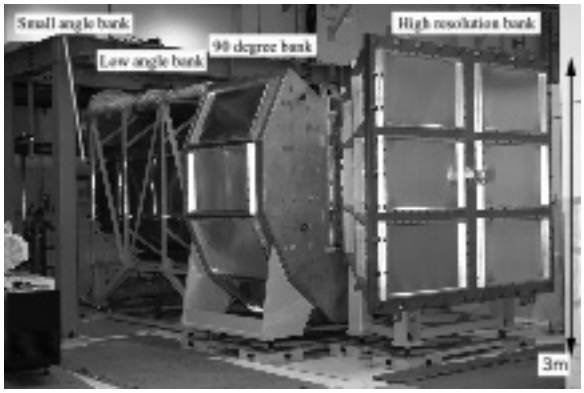

Figure 1. IBARAKI Materials Design Diffractometer, iMATERIA without detector for each bank and instrument shielding. The high-resolution bank, special environment bank (90 degree bank), and low angle bank, can be seen from right to left. The small angle detector bank, which is not shown in the picture, is situated in the low angle vacuum chamber (left hand of the picture).

Table 1. Instrumental parameters of iMATERIA. L2 is the scattered flight path. The d-range for each bank is the maximum value for the 2-measurement mode.

L1		26.5 m
Guide length		Total 14 m (3section)
Position of disk choppers		7.5 m (double)
		11.25 m (single)
		18.75 m (single)
High	2θ	$150° \le 2\theta \le 175$
Resolution	L2	2.0 - 2.3 m
Bank	d-range	$0.09 \le d(A°) \le 5.0°$
Special	2θ	$80° \le 2\theta \le 100°$
Environment	L2	1.5 m
Bank	d-range	$0.127 \le d(A°) \le 7.2$
Low	2θ	$10° \le 2\theta \le 40°$
Angle	L2	1.2 - 4.5 m
Bank	d-range	$0.37 \le d(A°) \le 58$
Small	2θ	$0.7° \le 2\theta \le 5°$
Angle	L2	4.5 m
Bank	d-range	$1.69 \le d(A°) \le 800$

3. Automatic sample changer

The automatic sample changer is the most important sample environment for high throughput experiments. Our automatic sample changer [2] consists of sample storage, two lines of an elevating system, two sets of pre-vacuum chambers and a sample sorting system. We can handle more than 600 samples continuously at room temperature without breaking the vacuum of the sample chamber. This year, we modified the drive system of the automatic sample changer. As a result, measurements speed increased. The sample exchange time was shortened from 5 to 2 minutes in this modification.

4. Small sample measurements

Since the beam power increased, it is possible to measure small-quantity (mg) samples and samples containing large neutron absorption elements for about one day of beam-time. Fig. 2 shows the Rietveld fitting pattern of "25.4 mg" $YBa_2Cu_3O_y$ sample for "18.5 h" at "300 kW" beam power. The good fitting in Fig. 2 is supported that the neutron diffraction experiment with mg sample can be performed. The occupation parameter for deficient oxygen site are 0.910(7) (1b site) and 0.067(5) (1e site), and it is almost identical with the result of a "1 g" sample measurement.

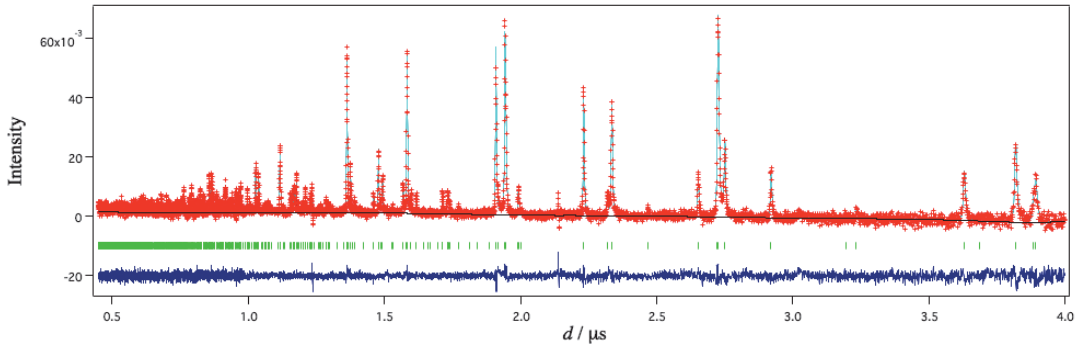

Figure 2. Rietveld refinment pattern of 25.4 mg $YBa_2Cu_3O_y$ by high resolution bank of iMATERIA using Z-Rietveld. The measurement time was 18.5 h at 300 kW.

References

[1] T. Ishigaki *et al.*, Nucl. Instr. Meth. Phys. Res. A 600 (2009) 189–191.

[2] A. Hoshikawa *et al.*, J. Phys.: Conf. Ser. 251 (2010) 012083.

T. Ishigaki[1], A. Hoshikwa[1], M. Yonemura[2,3], Y. Yoshida[1], T. Matsukawa[1], and T. Kamiyama[2,3]

[1]Frontier Research Center for Applied Nuclear Sciences, Ibaraki University; [2]Neutron Science Section, Materials and Life Science Division, J-PARC center; [3]Insitute of Materials Structure Science, KEK

Status of the High Intensity Total Diffractometer (BL21, NOVA)

1. In-situ measurement of the hydrogen absorption process of Pd under high-pressure gas atmosphere

In-situ H_2/D_2 gas atmosphere measurement is important to understand the mechanism of hydrogen absorption and desorption process in materials, since hydrogen contents of hydrogen storage materials is controlled by the temperature and the hydrogen gas pressure.

On NOVA, a sample environment to control hydrogen composition in a sample by controlling the sample temperature and the hydrogen pressure has been equipped. This environment is able to measure the Pressure-Composition isotherm (PCT) curve and the sample environment is called PCT environment. The highest H_2/D_2 gas pressure is 10 MPa with controlling the sample temperature from 50 K to 473 K.

Figure 1 shows PCT curve measured on the PCT environment of NOVA. A reasonable curve was obtained. At each deuterium contents, in-situ neutron diffraction measurements were performed and the observed profiles are shown in Fig. 2. Structural transitions from Pd to PdD_2 ((1) ~ (4)) and from PdD_2 to Pd ((4) ~ (6)) were observed successfully.

The time-transient measurement of the hydrogen absorption process is shown in Fig. 3. Pd to PdD_2 transition, indicated by the red arrow in Fig. 1, was measured in about 10 seconds.

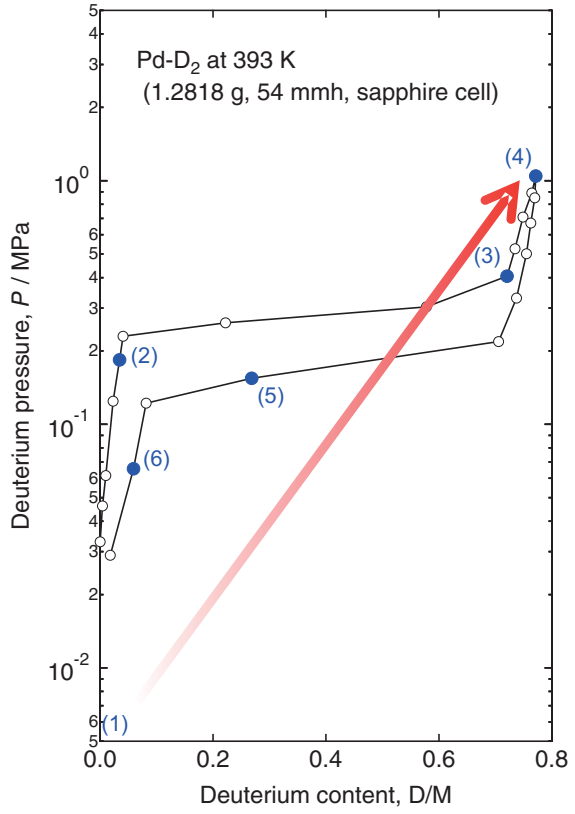

Figure 1. Pressure-Composition isotherm (PCT) curve of Pd at 393 K measured on NOVA.

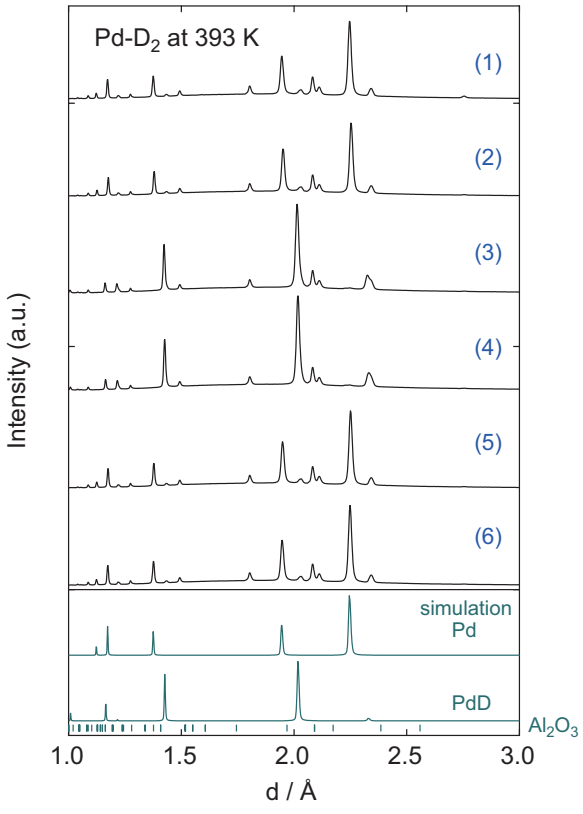

Figure 2. In-situ neutron diffraction patterns of Pd during hydrogen absorption and desorption process measured on NOVA. The numbers in parenthesis correspond to the numbers in Fig. 1. The sample cell was sapphire.

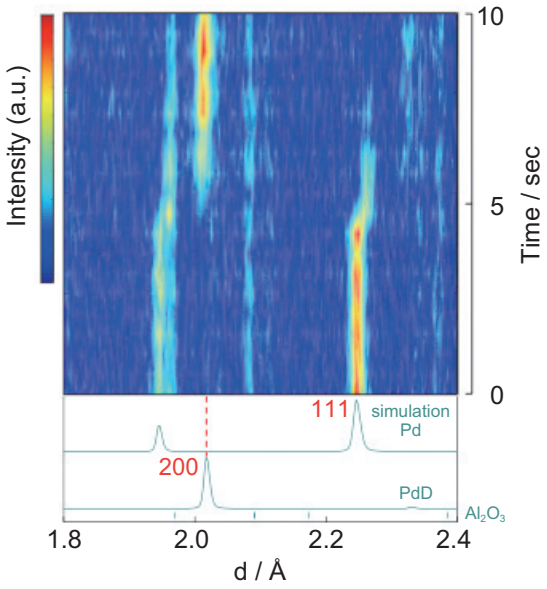

Figure 3. Time-transient measurement of the hydrogen absorption process of Pd.

2. Improvements of the sample cell for in-situ measurement under high-pressure gas atmosphere

For total scattering measurement, higher Signal-to-Noise ratio should be realized to obtain higher real space resolution in pair correlation function. Selection of a sample cell valid under 10 MPa is one of the keys. At first, the cell had been made with single sapphire but it does not display trivial Bragg spots at higher Q range above 10 $Å^{-1}$. Alternatively, vanadium was chosen and used successfully to make a cell for the high-pressure gas experiment. Figure 4 shows the Pair distribution function (PDF) of silicon powder. PDF with Vanadium cell for high-pressure is almost equivalent with the PDF with Vanadium cell for ambient pressure, while PDF with Sapphire cell shows very low real space resolution. Further improvements of the high-pressure cell and background reductions are underway.

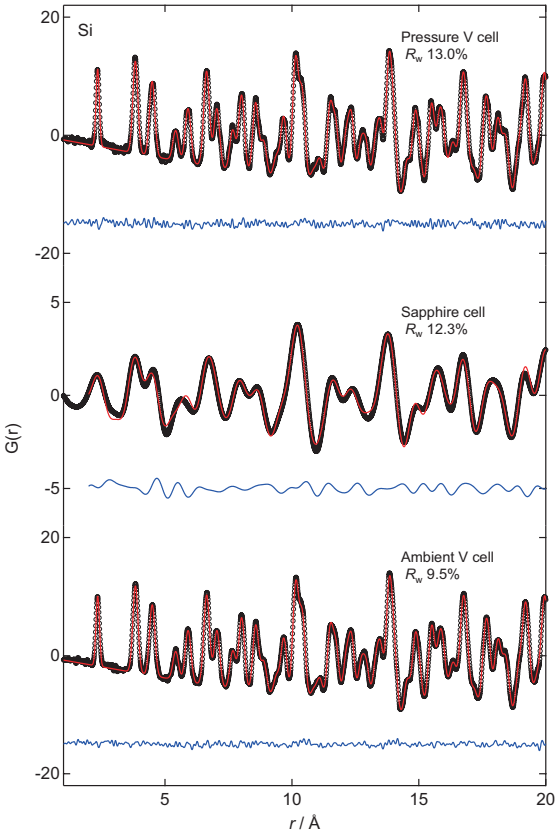

Figure 4. PDF of silicon powder measured in Vanadium cell for high-pressure (top), Sapphire cell for high-pressure (middle), and standard Vanadium cell for ambient pressure (bottom).

T. Otomo[1,2], K. Ikeda[1,2], H. Ohshita[1,2], N. Kaneko[1,2], T. Seya[2], and K. Suzuya[1]
[1]Neutron Science Section, Materials and Life Science Division, J-PARC center; [2]Institute of Materials Structure Science, KEK

BL22: Construction of Energy-resolved Neutron Imaging System "RADEN"

1. Introduction

The recent developments in the energy-resolved neutron imaging technique attract significant interest from the fields of science and industry. The pulsed neutron beam benefits this technique in many ways, because it makes it possible to perform precise measurements of energy dependent phenomena using the TOF method with fine energy resolution, and to use simultaneously neutrons with a wide energy range - from epithermal to cold neutrons. In J-PARC, we have been developing the pulsed neutron imaging technique [1] and we are now constructing a new instrument dedicated to the pulsed neutron imaging experiments fully using the pulsed neutron's nature.

Figure 1. External view of the beam line shielding.

2. Beam line construction

The energy-resolved neutron imaging system, named "RADEN", has two primal roles as a pioneering facility for energy-resolved neutron imaging in the world to perform Bragg-edge imaging [2], resonance absorption imaging [3], and polarized neutron imaging [4], and as a leading neutron radiography and tomography facility in Japan. Based on this idea, we determined the detailed design of the instrument, and started the construction.

During the shutdown period in FY 2013, several installation tasks were completed. At first, the shielding was built at the beam line of BL22 in the 2nd experimental hall of MLF (Fig. 1). Because this instrument not only uses the largest beam and sample size, but also transports high-energy neutrons, a massive shield is needed. Therefore, the shield wall consists of 4 layers, i.e., B_4C included mortar, polyethylene, steel, and concrete, to form an effective radiation shield. Next, we replaced the heavy shutter with a new one with 3 different holes, to enlarge the neutron beam homogeneously up to 300 mm $\times$ 300 mm at the sample position and change the L / D ratio.

Inside the preposition shield tunnel, several optical devices have been installed (Fig. 2): filters, a rotary collimator, a low speed double disk chopper, a fast shutter, another rotary collimator, and a B_4C slit, from upstream. The first rotary collimator makes a small pinhole to produce higher L / D ratio up to 7500 for high spatial resolution imaging. On the other hand, the second rotary collimator is used to limit the beam size and to suppress the high-energy neutron background. Filters, which consist of Cd, Pb, Bi, and acrylic resin plates, are used to transport only epithermal neutrons or to attenuate gamma rays created at the time of neutron generation for the resonance absorption imaging experiments. Later, a T0 chopper is also installed in front of the disk chopper.

A large sample stage with a load capacity of 1.0 ton has been set up in the experimental room (Fig. 3). This stage has three linear motion axes for precise sample positioning, and a rotation table sits on the top of the stage. In addition, a small sample stage was prepared for the CT experiments. Flight tubes filled with He gas, a polarization analysis apparatus, and sample chambers will be installed next year.

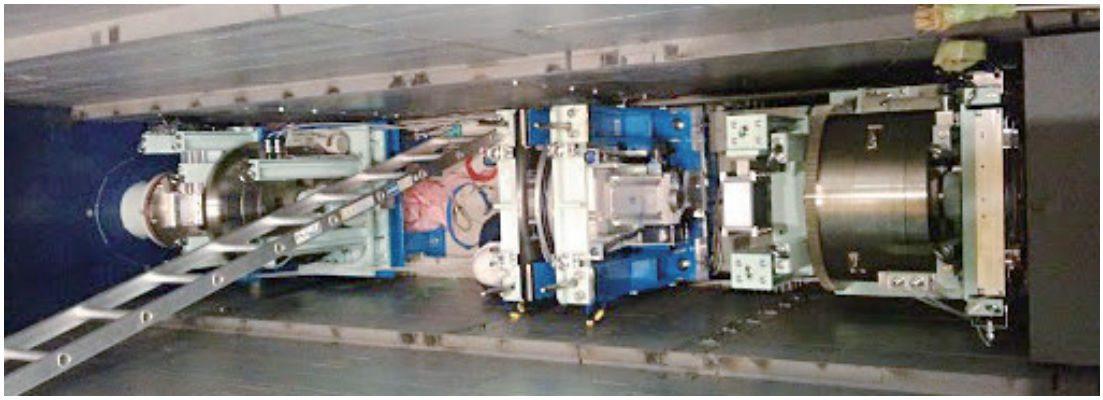

Figure 2. Optical devices inside the preposition shield tunnel.

Figure 3. Photograph of experimental room.

3. Schedule

The rest of construction work will be completed in FY 2014, including both the counting type and camera type neutron imaging detectors and computational environment for data analysis. The first beam will be accepted after the summer shut down of 2014, and we will start the commissioning study after that.

References

[1] Y. Kiyanagi *et al.*, Nucl. Inst. Meth. Physics Research, A **651** (2011) 16.

[2] H. Sato *et al.*, J. Phys.: Conf. Ser. **251** (2010) 012070.

[3] K. Kaneko *et al.*, J. Phys. Chem. Solids, **60** (1999) 1499.

[4] T. Shinohara *et al.*, Nucl. Inst. Meth. Physics Research, A **651** (2011) 121.

T. Shinohara[1], T. Kai[1], K. Oikawa[1], M. Ooi[1], M. Harada[1], K. Sakai[1], T. Nakatani[1], M. Segawa[2], H. Iikura[3], H. Hayashida[4], J. Parker[4], Y. Matsumoto[4], S. Zhang[4], T. Kamiyama[5], H. Sato[5], H. Yokota[6], T. Sera[7], Y. Saito[8], K. Mochiki[9], M. Kureta[2], K. Aizawa[1], M. Arai[1], and Y. Kiyanagi[10]

[1]Materials and Life Science Division, J-PARC center; [2]NSED, JAEA; [3]QuBS, JAEA; [4]Neutron R&D Division CROSS-Tokai; [5]Hokkaido University; [6]RIKEN; [7]Kyushu University; [8]KURRI; [9]Tokyo City University; [10]Nagoya University

Recent Progress on Polarized Inelastic Neutron Spectrometer POLANO

1. Introduction

Although the polarized neutron technique has been developed and used for many years, the application of the time-of-flight (TOF) method has only been realized in recent years. In particular, with regard to the inelastic spectrometer, the polarized neutron technique finds limited practical use in wide scattering angle instruments. In the light of recent discoveries in material science, many of the observed complex phenomena are largely due to the entangled physical degrees of freedom of spins, charges, orbitals, and even lattice vibration. In neutron scattering experiments, the varying dependence of momentum, energy, and temperature can be interpreted by these of degrees of freedoms. However, a unique, effective, and direct way to observe these properties separately is via the polarization analysis.

The polarization analysis neutron spectrometer POLANO enables polarization analysis of inelastic scattering experiments to investigate the dynamical properties of the above mentioned multiple degrees of freedom. POLANO is a collaborative project between KEK and Tohoku University under the aegis of KEK Inter-University Research Program. The project has been launched in 2009 starting as an S-type project with financial support from the KENS neutron facility. After the budget for the project was successfully sanctioned and obtained, the actual construction started in 2013. Although part of the instrumental design is still under discussion, the main conceptual design and manufacturing of the main components are expected to be completed by the end of 2014.

2. Design & Construction

The spectrometer concepts have compact design with reasonably wide sample space, higher neutron flux, higher neutron energy polarization up to 100 meV, and medium resolution. In order to achieve these concepts, the geometrical specifications of the spectrometer were chosen as follows, moderator-sample distance L1 = 17.5 m, sample-detector distance L2 = 2.0 m, and Fermi chopper-sample distance L3 = 1.85 m.

The shielding design was evaluated based on gamma and neutron ray tracing by using the Monte Carlo PHITS code. The POLANO is viewing a decoupled moderator, and the view of the moderator is 10 cm square in dimension. A radiation dosage of less than 6.25 μSv/h of surface dose was achieved with concrete, steel and boric acid as shielding materials. In certain parts of the shielding in the vicinity of the sample space, stainless steel was used as a non-magnetic material in order to make possible the conduction of high-magnetic field experiments.

To maximize the beam flux at the sample position, focusing supermirror guide tubes with $m = 4$ have been installed as reported in Ref. [1, 2]. The use of an elliptical guide tube provides a flux that is 10 times higher even for 100 meV of neutron energy. Since the focusing guide tubes affect the beam divergence, we estimate the beam profile as well. Figure 1 shows the intensity distribution at L = 16.435 m from the moderator, where a SEOP ^{3}He filter cell will be placed. The beam width at the ^{3}He filter has a full width of 8 cm at the bottom, and 4 cm at the half height. In the early stage, ^{3}He cells with a diameter of 5 cm will be used because the ^{3}He polarizing technique has already been established for 5 cm cells. Since cells with a diameter of 10 cm have now been developed, the beam exiting the polarizer will be almost fully polarized in the final stage. The details on spin polarization in POLANO and devices are reported in another article [3].

A vacuum chamber is to be installed at the sample-detector section to avoid air scattering and to ensure evacuated insulation for the refrigerator. To ensure flexible use of the sample space, the chamber is designed to be detachable, and is composed of three parts. In addition, B_4C vanes and liners are planned to be installed in the chamber [4]. At the end

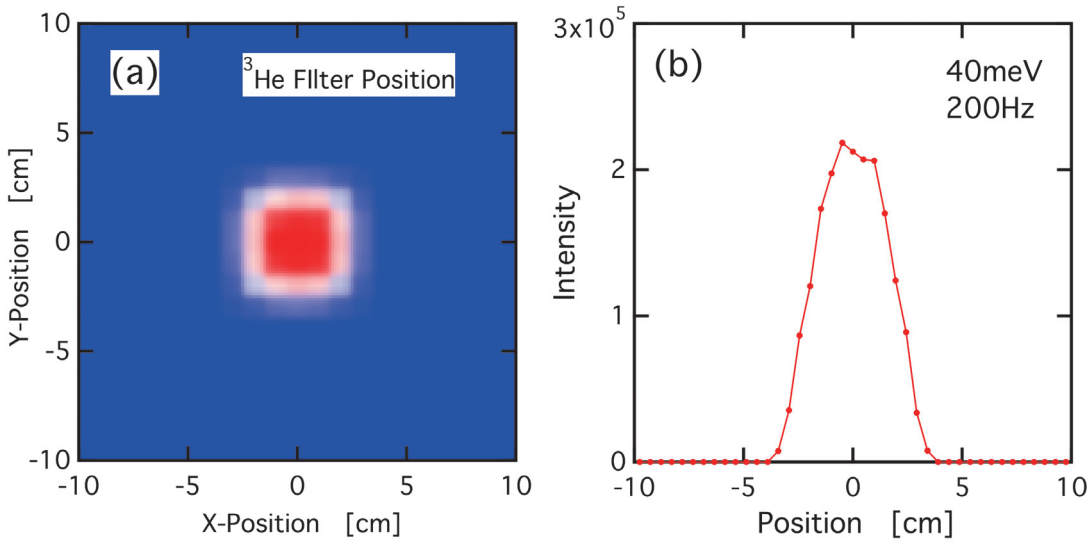

Figure 1. (a) Evaluated neutron intensity distribution at the ^{3}He cell position. (b) 1D plot of the distribution at Y = 0. (Ref. [9])

of the scattering chamber, position sensitive detectors (PSDs) are to be installed on the inside of the chamber. For energy range of the POLANO, large pressure of ^{3}He gas is not required to achieve reasonable detector efficiency. Therefore, we adopted the use of a 10 atm gas pressure PSD with 600 mm effective length and 3/4" diameter. An efficiency of about 70% is expected for 100 meV neutrons. The PSDs are arranged in three layers in the vacuum chamber. The horizontal scattering angle (detector angle) ranges from –30° to 130°, and the range is ±25° along the vertical direction. At first, only horizontal (center) layers are to be fully installed for polarization analysis experiments.

The polarizer, analyzer, and other magnetic devices installed in the POLANO are currently under development [5,6]. As of the polarizer, a cylindrical ^{3}He spin filter (HeSF) based on the spin-exchange optical pumping (SEOP) technique will be used to polarize neutrons in the wide energy range. In the second stage, a banana-shaped HeSF will be installed as a spin analyzer to study neutrons in the 100 meV region. The large solid angle HeSF will be installed at a position close to the sample and will be used in the off-laser mode; consequently, the polarization will undergo decay.

One of the most essential devices for this type of instrument is the chopper. We have developed several types of choppers originally for the high resolution chopper spectrometer HRC in the MLF [7, 8]. POLANO will basically use T0 and Fermi choppers with the same specifications as those of the HRC. In addition, we plan to use slow rotating disk choppers (band chopper) and a fast rotating disk chopper (correlation chopper) to achieve cross-correlation. The T0 chopper is known as a device that mechanically reduces the intensity of prompt gamma rays and fast neutrons. For POLANO a T0 chopper with a frequency of f = 100 Hz of Inconel X750 blade is adopted for the parameters of beam window width of w = 80 mm, width of the blade $w + 2\Delta w$ = 82 mm, length of the blade (along neutron beam direction) l = 300 mm, and radius of the blade R = 300 mm.

At 500 meV of energy (2000 μs of TOF) the background is reduced by nearly 1/100 of that of the incoming beam, and thus the chopper's performance can be considered satisfactory. Figure 2 shows the photograph of a manufactured Fermi chopper that is similar to the one developed for the HRC. The following are the design parameters: slit width w = 1.2 mm, slot (absorber) width d = 0.3 mm, and rotor diameter D = 98 mm. A boron-epoxy composite is used for the neutron absorbers in the slit package of the rotor. The maximum rotational frequency f_{max} = 600 Hz is controlled by 25 Hz steps as it tunes with the proton pulse repetition. The phase can be controlled fairly precisely; we achieved a phase accuracy of less than 0.3 μs at 600 Hz.

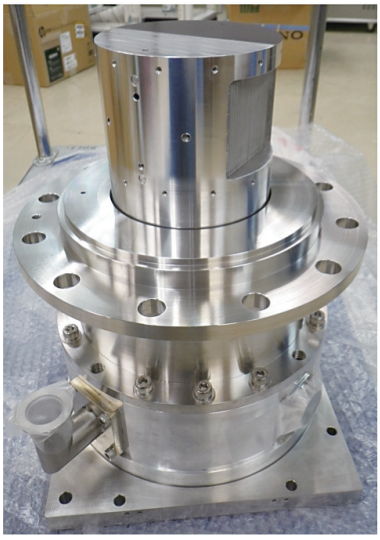

Figure 2. Newly assembled Fermi chopper for POLANO. (Ref. [9])

Two band choppers will be placed along the beamline to avoid frame overlap. This type of chopper is a single disk chopper made of aluminum coated with boron enriched B_4C with epoxy resin. Two disks rotate at 25 Hz with different opening angles to select the required channels. A fast rotating disk chopper is used to achieve cross correlation.

3. Summary

In summary, the construction of the POLANO spectrometer for neutron polarization analysis has begun. The design of most instruments has been completed, and the main components are to be installed by the end of 2014. R&D of certain devices, particularly the polarization and magnetic devices still needs to be performed. In 2015, we plan to carry out radiological assessments. The neutron beams for the POLANO are expected to be operational in the beginning of 2015.

References

[1] T. Yokoo *et al*., J. Phys. Soc. Jpn. **82**, SA035 (2013).

[2] T. Yokoo *et al*., J. Phys. Conf. Series **502**, 012046 (2014).

[3] K. Ohoyama *et al*., this issue.

[4] T. Yokoo et al., Review of Scientific Instruments **82**, 095109 (2011).

[5] K. Ohoyama *et al*., J. Phys. Soc. Jpn. **82**, SA036 (2013).

[6] K. Ohoyama *et al*., J. Phys. Conf. Series **502**, 012051 (2014).

[7] S. Itoh *et al*., Nucl. Instrum. Meth. A **661**, 86 (2012).

[8] S. Itoh *et al*., Nucl. Instrum. Meth. A **661**, 58 (2012).

[9] T. Yokoo *et al*., EPJ Web of Conferences, to be published.

T. Yokoo[1,2], K. Ohoyama[3,4], S. Itoh[1,2], K. Iwasa[5], N. Kaneko[1,2], J. Suzuki[6], M. Ohkawara[3], K. Aizawa[7], S. Tasaki[8], T. Ino[1,2], K. Taketani[1,2], S. Ishimoto[2], M. Takeda[1,9], T. Oku[7], H. Kira[10], K. Hayashi[3], H. Kimura[11], and T. J. Sato[11]

[1]Neutron Science Section, Materials and Life Science Division, J-PARC Center; [2]Institute of Materials Structure Science, KEK; [3]IMR, Tohoku University; [4]WPI-AIMR, Tohoku University; [5]Department of Physics, Tohoku University; [6]MEC, KEK; [7]Technology Development Section, Materials and Life Science Division, J-PARC Center; [8]Department of Engineering, Kyoto University; [9]Quantum Beam Science Center, JAEA; [10]Neutron R&D Division, CROSS-Tokai; [11]IMRAM, Tohoku University

Performance of Spin Devices for Polarized Neutrons of POLANO

1. Introduction

The polarization analysis technique is quite important in materials science, as it allows us to investigate complicated spin correlations and spin-lattice couplings in magnets, in particular, multipolar orderings in rare earth systems, high-T_C superconductors, multiferroic systems and so on.

POLANO, the instrument of this project, will be the first full polarization analysis spectrometer at J-PARC [1-3]. KEK has been financially supporting the POLANO project via the S-type project (2009S09, 2014S09) since 2009. Fortunately, the POLANO project was funded by a supplementary budget from the government in fiscal year 2012 (2012FY), so the full-scale construction started instantly.

In this article, we report the situations of polarization devices for POLANO and plans for their developments.

2. Polarizer

POLANO will have a cylindrical ^{3}He spin filter (HeSF) using the on-beam spin exchange optical pumping method (SEOP) as a polarizer because E_i = 100 meV is necessary to cover a higher Q region up to 10 Å^{-1}. ^{3}He polarization, P_{He}, of 72% has already been realized in Japan [4]. We will use a GE180 glass cell with a diameter of 3 ~ 5 cm in the first stage of the POLANO project. For a future project, HeSF cells with a diameter of 10 cm are already being prepared at Tohoku University. The polarization tests of the 10 cm cell are already in progress in JAEA in 2014FY.

An adiabatic fast passage (AFP) NMR will be installed on the SEOP system because AFP-NMR can be used as a spin flipper; this is important to reduce the distance between the Fermi chopper and the sample position, L_3.

3. Analyzer

The choice of polarization analyzers for POLANO is an important technical decision. In the first stage, we will focus on polarization analysis in $E_f < 30$ meV; thus, we will install a fan-shaped analyzer with 5.5Q_c Fe / Si supermirror benders, similar to those used on HYSPEC in SNS and FOCUS in PSI. The parameters of the bender analyzer of POLANO are summarized in Table1. The fan-shaped analyzer bender of POLANO consists of 260 mirrors, which will be installed by the end of 2014FY; the analyzer can cover 2θ of about 15~18°. The analyzer will be set on a table, which rotates around the sample in the vacuum chamber, thus, users can choose a 2θ position for the experiments. The magnet housing has an open angle of 40° so that future addition of supermirrors will be possible to cover wider scattering angles. For the next stage, banana-shape HeSF cells are under development.

The transmission of one slit of mirrors is estimated as 0.17 at E = 20 meV under the alignment of POLANO using McStas, which is consistent with the data from the supplier company. Figure 1 shows calculated scattering intensity counted at a pixel on a detector (2 × 2 cm^2) from a vanadium pipe with an outer diameter of 25 mm and inner diameter of 24 mm through the fan-shaped analyzer bender.

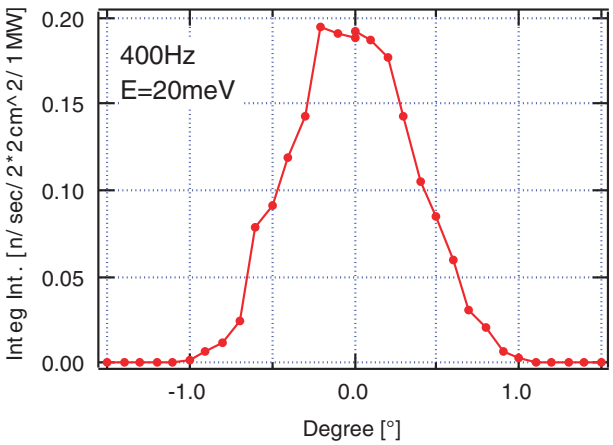

Figure 1. Calculated integrated intensity from a cylinder-shape vanadium rod counted at a detector (2 × 2 cm^2) through a 5.5Q_c supermirror bender analyzer by McStas. Horizontal axis is the angle of the optical axis of the supermirror.

Table 1. Parameters of the analyzer supermirror.

Mirror	$5.5Q_c$ (Concave side) $1.5Q_c$ (Convex side) Fe/Si
Gap	0.6 mm
Length	258 mm
Radius of Curvature	10500 mm
Length of Line-of-Sight	224.7 mm
Substrate	
Material	borosilicate glass
Thickness	0.3 mm

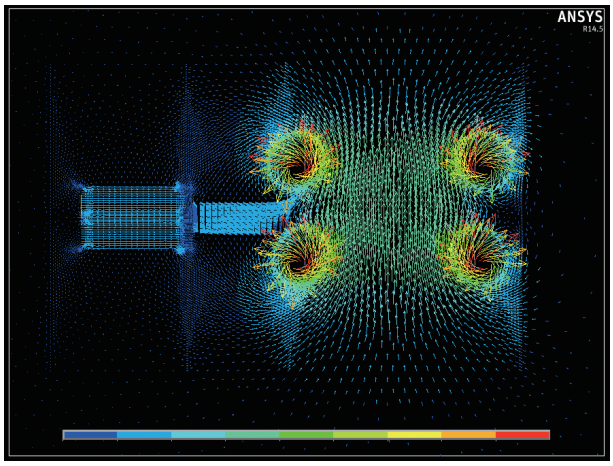

Figure 2. Side cross-section of magnetic field distributions from a solenoid coil for SEOP (left) to a Helmholtz coil for the sample calculated using ANSYS.

Figure 1 means that the analyzer bender has to be optimized with accuracy of ±0.2°. The rotation Table has an optimizing mechanism to satisfy this requirement.

4. Simulation of Distributions of Magnetic Fields

Needless to say, the control of magnetic fields is the most important factor for successful polarized neutron experiments. We are estimating the distribution of magnetic fields by the finite element method using ANSYS software. Figure 2 shows the distribution of magnetic fields around a solenoid coil for HeSF and a Helmholtz coil for the sample. Using the calculated magnetic field data, we could estimate the depolarization along the flight path from the SEOP polarizer to the supermirror analyzer by quantum mechanical treatment. Based on the simulations, optimized alignments of the magnetic field devices can be found, which minimizes the depolarization.

The qualitative estimation of magnetic fields is indispensable for all the instruments on which polarized neutrons are used. Thus, collaborative discussions about the technical issues have begun in MLF.

References

[1] K. Ohoyama, T. Yokoo, S. Itoh, J. Suzuki, K. Iwasa, T.J. Sato, H. Kira, Y. Sakaguchi, T. Ino, T. Oku, K. Tomiyasu, M. Matsuura, H. Hiraka, M. Fujita, H. Kimura, T. Sato, J. Suzuki, H. M. Shimizu, T. Arima, M. Takeda, K. Kaneko, M. Hino, S. Muto, H. Nojiri, C. H. Lee, J. G. Park, S. Choi, J. Phys. Soc. Jpn., **82**, SA036 (2013).

[2] K. Ohoyama, T. Yokoo, S. Itoh, T. Ino, M. Ohkawara, T. Oku, S. Tasaki, K. Iwasa, T. J. Sato, S Ishimoto, K. Taketani, H. Kira, Y. Sakaguch, M. Nanbu, H. Hiraka, H. M. Shimizu, M. Takeda, M. Hino, K. Hayashi, U. Fliges, P. Hautle, J. Phys.: Conf. Ser., **502**, 012051 (2014).

[3] T. Yokoo, K. Ohoyama , S. Itoh, J. Suzuki, K. Iwasa, T. J. Sato, H. Kira, Y. Sakaguchi , T. Ino, T. Oku, K. Tomiyasu, M. Matsuura, H. Hiraka, M. Fujita, H. Kimura, T. Sato, J. Suzuki, M. Takeda, K. Kaneko, M. Hino, S. Muto, J. Phys. Soc. Jpn., **82**, SA035 (2013).

[4] H. Kira, Y. Sakaguchi, T. Oku, J. Suzuki, M. Nakamura, M. Arai, K. Kakurai, Y. Endo, Y. Arimoto, T. Ino, H. M. Shimizu, T. Kamiyama, K. Tsutsumi, K. Ohoyama, H. Hiraka, K. Yamada, L. J. Chang, Physica, B **406**, 2433 (2011).

K. Ohoyama[1,2], T. Yokoo[3,4], S. Itoh[3,4], K. Iwasa[5], M. Ohkawara[2], M. Nanbu[2], T. Ino[3,4], S. Tasaki[6], T. Oku[3], K. Taketani[3,4], and S. Ishimoto[4]

[1]Advanced Institute for Materials Research, Tohoku University; [2]Institute for Materials Research, Tohoku University; [3]Neutron Science Section, Materials and Life Science Division, J-PARC Center; [4]Institute of Materials Structure Science, KEK; [5]Graduate School of Science, Tohoku University; [6]Graduate School of Engineering, Kyoto University

Status of Instrumentation for Dynamic Nuclear Polarization of Proton Spins

1. Introduction

Polarized neutron scattering is a useful method for studying materials science. A way to polarize neutron uses a polarized proton target (PPT). As neutron-proton scattering length of the triplet channel is much smaller than that of the singlet channel [1], the neutron beam transmitted through a PPT gets polarized.

A brute force way to polarize sufficient number of protons in the target is applying strong external magnetic field to it and cooling it down to low temperature. However, even if we cool it down to 1 K and apply external magnetic field of 5 T to it, the thermal equilibrium Boltzmann polarization of the protons is less than 1% and the target cannot be used as a practical neutron polarizer.

To highly polarize proton spins, we can use the dynamic nuclear polarization (DNP) method. In the above mentioned situation, although the polarization of protons is less than 1%, that of unpaired-electrons is nearly equal to unity as the magnetic moment of electron is much larger than that of proton. The DNP method exploits the microwave-irradiation-driven transfer of polarization from unpaired-electrons to protons. To test the enhancement of the proton polarization by this method for several target materials that contain protons and unpaired-electrons and estimate their performance as neutron polarizers, we are preparing instruments for DNP of proton spins.

2. Status

To cool a target down and apply external magnetic field to it, we use the cryostat that was used by Crabb and coworkers [2]. The ^{4}He evaporation refrigerator can cool the target down to 1 K and the split coil superconducting magnet can apply the magnetic field of 5 T to it. Using a ruthenium oxide thermometer and a pressure-gauge for evacuated gaseous helium, we checked the target holder temperature and found out that it cooled down to 1 K. We could also successfully supply a sufficient current for the superconducting magnet to generate the magnetic field of 5 T.

To measure the enhancement of the proton polarization, we prepared instruments, which are used in studies of continuous wave nuclear magnetic resonance (CW NMR) spectroscopy. Our system uses a coil that acts as a transmitter of the radio wave that is irradiated to the target and a receiver of the radio wave generated by the target material. When the energy difference between the two proton spin states due to the static magnetic field is equal to the photon energy of the radio wave generated by the coil, the radio wave is absorbed and the amplitude of the reflected voltage from the coil decreases. As this signal depends on the polarization of the protons and the radio wave frequency [3], we can estimate the polarization enhancement by measuring the radio wave frequency dependence on the reflected voltages.

To generate the radio wave, we used a frequency synthesizer (Programmed Test Sources Inc. PTS 250) to apply an oscillating voltage to the coil. The frequency can be controlled by a digital signal, which was generated by a digital I/O board (National Instruments, PCI 6509). To measure the amplitude of the reflected voltage from the coil, the homodyne method was used. The output DC signal was measured by an analog to digital converter (National Instruments, PCI 6281).

To test the CW NMR system, we installed a Teflon sheet, which contains fluorine nucleus whose magnetic moment is 6% smaller than that of proton. We scanned the radio wave frequency over the range around the Larmor frequency of fluorine and observed a clear absorption peak at the expected frequency as shown in figure 1.

To irradiate a microwave to the target, we prepared an extended interaction oscillator (Communication & Power Industries, VKT 2438P), which needs water cooling and has a mechanical frequency tuning

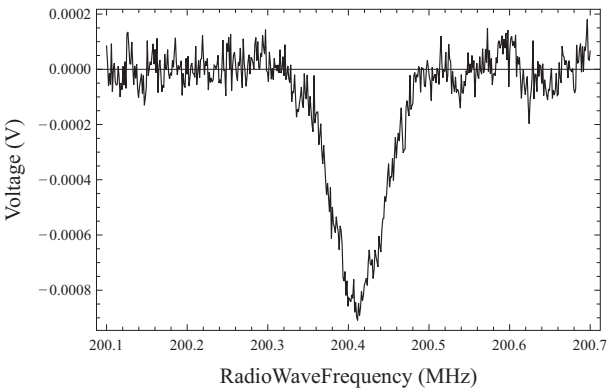

Figure 1. Observed NMR spectrum of a Teflon sheet. There is an absorption peak with expected frequency.

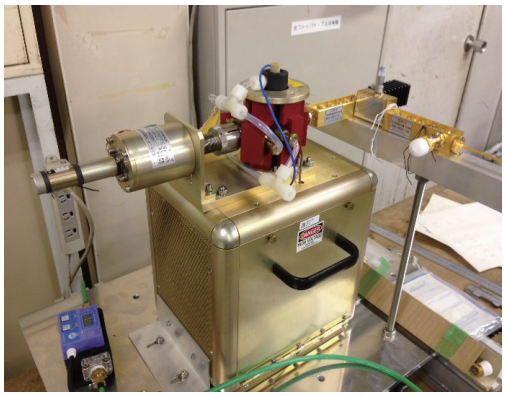

Figure 2. Photograph of the extended interaction oscillator, whose cooling water tubes are removed, the attenuator and the waveguide to transfer the microwave to the cryostat.

system. The center frequency, mechanical tuning frequency range and typical output power of this oscillator are 140 GHz, 1 GHz and 20 W, respectively. To optimize the polarization transfer efficiency, we control the power and frequency of the microwave. To control the microwave power without changing the applied voltages to the oscillator, we prepared an attenuator. We also prepared a spectrum analyzer (Agilent, EXA N9010A) and a harmonic mixer (OML Inc., M06HWD) to measure the power and frequency of the microwave. Figure 2 shows the photograph of the oscillator, whose cooling water tubes are removed, the attenuator and the waveguide that transfers the microwave to the cryostat.

3. Plans

After finishing the setup of the microwave apparatus, we can irradiate a frequency and power tunable microwave to the target applied 5 T external magnetic field and cooled down to 1 K. By comparing the CW NMR spectrums with and without microwave irradiation, we can estimate the proton polarization enhanced by the DNP method. Using this apparatus, we are going to measure the polarization enhancements for several materials which contains protons and unpaired electrons, such as TEMPO (2,2,6,6-tetra-methyl-piperidine-1-oxyl) doped polyethylene, and estimate their performance as neutron polarizers.

Acknowledgement

We thank Yusuke Tochigi for the cooperation in preparing the CW NMR system.

References

[1] H. A. Bethe and P. Morrison, *Elementary Nuclear Theory* (Wiley, 1956).

[2] D. G. Crabb, C. B. Higley, A. D. Krisch, R. S. Raymond, T. Roser, J. A. Stewart, and G. R. Court, Phys. Rev. Lett. 64, 2627 (1990).

[3] A. Abragam, *The Principles of Nuclear Magnetism* (Oxford University Press, 1961).

K. Taketani[1,2], S. Ishimoto[3], S. Itoh[1,2], K. Iwasa[4], K. Ohoyama[5,6], S. Suzuki[3], and T. Yokoo[1,2]

[1]Neutron Science Section, Materials and Life Science Division, J-PARC center; [2]Institute of Materials Structure Science, KEK; [3]Institute of Particle and Nuclear Studies, KEK; [4]Graduate School of Science, Tohoku University; [5]Advanced Institute for Materials Research, Tohoku University; [6]Institute for Materials Research, Tohoku University

Development of a Compact in-situ SEOP ^{3}He Neutron Spin Filter

1. Introduction

We have been developing a ^{3}He neutron spin filter (NSF) for efficient utilization of pulsed neutrons, because the ^{3}He NSF is effective for neutrons in a wide energy range. The ^{3}He NSF is effective especially for neutrons with energy higher than several-tens-MeV, and can cover a large solid angle and polarize neutrons without deflecting them from their original trajectory. In order to apply the ^{3}He NSF to experiments at a pulsed neutron experimental facility such as the J-PARC, it is important to make the system compact, stable and useful. In this study, we have developed a compact *in-situ* spin-exchange optical pumping (SEOP) ^{3}He-NSF with a spin flip function for the ^{3}He polarization based on the adiabatic fast passage (AFP) NMR.

2. The instrumental setup

Figure 1(a) shows the instrumental setup of the *in-situ* SEOP ^{3}He-NSF [1, 2]. The NSF consists of a laser diode, optical lenses and mirrors, and a solenoid coil. A cylindrical glass cell, which contains ^{3}He gas and a small amount of Rb, is mounted in an oven (Fig. 1(b)). A pickup coil and a radio frequency (RF) coil for the AFP-NMR are mounted around the ^{3}He cell (Fig. 1(b)) [3]. The oven is placed at the center of the solenoid. The temperature in the oven is kept at 450 K to vaporize the Rb while polarizing the ^{3}He based on the SEOP.

3. Calibration of the AFP-NMR

Pulsed neutron beams transmit through the ^{3}He-NSF, and are counted by a 2-dimensional position sensitive detector (2d-PSD). The intensity ratio R of the transmitted neutrons between a polarized and unpolarized ^{3}He cell is expressed as $R = \cosh(P_{3He}\sigma\rho l)$, where P_{3He}, σ and ρ are the polarization degree, the absorption cross section and the number density of ^{3}He. l is the thickness of the ^{3}He gas. The l is derived from the ratio $R_0 = \exp(-\sigma\rho l)$ of the neutron transmission with the cell containing ^{3}He gas and the empty cell. We evaluated the values of l and P_{3He} of three ^{3}He cells by measuring the R and R_0. The obtained values are listed in Table 1. In order to obtain the relation between P_{3He} and the NMR signal V_{NMR}, we measured the NMR signal based on the AFP-NMR method at the same time as the neutron transmission measurements, and determined the ratio $R_c = P_{3He}/V_{NMR}$.

Table 1. The measured values of l and P_{3He}.

	Cylindrical cell size	l	P_{3He}
Cell 1	ϕ34mm × 52mm-L	16.5 atm-cm	0.625
Cell 2	ϕ34mm × 52mm-L	10.8 atm-cm	0.436
Cell 3	ϕ50mm × 70mm-L	9.6 atm-cm	0.415

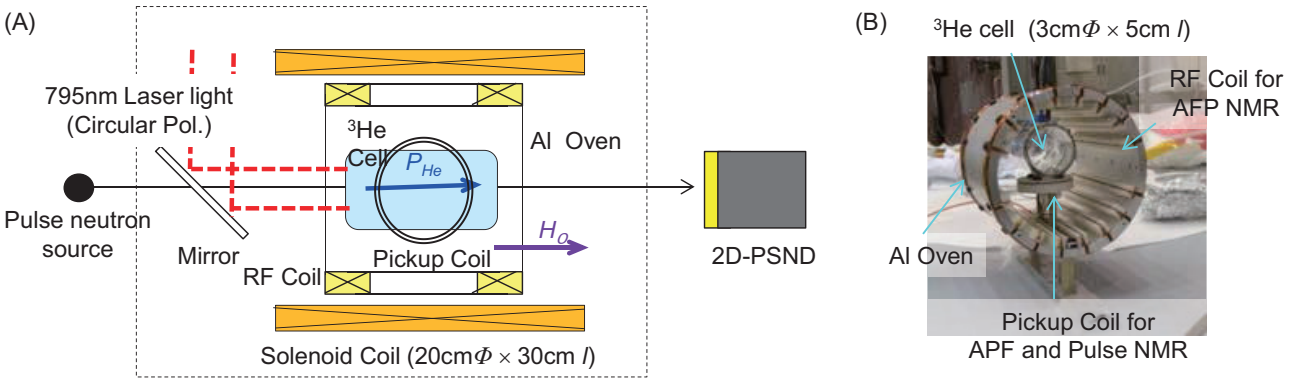

Figure 1. The instrumental setup of the *in-situ* SEOP ^{3}He-NSF.

4. Spin flip function

By flipping the polarity of the ^{3}He polarization, the polarity of the generated polarized neutron beam is alternated. Therefore, a flipping system for the ^{3}He polarization functions as a neutron spin flipper. By the AFP-NMR, polarity of the ^{3}He polarization can be π-flipped. In the case of the *in-situ* SEOP ^{3}He-NSF, polarity of the circularly-polarized laser for the SEOP must be flipped to keep the absolute polarization of the ^{3}He. To change the polarity of the laser, a half-wavelength plate was installed. The rotation angle of the half-wavelength plate was optimized, and a polarization of 98% was obtained for the circularly-polarized laser. The ^{3}He polarization reached 70% and was confirmed to be stable for over a week.

A demonstration of the ^{3}He-NSF was performed at the neutron reflectometer SHARAKU (BL17). The *in-situ* SEOP ^{3}He-NSF was located at 1200 mm downstream of the sample and used as a neutron spin analyzer. Cell 2 was used for the ^{3}He-NSF in this experiment (Table 1). A 2d-PSD was placed after the ^{3}He-NSF. A guide coil was set between the sample and the ^{3}He-NSF for the adiabatic neutron spin transport.

We performed polarized neutron reflection measurements from a Fe/Cr multilayered thin film with the giant magneto-resistance effect [4]. By flipping the spin polarity of incident and reflected neutrons, we measured the intensity distributions of (+, +), (–, –), (+, –) and (–, +) reflectivities. The first sign in the pair indicates spin polarity of incident polarized neutrons and the second that of reflected ones. Figure 2 shows the reflectivity distributions measured with the applied field of 200 Oe. Off-specular reflections around $Q_z = 0.08$ Å^{-1} were clearly measured in the cases of (+, –) and (–, +). This indicates the existence of the antiferromagnetic correlations, which align perpendicular to the applied field direction. The obtained data were well consistent with the results of Ref. [4].

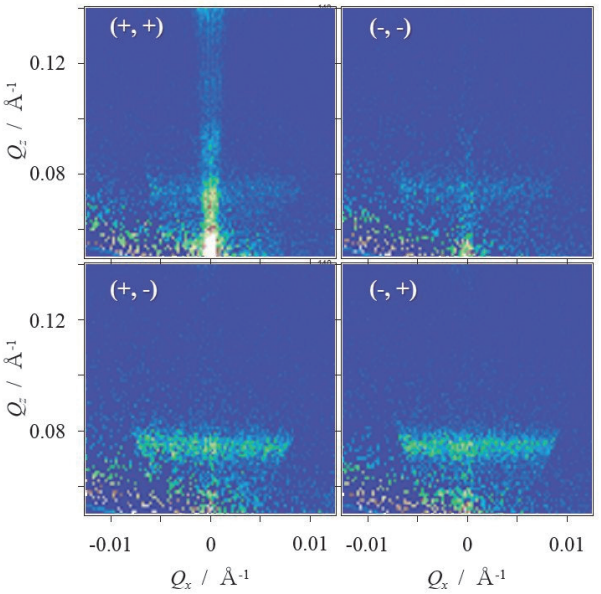

Figure 2. The obtained intensity distributions of the polarized neutron reflectivity from the Fe/Cr thin multi-layers.

5. Conclusion

We have developed a compact *in-situ* SEOP ^{3}He-NSF with a spin flip function for the ^{3}He polarization based on the AFP-NMR. As the relation between the V_{NMR} and P_{3He} was determined, we can estimate the P_{3He} by the AFP-NMR. By the AFP-NMR, polarity of the ^{3}He polarization can be π-flipped, resulting in the spin flip of the generated polarized neutrons. The spin flip function for the polarized neutrons was demonstrated by the polarization analysis experiment at the polarized neutron reflectometer SHARAKU (BL17).

References

[1] T. Ino, *et al.*, Physica B, V**404** 2667-2669 (2009).

[2] K. Sakai, *et al.*, J. Phys.: Conf. Ser. **340**, 012037 (2012).

[3] T. Ino, *et al.*, J. Phys.: Conf. Ser. **340**, 012006 (2012).

[4] M. Takeda, *et al.*, Physica B, **213&214**, 248 (1995).

T. Oku[1], H. Hayashida[1], K. Sakai[1], K. Hiroi[1], T. Shinohara[1], K. Aizawa[1], M. Arai[1], M. Takeda[2], K. Kakurai[2], H. Kira[3], N. Miyata[3], K. Akutsu[3], J. Suzuki[3], T. Ino[1,4], M. Ohkawara[5], and K. Ohyama[5]

[1]Neutron Science Section, Materials and Life Science Division, J-PARC Center; [2]Quantum Beam Science Center, JAEA; [3]Neutron R&D Division, CROSS-Tokai; [4]Institute of Materials Structure Science, KEK; [5]Institute for Material Research, Tohoku University

Sample Environment at MLF

1. Introduction

The sample environment (SE) team has been responsible for operating and maintaining of the beamline(BL)-common SE equipment and the development of the SE devices. In FY2013, the SE team was officially organized in Technology Development Section in MLF thus succeeding the previous ad hoc SE team. The newly organized SE team consists of staff members from JAEA, KEK and CROSS so as to be able to support any BL's across the boundaries of the institutes, no matter if it is a public BL or not. In this team, we aim at establishing a proper system composed of several professional sub-groups such as cryogenics and magnets, high temperature, high pressure, soft matter, and so on.

2. Operation and improvement of the BL-common SE equipment

At present, a vertical-field superconducting magnet, a ^{3}He-^{4}He dilution refrigerator insert, a high-temperature furnace with a Nb heater and a top-loading-type ^{4}He cryostat are available or under commissioning as the BL-common SE equipment. In April 2013, we operated the superconducting magnet at BL18 for its on-beam commissioning (Fig. 1). The maximum magnetic field of 6.85 T and the lowest temperature at VTI (Variable Temperature Insert) of 1.17 K were achieved by a single shot mode and kept for more than four hours. Following the operation at BL18, we also operated this magnet at BL14. The magnetic field was more carefully raised because of an iron frame of its vacuum tank, and then we applied the fields up to 4 T without any quench of the magnet.

For the high-temperature furnace, the accuracy of thermometry was improved. When we used it for the first time, the location of thermocouples inside a tube of the sample stick and the short length of homogeneous temperature area of the heater element made it impossible to measure the accurate temperature for a large sample (Fig. 2(a)). We replaced and extended the thermocouples to attach them directly to the top and bottom of the sample as shown in Fig. 2(b). Moreover, a control panel for vacuum pumps and an electric distribution board were installed for users' convenience and safety (left panel of Fig. 3). A gas inlet line was equipped

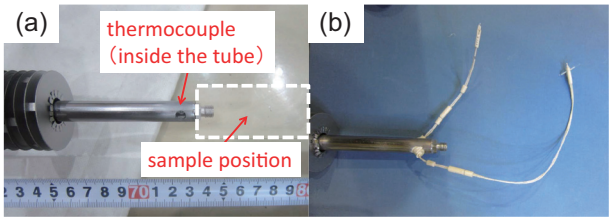

Figure 2. Sample stick of the Nb furnace, (a) before and (b) after the improvement of the thermocouple position.

Figure 1. Operation of the superconducting magnet at BL18.

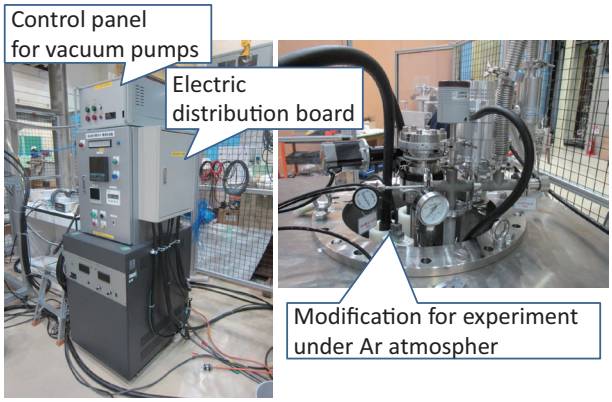

Figure 3. High-temperature furnace after the improvements.

and related modifications made to enable us to conduct a high-temperature experiment under Ar atmosphere. Taking into account the heating up of the outer case of the furnace, we decided on a rule that an experiment under Ar atmosphere must be performed below 1300°C.

3. Safety measures for top-loading cryostats

In 2012, there was an accident - the center stick of an orange cryostat was suddenly ejected when changing the sample due to rapid evaporation of accidentally condensed air inside the sample space. Responding to this problem, we have taken the following steps to prevent such accidents. We modified the center stick to have an open end and added a relief valve on the tube just below the top flange so that the excess pressure is released through the end hole, the relief valve on the center stick and the original relief valve on the cryostat even when the bottom of the sample space is sealed by an ice block. It is strongly recommended that such a safety system be introduced in all top-loading cryostats in MLF. As a further step, we applied “D-cuts” to the baffles. In addition, especially for the inserts with no hollow tubes, such as dilution refrigerator, a short detachable stainless wire is necessarily connected to the cryostat and its insert when the insert is pulled up for the sample exchange, to avoid ejection of the insert. Figure 4 shows examples of the applied safety measures. These modifications are also recommended for other top-loading cryostats in MLF.

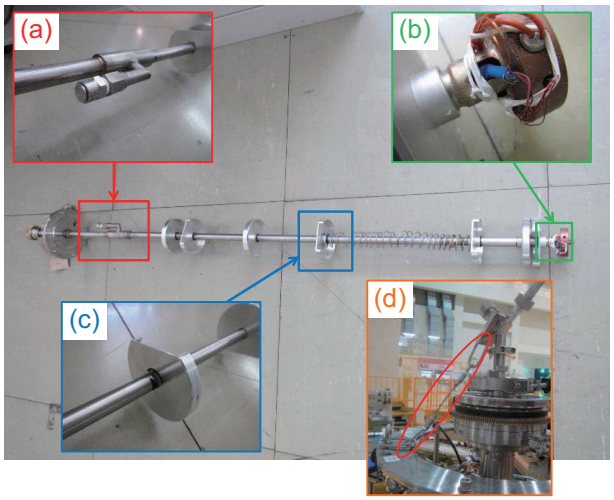

Figure 4. Examples of the applied safety measures; the inserted pictures indicate (a) a relief valve, (b) an open-end tube, (c) a D-cut baffle and (d) a detachable stainless wire.

4. Future plans

A new building for the MLF user support will be constructed in FY2014. A sample synthesis room and characterization rooms will be prepared on the first floor. We started to discuss the equipment to be installed there. There will be also a workshop (Fig. 5) for maintenance, long-term commissioning and modifications of SE equipment and choppers, whose number has gradually increased, while we carry out their preparation for user experiments and short-term commissioning at the SE area in MLF. Furthermore, we will work on development of the SE devices at the new workshop. We started to discuss the possible subjects of development for this fiscal year.

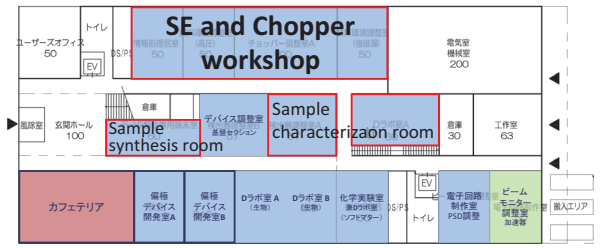

Figure 5. Sample synthesis room, characterization rooms and new SE workshop on the first floor of the new building.

T. Aso[1], Y. Yamauchi[1], Y. Sakaguchi[2], K. Munakata[2], M. Ishikado[2], S. Ohira-Kawamura[3], W. Kambara[1], S. Takata[3], T. Yokoo[3,4], and Y. Kawakita[3]

[1]Technology Development Section, Materials and Life Science Division, J-PARC Center; [2]Neutron R&D Division CROSS-Tokai; [3]Neutron Science Section, Materials and Life Science Division, J-PARC Center; [4]Institute of Materials Structure Science, KEK

IROHA Upgrade

1. Introduction

We have developed the flexible, scalable and common software framework unified data acquisition (DAQ) and device control [1] since the beginning of MLF. The software framework, named "IROHA", has been introduced and used in several instruments of MLF since 2008. Last year we started to plan the upgrade of IROHA to achieve higher flexibility and scalability. We have discussed and designed the improvement points in IROHA. The points of upgrade are specifically as follows.

1) Proper role-sharing between the device control and the instrument management
2) The interface of the MLF experimental database (MLF EXP-DB) for the management of measurement information
3) Platform-independent user interface.

In these articles, we will show the prototype of the new common software framework for the instrument control in MLF, named "IROHA2" (shown in Fig. 1).

2. Roles of the device control server and the instrument management server

In the original IROHA, several device control servers and the device management server were tightly coupled, which caused difficulty in the maintenance and some problems with the operation. We redefined the roles of the two servers and clearly separated these in independent software. The device control server is engaged in each device's control, such as operation, monitoring and logging of the devices. The instrument management server, whose role is the same as the device management server in the original IROHA, is engaged in the measurement management, including logging of measurements, authorization and certification of users. Each server is able to run in a stand-alone process as well as cooperatively. The typical use case is as follows:

1) Calibration of each device by using the device control server in the off-beam
2) Authorization and certification by the instrument management server
3) Configuration of the instrument control system combined with the DAQ system and the devices.
4) Calibration of the instrument by using the instrument management server
5) Measurements from the user interface through the instrument management server.

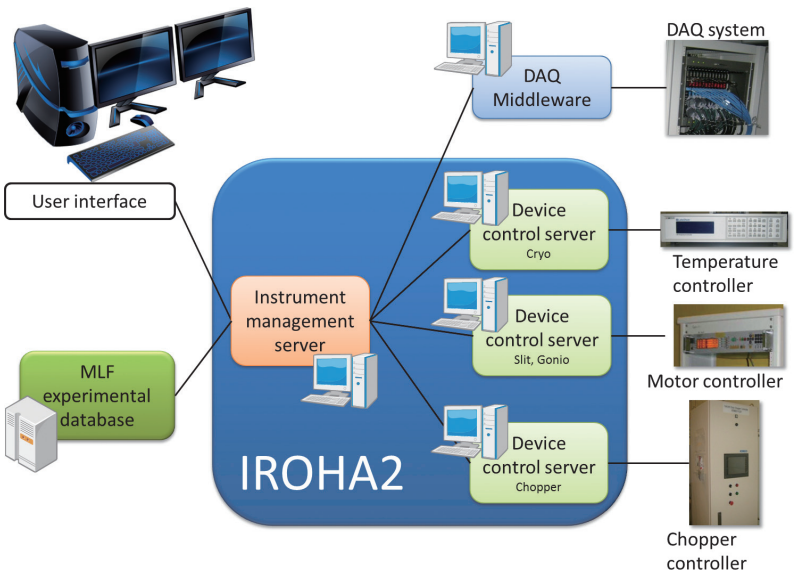

Figure 1. The schematic diagram of IROHA2.

3. Database interface for the management of measurement information

The aims of the MLF EXP-DB are to develop a central management system for experimental data generated at the facility, and to provide an interface that gives users' rapid and effective access to their own data by using identification information managed in the J-PARC Users Office database. One of the main roles of IROHA2 is the interface between the users' experimental data and the MLF EXP-DB.

When we do a measurement with IROHA2, the instrument management server collects and records the experimental meta-data, which includes the conditions of the DAQ system and the devices as "Run Information" in every measurement. The MLF EXP-DB automatically searches, registers and catalogues the Run Information and the experimental raw data, which is read out from the DAQ system and stored in the disk of the CPU DAQs.

The authorization and certification by the instrument management server is based on the user information obtained from the MLF EXP-DB. The instrument management server records the user account in the Run Information. Using this information, the MLF EXP-DB recognizes who obtained the experimental data.

4. Platform-independent user interface

At present time, the user interface by means of a web browser is one of the most platform-independent user interfaces. Particularly, the web pages designed by so-called "Responsive Web" are available for use from personal computers as well as tablet terminals and smart phones. We have decided to introduce the web user interfaces as the new user interface for IROHA2. We have adopted a framework, BOOTSTRAP [2], to realize the "Responsive Web" to the user interfaces of the device control servers and the instrument management server. Fig. 2 shows the web user interfaces of these servers made by BOOTSTRAP. We can calibrate the devices, manage the instrument control system and do a measurement with a web browser.

(a)

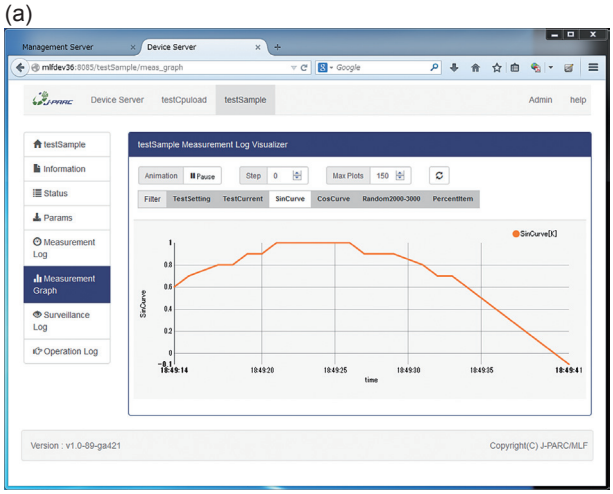

(b)

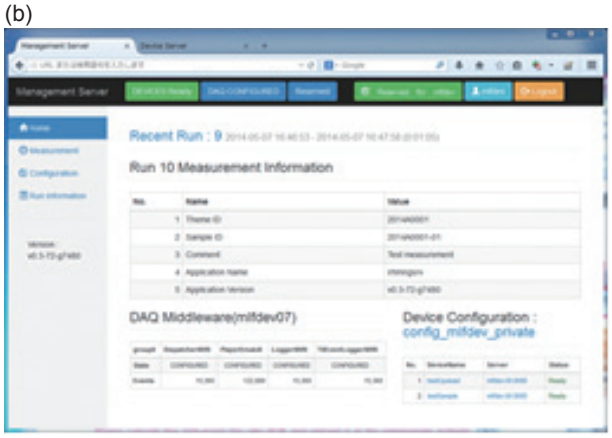

Figure 2. The web user interfaces of the device control server (a) and the instrument management server (b).

5. Future plan

We will develop several device control servers for the cryogenic refrigerator, beam narrowers, goniometer and chopper. In addition, the sequence management server for automatic measurements with web user interface will be developed. After these developments, we will introduce IROHA2 into 4SEASONS(BL01) in FY2014 and deploy several instruments in FY2015.

References

[1] T. Nakatani *et al.*, Proceedings of ICALEPCS2009 673-675 (2009).

[2] http://getbootstrap.com/

T. Nakatani[1], Y. Inamura[2], and T. Ito[3]

[1]Technology Development Section, Materials and Life Science Division, J-PARC Center; [2]Neutron Science Section, Materials and Life Science Division, J-PARC Center; [3]Neutron R&D Division, CROSS-Tokai

A Scintillator-Based Detector with Sub 100-μm Spatial Resolution for Time-of-Flight Neutron Imaging

1. Introduction

The time-of-flight neutron radiography and neutron tomography are powerful non-destructive techniques for visualizing an object and quantifying the amount of its elementals. However, the specifications required for neutron imaging place various challenges to the two-dimensional detectors; generally, these include small pixels, a spatial resolution of less than 100 μm, a timing resolution of a few microseconds and a count rate capability of more than 10^5 cps. We have developed a new type of neutron-counting time-of-flight neutron imager that employs extensively the scintillator and wavelength-shifting (WLS) fiber technologies. The detector exhibits a high spatial resolution down to the sub-100-μm level with a low gamma-ray sensitivity of less than 10^{-7} at ~ 1 MeV.

2. Scintillator/FOT WLS fiber type detector

Figure 1 shows a schematic view of the neutron-detecting head of the scintillator / Fiber optic taper (FOT) and WLS-fiber detector.

The neutron-detecting head comprises a single scintillator screen, an FOT, crossed WLS-fibre arrays. The ZnS / ^{6}LiF scintillator absorbs neutrons in a nuclear reaction of ^{6}Li(n,α)T, and the ZnS scintillator emits scintillation light. The scintillation light propagates through the FOT while magnifying the light image onto the WLS-fiber arrays. The scintillation image is magnified, in our case by a factor of 3.1; in other words the effective pixel size of the detector becomes about one-third of the fiber diameter. The WLS fiber reemits a shifted green light that is transmitted to the PMTs. The incident position of a neutron is calculated by the signal processing and encoder electronics according to the excitation pattern of the PMTs. In order to achieve the required spatial resolution, the detector components were carefully selected or developed. Important R&D points were: the thin scintillator screen with thickness of less than 100 μm, the FOT that can perform image magnification with good light transmission, and the crossed WLS-fiber arrays made with the dedicated 100-μm diameter fibers.

Figure 2 shows a photograph of the prototype detector. The scintillator with thickness of 100 ± 10 μm was made in house to match the range of the generated triton after the nuclear capture event, which is about 33 μm in the ZnS scintillator. This scintillator thickness was determined in order to achieve acceptable detector efficiency while minimizing the light dispersion. The WLS-fiber arrays comprised two fiber ribbons, one in the *x* and one in the *y* direction, each containing 224 fibers. The dye content in the fibers was optimized to maximize light collection efficiency. The effective diameter of the fiber was 105 ± 7 μm, which included the cumulative error due to the ribbon arrangement. This led to

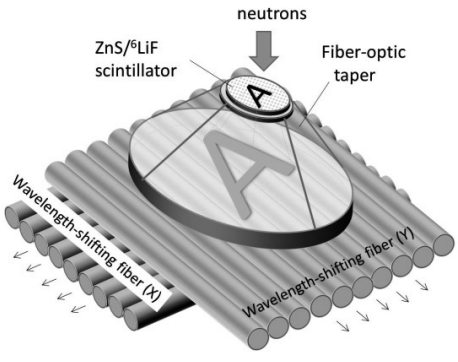

Figure 1. A schematic view of a neutron-detecting head of the prototype detector.

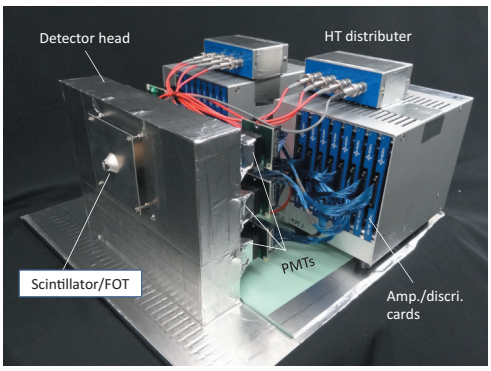

Figure 2. A photograph of the prototype scintillator-based time-of-flight neutron imager.

the pixel size of the detector to be 34 μm × 34 μm. The neutron-detecting area was limited to the size of the FOT, at 5 mm × 7 mm; this can be increased by using an FOT with a larger area [1].

Figure 3 provides the example of the measured beam profiles. Half of the detecting area was covered with a 1-mm-thick Cd plate, and the measured beam profile was fitted with the line-spread function. The mean spatial FWHM resolutions for ten sampled data points were 80 ± 7 μm and 61 ± 6 μm in the *x* and *y* directions (the mean values for each direction were derived while excluding the maximum data point).

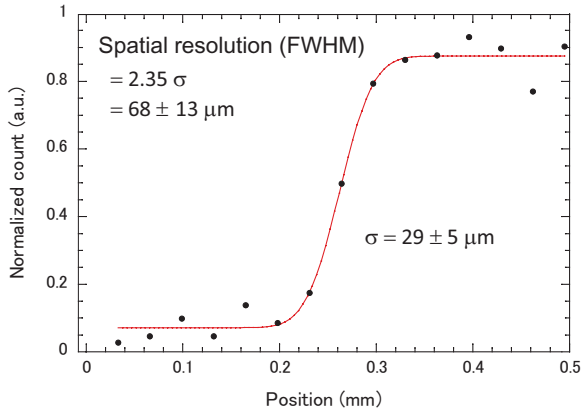

Figure 3. Beam profile with the Cd mask covering the detector face.

3. Demonstration of Bragg-edge-imaging

Figure 4 shows a photograph of a test piece and reconstructed neutron images with a TOF window measured at BL-10 in the J-PARC/MLF, respectively. The test piece had a cylindrical shape and was constructed from polycrystalline Cu and Fe (Figure 4a). The sample has a length of 6 mm. The detector was set at 12.7 m from the liquid-hydrogen moderator. In the TOF spectrum the dips appeared by Bragg reflections of the composite materials of the sample. The origin of the count dips was clearly identified: one at 13100 μs was due to the (110) reflection of Fe, and the other at 13500 μs was due to the (111) reflection of Cu. The reconstructed neutron images (Figures 4b, c and d) were for times of flight of 2500–38000, 13000–13200 and 13400–13600 μs, respectively.

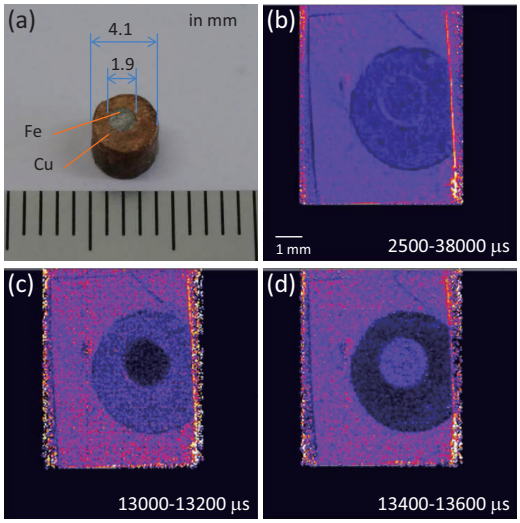

Figure 4. A photograph of a test piece (a), and reconstructed neutron images with a TOF window of 2500–38000 μs (b), 13000–13200 μs (c) and 13400–13600 μs (d), respectively. Each image pixel has time-of-flight information [2].

Figure 4b shows that there was no clear contrast in the image for a simple transmission measurement. On the other hand, the reconstructed images in Figure 4c and d contain clear signs of the Cu/Fe interface. These images demonstrate that the prototype detector produced clear images with fine mesh and high contrast by reconstructing the image with the appropriate TOF window. A separate test with a ^{60}Co gamma-ray source revealed that the detector also had a gamma-ray sensitivity of less than 10^{-7}.

4. Summary

We have developed a new type of scintillator-based time-of-flight neutron imager for energy-selective neutron imaging. The developed detector has a pixel size of 34 μm × 34 μm, and the exhibited spatial FWHM resolution is 80 ± 7 μm and 61 ± 6 μm in the *x* and *y* directions, respectively. The detector also has a superior ^{60}Co gamma-ray sensitivity of less than 10^{-7}.

References

[1] T. Nakamura *et al.*, 2011 IEEE Nucl. Sci. Sym. Conference Record, NP1. M-179.

[2] T. Nakamura *et al.*, Nuclear Inst. and Meth. Phys. Res., A737 176 (2014).

T. Nakamura[1], K. Toh[1], T. Kawasaki[2], K. Honda[1], K. Sakasai[1], and K. Soyama[1]

[1]Neutron Instrumentation Section, Materials and Life Science Division, J-PARC Center; [2]Neutron Science Section, Materials and Life Science Division, J-PARC Center

Two-Dimensional Multiwire Neutron Detector with Individual Line Readout and Optical Signal Transmission

A position-sensitive neutron detection system that consists of a multiwire-type detector element was developed for the J-PARC/MLF BL17. A photograph of the detector head is shown in Figure 1. The sensitive area is 128 × 128 mm^2 with a pitch of 1 mm in both directions (x and y), and the 256 signal lines are individually readout by signal-processing electronics [1]. The system uses optical devices for a long-distance signal transmission and insulation between an irradiation area and a data acquisition room.

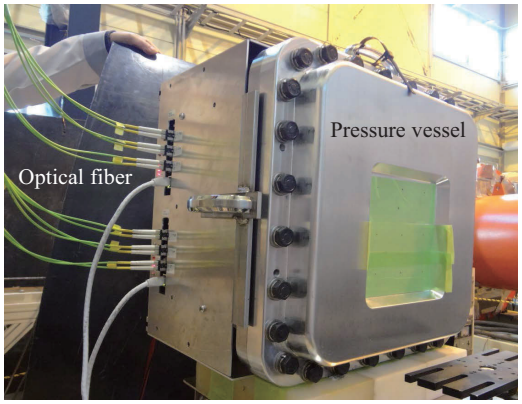

Figure 1. A photograph of the detector head.

Its basic performance was evaluated by an irradiation experiment using a Cf-252 neutron source [2]. The uniformity of all pixels in the two-dimensional image was 7.9% as seen in Figure 2. In our detector, the center of the track of secondary particles, proton and triton, is defined as the position of the incident neutron. Therefore, the intrinsic errors are caused by the differences of the track length between protons and tritons. The intrinsic errors are calculated from the records of all neutron event data and each track length of secondary particles, and plotted in one-directions in Figure 3. In the figure, the horizontal and vertical axes represent the error and the number of events, respectively. The intrinsic spatial error of the detector is evaluated by fitting the data with a Gaussian function, and the full width at half maximum (FWHM) of the spatial error is 1.55 mm.

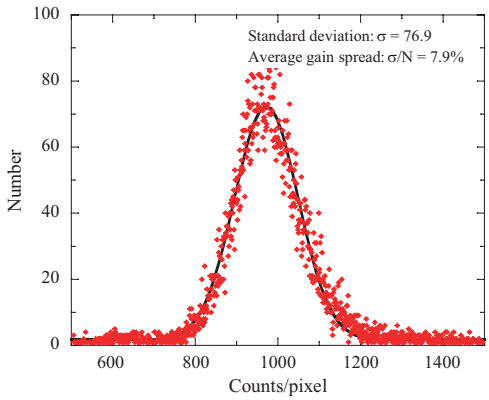

Figure 2. Histogram of the count distribution of the flat-field image.

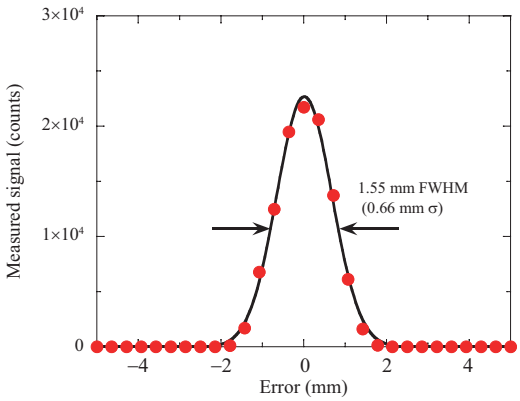

Figure 3. Errors in position detection.

References

[1] H. Yamagishi, K. Toh, T. Nakamura, K. Sakasai and K. Soyama, J. Instrum. **6** (2011) C12025.

[2] K. Toh, T. Nakamura, K. Sakasai, K. Soyama and H. Yamagishi, J. Phys.: Conf. Ser. **528** (2014) 012045.

K. Toh[1], T. Nakamura[1], K. Sakasai[1], K. Soyama[1], and H. Yamagishi[2]

[1]Neutron Instrumentation Section, Materials and Life Science Division, J-PARC Center; [2]Nippon Advanced Technology, Co. Ltd.

Study on the In-plane Magnetic Structure of the Neutron Polarizing Multilayer Mirror

1. Introduction

The neutron polarizing supermirrors are some of the most important optical elements to polarize neutron beams. Soft magnetic properties play a critical role in determining the performance of a polarizing supermirror because it needs to display high polarization efficiencies at low magnetic fields to meet a variety of research demands. The magnetic properties in thin films are known to be improved by annealing to eliminate stress and to alter the microstructure of the films [1]. This implies the importance of studies on the stress and microstructure of the films. Stress has been proven to be one of the key parameters for the soft magnetic properties of polarizing supermirrors in our previous work [2]. Regarding the microstructure, the magnetic properties of multilayers with polycrystalline grain size less than the ferromagnetic exchange length can be explained by the random anisotropy model, i.e. competition between the exchange interaction between neighboring spins and the local magnetocrystalline anisotropy [3]. Our purpose is to determine whether this model is valid in our system by observing the in-plane magnetic structure in the magnetization process. Off-specular scattering (OSS) measurement with polarized neutrons is a unique and powerful technique to observe the correlations of small magnetic objects in a layered system. This measurement gives access to the in-plane magnetic structure because the lateral correlation length obtained by the measurement corresponds to the size of an area with a uniform orientation of the magnetization. In this study, polarized neutron OSS measurement was performed for a Fe/Ge multilayer used for polarizing supermirrors.

2. Experimental

Polarized neutron OSS measurement was performed on the BL17 polarized neutron reflectometer with horizontal scattering geometry installed at the MLF of the J-PARC [4]. A polarized neutron beam with a wavelength range of $0.2 \leqq \lambda \leqq 0.8$ nm was available in BL17. The resolution in the momentum transfer in the out-of-plane direction was kept at less than 6.0%. The Fe/Ge multilayer, consisting of 15 bilayers with a bilayer thickness of 20 nm, was fabricated at JAEA by using an ion-beam sputtering system. The external field to the sample was set to 4.8×10^3 A/m, where the sample was magnetized to 70% of saturation, after being saturated in a field of 8.0×10^5 A/m opposing the guide field of the neutron beam. This value of the external field was chosen because the average deviation angle in areas with a uniform orientation of the magnetization in Fe layers can be considered as 45° so that the magnetic scattering equally contributes to the spin-flip and non-spin-flip channels. The data were collected by a single 3He tube because a 2-D position sensitive detector was not available in this beam time.

The measured OSS images are shown in Fig. 1. The specular reflection is located at $\alpha_i - \alpha_f = 0$, where α_i and α_f are the incident and exit angles, respectively. The first, second, and third Bragg peaks are observed at $\lambda = 0.7$, 0.4, and 0.28 nm, respectively. The scattering arising from the correlation of the interface roughness is seen in I_{++} channel when the momentum transfer in the out-of-plane direction satisfies the Bragg condition (corresponding to $(\alpha_i + \alpha_f)/\lambda = \text{const.}$ in Fig. 1). Such scattering is called a Bragg sheet and means that the interface roughness is correlated in the out-of-plane direction. Intense magnetic scattering is clearly observed in I_{+-} and I_{-+} channels where α_i or α_i coincides with the Bragg condition for spin-up state. This is caused by the large absolute value of the reflected amplitudes at the Bragg condition (corresponding to $\lambda = 0.68$ and $(\lambda - 0.8)/(\alpha_i - \alpha_f) = 0.57$ nm/deg in I_{+-} and I_{-+} channels, respectively, in Fig. 1). The obtained data demonstrated that BL17 is suited to measure the magnetic scattering from layered systems.

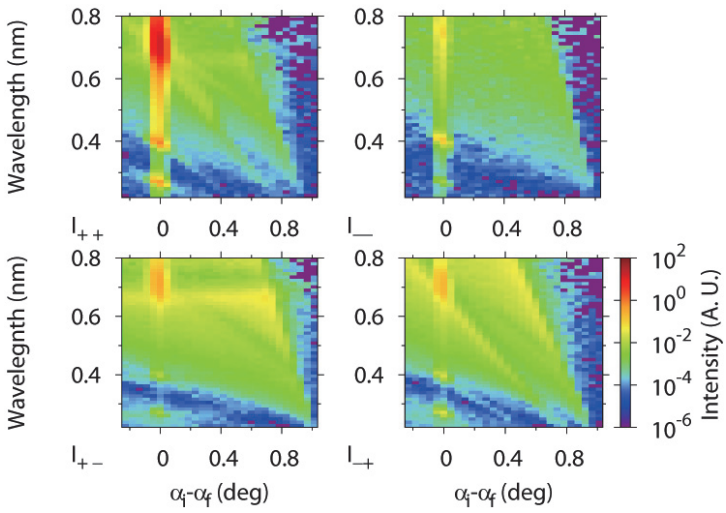

Figure 1. Measured polarized neutron OSS images for Fe/Ge multilayer consisting of 15 bilayers with a bilayer thickness of 20 nm.

3. Conclusions

Polarized neutron OSS measurement was performed on BL17 for a polycrystalline Fe/Ge multilayer with a grain size less than the ferromagnetic exchange length to gain insight into the mechanism that controls the magnetic properties, which are not present in the bulk. The magnetic scattering due to the fluctuated orientation of the magnetization with respect to the external field was successfully measured. The preparation of a detector covering a wide range of the scattered angle is definitely needed to increase the efficiency of the OSS measurement. The precise data analysis with a simulation based on the distorted wave Born approximation would lead to a good understanding of the in-plane magnetic structure of our system.

References

[1] W. Ishiwata, C. Wakabayashi, and T. Matsumoto, IEEE Trans. Magn. **24**, 3078 (1998).

[2] R. Maruyama, D. Yamazaki, S. Okayasu, M. Takeda, N. Zettsu, M. Nagano, K. Yamamura, H. Hayashida, and K. Soyama, J. Appl. Phys. **105**, 063904 (2012).

[3] G. Herzer, J. Magn. Mater. **112**, 258 (1992).

[4] M. Takeda, *et al.*, Chinese J. Phys. **50**, 161 (2012).

R. Maruyama[1], D. Yamazaki[1], H. Hayashida[1], M. Takeda[2,3], N. Miyata[4], K. Akutsu[4], and K. Soyama[1]

[1]Neutron Instrumentation Section, Materials and Life Science Division, J-PARC Center; [2]Quantum Beam Science Center, JAEA; [3]Neutron Science Section, Materials and Life Science Division, J-PARC Center; [4]Neutron R&D Division CROSS-Tokai

Scenes from the Neutron Experimental Hall

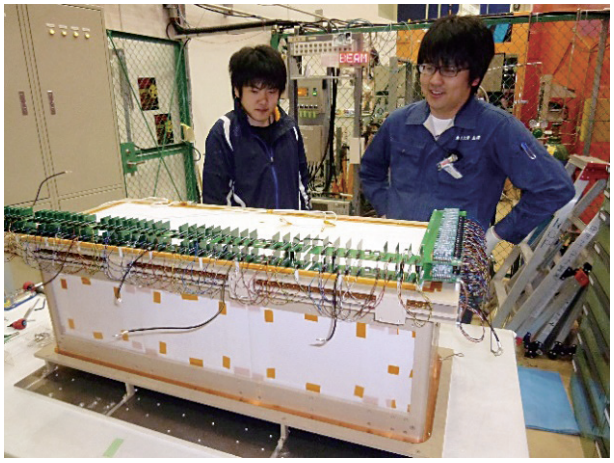

Genki Tanaka from Kyushu University (left) and Takahito Yamada from University of Tokyo (right) with a time projection chamber used for the neutron lifetime measurement at BL05.

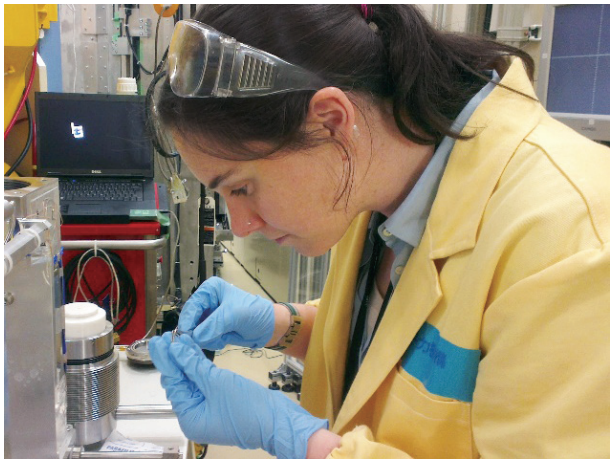

Maynard-Casely, Helen preparing the Mito cell for high-pressure neutron experiments at BL11.

Seiko Kawamura (left) and Tatsuya Kikuchi (right) setting the sample stick into a top-loading cryostat at BL14.

Norifumi Yamada checking a sample substrate for neutron reflectivity measurement at BL16 SOFIA.

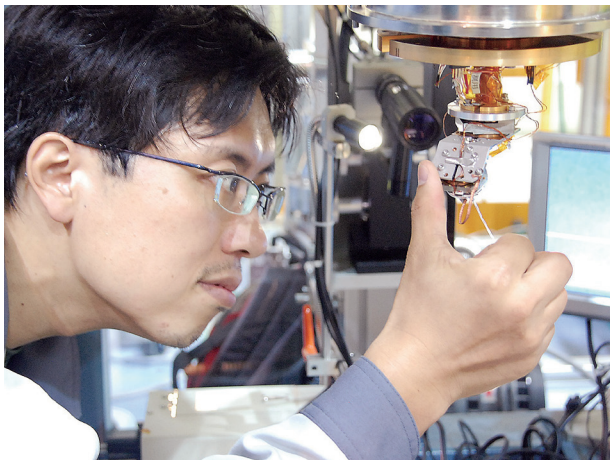

Takashi Ohhara checking and adjusting the 2-axes goniometer system of the cryostat for BL18, SENJU.

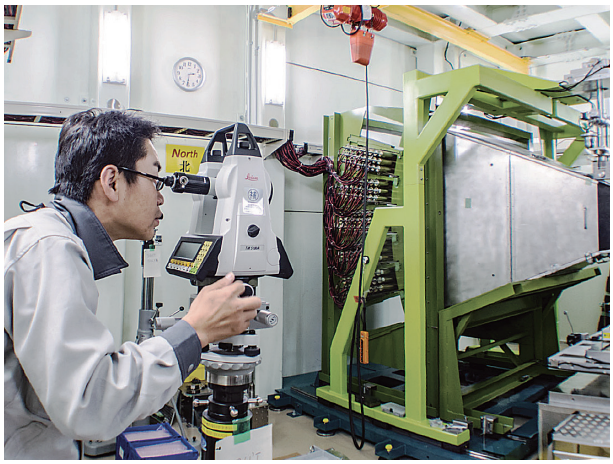

Takuro Kawasaki aligning a sample and optical devices at the Engineering Materials Diffractometer TAKUMI, BL19.

Muon Science

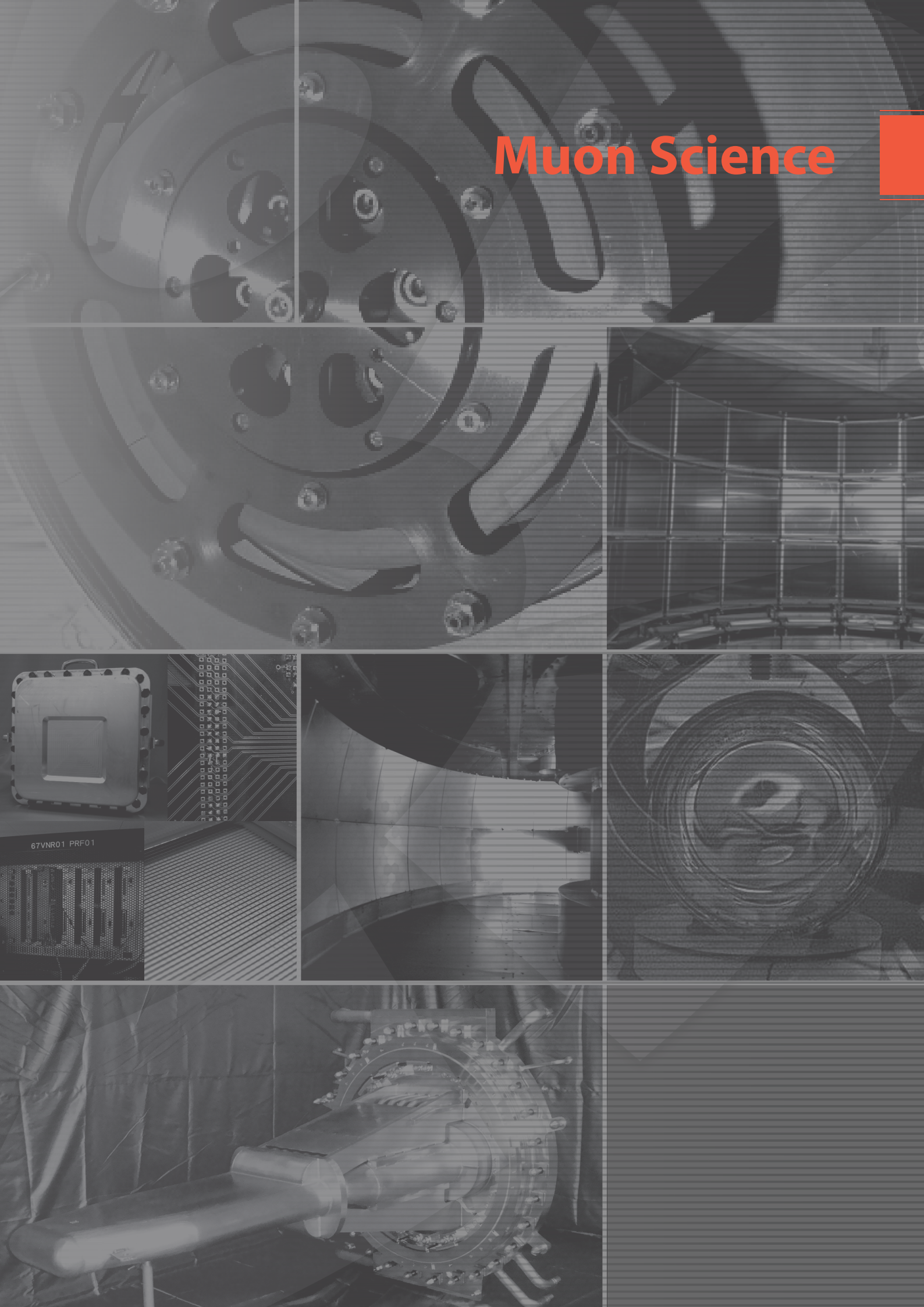

Status of J-PARC MUSE

The whole J-PARC operation had to be shut down in May 2013, because of the radioactive materials leakage incident at the Hadron Hall Experimental Facility. In this fiscal year, we worked on proving the reliability of the MUSE facility design and maintenance, which ensure the target's safety against radioactive materials leakage. Finally we managed to restart user's run in February 2014.

1. Reliability of the muon target safety

We have been adopting an edge-cooled non-rotating graphite target, the so-called 'fixed target,' because of its ease of handling during maintenance. In this target, graphite is indirectly cooled by the copper frame, which surrounds the graphite. This target assembly is equipped with 10 thermocouples. Those are incorporated into the interlock system. One is assigned to be MPS (Machine Protection System), and the other 9 thermometers are designed to alert the MLF shift leader at the MLF control room. Unlike the Hadron Facility, at the MUSE facility, we accept 3 GeV protons from RCS with the fast extraction, but not with the slow extraction. The graphite target is designed to accept 4 kW of heat deposit at maximum, with an irradiation of 1 MW from the proton beam, therefore it is not likely to be damaged.

This muon target assembly is contained in the large vacuum chamber, in the radiation control area. Even if the graphite evaporates, any radioactive contamination is designed to remain in the chamber. Also any exhaust from the chamber through the pumping is directed to the MLF stack, which is equipped with HEPA filters and a radiation monitoring system.

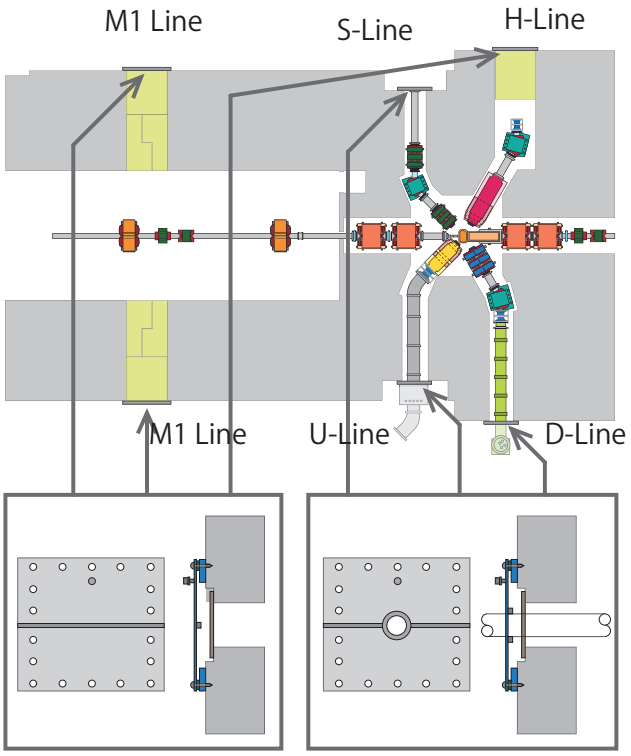

Figure 1. Six sealing hatches at the boundaries, for the D-Line, U-Line, S-Line, H-Line and two M1 beamline exits between M1, M2 tunnels & experimental areas.

2. Air-circulation

In the M2 tunnel, cooled air by a heat exchanger are designed to be supplied to the maintenance area (FL 4–6 m), and retrieved from the ducts under the M2 floor (FL 0.5 m), in order to prevent damage induced by NO_x, and to remove heat by about 5% of Joule heat from the six quadrupole magnets, four steering magnets, two sets of profile monitor assemblies, and nuclear reactions. The M2 tunnel air circulation system, as well as the M1 tunnel air circulation system, are designed to be circulating in the closed loop equipped with the pre-filter and HEPA filter. Therefore, any contamination is designed to be confined in the M1, M2 tunnel, not likely to be leaked into the outside of the control area, if the boundaries are sealed properly.

3. Sealing at the Boundaries

It is very important to have reliable sealing between the M1 and M2 areas where radioactive contamination can be produced by nuclear reactions, and experimental areas where users are breathing. There are six sealing hatches at the boundaries, for the D-Line, U-Line, S-Line, H-Line and the two M1 beamline exits between the M1 and M2 tunnels and the experimental areas. The structure of the sealing hatch is designed to be like double layers vacuum flange associated with rubber O-ring, which is shown in the inlets of Fig.1. We conducted helium leak check by introducing helium gas into the space between the double layers at the sealing hatch, which showed $1.2 \times 10^{-7} - 3 \times 10^{-6}$ Pa m^3/s of the leak rate. It turned out that the sealing hatch was very reliable, including the single layer's hatch. On the other hand, the experimental areas are equipped with HEPA filters and monitoring system to ensure radiation control even in the case of leakage.

Y. Miyake[1,2], N. Kawamura[1,2], K. Shimomura[1,2], P. Strasser[1,2], A. Koda[1,2], H. Fujimori[1,2], S. Makimura[1,2], Y. Kobayashi[1,2], J. Nakamura[1,2], K. Nishiyama[1,2], Y. Ikedo[1,2], K. M. Kojima[1,2], R. Kadono[1,2], W. Higemoto[1,3], and T. U. Ito[1,3]

[1]Muon Science Section, Materials and Life Science Division, J-PARC center; [2]Institute of Materials Structure Science, KEK; [3]Advanced Science Research Center, JAEA

Development of the Muon Production Target at MUSE

A pulsed muon beam with unprecedented intensity will be generated by a 3-GeV 333-microA proton beam on a muon target made of 20-mm thick isotropic graphite (IG-430) at J-PARC/MUSE (Muon Science Establishment). The energy deposited by a 1-MW proton beam is estimated to be 3.9 kW on the muon target [1]. The first muon beam was successfully generated on September 26th, 2008. Gradually upgrading the beam intensity, continuous 300-kW proton beam has been operated since January of 2013 [2, 3]. The current muon target with a fixed target method, called “muon fixed target”, has been utilized without replacements since the first muon beam generation. Proton irradiation causes radiation damage to material properties [4, 5]. In particular, the effect to the dimension is significant in our case. The proton-irradiation damage of the graphite in the case of the 1-MW proton beam operation shortens the lifetime of the muon fixed target to less than 1 year. Through evaluations of the irradiation damage, the fixed target was considered to be beyond its lifetime at that time of the scheduled long shutdown of 2013. To extend the lifetime, the developments of the muon rotating target, in which the radiation damage is distributed to a wider area, had been started since 2008 in parallel with the proton beam operation [6]. The developments, such as analyses, detailed designs, and durability tests with a heating and rotating mock-up were completed. Figure 1 shows the picture of the rotating target. Figure 2 shows the mock-up of the rotating target.

Safety reviews by relevant experts inside and outside J-PARC were conducted twice and the reviews validated the installation of the muon rotating target before the long shutdown of 2013. Figure 3 shows a picture taken during the reviews. However, considering the tight schedule and lack of manpower, we determined that we had to extend the time for installation of the muon rotating target. The muon rotating target will be installed in the scheduled long shutdown of 2014.

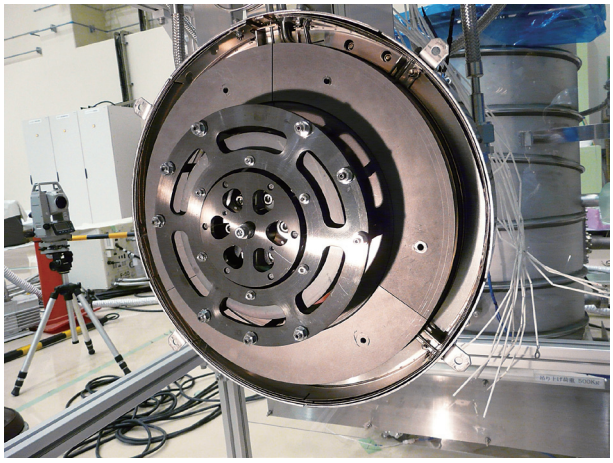

Figure 1. Picture of the rotating target.

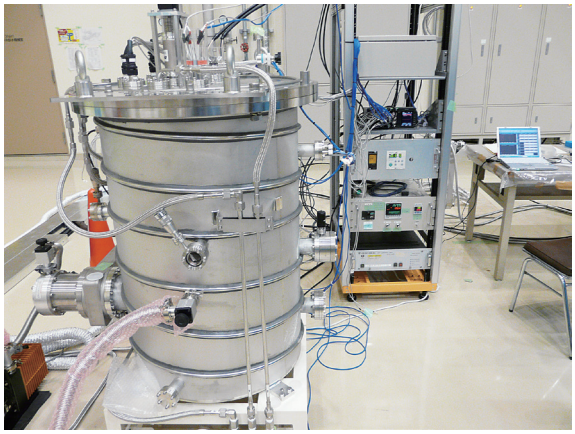

Figure 2. Picture of the mock-up for the rotating target.

Figure 3. Picture taken during the safety review.

Then, it was re-evaluated whether the use of the current fixed target could continue. The irradiation effect to the dimensional change of graphite is proportional to the irradiation dose in the anticipated range for our target. Actually, the rate of the dimensional change depends on the irradiation temperature. If the irradiation occurs below 570 K, the graphite will expand. If it occurs over 570 K, the graphite will shrink. The shrinkage rate is maximized at 1500 K to be 1% per 1 dpa (displacements per atom). Previously, the maximum shrinkage rate was applied to the evaluation of the lifetime from the point of view of a conservative approach. Then, the beam spot constrained by the un-irradiated surroundings was considered to shrink and crack. This time, the rate of the dimensional change depending on the irradiation temperature is applied to the evaluation. The irradiation temperature depends on the proton beam intensity, the beam profile on the muon target, and the thermal conductivities, which also depend on the irradiation dose. The thermal conductivities, which were actually obtained at MUSE [7], were introduced into the evaluation. As a result, the lifetime was confirmed to be long enough.

The muon fixed or rotating target is rigidly fabricated into the target rod. The target rod is integrated into the plug shield through four screws, which can be handled remotely. The assembled components are called target assembly. Because the muon target is highly activated by proton irradiation, the used muon target must be controlled by remote handling. The used target assembly will be transported by the shielding vessel, named muon transfer cask, and stored in the tentative storage pod at the Large Apparatus Handling Room, which is located at the floor level of 10 m [8]. Because the rotating target must stay in vacuum for corrosion control, a storage vessel for the muon rotating target assembly was installed in December of 2013, in addition to an existent vessel for the muon fixed target assembly. Figure 4 shows a picture of the tentative storage pod, in which the storage vessels. You can see the vessel for the fixed target on the left and the one for the rotating target on the right.

After short-term storage, the used target assembly will be transported to the remote handling room, i.e. Hot Cell. The used target rod on the target assembly is replaced with a new target rod. The new target assembly, of which the plug shield is re-used, will be transported to the beam line and installed again. For volume reduction of the highly radioactive components, the used target rod will be cut remotely into three pieces by the cutting device. They must be stored in the vessel with a function of support and enclosure, because they are not self-standing and radioactive. Because that vessel must be transported to another facility for long-term storage, it is called long-term storage vessel. The vessel must be transported by remote control, because its shielding is insufficient due to weight reduction. The long-term storage vessel was fabricated and the planning of the storage scenario was completed. Figure 5 shows a picture of the long-term storage vessel. The commissioning tests in Hot Cell will be performed from July to September of 2014.

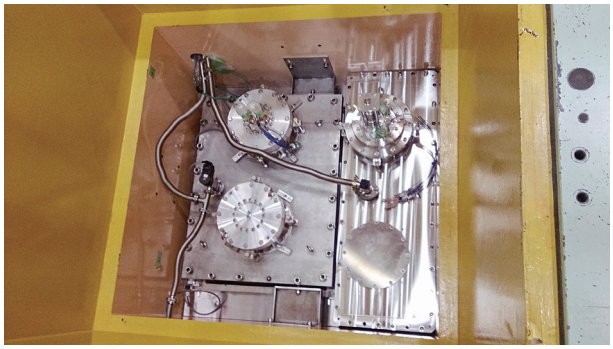

Figure 4. Picture of the vessels for the fixed and the rotating target in the tentative storage pod.

Figure 5. Picture of the long-term storage vessel.

References

[1] N. Kawamura *et al.*, Nuclear Instruments and Methods A 600 (2009) 114.

[2] S. Makimura *et al.*, Proceedings of the 8th Annual Meeting of Particle Accelerator Society of Japan, (2011) p1188–1191.

[3] S. Makimura *et al.*, Nuclear Instruments and Methods in Physics Research A:600 (2009) 146–149.

[4] T. Maruyama *et al.*, Journal of Nuclear Materials 195 (1992) 44–50.

[5] H. Matsuo, graphite 1991 [150] 290–302.

[6] S. Makimura *et al.*, KEK Progress Report 2010-3 M (2010) p6.

[7] S. Makimura *et al.*, Journal of Nuclear Materials 450 (2014) 110–116.

[8] S. Makimura *et al.*, Proceedings of the 7th Annual Meeting of Particle Accelerator Society of Japan, (2010) p479–483.

S. Makimura[1,2], N. Kawamura[1,2], S. Onizawa[3], Y. Matsuzawa[3], M. Tabe[4], Y. Kobayashi[1,2], R. Shimizu[3], Y. Taniguchi[1,2], H. Fujimori[1,2], Y. Ikedo[1,2], R. Kadono[1,2], A. Koda[1,2], K. M. Kojima[1,2], J. Nakamura[1,2], Y. Nakatsugawa[1,2], K. Nishiyama[1,2], K. Shimomura[1,2], P. Strasser[1,2], and Y. Miyake[1,2]

[1]*Muon Science Section, Materials and Life Science Division, J-PARC center;* [2]*Insitute of Materials Structure Science, KEK;* [3]*Nippon Advanced Technology Co., LTD (NAT);* [4]*Seekel Co., Ltd.*

Present Status of the D-Line

1. Spectrometer upgrade

The decay muon channel (D-line) of MUSE at J-PARC delivers 180,000 positive muons per pulse at the D1 experimental area for the 300 kW operation, which nowadays is regularly achieved. In order to take advantage of this high intensity of the pulsed muon beam for muon spin relaxation measurement (μSR), we have developed inexpensive and integrated detector system called Kalliope [1]. Employing 40 units of Kalliope detectors installed to a 0.4 T magnet, we have manufactured a 1280 channel (640 telescope pairs) spectrometer. The spectrometer is installed at the D1 experimental area as shown in Fig.1.

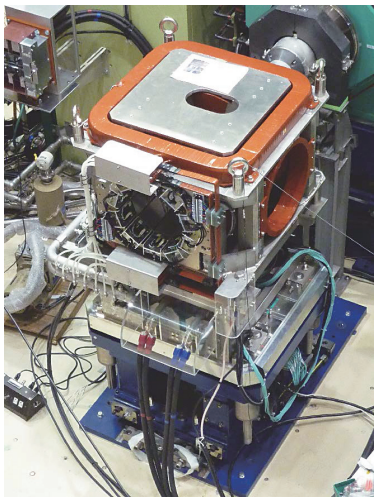

Figure 1. Full view of the new D1 spectrometer.

The arrangement of the Kalliope units relative to the magnet is shown in Fig.2. The ethernet hub, the NIM start-pulse distributor as well as the power supply for the Kalliope detectors are placed underneath the magnet, so that the cables are confined within the spectrometer.

We started a commissioning of the new spectrometer on February 18th, 2014, the day when the beam recovered after the Hadron incident. The procedure of the commissioning is (1) determination of the appropriate bias voltage (HV) for m-APD, threshold DAC (ThDAC) and amplifier DAC (AmpDAC) of ASIC, and (2) characterization of the μSR spectra such as the full asymmetry and the spectrum distortion. The m-APD is provided with a list of minimum operation voltages distributed within a 0.2 V range in our spectrometer (66.6–66.8 V). In order to perform (1), we have developed a computer program to scan the DAC values and record a preset number of accelerator pulses.

After determining ThDAC for a set of selective combinations of AmpDACs, we took the time spectrum of the μe decay (Fig.3) and tried to find the appropriate AmpDAC, ThDAC and bias voltages to ensure minimum distortion. Since we received 660k single hits in total for a 100 accelerator pulse, each counter received ~ 4 positron events (660k/120/1280 = 4.29) per pulse. This high rate of

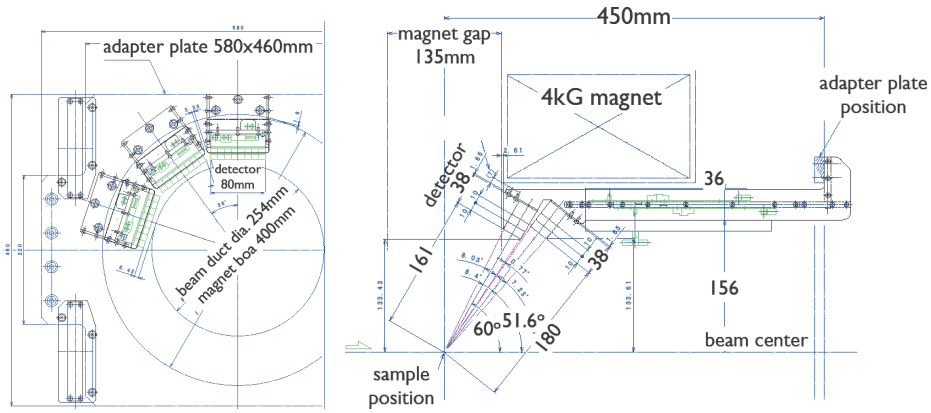

Figure 2. Diagram of the tail and the side view of the new D1 spectrometer.

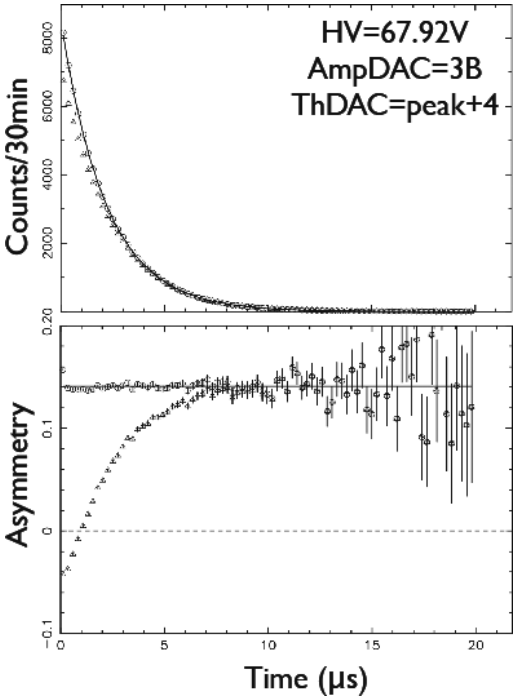

Figure 3. μe-decay spectrum (top panel) and asymmetry (bottom panel) of up-stream counter. Symbols are for before (triangle) and after (circle) the pile-up correction.

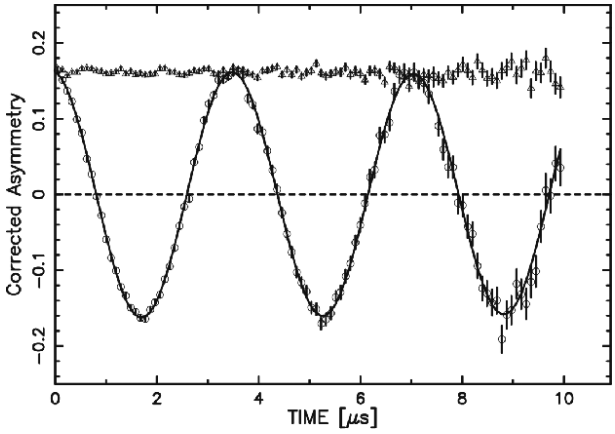

Figure 4. Forward-backward asymmetry of silver 20 × 20 mm sample in transverse-field of 2 mT and longitudinal-field of 10 mT. The data were taken within 10 minutes with kicker sliced single pulse operation.

decay positron signals resulted in a pile-up loss of counts in the early stage. We employed a theory of pile-up correction [2], and found that the simple non-extended correction scheme (eq.(2) of Ref. [2]) was sufficient to restore the μe-decay with the detector deadtime as an adjustable parameter. The characteristic detector deadtime was estimated to be $\tau \sim$ 100 ns for single counters. We phenomenologically used the same pile-up correction scheme for coincidenced counts which resulted in a longer deadtime of $\tau \sim$ 300 ns. This is because the registered counts in coincidence are reduced more than the single counts before coincidence, which determines the count loss. The deadtime could be improved eventually in electronics, because the recovery tail of the m-APD signal is typically ~ 40 ns.

In Fig.4, we show forward-backward asymmetry of a silver sample, after adjusting HV, DACs and deadtime parameters. The full asymmetry ~ 0.16 is significantly smaller than that of other general purpose μSR spectrometers (0.2–0.25), because the positron counters are placed at a high angle (51–60°: see Fig.2) relative to the beam axis, in order to maximize the detector solid angle while accommodating various kinds of inserts. Since the muon beam intensity is high enough, we plan to re-position the positron counters to gain higher asymmetry.

The data acquisition rate of the new spectrometer is 180 Mevents/hour for 20 × 20 mm sample in double pulse operation, being 4 times higher than that of the DΩ-1 spectrometer of J-PARC and/or the Argus spectrometer of RIKEN-RAL. This high rate of data accumulation requires an automated analysis procedure of μSR measurements, driving this technique to a new state of art.

2. Kicker system noise reduction

The muon kicker system is used to separate the muon pulses and feed them to two experimental areas (D1, D2) simultaneously. The dividing of the muon beam into two single-pulsed beams was successful, but required anti-noise measures. Later, the kicker noise level was drastically improved through RF-shield with copper sheets and refining both the ground lines of the kicker system and the detectors [3].

It turned out that the new spectrometer was influenced by the kicker noise even though in the prototype measures to reduce the kicker noise have been taken by refining the ground line of the detector. The new detector, which is an improved version, has circuit structures more susceptible to noise than the prototype.

An outline of the LC circuit is shown in Fig.5. The noise level of the new detector was ten times higher when the LC was connected with the power supply A compared to the power supply B. It was found that the source was RF noise from the LC itself, which was propagated through the power cables. The noise disappeared when two bypass capacitors were inserted between each terminal and the LC housing as shown in Fig.5. It should be noted that grounding to the LC housing was most effective among other groundings.

Five high-frequency capacitors of 20 nF in parallel were used as bypass capacitors at each terminal as shown in Fig.6.

Figure 7 shows a comparison between count rates resulting from the kicker noise with and without bypass capacitors. The noise levels were drastically improved after taking the above measures.

In regard to the influence of the kicker noise on the on-line refrigerator system for the superconducting solenoid magnet, a faulty operation of a bypass valve for thermoregulation in the refrigerator system caused by the kicker noise occurred during the beam time. The faulty operation of the bypass valve resulted in opening the load valve that controls the helium temperature. Fortunately that did not become a serious matter because the malfunction occurred only once during the day.

The bypass valve is controlled through a VME bus. Since noises arising from the kicker operation were confirmed at the housing of the VME bus, the ground line was reinforced with copper seats

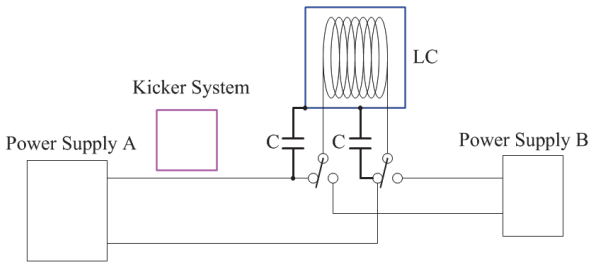

Figure 5. An outline of the LC circuit.

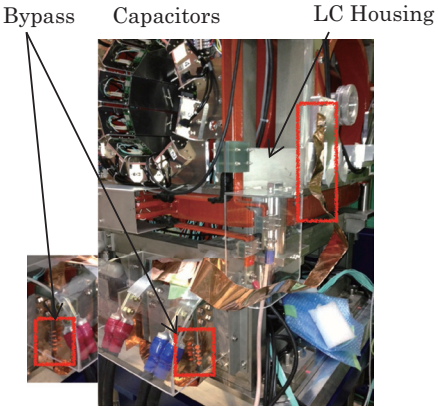

Figure 6. Bypass capacitors inserted between each terminal and the LC housing.

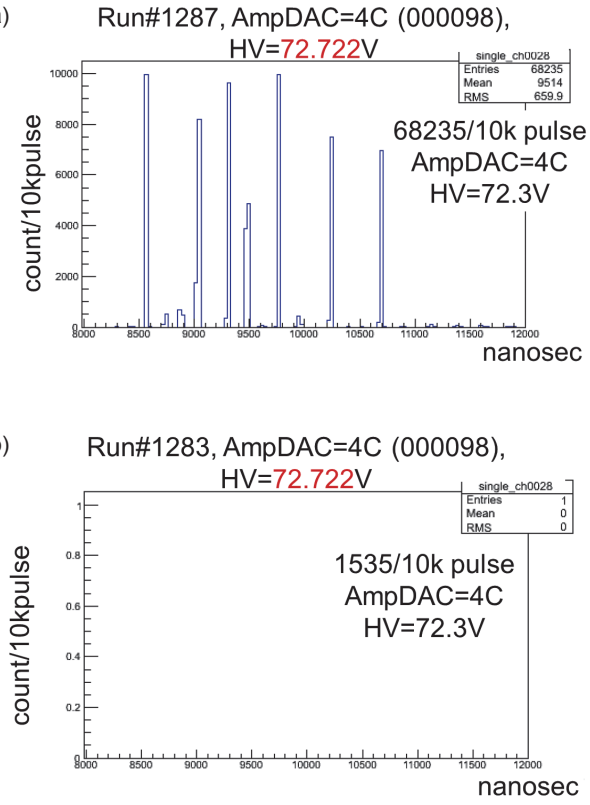

Figure 7. Count rates without bypass capacitors (a) and with bypass capacitors (b).

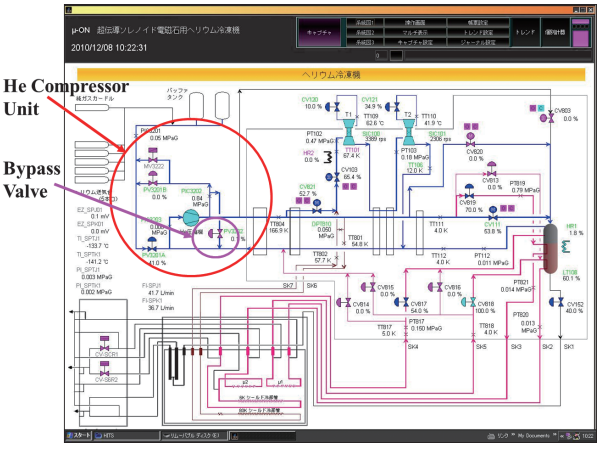

Figure 8. Monitoring system of the on-line refrigerator system.

to remove the high frequency components in the noise. Therefore, the noise level at the VME bus was decreased to about 1/4 as shown in Fig.9.

The urgent measures to reduce the kicker noise at the New D1-μSR spectrometer and the on-line refrigerator system succeeded. However, further improvements are required for negative muons and muonium experiments at the D2 area. Any conceivable means to reduce RF noises can be employed, therefore, electrically insulating the kicker chamber from the beam ducts and its base and reducing the ground impedance are considered as a next step.

A kicker system directed the two single-pulsed muon beams to the two existing experimental areas D1 and D2 simultaneously in March 2012. Now experiments with the new spectrometer in the D1 area can be performed with kicker-on without any noise problems, but the kicker noise level is still high to carry out experiments in the D2 area simultaneously. Further measures to reduce the kicker noise are in progress for the next beam operation.

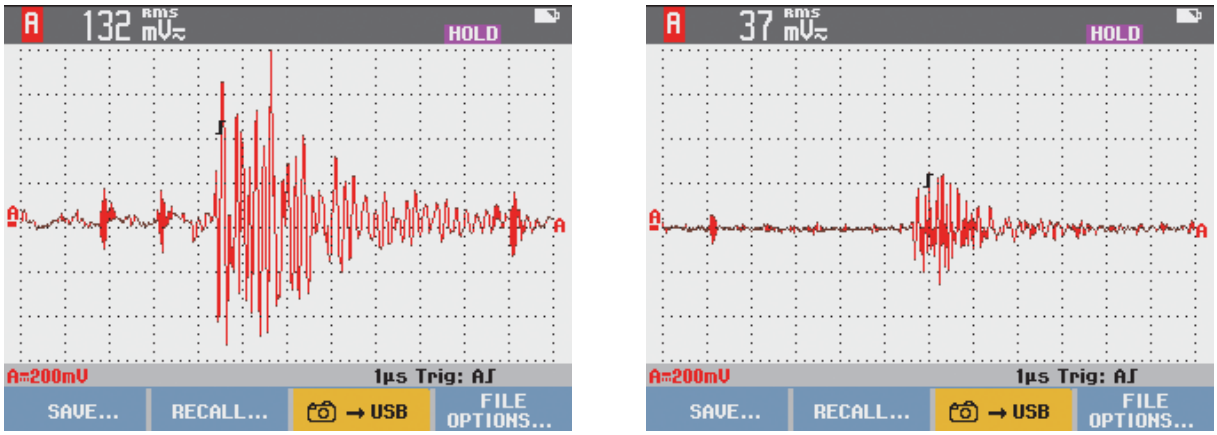

Figure 9. Noise level at the VME bus before/after improvement.

References

[1] K. M. Kojima *et al*., in KEK-MSL progress reports (2010, 2011 and 2012) and μSR 2014 proceedings, to appear in IOP Conference Series.

[2] T. Ida, and Y. Iwata, J. Appl. Cryst. **38** (2005) 426.

[3] H. Fujimori *et al*., KEK-MSL Report 2012 (2013) 16–17.

K. M. Kojima[1,2], and H. Fujimori[1,2]

[1]*Muon Science Section, Materials and Life Science Division, J-PARC center;* [2]*Institute of Materials Structure Science, KEK*

Present Status of the U-Line

1. Modification and upgrade of the U-line

At the Japan Proton Accelerator Research Complex (J-PARC), the second muon beamline, called U-line, was constructed in the Materials and Life Science Experimental Facility (MLF) [1]. The main role of the U-line is to provide an intense surface muon source for the ultra-slow muon beam [2]. The ultra-slow muon is an innovative muon beam that has novel characteristics, such as tunable energy from 0.1 to 60 keV, small beam size, below 5 mm in diameter, and short pulse width of 2 ns, and is expected to be a new subsurface and interface probe for investigating magnetism.

The installation of the U-line was completed in the summer of 2012, and the first beam extraction experiment and beam commissioning were performed right after the installation. These results have been already described elsewhere [9].

In general, the bulk of contamination in a muon beam comes from positrons, which have the same momentum as muons. The positrons are transported with the muon beam and may contribute as background signals in the detectors for several experiments that we are planning, such as the ultra-slow muon microscopy [2] and the g-2 experiment [3]. These positrons will prevent precise measurements, because the yield of positrons in the muon beam is a hundred times larger than that of muons, according to our simulation of the muon production process [4]. To avoid this problem, the positrons in the muon beam must be eliminated completely before the muons are focused on the experimental target. In order to ensure a wide separation of the same momentum particles, and also to keep the trajectories of the muons in a straight line for the muon transportation after the separator, we selected the Wien filter type separator for the U-line. The detailed properties and the dimensions of the separator, and the test for applying high voltage to the separators have been described elsewhere [9]. We found that it was very difficult to apply high voltage simultaneously, because of an electrical correlation between the separators. This might be due to some charged particles remaining between neighboring separators. To avoid this problem, we decided to change the transportation conditions of the axial focusing solenoid. We applied high voltage only to the second separator without exciting the two neighboring solenoids at the front and back, respectively. The transportation and focusing of the muon beam and positrons in the axial focusing solenoid were calculated using the Geant4 based Monte Carlo simulation program, G4beamline [8], and thus confirmed the muon beam transport and the elimination of the positrons from the muon beam [9] under these new conditions. Then, we started the beam commissioning experiments with applying up to $\pm$ 350 kV to the second separator.

We managed to extract high intensity muon beam in the U-line by applying the high voltage only to the second separator. To improve the stability of the high voltage power supply to the separator, *i.e.* to reduce the discharges in the power supply , we assume that the high electric field at the point of the high voltage power supply is reduced by changing the shape of the field relaxing ring of the power supply.

Since the third separator was not used in the new transport conditions, we decided to replace it with a fast closing valve (FCV). The FCV is required to protect researchers in the experimental hall from radiation exposure caused by unexpected accidents, which may occur in the area of the muon production target. The new design of the axial focusing solenoid is shown in Fig. 2. The size of the FCV is 320 mm in diameter; it is closed in several tens of a microsecond when the beamline vacuum worsens due to an accident. The FCV will be installed in the next summer shutdown of J-PARC in 2014.

The U-line was installed in the summer of 2012. The first muon beam extraction experiment was performed with only the second separator in operation. The result showed that the separator can

eliminate successfully the positrons from the muon beam. The muon rate was measured by μ-e decay counter and was 6.4 × 10^7 μ^+/s. This indicates that the U-line is currently the highest intensity surface muon source in the world.

According to the results of the test experiments for the separator and the beam commissioning, the modifications and upgrades of the U-line, such as the high voltage power supply of the separator and the installation of the FCV, are in progress.

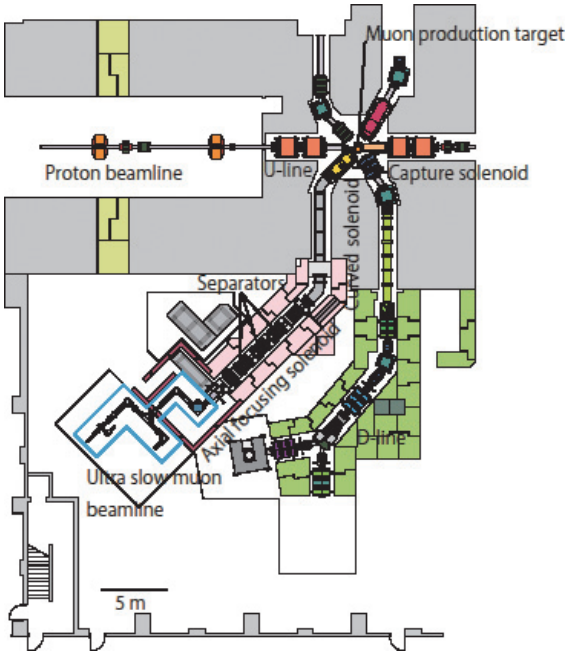

Figure 1. Layout of the muon area in experimental hall No. 2 of MLF/J-PARC.

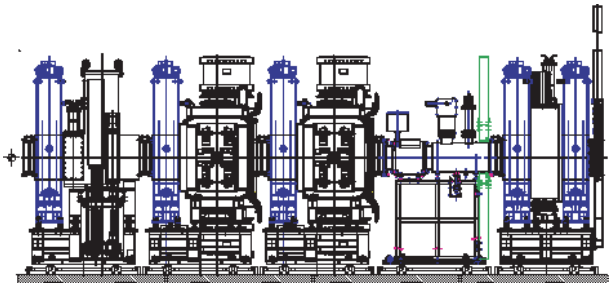

Figure 2. Picture of the muon beam profile at the focal position of the axial focusing solenoid.

2. Laser system

Nitrogen monoxide (NO) gas cell is used for measuring the intensity of coherent vacuum ultraviolet (VUV) pulsed radiations at the U-line. The concept of the NO gas cell is based on ion chambers, which are the simplest gas filled radiation detectors used for detection and quantitative intensity measurements of x-rays, particles and VUV radiations [10]. The gas cell was used at MSL-KEK [11], and a reevaluated one was prepared for the U-line. It contains parallel plate electrodes that accumulate nitrogen monoxide molecules ions.

Since the nitrogen oxide gas is toxic, it needs to be evaluated before using. When the NO gas is oxidized in the air, it converts into NO_2 gas. The reaction follows the following chemical formula and a third-order reaction rate equation.

$$2NO + O_2 \rightarrow 2NO_2$$

The NO_2 gas concentration is monitored by the NO-gas alarm detector. The occupational exposure limit value is 5 ppm, which should not be exceeded during any part of the working exposure. 25-ppm NO_2 gas irritates the eyes and the respiratory tract. Higher concentrations of NO_2 gas damage the lungs. Figure 4 shows a schematic diagram of the piping. The NO gas is used at the U1 area and a gas station. The gas station is under the stairs and goes up to the D cabin. The NO-gas pressure used at the gas cell is lower than 10 kPa. Even if NO gas leaks from the cell, the concentration is less than 0.3 ppm in a few minutes at the U1 area, and gradually decreases by the diffusion and the exhaust. The leak at the U1 area is considered to be a limited hazard. The worst potential accident would be a leak from a gas cylinder, which should be prevented with careful attention. In this case, the NO_2 concentration around the cylinder will increase by more than 10^3 ppm in a few seconds, and all the amount of the NO gas will be converted into NO_2 gas in 5 minutes. The concentration of the NO_2 gas at the experimental hall 2 is expected to decrease gradually through the air conducting, and become lower than 5 ppm in an hour. It means that the worst accident requires a one-hour evacuation.

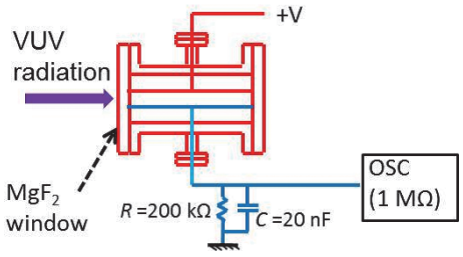

Figure 3. Schematic drawing of the electric circuit for the NO gas cell.

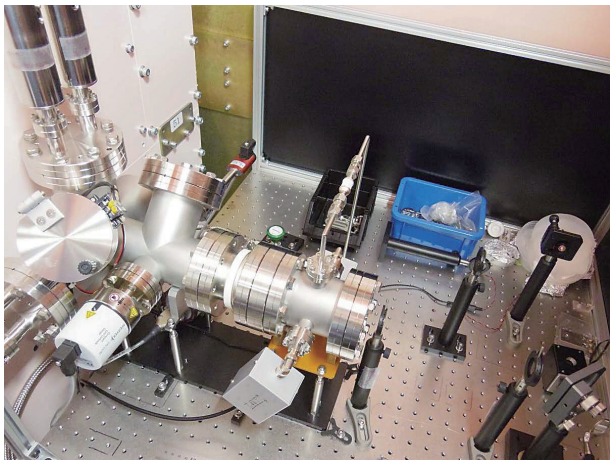

Figure 4. Photo of the NO gas cell at the U-line.

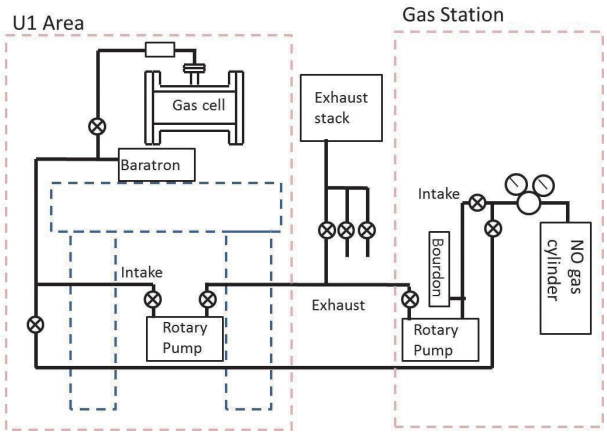

Figure 5. Piping for the NO gas cell.

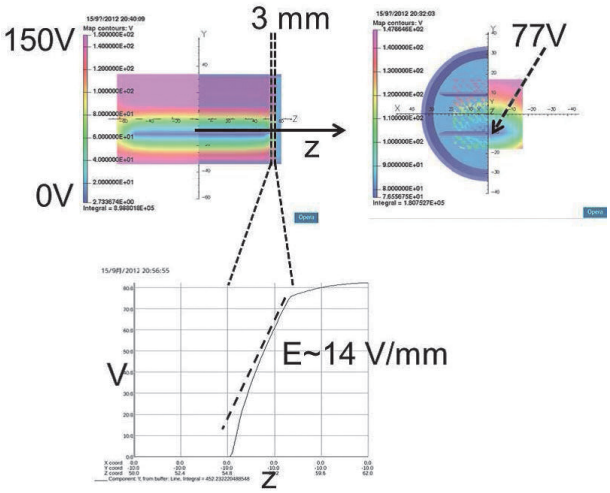

Figure 6. Electric field calculation of the NO gas cell.

The mechanism of the NO gas cell to detect the VUV radiation is following. The VUV radiation passes through the MgF_2 window, which is attached on an ICF114 flange, and ionizes the NO molecules. One of the parallel plates accumulates the NO^+ in the NO gas cell. The plate size is 104 mm (wide) × 50 mm (height), and the distance between plates is 20 mm. The ions rather than the electrons are considered to be collected, because of the photoelectric effect. The absolute intensity of the VUV radiation can be measured by simple analysis, because a molecule is ionized by one photon. Selective measurements of the VUV radiation are possible, because the absorption coefficient of the NO molecules for VUV radiation is larger than that for other coherent radiations [12]. It means that the NO gas is transparent for other radiations. Fig. 4 shows the electric field obtained by simulations of the NO gas cell with TOSCA / OPERA. The figure at the top left is the top view of the voltage distribution, and the figure at the top right is the side view. The figure at the bottom is an electric field between the window and the electrode plate. When the gap between the window and the electrode plate is shorter, a voltage drop near the window becomes larger. However, the electric field is not simply reduced. The efficiency of collection is considered to be dependant on the electric field. For effective collection of the NO^+, 3 mm is adopted for this gap. The 10-mm gap is estimated to create a smaller electric field.

Simple analysis from the measurement voltage to the intensity of the VUV radiation is following. After accumulating of the NO^+, a 20-nF capacitance (Fig.1) is charged Q_0 quickly. A measured voltage by an oscilloscope (OSC) follows the following formula. V, C, R, t is a voltage, a capacitance, a resistance, and a time, respectively. CR = 40 ms is suitable for our 25 Hz pulsed radiation.

$$V = Q_0 / C \exp(-t / CR)$$

If 1-mV high pulse is observed by oscilloscope, Q_0 is

$$Q_0 = V_0 C = 1 \text{ mV} \times 20 \text{ pF} = 2.0 \times 10^{-19} \text{ C}.$$

The intensity of 122-nm VUV radiation, EV UV is calculated with a charge of electron $Q_{electron}$ = 1.6 × 10^{-19} C, and a photon energy E_{photon} = 10.16 eV = 980.5 kJ / mol.

$$E_{VUV} = Q_0 / Q_{electron} \times E_{photon} = 2{:}0 \times 10^{-4} \text{ μJ}$$

The attenuation of the VUV radiation is also necessary to be considered. The total attenuation by mirrors and windows is estimated at approximately 0.45.

References

[1] Y. Miyake *et al.*, Physics Procedia **30**, 46 (2012)
[2] Y. Miyake *et al.*, AIP Conf. Proc. **1104**, 47 (2009)
[3] N. Saito *et al.*, AIP Conf. Proc. **1467**, 45 (2012).
[4] T. Adachi *et al.*, in preparation.
[5] Y. Ikedo *et al.*, Physics Procedia **30**, 34 (2012)
[6] Y. Ikedo *et al.*, Nuc. Inst. and Meth. B, in press (2013)
[7] K. Nakahara *et al.*, Nucl. Inst. and Meth. A **600**, 132 (2009).
[8] Muons, Inc. 522 Nm Batavia Avenue, Batavia, IL.
[9] Y. Ikedo *et al.*, in preparation.
[10] T. Kajiwara *et al.*, Rev. Laser Eng. **12,** 367 (1984); T. Masuoka *et al.*, Rev. Sci. Instrum. **45,** 1012 (1974)
[11] Y. Miyake *et al.*, Nucl. Inst. and Meth. B **95,** 265 (1995)
[12] K. Watanabe *et al.*, Phys. Rev. **91,** 1155 (1953)

Y. Ikedo[1,2], and J. Nakamura[1,2]

[1]*Muon Science Section, Materials and Life Science Division, J-PARC center;* [2]*Institute of Materials Structure Science, KEK*

Construction of the S-Line

The construction of the surface muon beamline (S-Line) in experimental hall No.1 of the Materials and Life science experimental Facility (MLF) building has started. In this fiscal year, the main beamline components to direct the muon beam toward the S1 experimental area, one of the four planned experimental areas, have been manufactured, as seen in Fig. 1. Three sets of triplet quadrupole magnets SQ7-8-9, SQ10-11-12, and SQ13-14-15 were fabricated by NEC TOKIN Corp. The basic design of the triplet magnets (magnet bore size of ϕ300 mm in diameter; magnetic pole length of 300 mm) is the same as that of DQ10-11-12, which was installed in the D-Line in experimental hall No. 2 by Advanced Science Research Center, Japan Atomic Energy Agency (JAEA-ASRC). In addition to this, the magnet support is detachable between the upper and lower parts, in order to facilitate the re-installation in the beamline after alignment. IDX Co., Ltd., refurbished the bending magnet SB2, which had been previously used in the D-Line as DB3. Hitachi, Ltd., newly designed and fabricated the septum magnet, which directs the beam towards the S1 and S2 experimental areas. The details of the septum magnet together with the new electric kicker system are discussed in another article in this issue [1].

The DC separator (SSEP) was manufactured by Irie Koken Co., Ltd., designed similarly to the one installed in the D-Line (DSEP); the electrode is 300 mm in width, 500 mm in length, the gap length is 200 mm, and the maximum applied high-voltage is $\pm$250 kV, respectively [2]. However, the HV feed-through was entirely modified. In the case of DSEP, HV is supplied through a ceramic insulator. In spite of the designed value of $\pm$250 kV, the operational voltage is limited to about $\pm$190 kV because of HV trips. On the other hand, in the case of the DC separator installed in the U-Line, the HV stack, which is designed to generate a HV of $\pm$400 kV by using a Cockcroft-Walton HV circuit, is directly attached to the vacuum chamber [3]. This avoids the exposure of the metallic part at HV to the atmospheric environment, thus preventing environment-related HV trips. Therefore, we decided to use the U-Line style HV power supply (PS) for SSEP. The HV PS's were manufactured by NICHICON Corp. with the same dimensions as those for the U-Line DC separator, so that the PS for the U-Line can be assembled with SSEP in the case of emergency. It is also noted that the connecting flange at the vacuum chamber is common with that of DSEP. If the PS of SSEP turns out to be operating successfully, possible upgrade of PS's for DSEP might be considered in the near future.

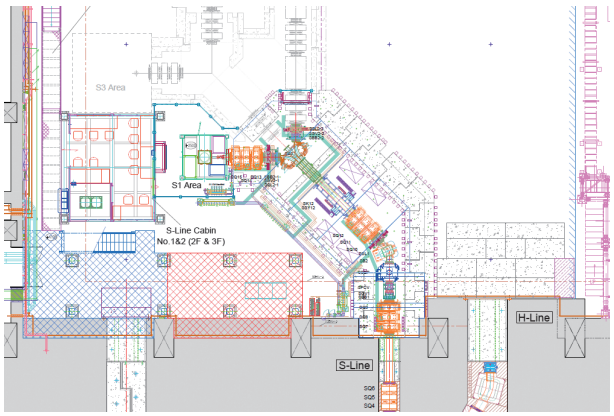

Figure 1. Beamline layout of the S-Line (phase1).

Figure 2. Construction of the power supply yard.

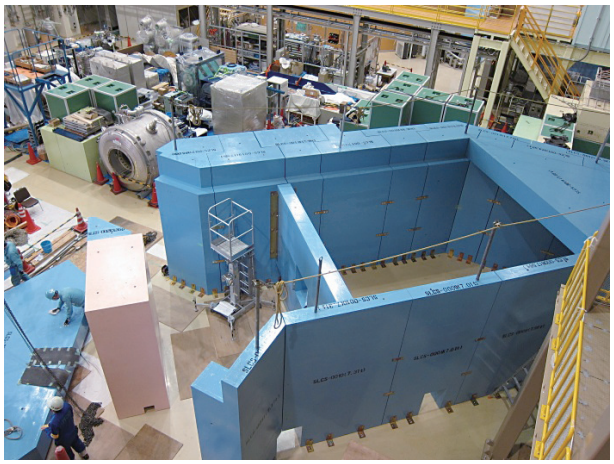

Figure 3. Installation of the S-Line concrete shields. The photo was taken without the ceiling shields.

In experimental hall No.1, the construction of the PS yard and the user cabins were completed, together with the plumbing works supplying cooling water to the PS's (Fig. 2). The PS yard consists of 3 floors. The upper deck is at 10 m above the floor level, which is the tallest structure constructed in experimental hall No. 1. The middle deck at the H-Line exit is connected to the mezzanine at the neutron experimental area. Nevertheless, emergency stairs between the upper and middle decks were installed. It is important to provide more than one evacuation route in case of emergency.

Shortly after the PS yard was completed, the concrete shields of the beamline were installed, as shown in Fig. 3. The shielding door and the beam stopper in the S1 experimental area, as well as the beam blocker in the S-Line beamline, were also placed; both are essential for the MLF operation, even though the muon beam is still not available at the S-Line. On the other hand, the new μSR spectrometer, which will be installed in the S1 area, as well as the equipment for data acquisition including the network data storage, were prepared by Kojima *et al.* [4].

The construction schedule of the S-Line was not finalized until the beam operation of MLF started again in February, 2014, after the long shutdown due to the radiation trouble at the J-PARC Hadron Hall in May, 2013. It turned out that the construction of the beamline by temporary removal of the concrete shields during the beam operation was difficult. Thus, the beamline components are going to be installed during the shutdown period in FY2014. The beam commissioning will start in the fall of 2014.

References

[1] P. Strasser *et al.*, KEK-MSL Report (this issue).
[2] K. Nishiyama *et al.*, KEK-MSL Report 2009, 7.
[3] K. Nishiyama *et al.*, KEK-MSL Report 2011, 19.
[4] K. M. Kojima *et al.*, KEK-MSL Report (this issue).

A. Koda[1,2], P. Strasser[1,2], N. Kawamura[1,2], H. Fujimori[1,2], K. Nishiyama[1,2], and J-PARC Muse staff
[1]*Muon Science Section, Materials and Life Science Division, J-PARC center;* [2]*Institute of Materials Structure Science, KEK*

Present Status of the H-Line

A brand new beam line, H-line, is planned to be constructed as the 4th beam line in MUSE. The new beam line is designed to have a large acceptance, momentum tune-ability, and the ability to be used as a kicker magnet and Wien filter. This beam line will provide an intense beam for experiments, which require high statistics and need to occupy the experimental areas for relatively long period. Several experiments in the field of fundamental physics studies have been proposed in the H-line [2-4].

From the muon production target, it is possible to extract 4 muon beam lines. The H-line is extracted to the south east direction.

At the primary stage of MUSE construction, only the D-line and the frontend magnets in the S-line were installed, and then the frontend magnets in the U-line were installed in 2009. In the H-line, temporary radiation-shield blocks were placed. J-PARC has been operating since 2008, and thus the activation around the muon production target becomes more serious year by year. According to the evaluation using a Monte-Carlo code [5], the dose rate beside the target chamber was estimated to be close to 1 Sv/h, and the summer shutdown in 2012 would be the actual time limit to install the frontend magnets in the H-line. Thus, the installation of the frontend devices, *i.e.* the muon-capture solenoid, HS1, the first bending magnet, HB1, and the vacuum components took precedence and were installed in 2012 as shown in Fig. 2 and 3. The measured highest radiation dose rate was about 250 mSv/h in the iron block placed just beside the target chamber. This is consistent with the prior evaluation. Thus, the construction scenario based on this estimation was confirmed to be reasonable.

In the other high intensity beam line in MUSE, the U-line, we adopted only axial focusing magnets to obtain high transmission efficiency [6]. On the other hand, in the H-line, the beam captured by an axial focusing large-aperture solenoid magnet

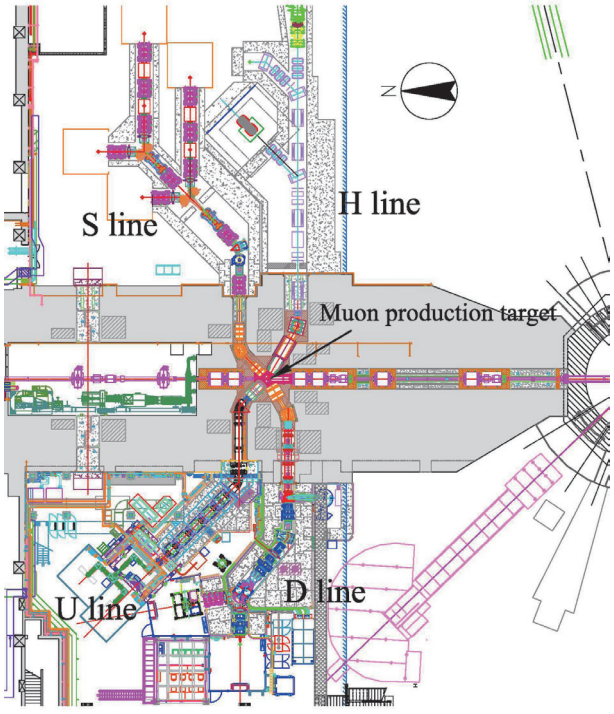

Figure 1. A layout plan of MUSE.

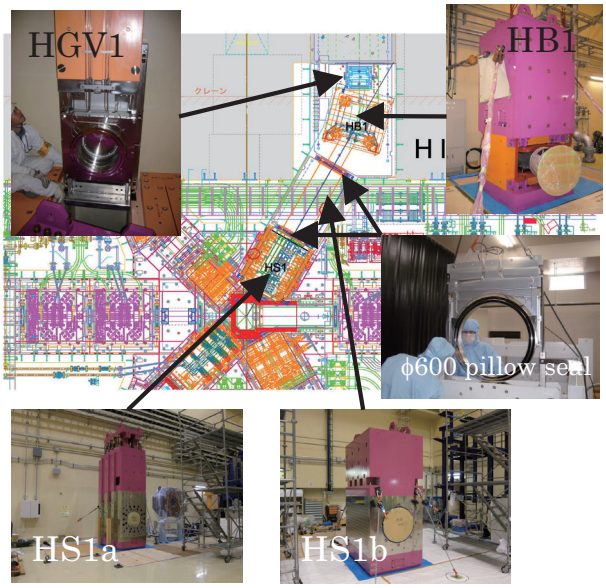

Figure 2. Devices installed in 2012.

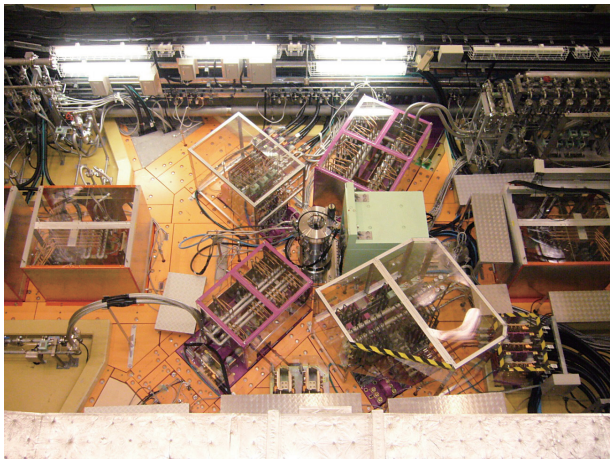

Figure 3. Picture taken on October 4 after completing the installation of the major devices.

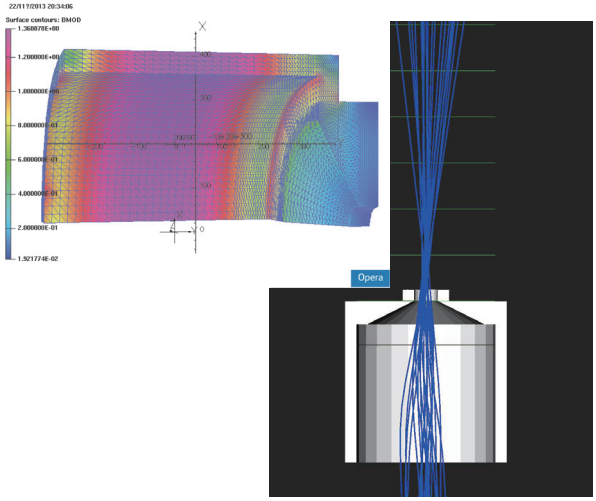

Figure 4. Final focusing magnet for g-2/EDM; field map (left) and beam trajectory (right). In this model, a solenoid magnet is examined with a field clump as an option.

is transmitted through bending magnets, although these non-axial focusing magnets increase the beam loss. To compensate for this and ensure high transmission efficiency, large aperture magnets and other devices are adopted in the H-line. A typical size of the aperture is 600 mm in diameter.

The magnets and other devices in the downstream are being designed. These devices are placed in the experimental hall, and thus they have many design options in sense of material selection, geometrical size and position and so on. In order to provide a satisfactory muon beam to all the planed experiments in the H-line, designing work is performed with the collaborations of the proposed experiments. For instance, the g-2/EDM experiment [3] needs to focus the surface muon beam on the muonium production target, which will be installed several tens cm apart from the exit of the last magnet. The beam spot size is required to be as small as possible. In addition, the magnetic field in the muonium production target is required to be smaller than 1 mT, thus the leakage field of the beam line magnet is not negligible in general. Several ideas are considered for the final focusing magnet. Figure 4 shows a typical result in a case using a solenoid magnet with a field clump.

The designing work of the radiation shield is also in progress similarly to the other beam lines [5]. Along the beam line a few meter thick concrete shield will be necessary to enclose the streaming neutrons and other radiation sources. Because the H-line adopts large aperture devices, the effects of the streaming neutrons are more serious than at the other beam lines. The evaluation of the streaming neutrons is important not only for the radiation safety but also to check its effect on the detectors and other devices in the experimental area. Figure 5 shows a typical result of the simulation. During the time when the proton beam is on, the dose rate in the experimental area is expected to exceed 100 μSv/h, and no one can enter into the area. By inserting a beam blocker which is a 40-cm thick copper block, the dose rate is decreased by a factor of ten. The beam blocker is essential for the interlock system.

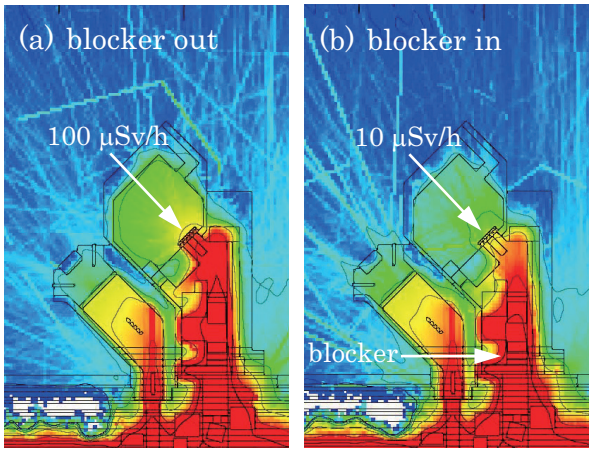

Figure 5. A typical simulated result of the radiation dose around the H-line. To enter the experimental area, a beam blocker is inserted on the right while no blocker is used on the left.

In the summer shutdown in 2014, the radiation shield between the M2 tunnel and the experimental hall is planned to be modified and reinforced for the preparation of the H-line construction in the following year.

References

[1] N. Kawamura *et al*. *2013 Journal of Physics: Conference Series* **408** 012072

[2] K. Shimomura *et al*. *ibid*.

[3] N. Saito *et al*. *ibid*.

[4] S. Mihara *et al*. *ibid*.

[5] N. Kawamura *et al.* 2009 *NIM A* **600** 114.

[6] K. Nakahara *et al.* 2010 AIP Conf. Proc. **1222** 420.

N. Kawamura[1,2], MuHFS collab., DeeMe collab., and g-2/EDM collab.

[1]*Muon Science Section, Materials and Life Science Division, J-PARC;* [2]*Institute of Materials Structure Science, KEK*

Scenes from the Muon Experimental Hall

Rotating muon production target to be installed in 2014 is assembled by the target team led by Shunsuke Makimura.

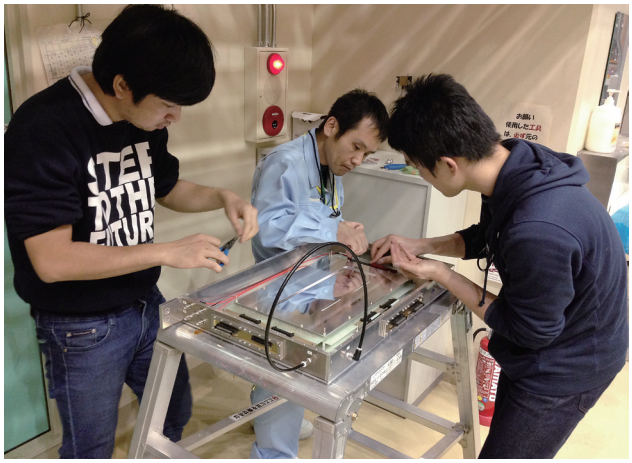

Yohei Nakatsugawa and his collaborators assembling a wire chamber which is a proto-type for DeeMe experiment planed in H-line.

A new muon beam profile monitor designed by Takashi Ito is installed to monitor the beam profile after replacing the spectrometer in D1 area.

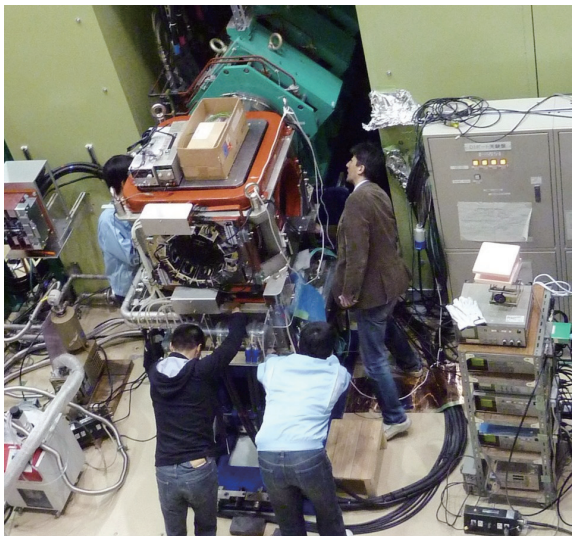

A new μSR spectrometer is installed in D1 area by Kenji Kojima, Masatoshi Hiraishi, Ichihiro Yamauchi, and Hua Li.

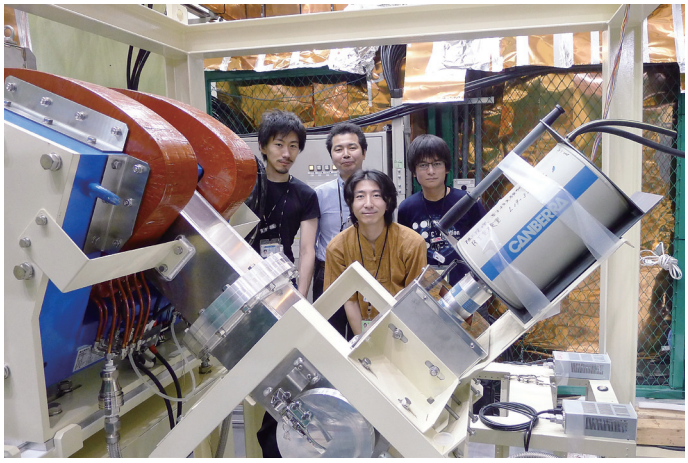

Kazuhiko Ninomiya, Makoto Inagaki, Go Yoshida (Osaka Univ.) and Takahito Osawa (JAEA) installing a new muonic X-ray spectrometer in D2 area toward non-destructive elemental analysis of a meteorite.

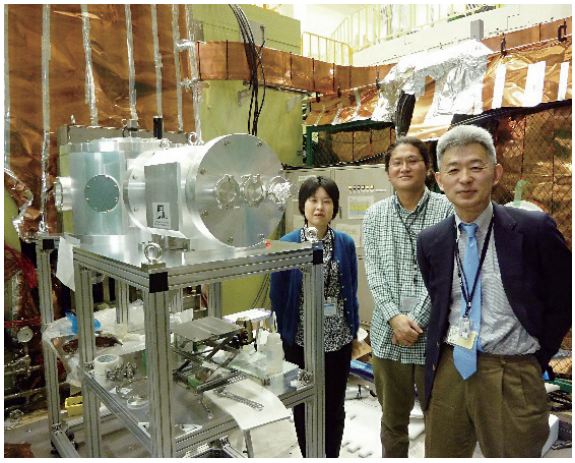

Jun Sugiyama, Izumi Umegaki (Toyota central R&D Lab.) and Motonobu Tampo conducting a test experiment for motion of Li in a battery by detecting muonic X-rays.

Radiation Safety

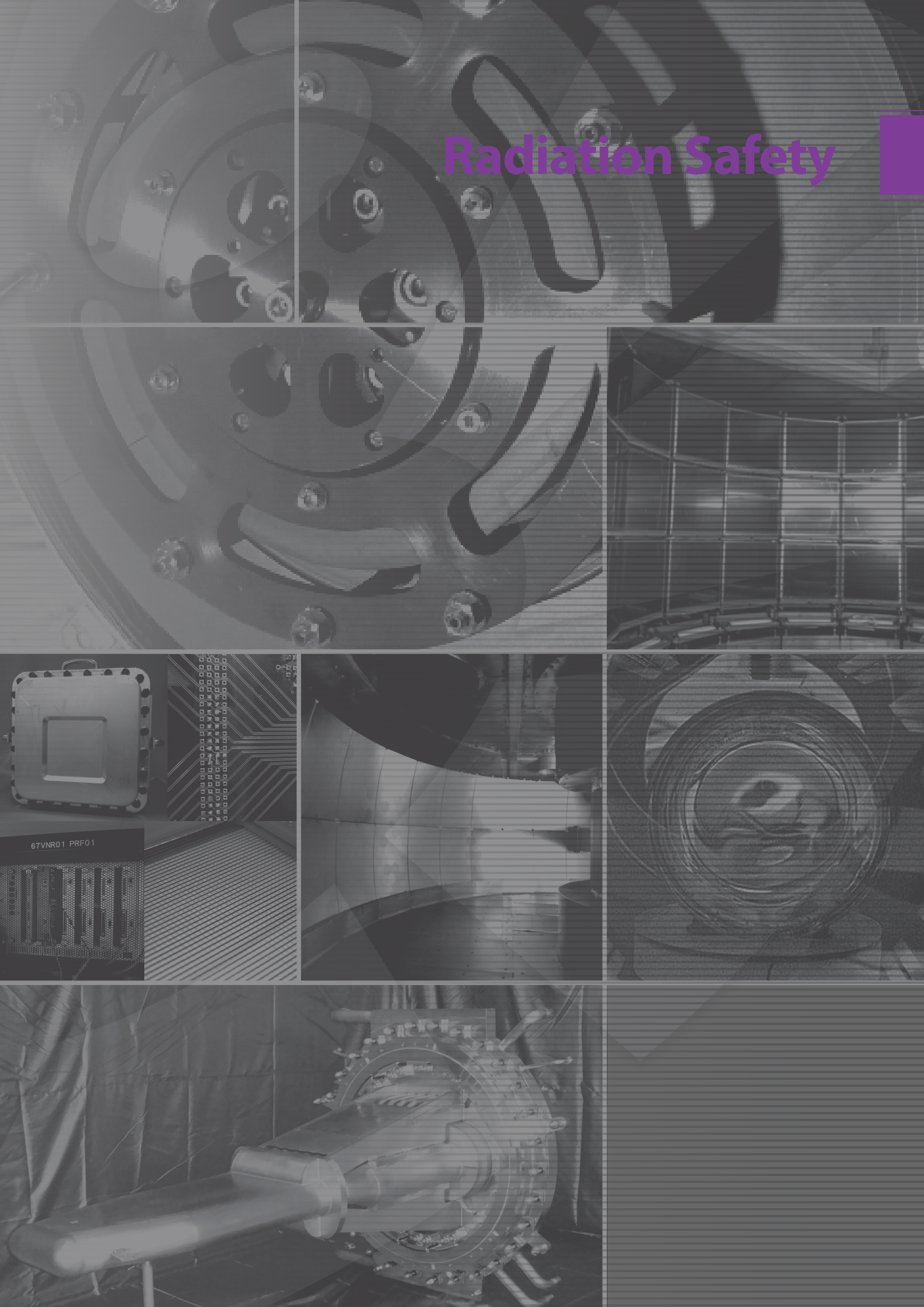

Radiation Safety

1. Revision of the J-PARC safety policy after the radiological incident at the Hadron Facility

The radioactive material leak incident occurred at the Hadron Experimental Facility (HD) on May 23, 2013, by accidental incidence of an abnormally short proton beam on the gold target [1][1]. The gold target partially melted after being rapidly heated, and the radioactive products accumulated within the target were released into the experimental hall since the air-tightness of the target and the primary beam line was insufficient.

Because of the incident, the beam operation was stopped immediately by the interlock system, which told us that an abnormal beam has been extracted to the target. In addition, the radiation dose in the experimental hall gradually increased to 4 μSv/h, which was definitely higher than usual. However, since such information was not collected and analyzed adequately, nobody could recognize what was really happening for several hours after the incident. The staff and the users stayed in the hall after the incident, even though the Hadron Experimental Hall was entirely contaminated with radioactivity. As a result, they received internal exposure[2].

Furthermore, since the ventilation fans of the hall were operating, radioactive materials were released uncontrollably into the environment outside the radiation controlled area[3].

The applicable laws and regulations say that we have the responsibility to report immediately radiological incidents to the national authorities and the local government. Since we misread the scales of the personnel exposures and the environmental release of radioactive materials in the early stage, the first report to the authorities was delivered at 10 p.m. on May 24; this means that one and half days had passed since the primary incident happened.

After we reported the incident, the beam operation of all J-PARC, including the Materials and Life Science Experimental Facility (MLF), had to be stopped indefinitely.

In order to resume the operation, we made significant efforts to check the radiation safety of all facilities other than HD, especially from the view point of radioactivity confinement capability. In addition, we established a new system for emergency response to abnormal incidents. Before the HD incident, we had only one status for response to a serious incident, called “Emergency” status. We learned from the HD incident that we should have an intermediate status for an abnormal incident before it develops into a serious accident; we call it “Alert” status. The conceptual drawing of the structure of the three kinds of risk-management status is shown in Figure 1.

The revision of the J-PARC risk management plan was reviewed by an external expert panel and reported to the national authority, the local governments and inhabitants in the vicinity of J-PARC. All staff members and users were introduced to the new safety framework and emergency drills were conducted several times. The operation for the MLF user program could be started on February 17, 2014[4]. This means that it took 8 months to resume the beam operation after the HD incident.

In the next chapter we cover in detail what was done to restart the MLF operation.

---

[1] At 11:55, due to the malfunction of the power supply system of a beam extraction magnet of the 50 GeV synchrotron, 2×10^{13} protons were extracted in 5 msec. (In the normal operation 3×10^{13} protons are slowly extracted over 2 sec.)

[2] The total number of personnel working in the radiation controlled area of HD during the incident was 102. As a result of the measurements with a whole-body counter, it was found that 34 personnel received detectable internal exposure in the range of 0.1-1.7 mSv.

[3] The “ventilation fun” is just a fan without filtering function for radioactive material. Ventilation system with filtering function had not been equipped in the hadron hall because that was assigned as an uncontaminated controlled area.

[4] It will take longer to resume the beam operation of HD since it will require the target exchange and upgrade of the ventilation systems.

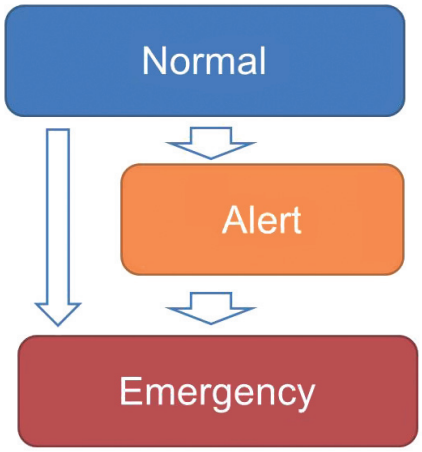

Figure 1. The conceptual structure of the new risk management system of J-PARC. The "Alert" status is newly installed between "Normal" and "Emergency". In the "Normal" status, a shift leader makes a declaration of transition to the "Alert" status when a specified event such as alarm activation from the Personnel Protection System occurs. In the "Alert" status, the facility manager or the deputy manage the status, and they are responsible for collecting information and analysis of the event together with the facility staff. If they find that the incident is developing or may develop to a real accident, he declares transition to the "Emergency" status. (In some cases such as fire or an undoubtable real accident, the shift leader has to make the transition directly from "Normal" to "Emergency" status.) In the "Emergency" status, the emergency headquarters are set up at the Tokai site.

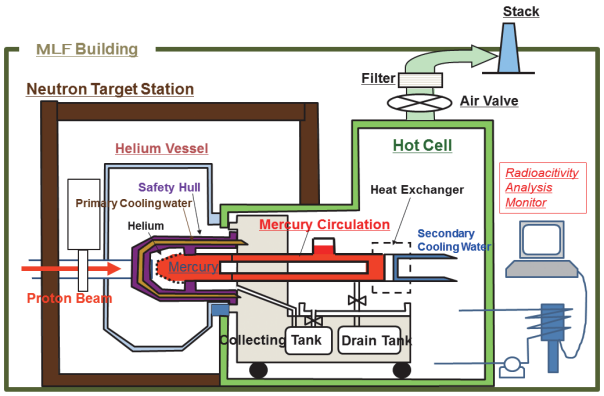

Figure 2. Conceptual drawing of the multiple protection system for radioactivity confinement of the neutron target at MLF. The mercury target has a double wall structure: the mercury container is covered by the safety hall which has channels of primary cooling water. Therefore, if the mercury container is ruptured due to pressure wave etc., leakage of radioactive mercury spills could be prevented. In addition, the helium vessel and the confinement of the neutron-target station also work as barriers for radioactivity. On the other hand, the mercury circulation located in the hot cell is single-barrier system: the single-barrier just corresponds to the piping wall of the circulation system, because there is little possibility for leakage from the piping. Nevertheless radioactive materials in the hot-cell are always monitored during the proton-beam operation in order to detect a small leak of radioactivity and to take measures to stop leakage as soon as possible.

2. Efforts to resume the MLF beam operation

The first thing we had to do to restart the MLF operation was to recheck the radioactivity-confinement capability of MLF by taking abnormal incidents into account and to explain the result to the proper authorities and the external expert panel. The drawing used for explanation of the concept of radioactivity confinement at MLF is shown in Figure 2.

The second thing was to introduce the new risk-control framework to the MLF management. Therefore, all operation and user manuals were fully revised. In addition, the following new manuals were introduced: shift leader manual, emergency calling manual, user-evacuation manual and instrument manager manual.

The third thing was training based on the new framework. All MLF staff, including CROSS and Ibaraki Prefecture staff, participated in the training. For user training, new video material was produced.

The fourth thing was to carry out emergency drills for radioactive-material leak incidents. The first drill was carried out on September 13, and the second one was done on November 15, 2013. The second drill was positioned as the final test before resuming the MLF operation, so that the performance was inspected by the local governments around the site[5]. The drill scenario was as follows:

- Radioactive gases are detected by the radioactivity monitor in the hot cell,
- Declaration of transition to "Alert" status by a shift leader,
- Collecting and analysis of radiation monitor data and other information under the direction of the MLF manager,

[5] The performance of the second drill was reported by a local TV station and a newspaper.

- Recognizing the mercury leak from the mercury circulation system,
- Declaration of transition to “Emergency” status by the MLF manager,
- User evacuation and radiological survey,
- Taking measures to stop the leakage,
- Reporting to the proper authorities .

3. Radiological license upgrade

Normally we have two chances of the application on radiological license upgrade in a year. This year, applications on the following items had been planned for each chance. In the first application, the following items were to be applied for:

a) Upgrade the proton beam power from 350 keV to 600 keV,
b) Installation of the slow-muon beam line,
c) Installation of the neutron beam line BL06,
d) Minor changes to the shielding configuration for preparation of installation of the new neutron beam lines BL22 and BL23,
e) Setting a radiation controlled area to the extended building hosting BL09.

In the second one, we planned the application on the following:

f) New installation of the BL22.

However, since the application procedure was delayed seriously due to the HD incident, we had only one chance in the year and we had to remove the items (a), (e) and (f) from the application. As a result, we could only apply for (b), (c) and (d). The application for (a), (e) and (f) was postponed for the next fiscal year.

Reference

[1] The detailed information on the HD incident can be found on the J-PARC web site. The address of the Japanese page is http://j-parc.jp/index.html and the English page is http://j-parc.jp/index-e.html.

Y. Kasugai
Neutron Source Section, Materials and Life Science Division, J-PARC Center

Scenes from the Emergency drill

Masatoshi Arai (Division Head) instructing at the MLF control room.

Members of the local emergency response headquarters of JAEA-Tokai site participating in the emergency drill.

Liaison team receiving messages from the JAEA local emergency response headquarters at the MLF control room.

The staff checking the MLF beam status on a display at the MLF control room.

The users evacuating from the MLF experimental hall with the user evacuation support team.

The users undergoing radiation survey at the MLF entrance after evacuation from the experimental hall.

What's new at the MLF in 2013?

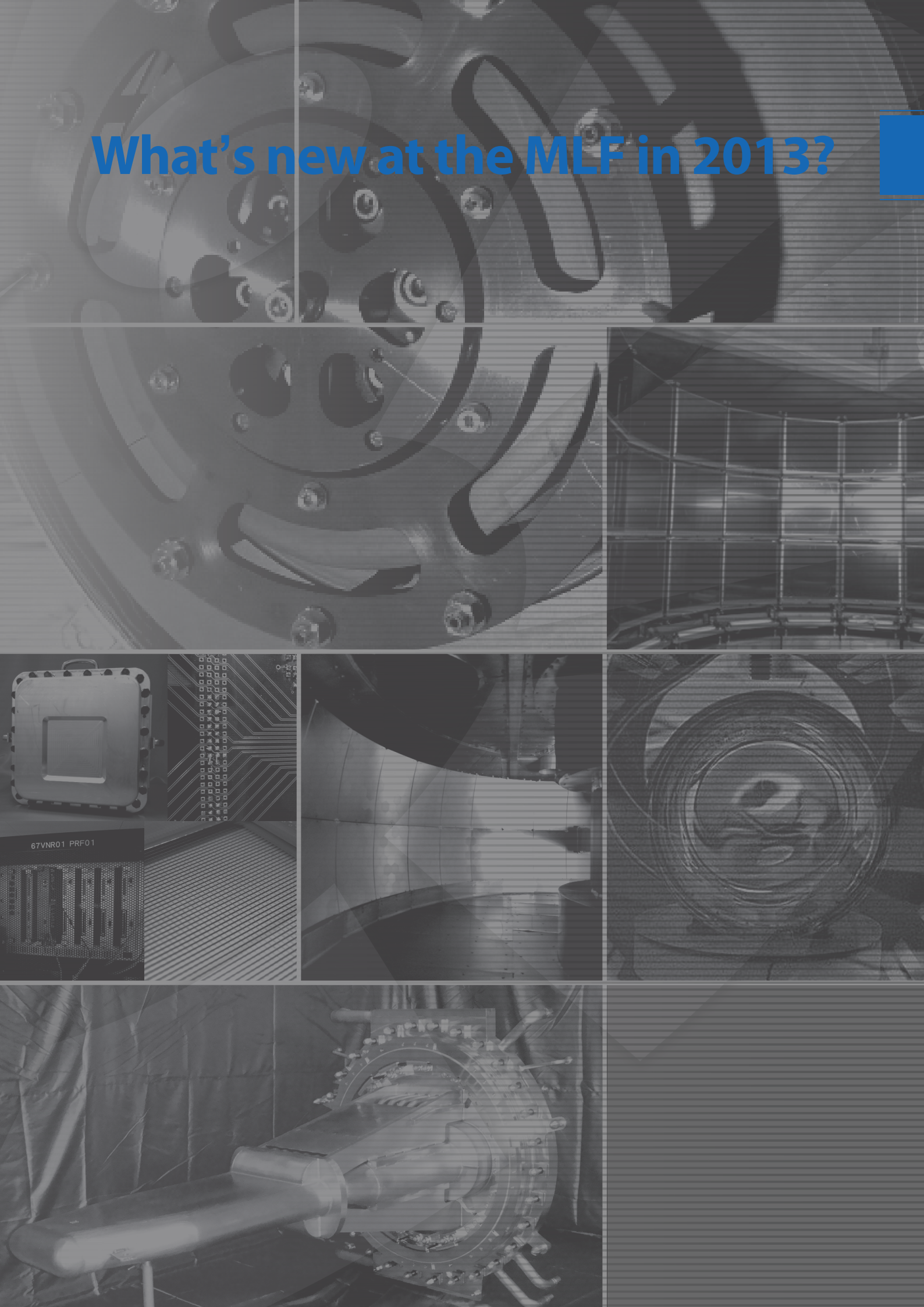

Activities of the Technology Development Section

1. Introduction

Activity of the Technology Development Section started in JFY 2013, which was organized in the MLF division. This section consists of JAEA and KEK staffs and its tasks are as follows:

(1) Development of common equipment for beamlines and instruments in the MLF
(2) Operation, maintenance and management of common equipment for beamlines and instruments in the MLF
(3) User support of common equipment for beamlines and instruments in the MLF

In order to perform those tasks, there are four subgroups in this section, as follows.

(1) Computer environment subgroup
(2) Radiation and general safety subgroup
(3) Technical support subgroup
(4) Sample environment subgroup

In the view point of unified operation for effective and safety managements of MLF, the common task staffs of the Comprehensive Research Organization for Science and Society (CROSS) work together with the Technology Development Section staffs. Also outsourcing staffs, who work together with subgroups members, are employed for various common tasks.

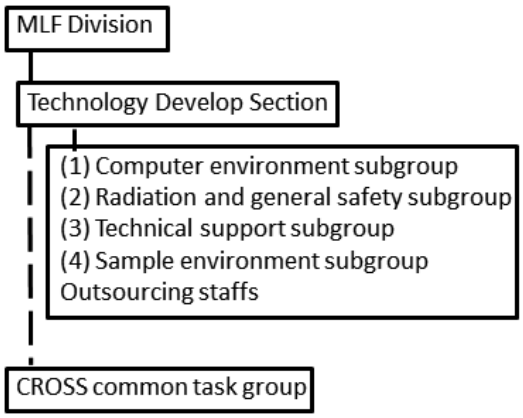

Figure 1. Structure of the neutron technology development section and its relation to CROSS.

2. Computer environment subgroup

This subgroup is responsible for the computational environment, data acquisition system and data analysis software.

The routine works include operation and maintenance of many computers (22 main servers, 3 storages, 3 web computers and 8 database computers, 2 analysis computers, 3 anti-virus computers, 1 system-monitoring computer, 2 backup computers). Experimental data backup, data transfer to storage, security update, account management, failure supports of hardware and software, monitoring of storage consumption and network traffic are included in the works.

A 5-year plan to upgrade the experimental control framework software, IROHA, was fulfilled in this fiscal year, which added a new function to the instrument management server and device control servers via web-UI stand-alone to the existing IROHA. A prototype remote-access function, which enables a user to monitor the experiment, conduct routine analysis and data download via web is provided and has been tested by the MLF staffs. Additional remote access functions dealing with remote login analysis and simulation for the IROHA upgrade will be introduced, and the experiment database improvement will be performed according to the 5-year plan. Data acquisition (DAQ) systems, including scintillator software, a ^{3}He gas tube and gas electron multiplier (GEM) based detectors have also been in a process of development.

Furthermore, the advanced computing environment for neutron instruments is being designed now. This environment consists of a high speed network, large volume storage, management server and analysis factory. The analysis factory has capability of new computational technique on user-friendly, instant, flexibility and visualization for large volume data.

3. Radiation and general safety subgroup

This subgroup is responsible for the radiation and general safety and maintenance of common experimental preparation apparatuses. For human safety and safe operation of the neutron instruments, the members perform safety examinations of the experimental samples and various kinds of equipment before the actual experiments. The examination consists of chemical safety check about toxicity, stability and activation of samples in experimental conditions, as well as mechanical and electric safety check of the equipment. Sample preparation apparatuses such as fume hood, glove box and various kinds of chemical tools are maintained by this subgroup. This subgroup also evaluates the radiation dose for new neutron instruments and prepares application forms for a license to use radiation apparatus.

As a 5-year plan, the deuteration laboratory for the biological macromolecule and polymer samples, which is planned at the new user building that will be opened in next fiscal year have been designed by this group. In the future, the users will be able to prepare complete deuterated samples in the laboratory before the experiment.

4. Technical support subgroup

This subgroup is responsible for the management of the construction schedule of new beamlines and improvements of various neutron devices. Also various supports of the neutron instruments' operation are included in this subgroup. For example, crane operation for experiment setup and installing new devices, handling and maintenance of mechanical and electric equipment of neutron instruments are also performed by this subgroup. In addition, it deals with the maintenance of the vacuum pump and various kinds of choppers.

The 5-year plan also envisions the developments of a T0 chopper with 100 Hz rotation speed and high speed disk chopper with 300 Hz rotation speed, which will be more stable mechanically and have longer lifetime than the existing choppers; the assembly of a new Si analyzer for DNA (BL02), which extends the covered q-ω space, is also being planned now.

5. Sample environment subgroup

This subgroup is responsible for the maintenance and technical support of common equipment, and developments of new sample environment apparatus. Standard sample environment apparatuses such as a 7 T superconducting magnet, an Nb heater furnace and a dilution refrigerator are maintained by this subgroup.

As a 5-year plan, developments of several kinds of advanced sample-environment equipment have been started in this fiscal year; they are a pulsed magnet field system for the strong magnetic field experiments, a combined system of a low temperature and a high pressure environments for the solid state physics and the earth science experiments and a general purpose Pressure-Composition-Temperature (PCT) system for *in-situ* observation of the behavior of hydrogen absorbing materials.

The development of a compact *in-situ* SEOP ^{3}He spin filter for polarized neutron experiments, which enables easier setup than the previous prototype, is advancing. Polarization analysis on polarized neutron reflectometry for Fe / Cr multilayers at SHARAKU (BL17) and separation for the coherent and incoherent scattering for the silver behenate ($CH_3(CH_2)_{20}COOAg$) at TAIKAN (BL15) were successfully carried out.

K. Aizawa, and T. Oku
Technology Development Section, Materials and Life Science Division, J-PARC Center

MLF Operations in 2013

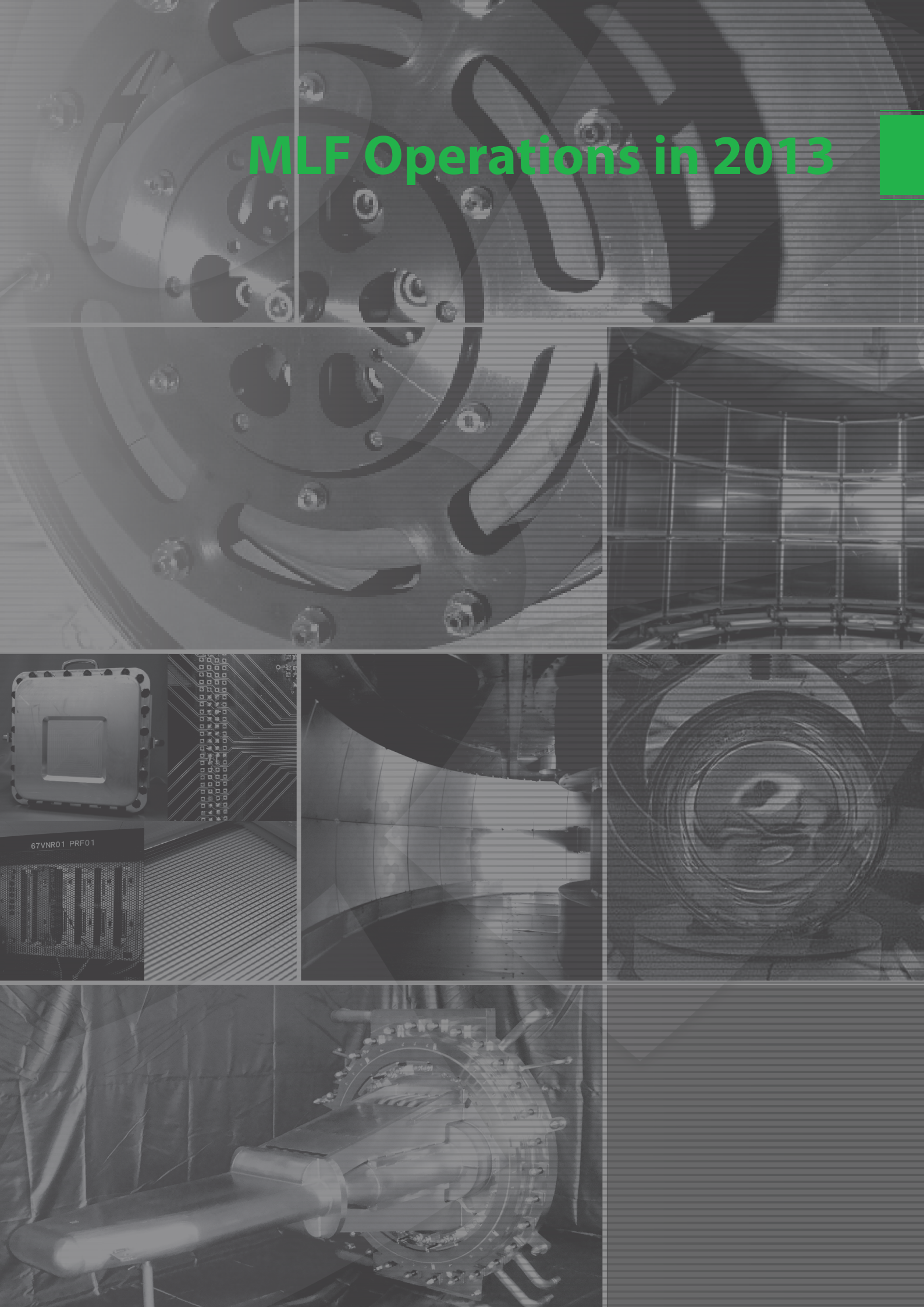

CROSS-Tokai 2013 Update

The Public Neutron Beam Facility at J-PARC

Consistent with its longstanding policy of promoting open access to major publicly-funded research facilities, the Japanese government established in July 2009 the Public Neutron Beam Facility at J-PARC. The Facility consists of the accelerators and target station used to generate pulsed neutron beams and a proportion of the beamlines that exploit the neutron beams for research purposes.

The legislative framework within which the Public Neutron Beam Facility was established requires that an independent third-party organization be responsible for the administration and support of the science program on the so-called 'Public Beamlines'. CROSS-Tokai was appointed to this role and began operations from its offices in the Ibaraki Quantum Beam Research Center adjacent to the J-PARC site in early 2011.

Although CROSS-Tokai is structurally independent of JAEA and KEK – the co-owners and operators of J-PARC – it maintains a high level of cooperation and collaboration with the two founding organizations and other stakeholders that is driven by shared scientific objectives.

The Role of CROSS-Tokai

CROSS-Tokai is entrusted with specific responsibilities relating to the Public Beamlines which, In practical terms, can be summarized as follows:

- *Manage proposal selection and beamtime allocation*
- *Provide user support and ancillary experimental facilities*
- *Provide assistance and expert advice to existing and potential users*
- *Initiate and undertake outreach and facility utilization promotion activities*
- *Manage the selection and assessment of* Contract Beamlines

The Public Beamlines at J-PARC MLF

The MLF has capacity to accommodate up to 23 neutron beamlines around the present target station. There are currently 18 neutron and 2 muon beam instruments in operation, 1 neutron instrument in commissioning and 3 new beamlines under construction. Of these, 6 beamlines have been designated as Public Beamlines as part of the Public Neutron Beam Facility and are supported by CROSS-Tokai.

Though not exhaustive in their experimental capabilities, the Public Beamlines cover a wide range of neutron scattering techniques and can be used in a variety of research fields. The Public Beamlines at J-PARC MLF are listed in Table 1 with examples of their research applications.

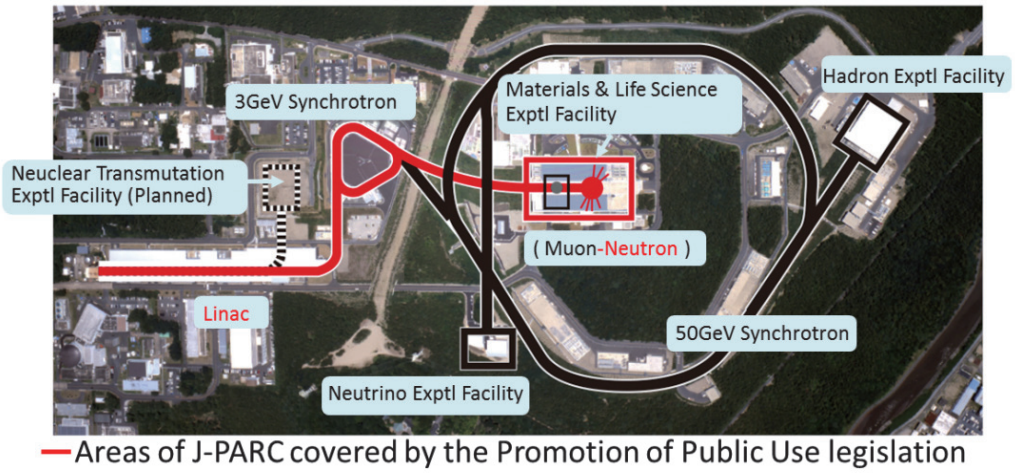

Figure 1. The Public Neutron Beam Facility at J-PARC (shown in red).

Table 1. The Public Beamlines at J-PARC MLF.

Number	Instrument	Applications
BL01	*4SEASONS* – 4D-Space Access Neutron Spectrometer	Lattice and spin dynamics in condensed matter over a wide range of 4D momentum-energy space
BL02	*DNA* – Biomolecular Dynamics Spectrometer	Atomic and spin dynamics of biological macromolecules soft matter and functional biomaterials
BL11	*PLANET* – High-Pressure Neutron Diffractometer	Structural analysis and radiography of materials under extreme pressure and temperature
BL15	*TAIKAN* – Small and Wide Angle Neutron Scattering Instrument	Nano and micro scale structural analysis of metals, magnetic materials, soft matter and bio-macromolecules
BL17	*SHARAKU* – Polarized Neutron Reflectometer	Structural analysis of functional and magnetic thin films, biological thin films and buried interfaces
BL18	*SENJU* – Extreme Environment Single Crystal Diffractometer	Microcrystalline and magnetic structural analysis of functional materials

Distribution of Beamtime on the Public Beamlines

The Selection Committee of CROSS-Tokai regularly reviews and sets policies for the distribution of beamtime on the Public Beamlines at the MLF. In line with the prescribed role of the Public Beamlines and taking into account operational requirements, beamtime is currently distributed in approximately the following ratios:

CROSS-Tokai in 2013

Overview

After three years of operation, CROSS-Tokai is now fully engaged in the full range of its mandated activities: proposal selection via an open and transparent assessment process, provision of high-quality user support, and facility utilization promotion within both the academic and industrial research sectors.

At the start of FY2013, CROSS-Tokai was supporting the user program on five fully-operational Public Beamlines: BL01 *4SEASONS*, BL02 *DNA*, BL15 *TAIKAN*, BL17 *SHARAKU* and BL18 *SENJU*., at the same time, BL11 *PLANET* entered service as the sixth Public Beamline and was opened to general users from the 2013B proposal round. In addition, construction work continued on the seventh Public Beamline – BL22 *RADEN* – which will be available to users in 2015. For information on the current status and science programs on the Public Beamlines, please see the individual beamline updates in Chapter 3 of this Report.

As the number of Public Beamlines at the MLF continues to increase, and with strong growth in user demand for beamtime, CROSS-Tokai has continued to grow as an organization. During FY2013, the total number of CROSS-Tokai staff rose to 55 with five new team members being employed: all of them in the Neutron R&D Division and working in direct support of the science program on the beamlines.

User operations at J-PARC during the past year, including those at the MLF, were severely disrupted

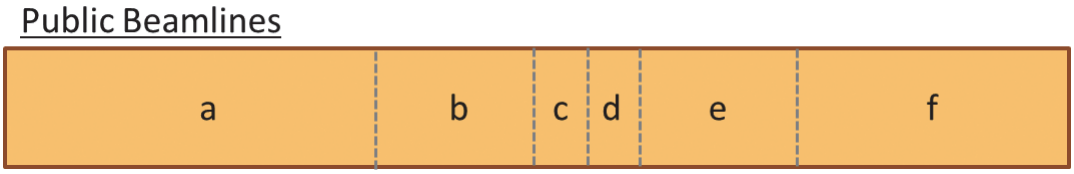

(a) General Use
(b) Elements Strategy Initiative (up to 15%)
(C) Trial Use (up to 5%)
(d) Director's Discretion (up to 5%)
(e) CROSS-Tokai Research (up to 15%)
(f) Facility Use (up to 25%)

Figure 2. Beamtime Distribution on the Public Beamlines.

by the Hadron Incident of May 2013 and its after effects. CROSS-Tokai staff – particularly the beamline teams – worked furiously with their MLF colleagues on upgrading safety systems and documentation as part of the safety audit and strengthening of safety protocols that was undertaken across the whole J-PARC site in response to the Hadron Incident. Ultimately, beamtime for experiments was available during April-May 2013 and mid-February to the end of March 2014 only. In spite of these challenges, the Public Beamlines hosted during FY2013, experiments associated with over 100 research proposals and CROSS-Tokai continued to vigorously promote facility utilization both in Japan and internationally.

CROSS-Tokai 2013 Highlights

PLANET begins user operations as the 6th Public Beamline

On 1 April 2013, BL11 *PLANET* became the sixth Public Beamline at the MLF and was made available for user operations for the first time in 2013B.

With the addition of *PLANET*, the range of science that can be undertaken on the Public Beamlines has been extended to include the study of liquids and solids under conditions of extreme temperature and pressure using specialist sample environment apparatus such as the 6-axis multi-anvil press *ATSUHIME*.

For more information about *PLANET* and its capabilities, please see the detailed beamline update in this report.

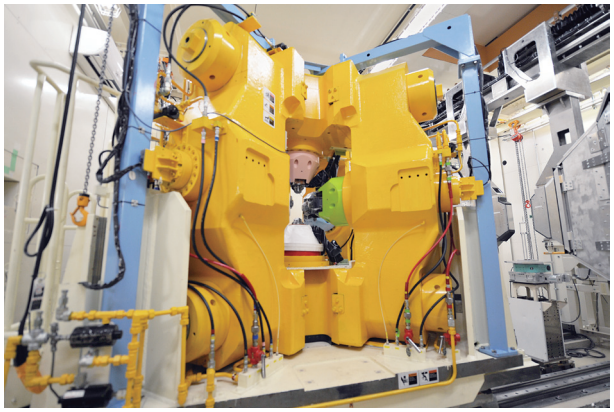

Figure 3. The *ATSUHIME* 6-axis multi-anvil press at BL11 *PLANET*.

Trial Use

An important part of CROSS-Tokai's work in promoting the utilization of the Public Beamlines is to grow the user community – particularly among industry-based researchers – through outreach and education activities. In addition, from 2012B, CROSS-Tokai has been operating the Trial Use Access Program that aims to assist novice users of neutron-based techniques gain experience and expertise that will allow them to become independent General Use applicants in the future.

The specific objectives of the Trial Use Access Program are:

- ♦ To grow the user community and,
- ♦ To promote the use and utility of pulsed neutrons through the development and demonstration of innovative new applications

Accordingly, up to a maximum of five percent (5%) of the total beamtime on each of the Public Beamlines at the MLF can be allocated for Trial Use experiments in each round.

Employing the specialist expertise and experience of the CROSS-Tokai Science Coordinators and other appropriate staff, the Trial Use system offers support to prospective users through the whole process of facility utilization including:

- Instrument selection and experiment feasibility assessment
- Proposal preparation
- Experiment design, planning and execution
- Data analysis and interpretation
- Publication of results

The Trial Use program continued to gather pace during Fy2013 with expressions of interest coming from 14 organizations in the industrial and academic sectors. Ultimately, nine projects were developed into full beamtime proposals and approved by the Selection Committee. A list of the Trial Use proposals approved in FY2013 is given in Table 2. It is particularly pleasing to note the diversity of science and the high degree of academia-industry collaboration that is being encouraged and supported by the Trial Use program.

We look forward to describing in future reports, scientific outcomes from the Trial use program as well as the return of Trial use applicants in future rounds as General Users.

Table 2. Trial Use proposals approved inFY2013.

Round	Beamline	Applicant organization	Industry	Research Area
2013A	BL02 *DNA*	Aisin Seiki Co.†	Automotive	Polymers
	BL15 *TAIKAN*	Kureha Corporation	Chemicals	Food packaging
	BL15 *TAIKAN*	Taiyo Kagaku Co.	Chemicals	Pharmaceuticals and cosmetics
	BL17 *SHARAKU*	Asahi Glass Co.†.	Inorganic materials	Glasses
2013B	BL01 *4SEASONS*	The University of Tokyo	University	Catalysis
	BL02 *DNA*	Fukuoka University	Automotive	Rechargeable batteries
	BL15 *TAIKAN*	TOYO Tire & Rubber Co.	Chemicals	Polymer science
	BL15 *TAIKAN*	RIKEN	Govt. Institute	Carbon materials
	BL17 *SHARAKU*	Tohoku University	University	Micro-electromechanical systems

† TU experiments approved by the Selection Committee but not carried out due to the Hadron Incident.

Figure 4. Food packaging applications of samples studied in the 2013 Trial Use Program.

Other Key CROSS-Tokai activities FY2013

Proposal Selection

- Selection Committee (22 Aug 2013)
  - ♦ First meeting of new 2-year term
  - ♦ New Chair (Prof. H. Fukuyama, Tokyo Univ. of Science) and Deputey Chair (Prof. T. Kanaya, Univ. of Kyoto) elected.
- Public Beamlines proposal selection for 2013B
  - ♦ Call for Proposals (Jun-Jul 2013) – 98 proposals submitted
  - ♦ Review by Expert Panels and Proposal Evaluation Committee (16-17 Oct 2013)
  - ♦ Selection Committee (28 Oct 2013) – 30 proposals approved (incl. 5 Trial Use and 1 Proprietary Use)
- Public Beamlines proposal selection for 2014A
  - ♦ Call for Proposals (Oct-Nov 2013) – 133 proposals submitted
  - ♦ Review by Expert Panels and Proposal Evaluation Committee (22-24 Jan 2014)
  - ♦ Selection Committee (3 Feb 2014) – 74 proposals approved (incl. 4 Trial Use and 2 Proprietary Use)
- CROSS Development Proposal Evaluation Panel (8 Jan 2014) – 3 one-year proposals approved for FY2014.

Proposal Evaluation Committee (16-17 Oct 2013)

Selection Committee (28 Oct 2013)

Figure 5. Public Beamlines proposal selection for 2013B.

User Support

CROSS-Tokai is now supporting user operations and ongoing instrument development activities on the six Public Beamlines with a Neutron R&D team of 34 scientists, programmers, engineers and technicians. Table 3 shows by type and operation period, the number of research proposals supported on the Public Beamlines during FY2013.

In addition to our work at the beamlines, CROSS-Tokai continues to develop and maintain ancillary user facilities in the Ibaraki Quantum Beam Research Center including:

- User Experiment Preparation Laboratories I (Sample processing), II (Hard Matter) and III (Soft Matter & Biomaterials).
- User Data Analysis Room
- User Lounge and "Refresh Rooms"

Table 3. Research proposals supported on the Public Beamlines in FY2013.

		BL01	BL02	BL11	BL15	BL17	BL18	TOTAL
2013A	GU	10	6	-	19	7	8	**50**
	TU	0	1	-	2	1	0	**4**
2013B	GU	3	2	7	6	3	4	**25**
	TU	1	1	0	2	1	0	**5**
Full year	ESI	1	0	0	1	0	0	**2**
	DP	1	1	0	2	0	0	**4**
	PU	3	3	0	6	3	2	**17**
	Instrum.	1	1	1	1	1	1	**6**
TOTAL		**20**	**15**	**8**	**39**	**16**	**15**	**114**

GU: General Use **TU**: Trial Use **ESI**: Element Strategy Initiative
DP: CROSS Development Proposals **PU**: JAEA Project Use **Instrum.**: Instrument Group Proposals

† BL11 was open to GU proposals from 2013B

User Experiment Preparation Laboratory I

User Experiment Preparation Laboratory II

User Experiment Preparation Laboratory III

User Data Analysis Room

User Lounge

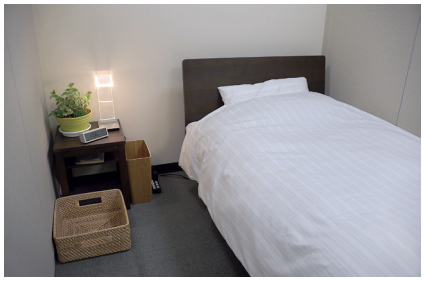

Refresh Rooms

Figure 6. User facilities in the Ibaraki Quantum Beam Research Center.

Contract Beamline Review

- Contract Beamline Evaluation Committee
  - ♦ 16 May 2013 - Finalised procedures, assessment criteria and assessment schedule for the mid-term review of Ibaraki Prefecture beamlines BL03 *iBIX* and BL20 *iMATERIA*.
  - ♦ 2 Dec 2013 – Met to discuss the outcome of review process.
  - ♦ 17 Jan 2014 – Finalised review outcome reports
- The reports prepared by the Contract Beamline Evaluation Committee were considered by the Selection Committee at the 3 Feb 2014 meeting and CROSS-Tokai advised Ibaraki Prefecture of the review outcomes on 20 Mar 2014.

Outreach and Facility Promotion

Throughout FY2013, CROSS-Tokai has continued to engage in a wide variety of outreach and facility utilization promotion activities. Both independently and in collaboration with other stakeholders in the neutron science community, CROSS-Tokai convened or otherwise supported in more than 20 events designed to inform new potential users about the research possibilities of neutrons, disseminate the latest research results and experimental capabilities and build opportunities for collaboration with other large-scale research facilities.

Highlights of these activities in 2013 included:

- Promotional booths at local and international conferences
- The CROSSroads Workshop Series
- Industrial Applications workshops and user meetings
- Complementary Use workshops
- Research presentations at local and international scientific meetings

Figure 7. The CROSS-Tokai promotional booth at ICNS (July 2013, Edinburgh UK).

For a comprehensive summary of workshops, symposiums, seminars, etc. hosted or supported by CROSS-Tokai in 2013, please see the full listing of events in Chapter 7 of this report.

Beam Operation Status at MLF

In Japanese Fiscal Year (JFY) 2013, the beam operation at MLF started with a beam power of 300 kW. Figure 1 shows the trend of the beam power from the first beam to the end of June 2014. For the accelerator study, a high-power beam of up to 600 kW operated shortly for less than one minute.

In Table 1, the scheduled time and availability are shown. In JFY2013, we had a good start with high availability. Due to the incident at the hadron facility, the beam operation plan was canceled between May 25 and the end of July so that the availability was very low in Run #49. During the summer of 2013, 400-MeV super conducting LINAC was installed. After the installation long-duration beam studies were performed in Run # 50 and 51. The user beam operation has started in Run #52 on February 18th, 2014, with a beam power of 100 kW due to the vacuum condition at the RCS. The beam operation with power of 300 kW resumed on February 28th after degas by the proton beam. During Run #52, failure events occurred on many occasions at the LINAC klystron, the LINAC water circulation system and the RCS shift bump. On average, we had a fairly good availability such as 75%.

Table 1. Run cycle, scheduled time and availability.

Run#	Scheduled Time (h).	Availability
48	250	99.0
49	993	58.6
50	No time for user	
51	No time for user	
52	889	86.2
Overall	2132	74.8

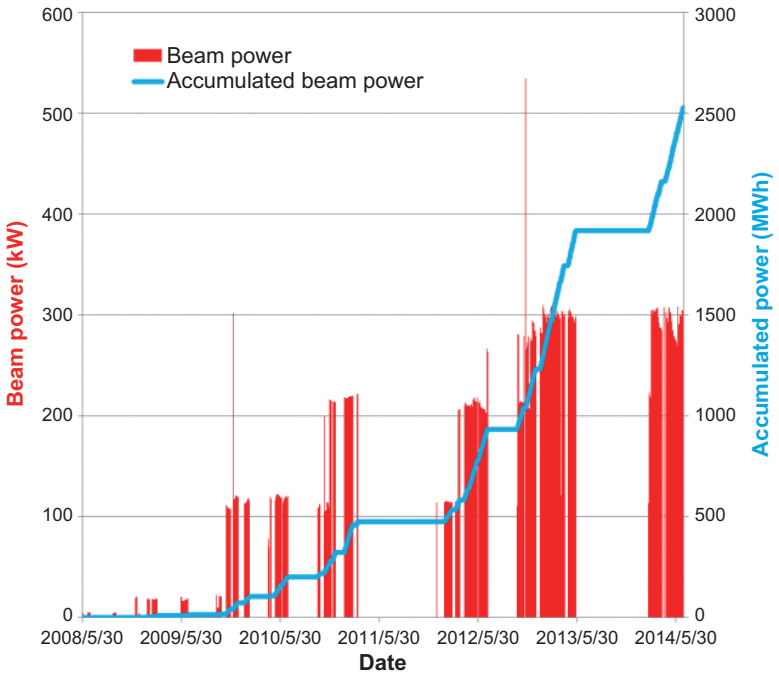

Figure 1. Beam power trend at MLF and cumulative beam power from the first beam to the summer of 2014.

Users at the MLF

In fiscal year 2013, there was a long period of the accelerator shutdown due to an incident in the Hadron Facility which is one of the facilities in J-PARC. The resumption of operation was approved in January 2014. Therefore, the number of neutron users at the MLF in fiscal year 2013 decreased from that in the previous fiscal year, while the number of muon users a little bit increased. Since upgrade of the linear accelerator is planned, more users than ever are expected to come to the MLF in the next fiscal year. The transition of the number of users at the MLF is summarized in Table and Figure for domestic and foreign users of neutron and muon experimental facilities.

Table. The number of domestic and foreign users in the period of fiscal year.

	FY2008		FY2009		FY2010		FY2011		FY2012		FY2013	
	Domestic Users	Foreign Users	Domestic Users	Foreign Users	Domestic Users	Foreign Users	Domestic Users	Foreign Users	Domestic Users	Foreign Users	Domestic Users	Foreign Users
Neutron	182		378		529		222		735		520	
	161	21	353	25	485	44	198	24	650	85	452	68
Muon	12		57		55		30		72		77	
	12	0	55	2	48	7	28	2	62	10	62	15

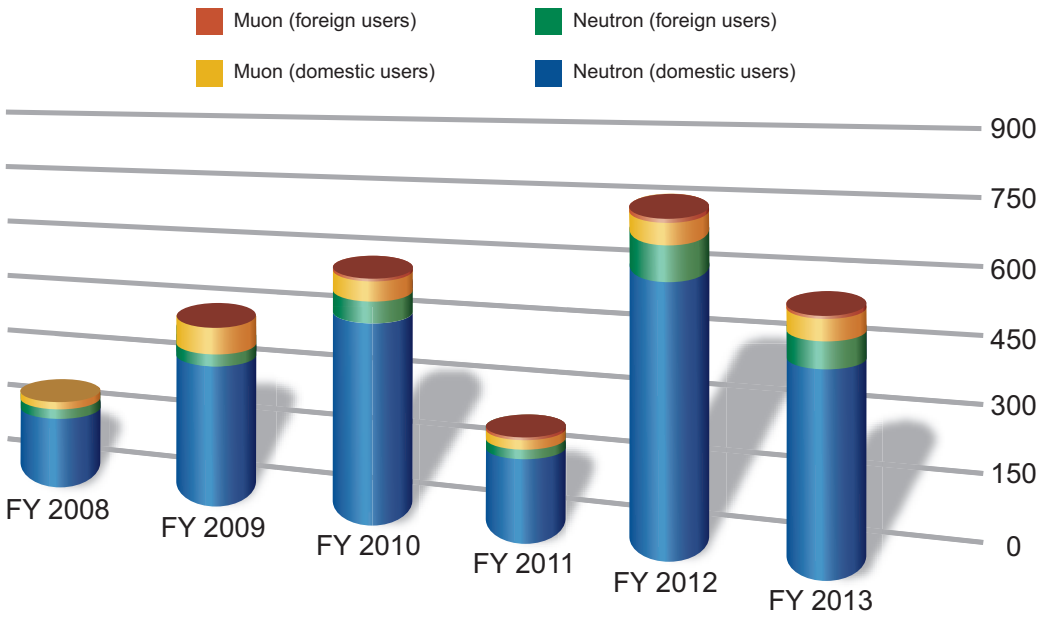

Figure. The number of domestic and foreign users in the period of fiscal year.

Proposal Review System

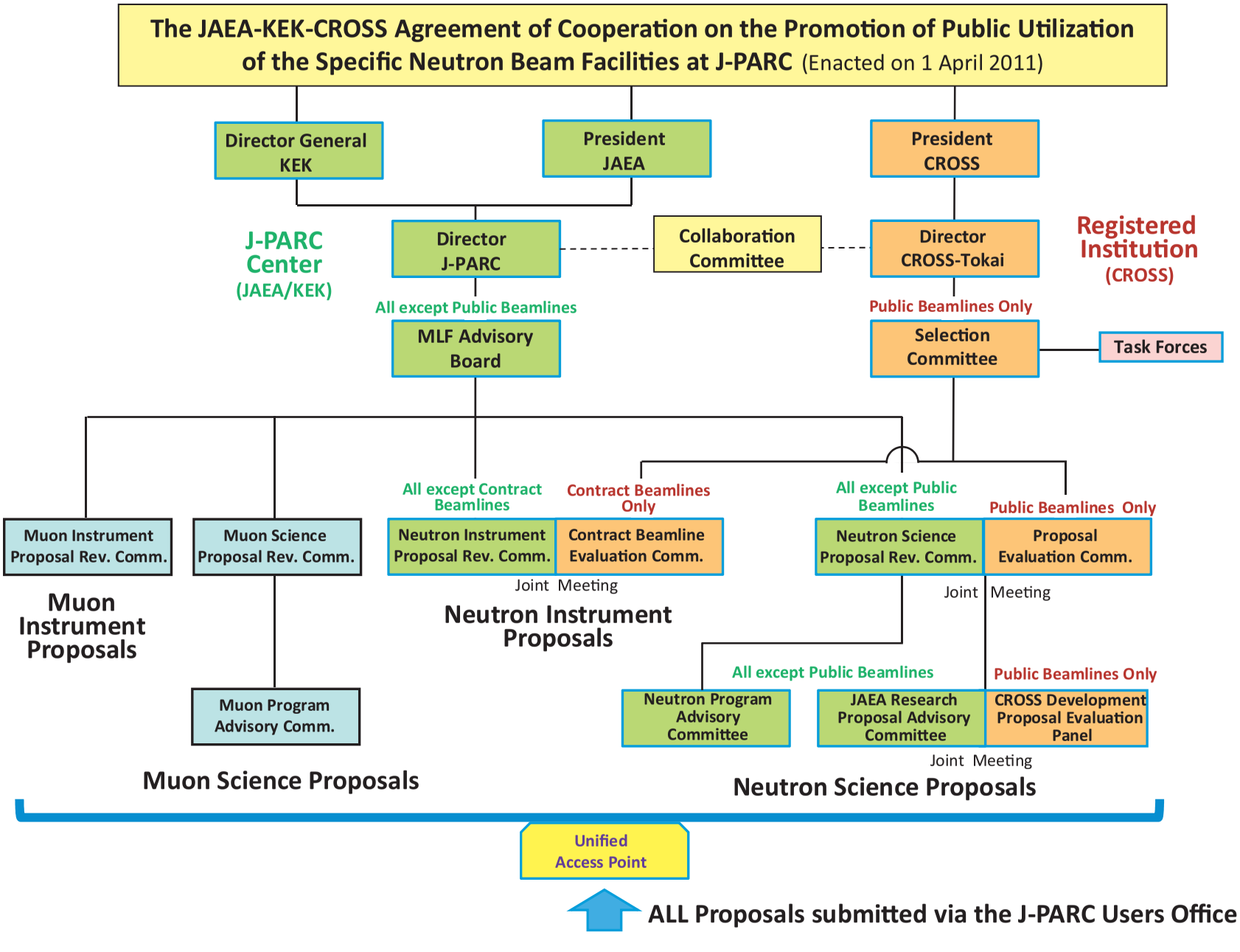

MLF Proposals Summary – FY2013

Table 1. Breakdown of Proposal Numbers for the 2013A & 2013B Rounds.

Beam-line	Instrument		2013A						2013B					
			Submitted			Approved			Submitted			Approved		
			GU	PU/S	IU	GU	PU/S	IU	GU	PU/S	IU	GU	PU/S	IU
BL01	4D-Space Access Neutron Spectrometer - ***4SEASONS***		12(1^{+})	3	2	10(1^{+})	3	2	13(1$^{\#}$, 1^{+})	3	2	5(1$^{\#}$, 1^{+})	3	2
BL02	Biomolecular Dynamics Spectrometer - ***DNA***		13(1$^{\#}$)	3	2	7(1$^{\#}$)	3	2	10(1$^{\#}$)	3	2	3(1$^{\#}$)	3	2
BL03	Ibaraki Biological Crystal Diffractometer - ***iBIX***	(100-β)‡	4	0	0	4	0	0	1	0	0	1	0	0
		(β)†	0	9	0	0	9	0	0	9	0	0	9	0
BL04	Accurate Neutron-Nucleus Reaction Measurement Instrument - ***ANNRI***		6	1	1	6	1	1	4	1	1	4	1	1
BL05	Neutron Optics and Physics - ***NOP***		1	1	0	1	1	0	3	1	0	3	1	0
BL08	Super High Resolution Powder Diffractometer - ***S-HRPD***		9	1	0	9	1	0	3	1	0	3	1	0
BL09	Special Environment Neutron Powder Diffractometer - ***SPICA***		0	1	0	0	1	0	0	1	0	0	1	0
BL10	Neutron Beamline for Observation and Research Use - ***NOBORU***		7	2	1	7	2	1	5	2	1	5	2	1
BL11	High-Pressure Neutron Diffractometer - ***PLANET***		0	1	0	0	1	0	7	1	0	7	1	0
BL12	High Resolution Chopper Spectrometer- ***HRC***		2	1	0	2	1	0	2	1	0	2	1	0
BL14	Cold-neutron Disk-chopper Spectrometer - ***AMATERAS***		11	2	1	11	2	1	6	2	1	6	2	1
BL15	Small and Wide Angle Neutron Scattering Instrument - ***TAIKAN***		27(2$^{\#}$, 1^{+})	6	3	22(2$^{\#}$, 1^{+})	6	3	30(2$^{\#}$, 1^{+})	6	3	9(2$^{\#}$, 1^{+})	6	3
BL16	High-Performance Neutron Reflectometer with a Horizontal Sample Geometry - ***SOFIA***		15	1	0	15	1	0	7	1	0	7	1	0
BL17	Polarized Neutron Reflectometer - ***SHARAKU***		9(1$^{\#}$)	3	1	9(1$^{\#}$)	3	1	15(1$^{\#}$)	3	1	5(1$^{\#}$)	3	1
BL18	Extreme Environment Single Crystal Neutron Diffractometer - ***SENJU***		8	2	2	8	2	2	4	2	2	4	2	2
BL19	Engineering Diffractometer - ***TAKUMI***		31(1^{+})	3	1	16(1^{+})	3	1	5	3	1	5	3	1
BL20	Ibaraki Materials Design Diffractometer - ***iMATERIA***	(100-β)‡	6	0	0	6	0	0	3	0	0	3	0	0
		(β)†	0	25	0	0	25	0	0	23	0	0	23	0
BL21	High Intensity Total Diffractometer - ***NOVA***		12	1	0	12	1	0	5	1	0	5	1	0
D1	Muon D1		19	1	1	19	1	1	5	1	1	5	1	1
D2	Muon D2		5	0	1	5	0	1	5	1	0	5	1	0
U	Muon U		0	1	0	0	1	0	0	1	0	0	1	0
Subtotal			229	79	19	169	68	16	279	76	18	87	67	15
Total			327			253			373			169		

GU : General Use **PU** : Project Use or Ibaraki Pref. Project Use **IU** : Instrument Group Use
S : S-type Proposals **†** : Ibaraki Pref. Exclusive Use Beamtime (β = 80% in FY2013)
‡ : J-PARC Center General Use Beamtime ((100-β = 20% in FY2013)
# : Proposal Numbers under Trial Use Access System in GU
+ : Proposal numbers under Element Strategy in GU

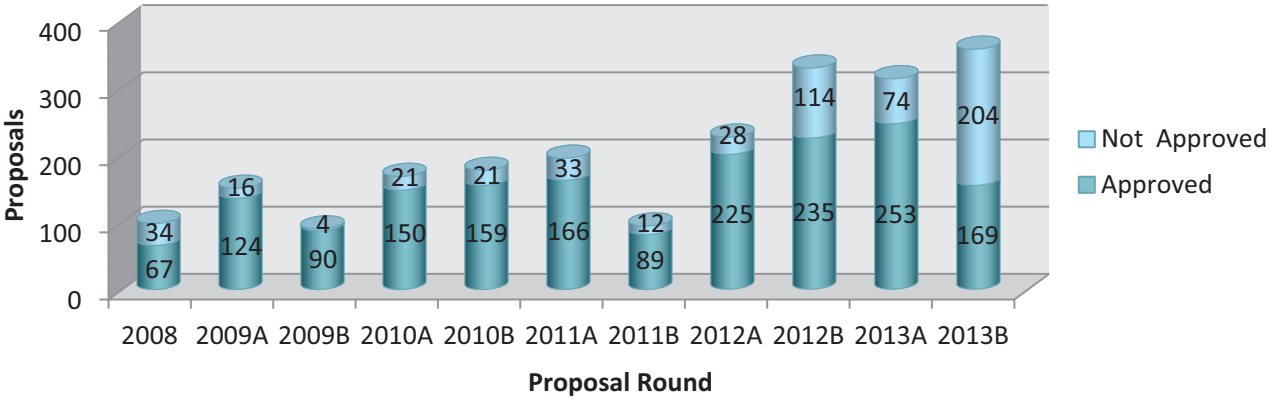

Figure 1. MLF Proposal Numbers over Time.

Table 2. Principal Investigator Affiliations in FY2013.

Universities (Japan)	JAEA	Companies (Japan)	KEK	Foreign Organizations	Research Institutes (Japan)
289	154	84	40	55	78

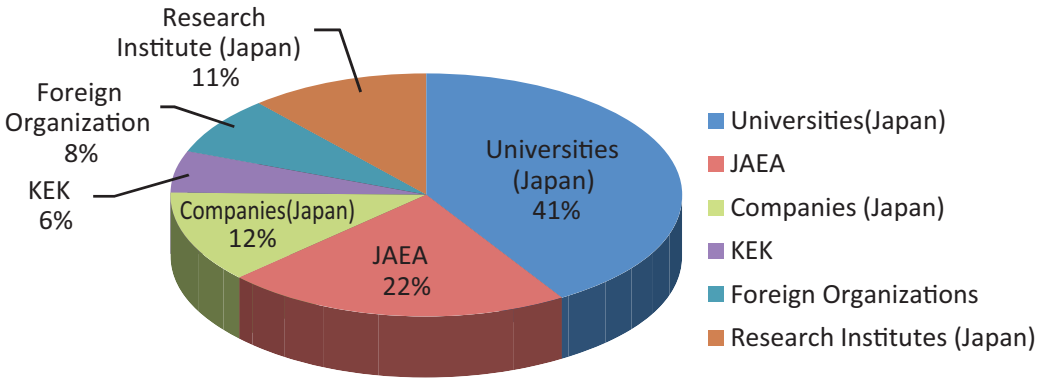

Figure 2. Origin of Proposals in FY2013.

Table 3. Proposals by Sub-committee/Expert Panel – FY2013.

Sub-committee Expert Panel	P1	P2	P3	P4	P5	P6	P7	P8	P9	P10	Q1	Q2
No. of Proposals 2013A	57	15	21	11	46	5	24	12	4	3	8	18
No. of Proposals 2013B	66	16	35	-	70	24	27	-	5	2	11	21

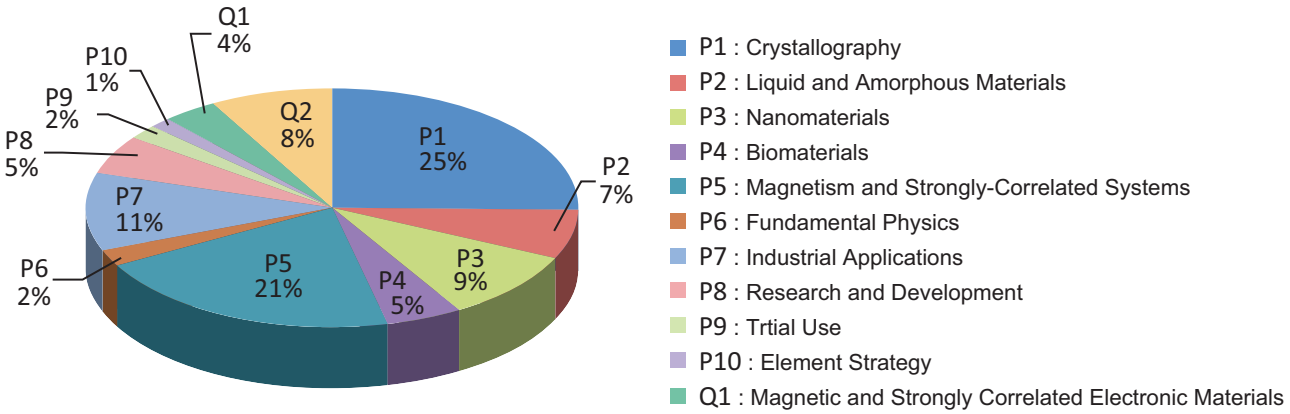

(a) 2013A

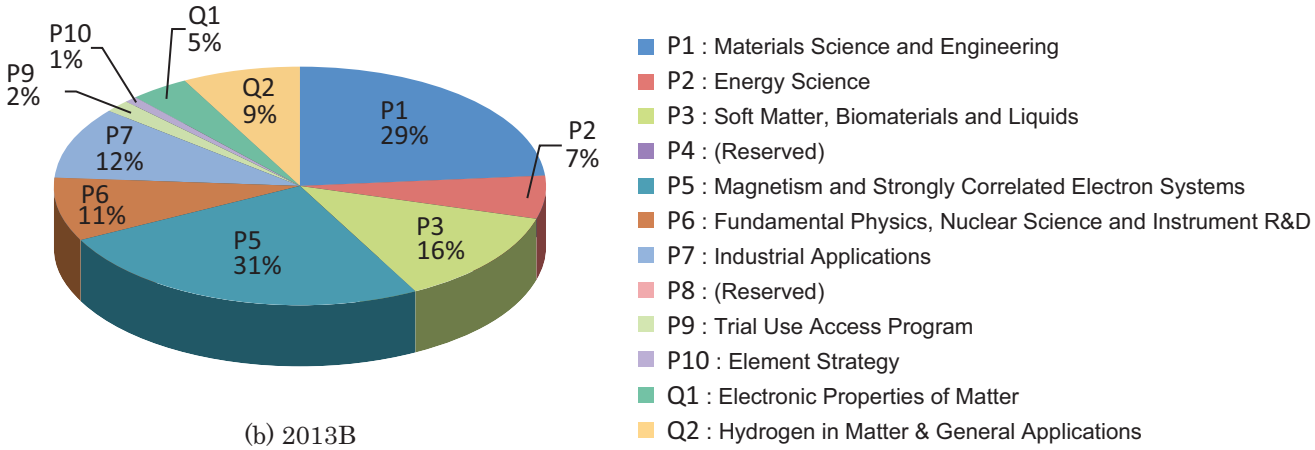

(b) 2013B

Figure 3. Submitted Proposals by Sub-committee/Expert Panel – FY2013.

MLF Division Staff 2013

Head	Masatoshi Arai (JAEA)
Deputy Head	Hideki Seto (KEK)
	Masatoshi Futakawa (JAEA)

Neutron Source Section

	JAEA	
Leader	Hiroshi Takada	Hideki Tatsumoto
Sub-Leader	Yoshimi Kasugai	Motoki Ohi
	Katsuhiro Haga	Yoshihiko Kawakami
	Shinichiro Meigo	Hideki Ueno
	Kenji Sakai	Tomoyuki Kawasaki
	Makoto Teshigawara	Takashi Naoe
	Hidetaka Kinoshita	Atsushi Akutsu
	Masahide Harada	Toru Suzuki
	Hiroyuki Kogawa	Masato Ida
	Takashi Wakui	Hideaki Ishii
	Masakazu Seki	Shizuka Yoshinari
	Akihiko Watanabe	Chieko Higuchi
	Akira Ogawa	Shoichi Hasegawa*
	Kiichi Ohtsu	Hiroki Matsui*
	Shinji Komori	Tomokazu Aso*
	Kiyomi Ikezaki	Kenichi Oikawa*
	Kohei Hanano	Tetsuya Kai*

Neutron Science Section

	KEK		
Leader	Takashi Kamiyama		Naokatsu Kaneko
	Hideki Seto		
	Toshiya Otomo		JAEA
	Hitoshi Endo	Sub-Leader	Yukinobu Kawakita
	Tetsuya Yokoo		Kentaro Suzuya
	Norifumi Yamada		Kenji Nakajima
	Shuki Torii		Ryoichi Kajimoto
	Kaoru Taketani		Takanori Hattori
	Kazutaka Ikeda		Mitsutaka Nakamura
	Masao Yonemura		Stefanus Harjo
	Haruhiro Hiraka		Nobuaki Takahashi
	Hidetoshi Ohshita		Takenao Shinohara
	Miki Nagao		Takashi Ohhara
	Shinichi Ito		Tetsuya Kai
	Takashi Ino		Kenichi Oikawa

	Seiko Kawamura	Shuichi Wakimoto*
	Shinichi Takata	Itaru Tamura*
	Ryoji Kiyanagi	Koji Kaneko*
	Kaoru Shibata	Satoru Fujiwara*
	Takuro Kawasaki	Hiroshi Nakagawa*
	Yasuhiro Inamura	Asami Sano*
	Tatsuya Kikuchi	Hidehito Asaoka*
	Taiki Tominaga	Masato Kubota*
	Takaaki Iwahashi	Hideo Harada*
	Tomonori Hosoya	Atsushi Kimura*
	Kazuhiro Aoyama	Shoji Nakamura*
	Chiho Tobe	Yosuke Toh*
	Naoko Shimizu	Mariko Segawa*
	Naoko Kawase	Hiroshi Iikura*
	Masayasu Takeda*	Masahide Harada*
	Toyotaka Osakabe*	Kazuya Aizawa*
	Kazuo Kurihara*	Wataru Kambara*

Technology Development Section

	JAEA	
Leader	Kazuya Aizawa	Mitsutaka Nakamura*
Sub-Leader	Takayuki Oku	Nobuaki Takahashi*
	Tomokazu Aso	Shinichi Takata*
	Takeshi Nakatani	Kaoru Sakasai*
	Wataru Kambara	Tatsuya Nakamura*
	Hiromichi Tanaka	
	Yukihiro Ito	KEK
	Yasuhiro Yamauchi	Masataka Sakaguchi
	Shino Ono	Tomohiro Seya
	Kentaro Moriyama	Setsuo Satoh
	Wu Gong	Tetsuya Yokoo*
	Yukino Inoue	Shuki Torii*
	Chikako Doda	Kaoru Taketani*
	Yoshimi Kasugai*	Takashi Ino*
	Kenji Sakai*	Naokatsu Kaneko*
	Tetsuya Kai*	Kenji Kojima*
	Hiroyuki Kogawa*	Naritoshi Kawamura*
	Motoki Ohi*	Hiroshi Fujimori*
	Kentaro Suzuya*	Shunsuke Makimura*

Neutron Instrumentation Section

	JAEA	
Leader	Kazuhiko Soyama	Hirotoshi Hayashida
	Kaoru Sakasai	Katsunori Honda
	Dai Yamazaki	Hiroyuki Suzuki
	Kentaro Toh	Hideshi Yamagishi
	Tatsuya Nakamura	Noriko Amezawa
	Ryuji Maruyama	Takuro Sakai*

Muon Science Section

	KEK	
Leader	Yasuhiro Miyake	Yutaka Ikedo
	Ryosuke Kadono	Masanori Miyazaki
	Koichiro Shimomura	Ichihiro Yamauchi
	Kenji Kojima	Takashi Nagatomo
	Patrick Strasser	Yohei Nakatsugawa
	Naritoshi Kawamura	Yoshitomo Takahashi
	Akihiro Koda	Masatoshi Hiraishi
	Hiroshi Fujimori	Motonobu Tampo
	Shunsuke Makimura	Koji Hamada
	Yasuhisa Nemoto	Li Hua
	Yasuo Kobayashi	Masato Tabe
	Jumpei Nakamura	
	Kusuo Nishiyama	JAEA
	Toshiro Irie	Wataru Higemoto
	Yutaka Taniguchi	Takashi Ito

*additional duties

CROSS-Tokai Staff 2013

Director Yasuhiko Fujii

Science Cordinators

Masatoshi Sato
Yoshiaki Fukushima

Neutron R&D Division

Head	Jun-ichi Suzuki	Tetsuya Kuroda
Head (Deputy)	Kenichi Funakoshi	Shinichi Machida
	Jun Abe	Masato Matsuura
	Kazuhiro Akutsu	Noboru Miyata
	Tadashi Futagami	Tazuko Mizusawa
	Takayasu Hanashima	Toshiaki Morikawa
	Hideyuki Hiramatsu	Taketo Moyoshi
	Kazuki Iida	Koji Munakata
	Kazuhiko Ikeuchi	Akiko Nakao
	Motoyuki Ishikado	Kazuki Ohishi
	Takayoshi Ito	Keiichi Ohuchi
	Hiroki Iwase	Nobuo Okazaki
	Kazuya Kamazawa	Masae Sahara
	Satoshi Kasai	Yoshifumi Sakaguchi
	Yukihiko Kawamura	Kaoru Sato
	Hiroshi Kira	Sayaka Suzuki
	Koji Kiriyama	Taiki Tominaga
	Akifumi Kishi	Takeshi Yamada
	Makoto Kobayashi	

Health and Safety Division

Head Toshiyuki Yamashita

Utilization Promotion Division

Head	Junichi Sato	Katsumi Kunigihara
Head (Deputy)	Garry John Foran	Junko Ohta
Adviser	Toru Matoba	Rei Ohuchi
	Toshiki Asai	Emi Takaha
	Yutaka Ebara	Aya Yamada
	Asami Inoue	Shinichi Yamaguchi
	Megumi Kawakami	

Admin and Finance Division

Head	Yasuo Seishi	Takahiro Koizumi
Head(Deputy)	Masaru Yokoyama	Mutsumi Shiraishi
	Mika Gunji	Tomoyuki Yabana

Committees and Meetings

Materials and Life Science Facility Advisory Board

物質・生命科学実験施設利用委員会

Kazuya Aizawa	Japan Atomic Energy Agency, Japan
Jun Akimitsu	Aoyama Gakuin University, Japan
Masatoshi Arai	Japan Atomic Energy Agency, Japan
Koichiro Asahi	Tokyo Institute of Technology, Japan
Yasuhiko Fujii	Comprehensive Research Organization for Science and Society, Japan
Masatoshi Futakawa	Japan Atomic Energy Agency, Japan
Makoto Hayashi	IBARAKI Prefectural Government, Japan
Shinichi Itoh	High Energy Accelerator Research Organization, Japan
Masahiko Iwasaki	RIKEN, Japan
Ryosuke Kadono	High Energy Accelerator Research Organization, Japan
Takashi Kamiyama	High Energy Accelerator Research Organization, Japan
Toshiji Kanaya	Kyoto University, Japan
Mikio Kataoka	Nara Institute of Science and Technology, Japan
Takashi Kato	Japan Atomic Energy Agency, Japan
Yukinobu Kawakita	Japan Atomic Energy Agency, Japan
Youji Koike	Tohoku University, Japan
Yasuhiro Miyake	High Energy Accelerator Research Organization, Japan
Toshiya Otomo	High Energy Accelerator Research Organization, Japan
Taku Sato	Tohoku University, Japan
Hideki Seto	High Energy Accelerator Research Organization, Japan
Mitsuhiro Shibayama (Chair)	University of Tokyo, Japan
Masaaki Sugiyama	Kyoto University, Japan
Jun Sugiyama	Toyota Central R&D Labs., Inc., Japan
Wataru Utsumi	Japan Atomic Energy Agency, Japan
Toshio Yamaguchi	Fukuoka University, Japan

Term of board appointments: 1 April 2013 - 31 March 2015

Neutron Instrument Proposal Review Committee

中性子実験装置部会

Masatoshi Arai	Japan Atomic Energy Agency, Japan
Koichiro Asahi	Tokyo Institute of Technology, Japan
Masatoshi Futakawa	Japan Atomic Energy Agency, Japan
Muneyuki Imafuku	Tokyo City University, Japan
Takashi Kamiyama	High Energy Accelerator Research Organization, Japan
Hideaki Kitazawa	National Institute for Material Science, Japan
Yoshiaki Kiyanagi (Chair)	Nagoya University, Japan
Yukio Morii	The Science and Technology Promotion Foundation of Ibaraki, Japan
Yukio Morimoto	Kyoto University, Japan
Kenji Nakajima	Japan Atomic Energy Agency, Japan
Kenji Ohoyama	Tohoku University, Japan

Toshiya Otomo	High Energy Accelerator Research Organization, Japan
Mamoru Sato	Yokohama City University, Japan
Hideki Seto	High Energy Accelerator Research Organization, Japan
Junichi Suzuki	Comprehensive Research Organization for Science and Society, Japan
Naoya Torikai	Mie University, Japan
Hideki Yoshizawa	University of Tokyo, Japan

Term of committee appointments: 1 April 2011 - 31 March 2013

Neutron Science Proposal Review Committee

中性子課題審査部会

Yoshiaki Akiniwa	Yokohama National University, Japan
Koichi Akita	Japan Atomic Energy Agency, Japan
Masatoshi Arai	Japan Atomic Energy Agency, Japan
Takahisa Arima	University of Tokyo, Japan
Samrath Chaplot	Bhabha Atomic Research Centre, India
Sung-Min Choi	Korea Advanced Institute of Science and Technology, Korea
Sergey Danilkin	Australian Nuclear Science and Technology Organization, Australia
Yoshiaki Fukushima	Comprehensive Research Organization for Science and Society, Japan
Masatoshi Futakawa	Japan Atomic Energy Agency, Japan
Makoto Hayashi	Ibaraki Prefectural Government, Japan
Yasushi Idemoto	Tokyo University of Science, Japan
Michael James	Australian Synchrotron, Australia
Hiroyuki Kagi	University of Tokyo, Japan
Takashi Kamiyama	High Energy Accelerator Research Organization, Japan
Yuji Kawabata	Kyoto University, Japan
Yukinobu Kawakita	Japan Atomic Energy Agency, Japan
Brendan Kennedy	University of Sydney, Australia
Guinyun Kim	Kyungpook University, Korea
Paul Langan	Oak Ridge National Laboratory, USA
Seung-Hun Lee	University of Virginia, USA
Masaaki Matsuda	Oak Ridge National Laboratory, USA
Yasuhiro Miyake	High Energy Accelerator Research Organization, Japan
Yukio Morii	The Science and Technology Promotion Foundation of Ibaraki, Japan
Yukio Noda	Tohoku University, Japan
Toshiya Otomo	High Energy Accelerator Research Organization, Japan
Anna Paradowska	Australian Nuclear Science and Technology Organization, Australia
Je-Geun Park	Seoul National University, Korea
Mamoru Sato	Yokohama City University, Japan
Hideki Seto	High Energy Accelerator Research Organization, Japan
Shinichi Shamoto	Japan Atomic Energy Agency, Japan
Hirohiko. M. Shimizu	Nagoya University, Japan
Masaaki Sugiyama	Kyoto University, Japan
Jun-ichi Suzuki	Comprehensive Research Organization for Science and Society, Japan
Toshio Yamaguchi (Chair)	Fukuoka University, Japan
Albert Young	North Carolina State University, USA

Term of committee appointments: 1 April 2013 - 31 March 2015

JAEA Research Proposal Advisory Committee

J-PARC物質・生命科学実験施設におけるJAEA研究課題諮問委員会

Masatoshi Arai	Japan Atomic Energy Agency, Japan
Toshiharu Fukunaga	Kyoto University, Japan
Mitsuhiro Hirai	Gunma University, Japan
Takashi Kato (Chair)	Japan Atomic Energy Agency, Japan
Yuji Kawabata	Kyoto University, Japan
Yukinobu Kawakita	Japan Atomic Energy Agency, Japan
Hideaki Kitazawa	National Institute for Material Science, Japan
Yoshiaki Kiyanagi	Nagoya University, Japan
Michiyasu Mori	Japan Atomic Energy Agency, Japan
Yoichi Murakami	High Energy Accelerator Research Organization, Japan
Kenji Nakajima	Japan Atomic Energy Agency, Japan
Hiroyuki Oigawa	Japan Atomic Energy Agency, Japan
Taku Sato	University of Tokyo, Japan
Hideki Seto	High Energy Accelerator Research Organization, Japan
Shinichi Shamoto	Japan Atomic Energy Agency, Japan
Hirohiko M. Shimizu	Nagoya University, Japan
Junichi Suzuki	Comprehensive Research Organization for Science and Society, Japan
Keisuke Tanaka	Meijo University, Japan
Yo Tomota	Ibaraki University, Japan
Eiko Torikai	University of Yamanashi, Japan
Kazuyoshi Yamada	High Energy Accelerator Research Organization, Japan

Term of committee appointments: 1 April 2011 - 31 March 2014

Neutron Program Advisory Committee

中性子共同利用実験審査委員会

Koichiro Asahi	Tokyo Institute of Technology, Japan
Masaki Azuma	Tokyo Institute of Technology, Japan
Michihiro Furusaka	Hokkaido University, Japan
Yasushi Idemoto	Tokyo University of Science, Japan
Shinichi Itoh	High Energy Accelerator Research Organization, Japan
Kazuaki Iwasa	Tohoku University, Japan
Ryosuke Kadono	High Energy Accelerator Research Organization, Japan
Hiroshi Kageyama	Kyoto University, Japan
Takashi Kamiyama	High Energy Accelerator Research Organization, Japan
Toshiji Kanaya	Kyoto University, Japan
Mikio Kataoka	Nara Institute of Science and Technology, Japan
Yukinobu Kawakita	Japan Atomic Energy Agency, Japan
Reiji Kumai	High Energy Accelerator Research Organization, Japan
Yutaka Moritomo	University of Tsukuba, Japan

Youichi Murakami	High Energy Accelerator Research Organization, Japan
Toshiya Otomo (Chair)	High Energy Accelerator Research Organization, Japan
Hideki Seto	High Energy Accelerator Research Organization, Japan
Mitsuhiro Shibayama	University of Tokyo, Japan
Hirohiko M. Shimizu	High Energy Accelerator Research Organization, Japan
Masaaki Sugiyama	Kyoto University, Japan
Noboru Yamamoto	High Energy Accelerator Research Organization, Japan

Term of committee appointments: 1 April 2013 - 31 March 2015

Muon Instrument Proposal Review Committee

ミュオン実験装置部会

Masatoshi Arai	Japan Atomic Energy Agency, Japan
Koichiro Asahi (Chair)	Tokyo Institute of Technology, Japan
Masatoshi Futakawa	Japan Atomic Energy Agency, Japan
Wataru Higemoto	Japan Atomic Energy Agency, Japan
Masahiko Iwasaki	RIKEN, Japan
Ryosuke Kadono	High Energy Accelerator Research Organization, Japan
Takashi Kato	Japan Atomic Energy Agency, Japan
Kenji Kojima	High Energy Accelerator Research Organization, Japan
Kenya Kubo (Chair)	International Christian University, Japan
Yoshitaka Kuno	Osaka University, Japan
Yasuhiro Miyake	High Energy Accelerator Research Organization, Japan
Nobuhiko Nishida	Tokyo Institute of Technology, Japan
Hiroyuki Nojiri	Tohoku University, Japan
Toru Ogitsu	High Energy Accelerator Research Organization, Japan
Koichiro Shimomura	High Energy Accelerator Research Organization, Japan
Yasunori Yamazaki	RIKEN, Japan

Term of committee appointments: 1 April 2013 - 31 March 2015

Muon Science Proposal Review Committee

ミュオン課題審査部会

Hiroshi Amitsuka	Hokkaido University, Japan
Masaharu Aoki	Osaka University, Japan
Masatoshi Arai	Japan Atomic Energy Agency, Japan
Koichiro Asahi	Tokyo Institute of Technology, Japan
Alan Drew	University of London, UK
Wataru Higemoto	Japan Atomic Energy Agency, Japan
Ryosuke Kadono	High Energy Accelerator Research Organization, Japan
Takashi Kamiyama	High Energy Accelerator Research Organization, Japan
Toshiji Kanaya	Kyoto University, Japan
Yoh Kohori	Chiba University, Japan
Yoji Koike (Chair)	Tohoku University, Japan
Kenji Kojima	High Energy Accelerator Research Organization, Japan

Tadashi Koseki	High Energy Accelerator Research Organization, Japan
Kenya Kubo	International Christian University, Japan
Reiji Kumai	High Energy Accelerator Research Organization, Japan
Roderick Macrae	Marian University, USA
Yasuyuki Matsuda	University of Tokyo, Japan
Yasuhiro Miyake	High Energy Accelerator Research Organization, Japan
Seiji Miyasita	University of Tokyo, Japan
Yasuo Nozue	Osaka University, Japan
Toshiya Otomo	High Energy Accelerator Research Organization, Japan
Hideki Seto	High Energy Accelerator Research Organization, Japan
Koichiro Shimomura	High Energy Accelerator Research Organization, Japan
Yoko Sugawara	Kitazato University, Japan
Shinji Tsuneyuki	University of Tokyo, Japan
Kazuyoshi Yoshimura	Kyoto University, Japan

Term of committee appointments: 1 April 2013 - 31 March 2015

Muon Program Advisory Committee

ミュオン共同利用実験審査委員会

Hiroshi Amitsuka	Hokkaido University, Japan
Masaharu Aoki	Osaka University, Japan
Masatoshi Arai	Japan Atomic Energy Agency, Japan
Koichiro Asahi	Tokyo Institute of Technology, Japan
Wataru Higemoto	Japan Atomic Energy Agency, Japan
Ryosuke Kadono (Chair)	High Energy Accelerator Research Organization, Japan
Toshiji Kanaya	Kyoto University, Japan
Yoh Kobori	Chiba University, Japan
Yoji Koike	Tohoku University, Japan
Kenji Kojima	High Energy Accelerator Research Organization, Japan
Tadashi Koseki	High Energy Accelerator Research Organization, Japan
Kenya Kubo	International Christian University, Japan
Reiji Kumai	High Energy Accelerator Research Organization, Japan
Yasuyuki Matsuda	University of Tokyo, Japan
Yasuhiro Miyake	High Energy Accelerator Research Organization, Japan
Seiji Miyashita	University of Tokyo, Japan
Yasuo Nozue	Osaka University, Japan
Toshiya Otomo	High Energy Accelerator Research Organization, Japan
Hideki Seto	High Energy Accelerator Research Organization, Japan
Koichiro Shimomura	High Energy Accelerator Research Organization, Japan
Yoko Sugawara	Kitazato University, Japan
Shinji Tsuneyuki	University of Tokyo, Japan
Kazuyoshi Yoshimura	Kyoto University, Japan

Term of committee appointments: 1 April 2013 - 31 March 2015

Selection Committee (CROSS)

選定委員会

Toshio Akai	Mitubishi Rayon co.,Ltd., Japan
Jun Akimitsu	Aoyama Gakuin University, Japan
Koichiro Asahi	Tokyo Institute of Technology, Japan
Hidetoshi Fukuyama (Chair)	Tokyo University of Science, Japan
Makoto Hayashi	IBARAKI Prefectural Government, Japan
Shinichi Kamei	Mitsubishi Research Institute Inc., Japan
Toshiji Kanaya	Kyoto University, Japan
Mikio Kataoka	Nara Institute of Science and Technology, Japan
Naoki Kishimoto	National Institute of Material Science, Japan
Tomoko Nakanishi(*)	University of Tokyo, Japan
Kazumi Nishijima	Mochida Pharmaceutical co.,Ltd., Japan
Taku Sato	Tohoku University, Japan
Mitsuhiro Shibayama	University of Tokyo, Japan
Masaaki Sugiyama	Kyoto University, Japan
Masaki Takada	RIKEN, Japan
Kiyoyuki Terakura	National Institute of Advanced Industrial Science and Technology, Japan
Toshio Yamaguchi	Fukuoka University, Japan

* Until 28 February 2014

Term of committee appointments: 1 May 2013 - 31 March 2015

Neutron Advisory Committee (NAC)

NAC-2014 convened 10-11 Feb 2014 at the KEK Tokai campus building, Tokai

List of NAC-2014 Members

Kurt N. Clausen (Chair)	Paul Scherrer Institute, Switzerland
Phillip Ferguson	Oak Ridge National Laboratory, USA
Mahn Won Kim	Korea Advanced Institute of Science and Technology, Korea
Yoshiaki Kiyanagi	Nagoya University, Japan
Dan A. Neumann	National Institute of Standards and Technology, USA
Robert Robinson	Australian Nuclear Science and Technology Organization, Australia
Uschi Steigenberger	Science and Technology Facilities Council, UK
Werner Wagner	Paul Scherrer Institute, Switzerland

Group photo of NAC-2014

Muon Science Advisory Committee (MuSAC)

MuSAC-12 convened 27-28 Feb 2014 at the KEK Tokai Campus building, Tokai

List of MuSAC-12 Members

Hiroshi Amitsuka	Hokkaido University, Japan
Toshiyuki Azuma	RIKEN, Japan
Klaus P. Jungman	University of Groningen, Netherlands
Elvezio Morenzoni (Chair)	Paul Scherrer Institute, Switzerland
Yasuo Nozue	Osaka University, Japan
Francis Pratt	ISIS, UK
Jeff E. Sonier	Simon Fraser University, Canada
Jun Sugiyama	Toyota Central R&D Labs., Inc., Japan

Workshops in 2013

With the increasing level of scientific activity at the facility, the number and scope of research workshops held under the auspices of the MLF rapidly expanded in 2013.

Conferences and workshops held jointly by J-PARC MLF and CROSS-Tokai

2nd IMSS Science Festa, 5th MLF Symposium, 31th PF Symposium
18–19 Mar. 2014, Tsukuba International Congress Center, Tsukuba

Workshops co-sponsored by J-PARC Center, CROSS-Tokai and other organizations

JSNS Annual Meeting 2013
12–13 Dec. 2013, Sawayaka Chiba Kenmin Plaza, Chiba

13th Japan-Korea Meeting on Neutron Science
16–18 Feb. 2014, Lotte Buyeo Resort, Korea

元素戦略プロジェクト＜研究拠点形成型＞・大型研究施設（CMSI・SPring-8・J-PARC・KEK）連携シンポジウム2014 ～大型研究施設を利用した物質・材料研究の課題共有と共創～
28 Feb. – 1 Mar. 2014, The University of Tokyo Kasiwa Campus, Chiba

Neutrons in Biology
27 Mar. 2014, Nuclear Science Research Institute, JAEA, Tokai

Workshops co-sponsored by J-PARC

2nd ANNRI Workshop
23 Aug. 2013, Ibaraki Quantum Beam Center, Tokai

Workshops held by KEK

4th Progress report meeting of J-PARC MUSE
6 Jun. 2013, KEK Tokai campus, Tokai (50 participants, 21 presentations)

CMRC workshop (Iron Pnictide-Oxides)
8 Jul. 2013, KEK Tsukuba campus, Tsukuba
(50 participants, 8 presentations)

Light and Particle Beams in Materials Science (LPBMS2013)
29–31 Aug. 2013, Tsukuba International Congress Center, Tsukuba
(200 participants, 62 oral and 126 poster presentations)

7th collaboration meeting on muon g-2/EDM experiment at J-PARC
5–7 Dec. 2013, KEK Tsukuba campus and Tokai campus, Ibaraki
(50 participants, 36 presentations)

Workshop co-sponsored and supported by CROSS-Tokai

2013 Workshop on Materials Science
31 Jul. 2013, KENKYUSHA EIGO Center, Tokyo

2013 Ibaraki Society for Promotion of Use of Neutrons Workshop on Texture Evaluation of Metal Material
28 Aug. 2013, KENKYUSHA EIGO Center, Tokyo

1st 2013 Workshop on Neutron Scattering from Soft Matter
6 Sep. 2013, KENKYUSHA EIGO Center, Tokyo

1st 2013 Workshop on Residual Stress and Strain
17 Sep. 2013, KENKYUSHA EIGO Center, Tokyo

2013 Workshop on Metallographic Structure
4 Oct. 2013, KENKYUSHA EIGO Center, Tokyo

1st 2013 Workshop on Structural Biology
9 Oct. 2013, ESSAM Kanda Hole, Tokyo

2013 Ibaraki Society for Promotion of Use of Neutrons Workshop on Texture Evaluation of Metal Material
15 Oct. 2013, Ibaraki Quantum Beam Center, Tokai

2012 The CROSS Trial Use and Ibaraki Beam Line Users Meeting
18 Oct. 2013, Kagaku-kaikan Hall, Tokyo

2013 Ibaraki Society for Promotion of Use of Neutrons Meeting on in situ of Magnet materials structure analysis
22 Oct. 2013, KENKYUSHA EIGO Center, Tokyo

2013 Workshop on Non-destructive Visualization and Analysis Methods
5 Nov. 2013, KENKYUSHA EIGO Center, Tokyo

2013 Ibaraki Society for Promotion of Use of Neutrons Meeting on in situ of Battery materials
2 Dec. 2013, KENKYUSHA EIGO Center, Tokyo

2013 Workshop on Magnetic Materials
20 Dec. 2013, KENKYUSHA EIGO Center, Tokyo

2013 Workshop on Surfaces and Interfaces
17 Jan. 2014, ESSAM Kanda Hall, Tokyo

2013 Ibaraki Society for Promotion of Use of Neutrons Workshop on Organic and Polymeric Materials Neutron Structure Elucidation
30 Jan. 2014, KENKYUSHA EIGO Center, Tokyo

5th Workshop on Analytical Methods In Small Angle Scattering
3 Mar. 2014, KENKYUSHA EIGO Center, Tokyo

2nd 2013 Workshop on Soft Matter Neutron Scattering

4 Mar. 2014, ESSAM Kanda Hall, Tokyo

2nd 2013 Workshop on Residual Stress and Strain

7 Mar. 2014, KENKYUSHA EIGO Center, Tokyo

3rd 2013 Workshop on Soft Matter Neutron Scattering

14 Mar. 2014, ESSAM Kanda Hole, Tokyo

2nd 2013 Workshop on Structural Biology

17 Mar. 2014, KENKYUSHA EIGO Center, Tokyo

Workshops held by CROSS-Tokai

The 7th CROSSroads of Users and J-PARC Functional Interfaces and Reactive Surfaces
20–21 Aug. 2013, Ibaraki Quantum Beam Center, Tokai

The 8th CROSSroads of Users and J-PARC
Neutron Scattering and Nano-second Dynamics - What is the future?
11–12 Nov. 2013, Ibaraki Quantum Beam Center, Tokai

The 9th CROSSroads of Users and J-PARC Superconductivity, Magnetism and Frustration
3–5 Dec. 2013, KEK Tokai campus, Tokai

The 10th CROSSroads of Users and J-PARC Frontier Research on Bio-membranes and Colloids
18–19 Dec. 2013, Ibaraki Quantum Beam Center, Tokai

Seminars and Courses in 2013

Seminars co-convened and supported by CROSS-Tokai with other organizations

Industrial Applications of Neutron Scattering
27 Sep. 2013, Furukawa Electric Co. Ltd., Kanagawa

Synchrotron Radiation-Neutron Linkage Use Seminar in Aichi
15 Jan. 2014, Aichi Center for Industry and Science Technology, Aichi

Industrial Applications of Neutron Scattering
21 Jan. 2014, Nitto Denko Corporation, Osaka

Seminar About The Industrial Application by The Complementarity Use of Synchrotron Radiation and The Neutron in Kobe
24 Feb. 2014, Hyogo Prefecture Citizens' Hall, Hyogo

Short Courses co-sponsored by J-PARC Center, CROSS-Tokai and other organizations

Z-Code Training Course
25–26 Mar. 2014, LMJ Tokyo, Tokyo

Schools in 2013

KEK Summer Challenge
16–25 Aug. 2013, KEK, Tsukuba

Credit : KEK

Award List

The JSNS Outstanding Achievement Prize
Neutron Optics and the Instrumentations
The Japanese Society for Neutron Science
Toru Ebisawa, December 2013

The JSNS Young Researcher Prize
Development of the Magnetic Field Imaging using Polarized Pulsed Neutrons
The Japanese Society for Neutron Science
Takenao Shinohara, December 2013

The JSNS Young Researcher Prize
Development of Model-free Analysis Method on Quasi-elastic Neutron Scattering and Application to Liquid Water
The Japanese Society for Neutron Science
Tatsuya Kikuchi, December 2013

The JSNS Technology Prize
Development of a Chopper Spectrometer with a Pulse-shaping Chopper at a Pulsed Source
The Japanese Society for Neutron Science
Kenji Nakajima, Seiko Kawamura, Katsuhiko Yoshida, Mitsutaka Nakamura, Ryoichi Kajimoto, and Masatoshi Arai, December 2013

平成 24 年度　日本中間子科学会若手奨励賞
μSR による鉄系超伝導体 $CaFe_{1-x}Co_xAsF$ における超伝導と磁性の研究
竹下聡史
平成 25 年 3 月 26 日

平成 26 年度　科学技術分野の文部科学大臣表彰 若手科学者賞
(The Commendation for Science and Technology by the Minister of Education, Culture, Sports, Science and Technology: The Young Scientists' Prize)
地球深部における鉱物中の水素結合と同位体効果の研究
佐野亜沙美
平成 26 年 4 月 15 日

平成 25 年度理事長表彰　研究開発功績賞（日本原子力研究開発機構）
大強度中性子ビームを用いた ^{244}Cm 及び ^{246}Cm の中性子捕獲断面積の高精度化研究
木村敦、古高和禎、原かおる 、原田秀郎、北谷文人、小泉光生、中村詔司、藤暢輔
平成 25 年 10 月 15 日

平成 25 年度理事長表彰　創意工夫功労賞（日本原子力研究開発機構）
大強度パルス中性子対応 $ZnS/^{10}B_2O_3$ セラミックシンチレータ検出器の開発とその実用化
中村龍也、藤健太郎、坂佐井馨、曽山和彦、美留町厚、海老根守澄
平成 25 年 10 月 15 日

平成 25 年度理事長表彰　理事長奨励賞（日本原子力研究開発機構）
国家課題対応型研究開発推進事業―光・量子融合連携研究開発プログラム―
［実用製品中の熱、構造、磁気、元素の直接観察による革新エネルギー機器の実現］
新井正敏
平成 25 年 10 月 15 日

MLF Publication 2013

1 K. Aizawa, W. Gong, S. Harjo, J. Abe, T. Iwahashi, and T. Kamiyama
In-Situ Neutron Diffraction Study on Tensile Behavior of LPSO Mg-Zn-Y Alloys
Materials Transactions **54** 1083 (2013)

2 H. Anzai, A. Ino, M. Arita, H. Namatame, M. Taniguchi, M. Ishikado, K. Fujita, S. Ishida, and S. Uchida
Relation between the nodal and antinodal gap and critical temperature in superconducting Bi2212
Nature Communications **4** 1815 (2013)

3 M. Arai, R. Kajimoto, M. Nakamura, Y. Inamura, K. Nakajima, K. Shibata, N. Takahashi, J. Suzuki, S. Takata, T. Yamada, and S. Itoh
Recent Developments of Instruments in a Spallation Neutron Source at J-PARC and Those Prospects in the Future
Journal of the Physical Society of Japan **82** SA024 (2013)

4 H. Arai, K. Mori, Y. Onodera, T. Fukunaga, M. Yonemura, T. Kamiyama, M. Nagao, and I. S. Torii
Expectation of Analysis Using BL09/SPICA, the World's First Neutron Beamline Dedicated for Battery Analysis
世界初の蓄電池専用中性子ビームライン BL09/SPICA を用いた解析への期待（超の世界）
Journal of Society of Automotive Engineers of Japan/ 自動車技術 **67** 108 (2013)

5 T. Arimori, N. Kawamoto, S. Shinya, N. Okazaki, M. Nakazawa, K. Miyatake, T. Fukamizo, M. Ueda, and T. Tamada
Crystal structures of the catalytic domain of a novel glycohydrolase family 23 chitinase from Ralstonia sp. A-471 reveals a unique arrangement of the catalytic residues for inverting chitin hydrolysis
The Journal of Biological Chemistry **288** 18696 (2013)

6 H. Arita, K. Mitamura, M. Kobayashi, N. L. Yamada, H. Jinnai, and A. Takahara
Chain-mixing behavior at interface between polystyrene brushes and polystyrene matrices
Polymer Journal **45** 117 (2013)

7 S. Asai, R. Okazaki, I. Terasaki, Y. Yasui, W. Kobayashi, A. Nakao, K. Kobayashi, R. Kumai, H. Nakao, Y. Murakami, N. Igawa, A. Hoshikawa, T. Ishigaki, O. Parkkima, M. Karppinen, and H. Yamauchi
Spin State of Co^{3+} in $LaCo_{1-x}Rh_xO_3$ Investigated by Structural Phenomena
Journal of the Physical Society of Japan **82** 114606 (2013)

8 P. Bakule, G. A. Beer, D. Contreras, M. Esashi, Y. Fujiwara, Y. Fukao, S. Hirota, H. Iinuma, K. Ishida, M. Iwasaki, T. Kakurai, S. Kanda, H. Kawai, N. Kawamura, G. M. Marshall, H. Masuda, Y. Matsuda, T. Mibe, Y. Miyake, S. Okada, K. Olchanski, A. Olin, H. Onishi, N. Saito, K. Shimomura, P. Strasser, M. Tabata, D. Tomono, K. Ueno, K. Yokoyama, and S. Yoshida
Measurement of muonium emission from silica aerogel
Progress of Theoretical and Experimental Physics 103C01 (2013)

9 W. Chuajiw, M. Nakano, K. Takatori, T. Kojima, Y. Wakimoto, and Y. Fukushima
Effects of amine, amine salt and amide on the behaviour of carbon dioxide absorption into calcium hydroxide suspension to precipitate calcium carbonate
Journal of Environmental Sciences **25** 2507 (2013)

10 M. Fujita, C. D. Frost, S. M. Bennington, R. Kajimoto, M. Nakamura, Y. Inamura, F. Mizuno, K. Ikeuchi, and M. Arai
Temperature Dependence of Spin Excitations in the Frustrated Spin Chain System $CuGeO_3$
Journal of the Physical Society of Japan **82** 84708 (2013)

11 S. Fujiwara, T. Yamada, T. Matsuo, N. Takahashi, K. Kamazawa, Y. Kawakita, and K. Shibata
Internal Dynamics of a Protein That Forms the Amyloid Fibrils Observed by Neutron Scattering
Journal of the Physical Society of Japan **82** SA019 (2013)

12 S. Ghosh, E. Ohtani, K. D. Litasov, A. Suzuki, D. Dobson, and K. Funakoshi
Effect of water in depleted mantle on post-spinel transition and implication for 660 km seismic discontinuity
Earth and Planetary Science Letters **371–372** 103 (2013)

13 W. Gong, K. Aizawa, S. Harjo, J. Abe, T. Iwahashi, and T. Kamiyama
Neutron Diffraction on LPSO Structure in Mg-Zn-Y Alloys
Materials Transactions **54** 974 (2013)

14 W. Gong, Y. Tomota, Y. Adachi, A. M. Paradowska, J. F. Kelleher, and S. Y. Zhang
Effects of ausforming temperature on bainite transformation, microstructure and variant selection in nanobainite steel
Acta Materialia **61** 4142 (2013)

15 T. Hagiwara, H. Yamamura, K. Nomura, and M. Igawa
Relationship between crystal structure and oxide-ionconduction in $Ln_2Zr_2O_7$ (Ln=Eu, Nd and La) system deduced by neutron and X-ray diffraction
Journal of the Ceramic Society of Japan **121** 205 (2013)

16 T. Hanna, S. Matsuishi, K. Kodama, T. Otomo, S. Shamoto, and H. Hosono
From antiferromagnetic insulator to ferromagnetic metal: Effects of hydrogen substitution in LaMnAsO
Physical Review B **87** 20401 (2013)

17 K. Y. Hara, H. Harada, Y. Toh, and J. Hori
γ-Flash suppression using a gated photomultiplier assembled with an $LaBr_3$(Ce) detector to measure fast neutron capture reactions
Nuclear Instruments and Methods in Physics Research Section A **723** 121 (2013)

18 M. Harada, J. D. Parker, T. Sawano, H. Kubo, T. Tanimori, T. Shinohara, F. Maekawa, and K. Sakai
Quantitative Measurement of Element Distributions using the Neutron-transmission Resonance-absorption Method
Physics Procedia **43** 314 (2013)

19 S. Harjo, N. Tsuchida, W. Gong, J. Abe, and K. Aizawa
TRIP Steel Deformation Behavior by Neutron Diffraction
Materials Research Society Symposium Proceedings **1528** (2013)

20 S. Hasegawa, S. Takahashi, H. Iwase, S. Koizumi, M. Ohnuma, and Y. Maekawa
Crystal morphology-dependent graft polymerization in poly(ether ether ketone) films
Polymer **54** 2895 (2013)

21 H. Hayashida, M. Takeda, D. Yamazaki, R. Maruyama, K. Soyama,

M. Kubota, T. Mizusawa, N. Yoshida, and Y. Sakaguchi
Design and Demonstration of a Neutron Spin Flipper for a New Neutron Reflectometer SHARAKU at J-PARC
Physics Procedia **42** 130 (2013)

22 T. Hemmi, S. Harjo, Y. Nunoya, H. Kajitani, N. Koizumi, K. Aizawa, S. Machiya, and K. Osamura
Neutron diffraction measurement of internal strain in the first Japanese ITER CS conductor sample
Superconductor Science and Technology **26** 84002 (2013)

23 M. Hiroi, T. Hisamatsu, T. Suzuki, K. Ohishi, Y. Ishii, and I. Watanabe
Muon spin relaxation study of spin-glass freezing in the Heusler compound $Ru_{1.9}Fe_{0.1}CrSi$
Physical Review B **88** 24409 (2013)

24 K. Hirose, K. Furutaka, K. Y. Hara, H. Harada, A. Kimura, T. Kin, F. Kitatani, M. Koizumi, S. Nakamura, M. Oshima, Y. Toh, M. Igashira, T. Katabuchi, M. Mizumoto, T. Kamiyama, K. Kino, Y. Kiyanagi, and J. Hori
Cross-section measurement of ^{237}Np (n, γ) from 10 meV to 1 keV at Japan Proton Accelerator Research Complex
Journal of Nuclear Science and Technology **50** 188 (2013)

25 A. Hoshikawa, T. Ishigaki, and M. Yonemura
Development of Automatic Sample Exchange and Transfer System in iMATERTA
iMATERIA における自動試料交換搬送機構の開発
Hamon/ 波紋 **23** 204 (2013)

26 N. Hoshino, F. Iijima, G. N. Newton, N. Yoshida, T. Shiga, H. Nojiri, A. Nakao, R. Kumai, Y. Murakami, and H. Oshio
Three-way Switching in a Cyanide-bridged [FeCo] Chain
熱・光によって磁性・電気伝導性が変化するシアン化物イオン架橋混合原子価 [Fe-Co] 一次元鎖錯体
Photon Factory News **31** 12 (2013)

27 S. Iimura, S. Matsuishi, M. Miyakawa, T. Taniguchi, K. Suzuki, H. Usui, K. Kuroki, R. Kajimoto, M. Nakamura, Y. Inamura, K. Ikeuchi, S. Ji, and H. Hosono
Switching of intra-orbital spin excitations in electron-doped iron pnictide superconductors
Physical Review B **88** 60501 (2013)

28 Y. Ikedo, Y. Miyake, K. Shimomura, P. Strasser, N. Kawamura, K. Nishiyama, S. Makimura, H. Fujimori, A. Koda, J. Nakamura, T. Nagatomo, Y. Kobayashi, T. Adachi, A. D. Pant, T. Ogitsu, T. Nakamoto, K. Sasaki, H. Ohata, R. Okada, A. Yamamoto, Y. Makida, M. Yoshida, T. Okamura, R. Okubo, W. Higemoto, T. U. Ito, K. Nakahara, and K. Ishida
Positron separators in Superomega muon beamline at J-PARC
Nuclear Instruments and Methods in Physics Research Section B **317** 365 (2013)

29 K. Ikeuchi, R. Kajimoto, F. Mizuno, M. Fujita, Y. Inamura, M. Nakamura, K. Nakajima, K. Aizawa, and M. Arai
Anisotropic spin excitations in spin-Peierls $CuGeO_3$
Journal of the Korean Physical Society **63** 333 (2013)

30 K. Ikeuchi, M. Nakamura, R. Kajimoto, and M. Arai
Optimization of a Fermi Chopper for an Inelastic Neutron Spectrometer with Focusing Guide
Journal of the Physical Society of Japan **82** SA038 (2013)

31 Y. Inamura, T. Nakatani, J. Suzuki, and T. Otomo
Development Status of Software "Utsusemi" for Chopper Spectrometers at MLF, J-PARC
Journal of the Physical Society of Japan **82** SA031 (2013)

32 M. Inutsuka, N. L. Yamada, K. Ito, and H. Yokoyama
High Density Polymer Brush Spontaneously Formed by the Segregation of Amphiphilic Diblock Copolymers to the Polymer/ Water Interface
ACS Macro Letters **2** 265 (2013)

33 T. U. Ito, W. Higemoto, T. D. Matsuda, A. Koda, and K. Shimomura
Shallow donor level associated with hydrogen impurities in undoped $BaTiO_3$
Applied Physics Letters **103** (2013)

34 S. Itoh
Anomalous Spin Diffusion in Two-Dimensional Percolating Antiferromagnet
Journal of the Physical Society of Japan **82** SA022 (2013)

35 S. Itoh
Anomalous spin diffusion on the two-dimensional percolating network in $Rb_2Mn_{0.6}Mg_{0.4}F_4$
Journal of the Korean Physical Society **63** 310 (2013)

36 S. Itoh, Y. Endoh, T. Yokoo, D. Kawana, Y. Kaneko, Y. Tokura, and M. Fujita
Neutron Brillouin Scattering with Pulsed Spallation Neutron Source – Spin-Wave Excitations from Ferromagnetic Powder Samples –
Journal of the Physical Society of Japan **82** 43001 (2013)

37 S. Itoh, T. Yokoo, D. Kawana, and Y. Endoh
Neutron Brillouin Scattering on High Resolution Chopper Spectrometer, HRC
Journal of the Physical Society of Japan **82** SA034 (2013)

38 S. Itoh, T. Yokoo, D. Kawana, H. Yoshizawa, T. Masuda, M. Soda, T. J. Sato, S. Satoh, M. Sakaguchi, and S. Muto
Progress in High Resolution Chopper Spectrometer, HRC
Journal of the Physical Society of Japan **82** SA033 (2013)

39 K. Iwasa, H. Kobayashi, T. Onimaru, K. T. Matsumoto, N. Nagasawa, T. Takabatake, S. Ohira-Kawamura, T. Kikuchi, Y. Inamura, and K. Nakajima
Well-Defined Crystal Field Splitting Schemes and Non-Kramers Doublet Ground States of f Electrons in PrT_2Zn_{20} (T= Ir, Rh, and Ru)
Journal of the Physical Society of Japan **82** 43707 (2013)

40 X. Jin, T. Nakamoto, S. Harjo, T. Hemmi, T. Umeno, T. Ogitsu, A. Yamamoto, M. Sugano, K. Aizawa, J. Abe, W. Gong, and T. Iwahashi
Development of a cryogenic load frame for the neutron diffractometer at Takumi in Japan Proton Accelerator Research Complex
Review of Scientific Instruments **84** 063106 (2013)

41 R. Kajimoto, K. Nakajima, S. Ohira-Kawamura, Y. Inamura, K. Kakurai, T. Hokazono, S. Oozono, and T. Okuda
Effects of Mg, Ag, and Al Substitutions on Magnetic Excitations in the Triangular-Lattice Antiferromagnet $CuCrO_2$
Journal of the Physical Society of Japan **82** 54702 (2013)

42 R. Kajimoto, M. Nakamura, Y. Inamura, K. Ikeuchi, S. Ji, K. Nakajima, S. Ohira-Kawamura, W. Kambara, M. Sawabe, A. Kamiya, K. Inoue, T. Futagami, M. Kobayashi, A. Kishi, K. Satou, K. Aizawa, and M. Arai
Recent Improvement of the Signal-to-Noise Ratio on the Fermi Chopper Spectrometer 4SEASONS
Journal of the Physical Society of Japan **82** SA032 (2013)

43 R. Kajimoto, M. Nakamura, K. Nakajima, and M. Fujita
Contamination from the next higher incident energy in inelastic

neutron scattering measurements with multiple incident energies on chopper spectrometers
Nuclear Instruments and Methods in Physics Research Section A **729** 365 (2013)

44 T. Kamiyama, M. Yonemura, S. Torii, M. Nagao, and Y. Ishikawa
Application of Pulsed Neutron for Battery Research
パルス中性子で何ができるか : 蓄電池
Ionizing radiation/ 放射線 **39** 65 (2013)

45 T. Kamiyama, M. Yonemura, S. Torii, M. Nagao, and Y. Ishikawa
J-PARC MLF BL08: 粉末中性子回折装置
Photon Factory News **30** 35 (2013)

46 N. Kawamura, A. Toyoda, M. Aoki, N. Saito, S. Mihara, K. Shimomura, and Y. Miyake
The H line: a brand new beam line for fundamental physics at the J-PARC muon facility
Journal of Physics: Conference Series **408** 12072 (2013)

47 K. Sasaki, M. Sugano, H. Iinuma, T. Ogitsu, N. Saito, K. Shimomura, and A. Yamamoto
Development status of superconducting solenoid for the MuHFS experiment at the J-PARC
Journal of Physics: Conference Series **408** 12074 (2013)

48 T. Kikuchi, K. Nakajima, S. Ohira-Kawamura, Y. Inamura, O. Yamamuro, M. Kofu, Y. Kawakita, K. Suzuya, M. Nakamura, and M. Arai
Mode-distribution analysis of quasielastic neutron scattering and application to liquid water
Physical Review E **87** 62314 (2013)

49 H. Kinoshita, M. Kaminaga, K. Haga, A. Terada, and R. Hino
Experimental study on heat transfer and pressure drop in mercury flow system for spallation neutron source
Journal of Nuclear Science and Technology **50** 400 (2013)

50 Y. Kobayashi, T. Iida, K. Suzuki, T. Kawamata, M. Itoh, and M. Sato
^{75}As NQR and NMR Studies on the Superconducting State of $Ca_{10}Pt_4As_8(Fe_{1-x}Pt_xAs)_{10}$
Journal of the Physical Society of Japan **83** 014712 (2013)

51 Y. Kobayashi, A. Ichikawa, M. Toyoda, M. Itoh, and M. Sato
In-plane anisotropy of the magnetic and the electric properties of the Fe pnictide $Ba(Fe_{1-x}Co_x)_2As_2$
Journal of the Korean Physical Society **63** 481 (2013)

52 Y. Kobayashi, S. Saiki, S. Kototani, M. Itoh, and M. Sato
Phase separation of antiferromagnetism and superconductivity in $Rb_xFe_{2-y}Se_2$ observed by using Rb NMR
Journal of the Korean Physical Society **63** 448 (2013)

53 K. Kodama, N. Igawa, S. Shamoto, K. Ikeda, H. Oshita, N. Kaneko, T. Otomo, and K. Suzuya
Local Lattice Distortion Caused by Short Range Charge Ordering in $LiMn_2O_4$
Journal of the Physical Society of Japan **82** 94601 (2013)

54 M. Kofu, T. Kajiwara, J. S. Gardner, G. G. Simeoni, M. Tyagi, A. Faraone, K. Nakajima, S. Ohira-Kawamura, M. Nakano, and O. Yamamuro
Magnetic relaxations in a Tb-based single molecule magnet studied by quasielastic neutron scattering
Chemical Physics **427** 147 (2013)

55 M. Kofu, O. Yamamuro, T. Kajiwara, Y. Yoshimura, M. Nakano, K. Nakajima, S. Ohira-Kawamura, T. Kikuchi, and Y. Inamura
Hyperfine structure of magnetic excitations in a Tb-based single-molecule magnet studied by high-resolution neutron spectroscopy
Physical Review B **88** 64405 (2013)

56 K. Kojima
PSI 流 μSR データ解析ツール "musrfit"
日本中間子科学会 めそん **38** 37 (2013)

57 K. Komatsu, M. Moriyama, T. Koizumi, K. Nakayama, H. Kagi, J. Abe, and S. Harjo
Development of a new P–T controlling system for neutron-scattering experiments
High Pressure Research **33** 208 (2013)

58 S. Kubota, D. Naito, Y. Tomota, S. Harjo, C. Iio, and S. Yamaguch
Effect of Microstructure on Mechanical Properties and Machinability of Spheroidal Graphite Cast Iron
球状黒鉛鋳鉄の機械的性質と切削性に及ぼすミクロ組織の影響
Journal of Japan Foundry Engineering Society/ 鋳造工学 **85** 489 (2013)

59 M. Kureta, A. Ohzu, M. Haruyama, M. Takase, N. Kurata, N. Kobayashi, K. Soyama, T. Nakamura, H. Nakamura, and M. Seya
Design of an Alternative Plutonium Canister Assay system (APCA) using ceramic scintillator neutron detectors for the safeguards NDA
Proceedings of the 54th INMM Annual Meeting #176 (2013)

60 K. Kusaka, T. Hosoya, T. Yamada, K. Tomoyori, T. Ohhara, M. Katagiri, K. Kurihara, I. Tanaka, and N. Niimura
Evaluation of performance for IBARAKI biological crystal diffractometer iBIX with new detectors
Journal of Synchrotron Radiation **20** 994 (2013)

61 T. Kusano, H. Iwase, K. Akutsu, T. Yoshimura, and M. Shibayama
Structural Study of Organic Salts Effect on the Trimeric Surfactant Aggregates
構造学的視点から観た三鎖界面活性剤会合体への塩効果の考察
Photon Factory News **31** 9 (2013)

62 K. D. Litasov, I. S. Sharygin, P. I. Dorogokupets, A. Shatskiy, P. N. Gavryushkin, T. S. Sokolova, E. Ohtani, J. Li, and K. Funakoshi
Thermal equation of state and thermodynamic properties of iron carbide Fe_3C to 31 GPa and 1473 K
Journal of Geophysical Research: Solid Earth **118** 5274 (2013)

63 K. D. Litasov, A. Shatskiy, P. N. Gavryushkin, I. S. Sharygin, P. I. Dorogokupets, A. M. Dymshits, E. Ohtani, Y. Higo, and K. Funakoshi
P–V–T equation of state of siderite to 33 GPa and 1673 K
Physics of the Earth and Planetary Interiors **224** 83 (2013)

64 Z. L. Mahyari, A. Cannell, E. V. L. de Mello, M. Ishikado, H. Eisaki, R. Liang, D. A. Bonn, and J. E. Sonier
Universal inhomogeneous magnetic-field response in the normal state of cuprate high-Tc superconductors
Physical Review B **88** 144504 (2013)

65 M. Martin, and S. Jun
Muon-spin relaxation study on Li- and Na-diffusion in solids
Physica Scripta **88** 68509 (2013)

66 G. Matsuba, M. Sakurai, T. Tominaga, and S. Takata
Shish-kebab formation process observation using new SANS spectrometer TAIKAN
Proceedings of The 12th Asian Textile Conference 55 (2013)

67 K. Matsuda, T. Nagao, Y. Kajihara, M. Inui, K. Tamura, J. Nakamura, K. Kimura, M. Yao, M. Itou, Y. Sakurai, and N.

Hiraoka
Electron momentum density in liquid silicon
Physical Review B **88** 115125 (2013)

68 M. Medarde, M. Mena, J. L. Gavilano, E. Pomjakushina, J. Sugiyama, K. Kamazawa, V. Y. Pomjakushin, D. Sheptyakov, B. Batlogg, H. R. Ott, M. Månsson, and F. Juranyi
1D to 2D Na Ion Diffusion Inherently Linked to Structural Transitions in $Na_{0.7}CoO_2$
Physical Review Letters **110** 266401 (2013)

69 S. Meigo, M. Ooi, A. Akutsu, K. Ikezaki, H. Fujimori
Development of beam flattening system using non-linear beam optics at J-PARC
Proceedings of International Topical Meeting on Nuclear Applications of Accelerators TUPAT06 (2013)

70 S. Meigo, M. Ooi, K. Ikezaki, A. Akutsu, S. Sakamoto, M. Futakawa
Development of profile monitor system for high intense spallation neutron source
Proceedings of International Beam Instrumentaion Conference, IBIC2012 MOPB68 (2013)

71 K. Mitamura, N. L. Yamada, H. Sagehashi, N. Torikai, H. Arita, M. Terada, M. Kobayashi, S. Sato, H. Seto, S. Goko, M. Furusaka, T. Oda, M. Hino, H. Jinnai, and A. Takahara
Novel neutron reflectometer SOFIA at J-PARC/MLF for in-situ soft-interface characterization
Polymer Journal **45** 100 (2013)

72 Y. Miyake, Y. Ikedo, K. Shimomura, P. Strasser, N. Kawamura, K. Nishiyama, A. Koda, H. Fujimori, S. Makimura, J. Nakamura, T. Nagatomo, R. Kadono, E. Torikai, M. Iwasaki, S. Wada, N. Saito, K. Okamura, K. Yokoyama, T. Ito, and W. Higemoto
Ultra slow muon microscopy by laser resonant ionization at J-PARC, MUSE
Hyperfine Interactions **216** 79 (2013)

73 K. Mukai, Y. Ikedo, K. Kamazawa, J. H. Brewer, E. J. Ansaldo, K. H. Chow, M. Mansson, and J. Sugiyama
The gradient distribution of Ni ions in cation-disordered $Li[Ni_{1/2}Mn_{3/2}]O_4$ clarified by muon-spin rotation and relaxation (μSR)
RSC Advances **3** 11634 (2013)

74 D. Naito, S. Kubota, S. Harjo, and Y. Tomota
In Situ Neutron Diffraction during Tension-Compression Deformation for Nodular Graphite Cast Irons
ISIJ International **53** 1292 (2013)

75 T. Nakamura, K. Toh, T. Kawasaki, K. Honda, H. Suzuki, M. Ebine, A. Birumachi, K. Sakasai, K. Soyama, and M. Katagiri
Evaluation of angular dependence of neutron detection efficiencies of ZnS scintillator detectors
IEEE Nuclear Science Symposium Conference Record NPO1-211 (2013)

76 T. Nakamura, K. Toh, K. Sakasai, H. Suzuki, K. Soyama, M. Kureta, A. Ohzu, M. Takase, H. Nakamura, and M. Seya
Development of a ZnS/$^{10}B_2O_3$ ceramic scintillator neutron detector for safeguards NDA systems
Proceedings of the 54th INMM Annual Meeting #227 (2013)

77 T. Naoe, and M. Futakawa
Optically observation of mercury cavitation bubble collapsing
Experimental Thermal and Fluid Science **44** 550 (2013)

78 K. Nishida, Y. Kono, H. Terasaki, S. Takahashi, M. Ishii, Y. Shimoyama, Y. Higo, K. Funakoshi, T. Irifune, and E. Ohtani
Sound velocity measurements in liquid Fe–S at high pressure: Implications for Earth's and lunar cores
Earth and Planetary Science Letters **362** 182 (2013)

79 Y. Noda, D. Yamaguchi, A. Putra, S. Koizumi, Y. Sakaguchi, T. Oku, and J. Suzuki
Polarization Analysis Equipment in SANS-J-II: Study of Polymer Electrolyte Membrane for Fuel Cell
Physics Procedia **42** 46 (2013)

80 H. Nozaki, M. Harada, S. Ohta, N. H. Jalarvo, E. Mamontov, I. Watanabe, Y. Miyake, Y. Ikedo, and J. Sugiyama
Diffusive Behavior of Li Ions in Garnet $Li_{5+x}La_3Zr_xNb_{2-x}O_{12}$ (x = 0–2)
Journal of the Physical Society of Japan **82** SA004 (2013)

81 H. Nozaki, M. Månsson, B. Roessli, V. Pomjakushin, K. Kamazawa, Y. Ikedo, H. E. Fischer, T. C. Hansen, H. Yoshida, Z. Hiroi, and J. Sugiyama
Magnetic structure of the metallic triangular antiferromagnet Ag_2NiO_2
Journal of Physics: Condensed Matter **25** 286005 (2013)

82 Y. Ogata, D. Kawaguchi, N. L. Yamada, and K. Tanaka
Multistep Thickening of Nafion Thin Films in Water
ACS Macro Letters **2** 856 (2013)

83 S. Ogo, K. Ichikawa, T. Kishima, T. Matsumoto, H. Nakai, K. Kusaka, and T. Ohhara
A Functional [NiFe]Hydrogenase Mimic That Catalyzes Electron and Hydride Transfer from H_2
Science **339** 682 (2013)

84 K. Ohishi, M. Sato, S. Kototani, S. Saiki, Y. Kobayashi, and M. Itoh
Magnetism and superconductivity in $Rb_xFe_{2-y}Se_2$
Journal of the Korean Physical Society **62** 1994 (2013)

85 K. Ohoyama, T. Yokoo, S. Itoh, J. Suzuki, K. Iwasa, T. J. Sato, H. Kira, Y. Sakaguchi, T. Ino, T. Oku, K. Tomiyasu, M. Matsuura, H. Hiraka, M. Fujita, H. Kimura, T. Sato, J. Suzuki, H. M. Shimizu, T. Arima, M. Takeda, K. Kaneko, M. Hino, S. Muto, H. Nojiri, C. H. Lee, J. G. Park, and S. Choi
Basic Concepts of Polarisation Analysis for Neutron Chopper Spectrometer POLANO at J-PARC
Journal of the Physical Society of Japan **82** SA036 (2013)

86 A. Ohzu, T. Nakamura, M. Takase, N. Kurata, M. Haruyama, M. Kureta, K. Soyama, and M. Seya
Optical guide property of alternative He-3 neutron detectors using solid scintillators for nuclear safeguards
IEEE Nuclear Science Symposium Conference Record NPO1-195 (2013)

87 T. Okuchi, M. Yoshida, Y. Ohno, N. Tomioka, N. Purevjav, T. Osakabe, S. Harjo, J. Abe, K. Aizawa, and S. Sasaki
Pulsed neutron powder diffraction at high pressure by a capacity-increased sapphire anvil cell
High Pressure Research **33** 777 (2013)

88 T. Okuda, R. Kajimoto, M. Okawa, and T. Saitoh
Effects of Hole-Doping and Disorder on the Magnetic States of Delafossite $CuCrO_2$ Having a Spin-3/2 Antiferromagnetic Triangular Sublattice
International Journal of Modern Physics B **27** (2013)

89 M. Ooi, K. Sakai, A. Watanabe, A. Akutsu, and S. M. Takada
UPGRADE OF J-PARC/MLF GENERAL CONTROL SYSTEM WITH EPICS/CSS
Proceedings of ICALEPCS2013 MOPPC017 (2013)

90 M. Ooi, M. Teshigawara, T. Kai, M. Harada, F. Maekawa, M. Futakawa, E. Hashimoto, M. Segawa, M. Kureta, A. Tremsin, T. Kamiyama, and Y. Kiyanagi
Neutron Resonance Imaging of a Au-In-Cd Alloy for the JSNS
Physics Procedia **43** 337 (2013)

91 K. Osamura, S. Machiya, Y. Tsuchiya, H. Suzuki, T. Shobu, M. Sato, S. Harjo, K. Miyashita, Y. Wadayama, S. Ochiai, and A. Nishimura
Thermal strain exerted on superconductive filaments in practical Nb_3Sn and Nb_3Al strands
Superconductor Science and Technology **26** 94001 (2013)

92 T. Otomo, K. Ikeda, H. Ohshita, and K. Suzuya
Studies of Hydrogen Storage Mechanism with High Intensity Neutron Total Scattering
高強度中性子を用いた全散乱法による水素貯蔵機構の解明
Materia Japan/ まてりあ **52** 346 (2013)

93 S.-W. Park, H. Mizoguchi, K. Kodama, S. Shamoto, T. Otomo, S. Matsuishi, T. Kamiya, and H. Hosono
Magnetic Structure and Electromagnetic Properties of LnCrAsO with a ZrCuSiAs-type Structure (Ln = La, Ce, Pr, and Nd)
Inorganic Chemistry **52** 13363 (2013)

94 J. D. Parker, M. Harada, K. Hattori, S. Iwaki, S. Kabuki, Y. Kishimoto, H. Kubo, S. Kurosawa, Y. Matsuoka, K. Miuchi, T. Mizumoto, H. Nishimura, T. Oku, T. Sawano, T. Shinohara, J. Suzuki, A. Takada, T. Tanimori, and K. Ueno
Spatial resolution of a μPIC-based neutron imaging detector
Nuclear Instruments and Methods in Physics Research Section A **726** 155 (2013)

95 J. D. Parker, M. Harada, K. Hattori, S. Iwaki, S. Kabuki, Y. Kishimoto, H. Kubo, S. Kurosawa, Y. Matsuoka, K. Miuchi, T. Mizumoto, H. Nishimura, T. Oku, T. Sawano, T. Shinohara, J. Suzuki, A. Takada, T. Tanimori, K. Ueno, M. Ikeno, M. Tanaka, and T. Uchida
Development of a Time-resolved Neutron Imaging Detector Based on the μPIC Micro-Pixel Chamber
μPIC (Micro-Pixel Chamber) を用いた中性子イメージング検出器の開発
Hamon/ 波紋 **23** 218 (2013)

96 J. D. Parker, K. Hattori, H. Fujioka, M. Harada, S. Iwaki, S. Kabuki, Y. Kishimoto, H. Kubo, S. Kurosawa, K. Miuchi, T. Nagae, H. Nishimura, T. Oku, T. Sawano, T. Shinohara, J. Suzuki, A. Takada, T. Tanimori, and K. Ueno
Neutron imaging detector based on the micro-pixel chamber
Nuclear Instruments and Methods in Physics Research Section A **697** 23 (2013)

97 K. Sadakane, M. Nagao, H. Endo, and H. Seto
Membrane formation by preferential solvation of ions in mixture of water, 3-methylpyridine, and sodium tetraphenylborate
The Journal of Chemical Physics **139** (2013)

98 T. Sakamaki, A. Suzuki, E. Ohtani, H. Terasaki, S. Urakawa, Y. Katayama, K. Funakoshi, Y. Wang, J. W. Hernlund, and M. D. Ballmer
Ponded melt at the boundary between the lithosphere and asthenosphere
Nature Geoscience **6** 1041 (2013)

99 K. Sakasai, K. Toh, T. Nakamura, K. Takakura, C. Konno, and Y. Iwamoto
Application of KCl:Eu^{2+} Storage Phosphors to Wide-range Neutron Detection
IEEE Nuclear Science Symposium Conference Record NPO1-26 (2013)

100 S. Lee, J. R. Zhang, S. Torii, S. Choi, D. Y. Cho, T. Kamiyama, J. Yu, K. A. McEwen, and J. G. Park
Large in-plane deformation of RuO_6 octahedron and ferromagnetism of bulk $SrRuO_3$
Journal of Physics: Condensed Matter **25** 465601 (2013)

101 S. Sanna, P. Carretta, R. De Renzi, G. Prando, P. Bonfà, M. Mazzani, G. Lamura, T. Shiroka, Y. Kobayashi, and M. Sato
Onset of magnetism in optimally electron-doped L $Fe_{1-x}Ru_xAsO_{1-y}F_y$ (L=La, Nd, or Sm) superconductors around x =1/4
Physical Review B **87** 134518 (2013)

102 K. Sasaki, M. Sugano, R. Ohkubo, T. Ogitsu, N. Saito, K. Shimomura, and A. Yamamoto
Superconducting Magnet Design for the Hyperfine Structure Measurement of Muonium at the J-PARC
Applied Superconductivity, IEEE Transactions on **23** 4500704 (2013)

103 M. Sato, Y. Kobayashi, T. Kawamata, Y. Yasui, K. Suzuki, M. Itoh, R. Kajimoto, K. Ikeuchi, M. Arai, and P. Bourges
On the superconducting symmetry of Fe-based systems — Impurity effect studies and neutron scattering measurements
Journal of the Korean Physical Society **62** 1726 (2013)

104 K. Sato, M. Matsuura, M. Fujita, R. Kajimoto, S. Ji, K. Ikeuchi, M. Nakamura, Y. Inamura, M. Arai, M. Enoki, and K. Yamada
High-energy magnetic excitations in underdoped $La_{1.90}Sr_{0.10}CuO_4$
Journal of the Korean Physical Society **62** 1836 (2013)

105 M. Sato, Y. Kobayashi, T. Kawamata, Y. Yasui, K. Suzuki, M. Itoh, R. Kajimoto, K. Ikeuchi, M. Arai, and P. Bourges
On the superconducting symmetry of Fe-based systems — Impurity effect studies and neutron scattering measurements
Journal of the Korean Physical Society **62** 1726 (2013)

106 M. Segawa, T. Kai, T. Sakai, M. Ooi, and M. Kureta
Development of a high-speed camera system for neutron imaging at a pulsed neutron source
Nuclear Instruments and Methods in Physics Research Section A **697** 77 (2013)

107 A. Shatskiy, I. S. Sharygin, P. N. Gavryushkin, K. D. Litasov, Y. M. Borzdov, A. V. Shcherbakova, Y. Higo, K. Funakoshi, Y. N. Palyanov, and E. Ohtani
The system K_2CO_3-$MgCO_3$ at 6 GPa and 900–1450 °C
American Mineralogist **98** 1593 (2013)

108 A. Shatskiy, P. N. Gavryushkin, I. S. Sharygin, K. D. Litasov, I. N. Kupriyanov, Y. Higo, Y. M. Borzdov, K.-i. Funakoshi, Y. N. Palyanov, and E. Ohtani
Melting and subsolidus phase relations in the system Na_2CO_3-$MgCO_3$±H_2O at 6 GPa and the stability of $Na_2Mg(CO_3)_2$ in the upper mantle
American Mineralogist **98** 2172 (2013)

109 P. Strasser, Y. Ikedo, Y. Miyake, K. Shimomura, N. Kawamura, K. Nishiyama, S. Makimura, H. Fujimori, A. Koda, J. Nakamura, T. Nagatomo, T. Adachi, A. D. Pant, T. Ogitsu, Y. Makida, M. Yoshida, K. Sasaki, T. Okamura, H. Ohhata, T. Nakamoto, R. Okada, R. Ohkubo, A. Yamamoto, W. Higemoto, T. U. Itoh, K. Ishida, and K. Nakahara
Superconducting curved transport solenoid with dipole coils for charge selection of the muon beam
Nuclear Instruments and Methods in Physics Research Section B **317** 361 (2013)

110 M. Sugano, K. Sasaki, R. Ohkubo, T. Kume, N. Kimura, R. Okada, T. Okamura, K. Shimomura, N. Saito, T. Ogitsu, and A. Yamamoto
Cryogenic Design of a Superconducting Solenoid for Muonium

Hyperfine Structure Measurement
IEEE Transactions on Applied Superconductivity **23** 3800204 (2013)

111 M. Sugawara, T. Hayakawa, M. Oshima, Y. Toh, A. Osa, M. Matsuda, T. Shizuma, Y. Hatsukawa, H. Kusakari, T. Morikawa, Z. G. Gan, and T. Czosnyka
Possible band termination in ^{99}Rh
Physical Review C **87** 64319 (2013)

112 J. Sugiyama
Ion Diffusion in Solids Probed by Muon-Spin Spectroscopy
Journal of the Physical Society of Japan **82** SA023 (2013)

113 H. Suzuki, and S. Harjo
Neutron diffraction studies on strain-dependence of superconducting properties in practical superconducting composite
Neutron News **24** 18 (2013)

114 H. Suzuki, S. Harjo, J. Abe, P. Xu, K. Aizawa, and K. Akita
Effects of gauge volume on pseudo-strain induced in strain measurement using time-of-flight neutron diffraction
Nuclear Instruments and Methods in Physics Research Section A **715** 28 (2013)

115 S. Takahashi, E. Ohtani, H. Terasaki, Y. Ito, Y. Shibazaki, M. Ishii, K. Funakoshi, and Y. Higo
Phase relations in the carbon-saturated C–Mg–Fe–Si–O system and C and Si solubility in liquid Fe at high pressure and temperature: implications for planetary interiors
Physics and Chemistry of Minerals **40** 647 (2013)

116 S. Takai, Y. Doi, S. Torii, J. Zhang, T. Y. S. P. Putra, P. Miao, T. Kamiyama, and T. Esaka
Structural and electrical properties of Pb-substituted $La_2Mo_2O_9$ oxide ion conductors
Solid State Ionics **238** 36 (2013)

117 S. Takai, T. Esaka, and T. Kamiyama
Defect Structure and Oxide-Ion Conduction Properties of Pb-Substituted $La_2Mo_2O_9$
Pb を添加した $La_2Mo_2O_9$ の欠陥構造と酸化物イオン伝導特性
Photon Factory News **31** 27 (2013)

118 I. Tanaka, and K. Kusaka
Biomacromolecular Neutron Crystallography
Sample Preparation, Diffractometers, Measurements and Data Reduction for Neutron Protein Crystallography
生体分子の中性子単結晶解析
タンパク質中性子結晶構造解析のための試料作成、回折計、測定およびデータ処理
Hamon/ 波紋 **23** 288 (2013)

119 Y. Toh, C. J. Chiara, E. A. McCutchan, W. B. Walters, R. V. F. Janssens, M. P. Carpenter, S. Zhu, R. Broda, B. Fornal, B. P. Kay, F. G. Kondev, W. Królas, T. Lauritsen, C. J. Lister, T. Pawłat, D. Seweryniak, I. Stefanescu, N. J. Stone, J. Wrzesiński, K. Higashiyama, and N. Yoshinaga
Evidence for rigid triaxial deformation at low energy in ^{76}Ge
Physical Review C **87** 41304 (2013)

120 K. Toh, T. Nakamura, K. Sakasai, K. Soyama, M. Hino, M. Kitaguchi, and H. Yamagishi
Development of two-dimensional multiwire-type neutron detector system with individual line readout and optical signal transmission
Nuclear Instruments and Methods in Physics Research Section A **726** 169 (2013)

121 Y. Tomota, and S. Harjo
Deformation Behavior of Ferrous Materials Studied by Using Neutron Diffraction
中性子回折を用いた鉄系材料の変形特性の解析
Journal of the JSTP/ 塑性と加工 **54** 891 (2013)

122 K. Tomoyori, K. Kusaka, T. Yamada, T. Hosoya, T. Ohhara, K. Kurihara, I. Tanaka, M. Katagiri, and N. Niimura
Profile functions to reproduce Bragg reflection shapes observed by a time-of-flight single-crystal diffractometer installed at a coupled moderator pulsed neutron source in J-PARC
Nuclear Instruments and Methods in Physics Research Section A **723** 128 (2013)

123 N. Tsujino, Y. Nishihara, Y. Nakajima, E. Takahashi, K.-i. Funakoshi, and Y. Higo
Equation of state of γ-Fe: Reference density for planetary cores
Earth and Planetary Science Letters **375** 244 (2013)

124 T. Wakui, H. Ishii, T. Naoe, T. Wan, X. Zhihong, K. Haga, H. Takada, and M. Futakawa
Investigation on HIP diffusion bonding of invar ally to stainless steel
Proceedings of IJST2013 85 (2013)

125 T. Wan, T. Wakui, T. Naoe, M. Futakawa, K. Kawashima, and K. Maekawa
Pitting damage imaging by non-linear ultrasonic technique: comparison between resonance and non-resonance modes
International Journal of Materials and Product Technology **46** 141 (2013)

126 T. Wan, T. Wakui, T. Naoe, M. Futakawa, and K. Maekawa
A Novel Ultrasonic Evaluation Process for Cavitation Damage by Combination of Attenuation and Higher Harmonics
Journal of JSEM/ 実験力学 **13** 387 (2013)

127 H. Wang, C. Yang, J. Lu, M. Wu, J. Su, K. Li, J. Zhang, G. Li, T. Jin, T. Kamiyama, F. Liao, J. Lin, and Y. Wu
On the Structure of α-$BiFeO_3$
Inorganic Chemistry **52** 2388 (2013)

128 R. Wang, C. Yang, M. Fan, M. Wu, C. Wang, X. Yu, J. Zhu, J. Zhang, G. Li, Q. Huang, D. Chen, T. Jin, T. Kamiyama, F. Liao, and J. Lin
Phase relationship of the $TbO_{1.81}$–Mn_3O_4–Fe_2O_3 system synthesized at 1200°C
Journal of Alloys and Compounds **554** 385 (2013)

129 A. Watanabe, K. Sakai, M. Ooi, S. Meigo, and H. Takada
Upgrade of general control system employed for Materials and Life Science Experimental Facility of J-PARC
J-PARC 物質・生命科学実験施設の全体制御システムのアップグレード
JAEA-Technology 2013-028 (2013)

130 T. Xia, H. Ogawa, R. Inoue, K. Nishida, N. L. Yamada, G. Li, and T. Kanaya
Dewetting Process of Deuterated Polystyrene and Poly(vinyl methyl ether) Blend Thin Films via Phase Separation
Macromolecules **46** 4540 (2013)

131 N. Yabuuchi, Y. Kawamoto, R. Hara, T. Ishigaki, A. Hoshikawa, M. Yonemura, T. Kamiyama, and S. Komaba
A Comparative Study of $LiCoO_2$ Polymorphs: Structural and Electrochemical Characterization of O^{2-}, O^{3-}, and O^{4-}type Phases
Inorganic Chemistry **52** 9131 (2013)

132 T. Yamada, T. Yamada, M. Tyagi, M. Nagao, H. Kitagawa, and O. Yamamuro
Phase Transition and Dynamics of Water Confined in Hydroxyethyl Copper Rubeanate Hydrate

Journal of the Physical Society of Japan **82** SA010 (2013)

133 S. Yano, S. Itoh, T. Yokoo, S. Satoh, D. Kawana, Y. Kousaka, J. Akimitsu, and Y. Endoh
Magnetic excitations in ferromagnetic phase of MnP
Journal of Magnetism and Magnetic Materials **347** 33 (2013)

134 T. Yokoo, K. Ohoyama, S. Itoh, J. Suzuki, K. Iwasa, T. J. Sato, H. Kira, Y. Sakaguchi, T. Ino, T. Oku, K. Tomiyasu, M. Matsuura, H. Hiraka, M. Fujita, H. Kimura, T. Sato, J. Suzuki, M. Takeda, K. Kaneko, M. Hino, and S. Muto
Newly Proposed Inelastic Neutron Spectrometer POLANO
Journal of the Physical Society of Japan **82** SA035 (2013)

135 T. Yokoyama, M. Mizuguchi, and K. Kusaka
Hydrogen-bond Network and pH Sensitivity in Transthyretin
トランスサイレチンにおける水素結合ネットワークと pH 感受性
Hamon/ 波紋 **23** 142 (2013)

136 T. Yokoyama, M. Mizuguchi, Y. Nabeshima, K. Kusaka, T. Yamada, T. Hosoya, T. Ohhara, K. Kurihara, I. Tanaka, and N. Niimura
Hydrogen-bond network and pH sensitivity in human transthyretin
Journal of Synchrotron Radiation **20** 834 (2013)

137 M. Yonemura
BL09"Special Environment Neutron Powder Diffractometer (SPICA)"
BL09「特殊環境中性子回折装置（SPICA）」
SHIKI (Industrial Users Society for Neutron Application) / 中性子産業利用推進協議会季報「四季」**19** 2 (2013)

138 T. Yoshiie, M. Futakawa, T. Naoe, M. Komatsu, K. Sato, Q. Xu, and M. Kawai
Pitting Damage in Metals by Mercury Cavitation with MIMTM
MIMTM を用いた水銀キャビテーションによる金属の壊食損傷構造
Materia Japan/ まてりあ **52** 390 (2013)

139 J. Zhu, W. Han, J. Zhang, H. Xu, S. C. Vogel, C. Jin, F. Izumi, K. Momma, Y. Kawamura, and Y. Zhao
Nuclear and charge density distributions in ferroelectric $PbTiO_3$: maximum entropy method analysis of neutron and X-ray diffraction data
Powder Diffraction **28** 276 (2013)

Editorial Board - MLF Annual Report 2013

J-PARC 14-03
KEK Progress Report 2014-4

J-PARC/MLF

Materials and Life Science Division
J-PARC Center
Tokai, Naka-gun, Ibaraki 319-1195, Japan
http://j-parc.jp/MatLife/en/index.html

CROSS

Comprehensive Research Organization for Science and Society
http://www.cross-tokai.jp/